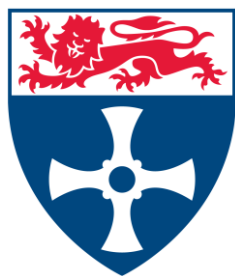


Hybrid dye-sensitised photocathodes for photoelectrochemical hydrogen evolution

Nils Põldme

A thesis submitted for the degree of
Doctor of Philosophy in Chemistry



School of Natural and Environmental Sciences

Newcastle University

September 2019

Abstract

Nanostructured materials offer new, cost-efficient and sustainable opportunities for converting sunlight into electricity and fuels. The complexity of photoelectrochemical water splitting needs thorough understanding of the system and new ideas to overcome the limiting factors in the process. My work has been focused on investigating new hybrid dye-sensitised photocathodes for photoelectrochemical water splitting and developing a system that enables efficient photoelectrochemical H₂ production.

Firstly, the effect of the experimental environment to photoelectrochemical performance of the dye-sensitised NiO photocathode was investigated. For that, an optimal electron acceptor for photocurrent generation was chosen and applied in all experiments, while changing the experimental conditions. The effect of electrolyte composition, the pH of the electrolyte and the concentration of the electron acceptor were studied. It was observed that the highest photocurrent was obtained with 4,4'-dithiodipyridine electron acceptor with 5 mM concentration in pH 3 aqueous electrolyte. After determining the optimal conditions for photocurrent generation using the most robust dye available, the system was tested for H₂ evolution with electrodeposited Pt catalyst. In addition, the NiO photocathode was tested with another dye with a polymeric structure and with a commercially available benchmark organic dye. Both systems were studied photoelectrochemically under the optimal conditions determined previously and also tested for H₂ evolution with electrodeposited catalysts on the surface. The highest photocurrents were observed with the commercially available benchmark organic dye with an electron acceptor and H₂ evolution was also shown on the same system with catalyst on the surface.

Secondly, a new approach to increase the faradaic efficiency of dye-sensitised photocathodes for H₂ evolution from water was investigated using integrated photocatalysts. Superiority to previously reported photocathodes was demonstrated, producing photocurrent densities of 30–35 $\mu\text{A cm}^{-2}$ at an applied bias of -0.2 V vs. Ag/AgCl over 1 hour of continuous white light irradiation, resulting in the generation of 0.41 mmol h⁻¹ cm⁻² of H₂ with faradaic efficiencies of up to 90%. Surface analysis of the photocathodes before and after photoelectrocatalysis revealed that the photocatalyst was photochemically stable, highlighting the benefits of the approach towards robust, hybrid solar-to-fuel devices.

Furthermore, CuCrO_2 as an alternative material to NiO was studied as a photocathode for photoelectrochemical H_2 evolution. The aim was to show that the post-calcination of the photocathodes under N_2 atmosphere changes the surface chemistry of the CuCrO_2 photocathodes which translates into superior stability and efficiency. The origin of these properties was discussed with the help of X-ray photoelectron spectroscopy surface analysis. Stable H_2 production on the CuCrO_2 photocathode from aqueous buffer solution was shown and the efficiency of the process was further increased with the use of inorganic cobalt co-catalyst in solution. In addition, successful sensitisation of the CuCrO_2 photocathode with an organic dye was demonstrated resulting in considerable increase in photocurrent when using an electron acceptor in solution. An additional study was made where Fe was added to the CuCrO_2 to form $\text{CuCr}_{0.5}\text{Fe}_{0.5}\text{O}_2$ mixed metal delafossite. The aim of this study was to see how the Fe^{3+} addition to the delafossite crystal lattice influences the photoelectrochemical performance and stability of the material.

Finally, the photoelectrochemical cell was modelled and studied by building a simplified model in COMSOL Multiphysics and changing the exchange current density value on the electrode-electrolyte boundary based on experimental data obtained from photoelectrochemical measurement with different systems presented in this thesis. Results obtained from the model were discussed along with discussion on future optimisation possibilities of the model to increase the output of meaningful data.

Acknowledgements

Firstly, I would like to thank my supervisor Dr. Elizabeth Gibson for giving me the opportunity to conduct research in the exciting field of solar hydrogen production and for guidance throughout my PhD project. I highly value her opinion and I am grateful for the numerous opportunities she gave me to travel and broaden my scientific horizon to explore new areas of research.

Secondly, I would like to thank my second supervisor Dr. Prodip Das for helping me with my project and for advice on overall questions related to the work as a starting researcher. I am very grateful for all his help and advice.

I would like to thank my colleagues and friends in the Gibson group, past and present, who helped me throughout my years in Newcastle and who gave me valuable support and advice when it was needed. I would like to give my special thanks John, Heather, Richard, Nathan, Gareth, Fiona, Dumitru, Elisabetta, Kripa, and Zhiji. Thank you for making my PhD experience exciting and enjoyable. Especially, I would like to thank Chris, for being an amazing friend and supporting me with good advice and company.

I would like to thank our collaborators Laura O'Reilly and Mary Pryce in Dublin City University, with whom I was able to publish my first article. I would also like to thank Guillaume Zoppi and Pietro Maiello in Northumbria University, who assisted me with measurements and let me use their facilities for research throughout the years of my project. In addition, I would like to thank Priscilla for her collaboration in our lab, which expanded my knowledge about new fields in research, and more importantly for being a great friend.

Finally, I would like to thank my family for valuable support throughout my years in Newcastle and my wonderful girlfriend Hele-Riin. Without her support and advice this thesis would not have been possible.

Publications

The following publications contain work by the author which is included in this thesis.

- 1 N. Põldme, L. O'reilly, I. Fletcher, J. Portoles, I. V. Sazanovich, M. Towrie, C. Long, J. G. Vos, M. T. Pryce, E. A. Gibson. *Photoelectrocatalytic H₂ evolution from integrated photocatalysts adsorbed on NiO*. Chem. Sci., 2019, 10, 99.
- 2 N. Põldme, J. Mallows, G. Summers, F. Black, E. Gibson. *Benchmarking the dye sensitised NiO photocathode for photoelectrochemical H₂ evolution*. Manuscript in preparation.
- 3 N. Põldme, E. Benazzi, J. Mallows, K. Sardar, P. Maiello, G. Zoppi, E. Gibson. *Investigating the effect of N₂ annealing on photoelectrochemical H₂ evolution on CuCrO₂ photocathodes*. Manuscript in preparation.

Contents

Abstract	i
Acknowledgements.....	iii
Publications	v
Abbreviations.....	xi
Chapter 1. Introduction	1
1.1 Global energy landscape	1
1.2 Sustainable energy for the changing world.....	4
1.3 Solar energy.....	6
1.4 Hydrogen as a solar fuel for sustainable energy storage and production.....	7
1.5 Photoelectrochemical water splitting.....	8
1.5.1 Semiconductor fundamentals	9
1.5.2. The semiconductor-electrolyte interface.....	12
1.5.3 Photoelectrochemical water splitting.....	20
1.5.4 Photoelectrochemical cell	23
1.5.5 Dye-sensitised photoelectrochemical cell	26
1.7 Aims.....	31
References	32
Chapter 2. Experimental procedures and methodology	37
2.1 General Methods.....	37
2.2 Chemical Methods	37
2.2.1 NiO photocathode fabrication	37
2.2.2 Synthesis of CuCrO ₂	37
2.2.3 Synthesis of CuCr _{0.5} Fe _{0.5} O ₂	38
2.2.4 Paste preparation and thin film deposition.....	38
2.2.5 Dye-sensitisation of photocathodes	39
2.2.6 Synthesis of C1 catalyst	39
2.2.7 Electrolyte preparation.....	40

2.3	Physical characterisation methods	42
2.3.1	UV-visible spectroscopy	42
2.3.2	Scanning electron microscopy.....	42
2.3.3	Powder X-ray diffraction	42
2.3.4	X-ray photoelectron spectroscopy	42
2.3.5	Time-of-flight secondary ion mass spectrometry	43
2.3.6	Electrochemical and photoelectrochemical characterisation methods	43
2.3.7	Gas chromatography	46
2.4	Theoretical background.....	46
2.4.1	UV-visible spectroscopy	47
2.4.2	Scanning Electron Microscopy.....	48
2.4.3	Powder X-ray Diffraction.....	49
2.4.4	X-ray photoelectron spectroscopy	50
2.4.5	Time-of-flight secondary ion mass spectrometry	51
2.4.6	Electrochemical and photoelectrochemical methods.....	53
2.4.7	Gas Chromatography	58
	References	59
Chapter 3. Benchmarking dye-sensitised NiO photocathodes for photoelectrochemical H ₂ evolution.....		
	Abstract.....	61
3.1	Introduction	61
3.2	Properties of NiO.....	62
3.3	Previous studies on NiO.....	62
3.4	Motivation and aims of the project.....	64
3.5	Results and discussion	64
3.5.1	Dye-sensitised NiO photocathode with BODIPY dye.....	64
3.5.2	Photoelectrochemistry of D2 BODIPY polymer dye on NiO.....	82
3.5.3	Dye-sensitised NiO photocathode with a benchmark donor-acceptor organic dye	

3.6	General discussion	103
3.7	Conclusions.....	106
	References	109
Chapter 4. Photoelectrocatalytic H ₂ evolution from integrated.....		113
photocatalysts adsorbed on NiO		113
	Abstract	113
4.1	Introduction	113
4.2	Results and discussion	115
4.2.1	Photocatalyst adsorption	115
4.2.3	Photoelectrochemistry and H ₂ evolution.....	116
4.2.4	Electrode characterisation pre- and post-catalysis.....	121
4.3	General discussion	127
4.4	Conclusions	129
	References	130
Chapter 5. CuCrO ₂ as alternative photocathode material for photoelectrochemical H ₂ evolution.....		133
	Abstract	133
5.1	Introduction	133
5.2	Properties of CuCrO ₂	136
5.3	Previous studies on CuCrO ₂	137
5.4	Motivation	138
5.5	Results and discussion	139
5.5.1	Synthesis of CuCrO ₂	139
5.5.3	Electrochemical and photoelectrochemical characterisation	143
5.5.4	Optical characterisation.....	149
5.5.5	Surface characterisation	150
5.5.6	Electrochemical impedance spectroscopy.....	151
5.5.7	H ₂ evolution and faradaic efficiency	153
5.5.8	Functionalisation of CuCrO ₂ with an organic dye.....	157

5.6	Effect of partial chromium substitution with iron: photoelectrochemical study of $\text{CuCr}_{0.5}\text{Fe}_{0.5}\text{O}_2$	160
5.6.1	Introduction	160
5.6.2	Results and discussion	160
5.7	Conclusions	167
	References	169
Chapter 6. Photocathode exchange current density estimation and PEC cell modelling using finite element analysis.....		
	Abstract.....	173
6.1	Introduction	173
6.2	Current density and overpotential relationship.....	174
6.4.	Results and discussion	176
6.4.1.	Exchange current density estimation.....	176
6.4.2.	PEC cell modelling.....	181
6.5.	Discussion.....	184
6.6.	Conclusions.....	185
	References	186
Chapter 7. Conclusions		
Appendix		
	Appendix to Chapter 3	190
	Appendix to Chapter 4	191

Abbreviations

Ag/AgCl	Silver / silver chloride
ALD	Atomic layer deposition
AM	Air mass
CA	Chronoamperometry
CB	Conduction band
CuCrO ₂	Copper chromium oxide
CuCr _{0.5} Fe _{0.5} O ₂	Copper chromium iron oxide
CV	Cyclic voltammetry
ΔG_{et}	Gibbs free energy of electron transfer
DSSC	Dye sensitised solar cell
ε	Molar extinction coefficient
E^0_{redox}	Formal energy of the electrolyte
EA	Electron acceptor
E_{appl}	Applied potential
E_{CB}	Conduction band potential
E_{F}	Fermi potential of the electrode
E_{g}	Band gap potential
E_{photo}	Photopotential
E_{redox}	Redox potential of the electrolyte
E_{VB}	Valence band potentials
FTO	Fluorine-doped tin oxide
GC	Gas chromatography
J_{dark}	Current density in the dark
J_{photo}	Photocurrent density

HOMO	Highest occupied molecular orbital
IPCE	Incident photon-to-current conversion efficiency
LSV	Linear sweep voltammetry
LUMO	Lowest unoccupied molecular orbital
η_{Far}	Faradaic efficiency
NHE	Normal hydrogen electrode
NiO	Nickel oxide
PEC	Photoelectrochemical
RHE	Reversible hydrogen electrode
SEM	Scanning electron microscopy
TON	Turnover number
UV	Ultraviolet
VB	Valence band
XPS	X-ray photoelectron spectroscopy

Chapter 1. Introduction

1.1 Global energy landscape

The development of our society has always been strongly dependent on the energy resources available at a given time. Starting from the industrial revolution in the eighteenth century, when coal became the main source of energy replacing wood, up until the current information age, the prevalent energy resources have been the fossil fuels. The use of coal, oil and natural gas has propelled our society with an unprecedented pace to the level of development we are today. The discovery and use of those resources have fuelled the development of technologies that have helped to increase our standard of living to a level which would have been unimaginable for our ancestors, couple hundred years ago. The development of modern medicine has increased our life-expectancy, the development of the transport sector has made us mobile enabling travel to distant countries, and the development of the information technology sector has made us connected with the world and each other more than ever before. In general, the development of various technologies fuelled by the energy extracted from fossil fuels has made our lives longer, easier and safer.

This steady increase in quality of life globally has also led to a considerable increase in global population. According to the UN Population Division, the global population is expected to reach 11 billion people by the end of this century.¹ This would be an increase of 8.5 billion in 150 years as the global population in 1950 was just 2.5 billion. An increase like that also means that the energy consumption will increase drastically. This increase in energy demand due to the increase in global population is even more enhanced due to the industrialisation of the developing countries like India and states in Africa. The continuing economic growth in China also plays a major role. According to the International Energy Outlook 2018 from the U.S. Department of Energy, the global energy consumption has increased from 356 quadrillion Btu at 1990 to *ca.* 600 quadrillion Btu at 2018 and is projected to reach 739 quadrillion Btu by year 2040 (1 Btu = 1050 J).² This increase is led by countries in Asia as the living standards improve and industrialisation intensifies and they are predicted to account for two thirds of the total global consumption by year 2040. At the same time, the fossil fuels needed to satisfy this increasing demand for energy are unsustainable in their nature. According to the known reserves and considering the predicted global consumption, the coal will be depleted roughly in 115 years and there are *ca.* 50 years of both oil and gas

left.³ Therefore, alternative energy resources are needed to replace the fossil fuels to satisfy this insatiable hunger for energy by our society.

However, the extensive use of fossil fuels has created more pressing problems than the inevitable depletion of the fossil fuel reserves. Most of these are to do with the devastating effects the use of fossil fuels have on our environment. The anthropogenic climate change is probably the most talked about and most concerning. It is the increase of the global average temperature due to the continuous accumulation of greenhouse gases in the atmosphere originating mostly from the combustion of fossil fuels and lesser extent from other anthropogenic gas emitting practices like landfill decomposition, extensive livestock farming and soil cultivation using fertilisers.⁴ Greenhouse gases are chemical compounds in the atmosphere which trap the heat radiating from the Earth's surface into space. Carbon dioxide is one of those gases with most detrimental effect on the global environment. It occurs naturally in the atmosphere originating from respiration of living organisms and volcano eruptions. However, the burning of fossil fuels has increased the average concentration of carbon dioxide in the atmosphere over 30% since the beginning of the industrial revolution.⁴ This is said to be the main driver of the increase in global average temperature, which has risen ca. 0.9 °C compared to the average temperature in the middle of the 19th century. The evidence to support the fact that this temperature increase is man-made is unequivocal and there is a consensus among the leading climate scientists supporting this.⁵ Another greenhouse gas which also contributes to the global average temperature rise is nitrous oxide. It is produced by burning fossil fuels, but also burning biomass and soil cultivation. It is a highly potent greenhouse gas but its concentration in the atmosphere is quite modest compared to carbon dioxide. The increase in concentration of those two gases is mostly directly man-made. However, there is another greenhouse gas which is actually most abundant in the atmosphere and the increase of its concentration is a result of the anthropogenic global temperature rise. This gas is water vapour and it has always had a very important role in our atmosphere shaping the global climate and enabling the life on our planet as we know it. But sudden abrupt increase in its concentration can cause our climate to change in a way which the human population is not prepared for. The increase in global average temperature increases the evaporation from the oceans and other bodies of water on our planet increasing the concentration of water vapour in the atmosphere. This, in turn, helps to trap even more heat radiating from the Earth's surface while also causing more precipitation and extreme weather conditions like hurricanes and floods. The extreme weather conditions can, in turn, devastate communities, destroy food supplies and cause mass emigration. The trapped heat in the atmosphere is in large extent absorbed by the Earth's

oceans and this creates a range of effects, like melting of the polar ice sheets and extinction of various living organisms in the oceans, like corals for example.⁶ The melting and disappearance of the ice sheets on Greenland and on north and south pole due to the warming of the oceans has a range of consequences. It induces the sea level rise, which can cause devastation on the coastal areas around the globe. The global sea level rise in the last 20 years has been measured to be approximately double of the rise that was measured for the whole last century.⁷ The polar ice sheet melting on that scale can also cause the desalination of the oceans, which can cause extinction of various species. The desalination can also cause the changes in gulf streams around the globe, which in turn can change our weather patterns causing extreme weather conditions.⁶

As it can be derived from this discussion, anthropogenic climate change is not a problem that can be sidestepped, and decisive actions need to be taken right now. In 2016 the Paris agreement was ratified by 134 countries around the globe to tackle the issue of climate change. With the ratification of the agreement, the countries involved promised to reduce their carbon dioxide emissions with the aim of keeping the global temperature rise by the end of this century below 2 °C and further implement strategies necessary to limit the global temperature rise to 1.5 °C.⁸ This goal, however, already seems to be unrealistic. According to the report published by the Intergovernmental Panel on Climate Change (IPCC) in 2018, the global average temperature rise will reach the 1.5 °C already by the year 2052.⁹ This will happen if the current rate of carbon dioxide emissions stays unchanged. It also means that by the end of the century, the rise in global temperature would be approximately 2.5 °C. The effects of this increase are hard to predict and depend on different variables, like annual peak temperatures, changes in weather patterns and the impact of these changes to natural and human systems.

Indeed, the possible negative outcomes of climate change are ominous, but at the same time there are solutions already available. One of the main solutions is to drastically lower the carbon dioxide emissions to the atmosphere. To achieve that, the use of fossil fuels also must be drastically lowered. This has proven to be an extremely challenging task as already seen from the latest IPCC report.⁹ One of the reasons for this is the fact that in many parts of the world, the climate change is not the primary issue for a vast number of people. The starvation, lack of clean water, poor access to healthcare and education, and armed conflicts taking place in several parts of the world make the climate change seem like a problem of the developed countries. However, this is not the case as the effects of climate change will most probably affect the developing countries first and they are the ones that are also least prepared for those

effects. But it does show that to effectively solve the problem of climate change, other problems in the world need to be dealt with as well. And there is a link between the climate change and the current societal problems listed above. The fossil fuel reserves are very unevenly distributed across the planet and lot of those reserves are located in regions where geopolitical instability and armed conflicts are taking place.³ Arguably, these reserves have a part to play in the development of those conflicts which in turn have created destruction of vital infrastructure abruptly lowering the quality of life and resulting in mass emigration. Decentralised energy production, however, would decrease the influence of the current major players in global energy politics and increase the global geopolitical stability. If decentralised energy system would be adopted globally and especially in the developing countries, not only would it make the problematic regions more geopolitically stable, but it would also enable access to electricity for approximately 1 billion people (1.1 billion people did not have access to electricity in 2016).¹⁰ The access to electricity would in turn enable access to clean water, healthcare and education, the crucial building blocks of a safe and peaceful society.

The benefits of changing our energy landscape are numerous. The current energy model based on burning fossil fuels is just not sustainable and a different model needs to be implemented and fast. Alternative energy sources which are environmentally sustainable and decentralised must be used to satisfy the energy need of our society. It is one of the key solutions to help to tackle the climate change and hopefully stop it while it is not too late. It would also help to establish global political stability and create more equality. In the next chapter different sustainable alternative energy sources are discussed, some which are already implemented, and some which are still under development.

1.2 Sustainable energy for the changing world

The future energy landscape is most probably not going to include only one main energy resource, but several, which together will satisfy the energy needs of our society. The main sustainable alternative energy technologies, which will be included in the future energy mix, are hydropower, wind energy and solar energy. There are additional energy technologies like geothermal energy, tidal energy and wave energy, but these will not be discussed in here.

Hydropower is currently the largest source of renewable electricity. The total installed capacity in the form of run-of-river hydropower plants, reservoir hydropower plants and pumped storage plants amount to more than 1200 GW producing approximately 16% of

global electricity.¹¹ The electricity is produced directly by converting the kinetic energy of running water into electrical energy using turbines. The benefit of hydropower is the large and stable energy output from one plant. The disadvantages are however that the technology is decentralised and very dependent on location, which makes it possible to be applied only in certain mountainous regions near large rivers. Therefore, in some countries hydropower can be the main source of energy, like Norway or Georgia, while in others it is not applied at all.

Wind is another vastly abundant and sustainable clean energy resource. In recent years there has been a steady increase in the instalment of wind turbines to convert the energy from the wind to electricity. The working principle of this conversion using a wind turbine is as follows. When the wind blows on the blades of the wind turbine the blades start to rotate creating kinetic energy. The rotation of the blades turns the shaft in the wind turbine and the shaft drives the generator which converts the kinetic energy into electricity.¹² The installed wind turbines worldwide amounted to wind energy capacity of 515 GW in 2017 and the electricity produced by the wind turbines was approximately 4% of the global electricity production.¹¹ The advantage of wind power is that it produces clean energy and it can be considered as a decentralised energy technology which can be installed wherever there is enough wind. The wind turbines also come in different sizes and therefore different needs of different consumers can be met. However, the drawback of the technology is still the large investment needed for the instalment of the wind turbine, which makes it far too expensive for a single household, and the intermittent nature of the electricity production, which creates a need for energy storage or for a direct connection with a larger energy grid to compensate the electricity supply when wind turbine is not producing enough electricity.

The third sustainable energy resource discussed here is by far the most abundant on our planet. It is solar energy. It is the ultimate source of energy which has created and sustains the life on our planet. At any given moment the solar power reaching to earth's surface is equal to the power generated by 130 million 500 MW power plants.¹³ In the light of the overwhelming concerns over the use of fossil fuels and growing demand for environmentally friendly sustainable energy resources, which could also cover the energy need of the next generations to come, the prospect of harvesting solar energy is becoming more and more popular as one of the main solutions to our global energy problem. However, there are still several challenges on the way. The technologies for solar energy harvesting along with the advantages and disadvantages of solar energy are discussed in the following chapter.

1.3 Solar energy

The main technology to convert sunlight to electricity is the photovoltaics (PV). The principle of the technology is to use semiconductors with specific properties to absorb photons of light generating charge carriers in the material which are then transferred to the external circuit. The development of PV technology started in the 1950's and has reached to a level where the cost of electricity generated is now cheaper than the electricity produced from fossil fuels, according to the latest report from International Renewable Energy Agency.¹⁴

Compared to other sources of energy, solar power has numerous advantages. It can be considered as free and inexhaustible energy resource with several technologies available for harvesting it. It has minimal direct environmental impact which can be measured for example by the land used for the solar panels. The overall environmental impact can be evaluated by measuring the environmental impact of the production of devices used for solar energy harvesting. This is all negligible compared to the environmental impact imposed to our planet by the use of fossil fuels. It is also considered to be an energy source with zero contribution to the increase of CO₂ level in our atmosphere.

In addition to monetary and environmental impact, there is also a social impact which can be derived from the decentralised nature of the technology available for solar energy harvesting. The solar energy has the potential to be distributed to the limit that a single individual can act as an independent energy producer and provider and has control over the energy she/he lives on. This has also beneficial effect on the geopolitical stability.¹⁸ Cyber- or physical attacks on energy infrastructure are not possible due to the decentralised system and therefore the overall safety of a community or a country is increased. In addition, the price of energy is not influenced any more by the fluctuations of the market and individuals have more long-term control over their household budget.

However, there are also several challenges need to be overcome before solar energy can be considered as the primary energy source. The flux of solar energy varies daily and seasonally and this creates the need for large scale energy storage. One solution would be to use rechargeable batteries for energy storage and there is a variety of different technologies available, some already commercial, some still in research phase. But this technology is still limited by the use of expensive or rare materials and energy exhaustive production processes. In addition, due to the rapid increase in production of electrical vehicles, the production of existing battery technology quite likely can't keep up with the market demand for storage capacity needed for both the electrical vehicles and storing solar energy. Especially when the

aim is to have solar energy as the primary energy source in our planet. Hence, an alternative technology for solar energy storage is needed. This brings us to solar fuels.

1.4 Hydrogen as a solar fuel for sustainable energy storage and production

The concept of solar fuels is straightforward. It is to use energy of sunlight to directly produce chemicals which can be used in various applications as fuels instead of using fossil fuels. The main fuels that can be produced are hydrogen and carbon-based fuels like carbon monoxide and methane. Currently, most of hydrogen is produced using a process called methane reforming, where natural gas is reacted with water vapour under high pressure to produce a mixture of hydrogen and carbon monoxide (syngas).¹⁵ The majority of the produced syngas or just hydrogen is then used in gas turbines to produce electricity or in various industrial chemical processes. However, hydrogen as a solar fuel would be produced from water thereby avoiding the colossal negative environmental impact which comes with using the fossil fuels. It is important to note that sustainable hydrogen can be produced from water also by using different sustainable technologies like wind energy combining it with electrolysis, but this is not the focus of this thesis and relevant material can be found elsewhere.¹⁶

The benefit of the solar hydrogen in addition to the fact that its production would be clean and environmentally friendly, is that it would act as an energy storage mechanism for intermittent solar energy. It can either be produced indirectly storing the electricity produced by PV applications (solar cells) or it is produced directly through water splitting reaction mimicking nature's photosynthesis. The latter is the focus of this thesis which will be discussed in depth in the following chapters. Stored hydrogen can then be used directly as a fuel of the future transportation powering the fuel cell "engines" in cars, buses and trains, or it can be used in industry to produce chemicals and materials, replacing hydrogen produced from fossil fuels.^{17,39}

1.5 Photoelectrochemical water splitting

There are two main strategies for producing solar fuels where nature is taken as an example by trying to mimic the photosynthesis process. There is an indirect conversion path, where the light harvesting, and chemical production is separated from each other. In this approach the charge carriers (electrons and holes) are generated from light by photovoltaic cells and transferred to electrodes through external wiring. The chemical reactions producing the solar fuel are then driven by the provided charge carriers on the electrodes which are immersed in water and usually also functionalised with catalysts to lower the activation energy needed for the reactions. In case of direct conversion of light to chemicals, the charge carrier generation, charge transport and chemical reactions are facilitated all in a single device and carried out by a single photoactive material or a combination of materials owing to different functions of the whole water splitting process.¹⁸

The general term used for a device that is used to produce solar fuels in a direct way is a solar fuel generator. There are many different device designs available for solar fuel generators depending on the method of charge separation. One of the approaches to separate charge carriers is to utilise the solid conductor - ionic conductor junction. Since the solid used in the device is usually a semiconductor, the junction is also referred to as semiconductor-electrolyte interface, a term also used in this thesis. These devices that utilise the semiconductor-electrolyte interface for solar fuel production go under a general term of photoelectrochemical (PEC) cells. In these devices the photovoltage and photocurrent are generated through illumination with radiant light and originate from the electrochemical potential differences of the solid and the electrolyte as well as from the imbalance in the charge-transfer kinetics for electrons and holes across the semiconductor-electrolyte interface. It is important to note that there are different types of PEC cells and a PEC cell which produces chemicals on the semiconductor-electrolyte interface is called a photoelectrosynthetic cell. This is the type of PEC cell that is discussed in this thesis for hydrogen production.²⁰

To understand how these types of devices function, the physics of semiconductors needs to be explained first. In addition, it is crucial to understand the physico-chemical processes taking place at the semiconductor-electrolyte interface. These subjects will be addressed in the following chapters including also the fundamental principles of water splitting to produce hydrogen, the solar fuel which is the emphasis of this thesis. The chemistry and thermodynamics of the water splitting is explained addressing also the

limitations and challenges connected to the device development, which are important to consider when the aim is to develop efficient but also cheap and sustainable devices.

In addition, different types of PEC cells are introduced explaining the functions of the different parts of the devices and explaining the pros and cons of each type of cell. Special emphasis is on the dye-sensitised PEC cell, which is a hybrid PEC cell where the light absorption, charge separation, charge transfer and chemical reactions are facilitated by different materials combined in the device to function synergistically.

1.5.1 Semiconductor fundamentals

In a molecule, atoms are quite far apart from each other with filled orbitals and vacant orbitals forming thereby discrete molecular orbital energy levels and therefore the electrons cannot move freely between atoms. Now, when atoms with filled and vacant orbitals are packed together in a crystal lattice, new orbitals are formed which overlap each other creating uniform energy bands as shown schematically on Figure 1.1. The energy band which was formed from the filled atomic orbitals is called a *valence band*, VB, and the band formed from the vacant orbitals is called a *conduction band*, CB.

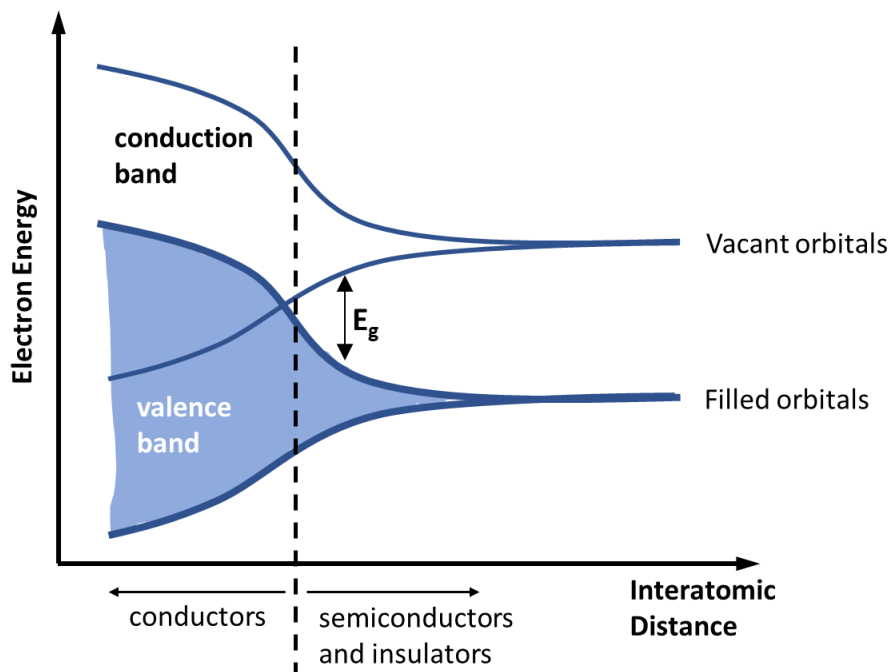


Figure 1.1. Schematic illustration of the energy band formation in solids. At larger interatomic distances the filled and vacant orbitals in atoms have discrete separate energy levels, which then form energy bands when the atoms are more packed together in crystal lattice.²²

The energy difference between those bands is called a *band gap*, E_g , and the magnitude of that determines the electronic properties of the material.^{22,23}

When the band gap is very small or when the valence and conduction band overlap, electrons need very little energy to move from the VB to the CB where they can move freely across the lattice. The electron transfer between bands in these types of materials occurs already via the intrinsic thermal excitation at room temperature resulting in high conductivities. These materials are called conductors and most metals belong to this group.

When in case of conductors the definition is quite clear, then in case of semiconductors and insulators the distinction between the two is more arbitrary and depends on the value of the E_g . Material is usually considered to be a semiconductor when its E_g value is in range of 1 to 4 eV. Materials which E_g is larger than 4 eV are considered to be insulators. In a steady state at 0 K without any external energy input, semiconductor material is not electrically conducting, because almost all electrons are localised in VB and the CB is almost vacant. But when there is an external energy applied, for example heat or light, electrons are excited from the valence band to the conduction band, given that the energy received is larger than the E_g of the material. When excited to the CB, electrons become electrically mobile and can transfer freely across the vacant energy levels in the CB. The excitation also leaves behind vacant energy regions in the VB called “holes” which are mobile because they can shift between the filled energy levels. Semiconductor material where these processes take place in equal rate is called an *intrinsic semiconductor*. Both electrons and holes are called *charge carriers* and in an intrinsic semiconductor the charge carriers are in a dynamic equilibrium, meaning that while there are continuous dissociation and recombination of electron and holes taking place, the concentration of electrons, n_i , and holes, p_i , stay equal in the material and are expressed by the following equation.^{22,23}

$$n_i^2 = p_i^2 \approx N_0 \exp\left(\frac{-E_g}{kT}\right) [cm^{-3}] \quad (1.1)$$

Where $N_0 = N_{CB}N_{VB}$ is the product of the density of states at the lower edge of CB and the top edge of VB and is about 10^{38} cm^{-3} and k is the Boltzmann constant ($8.617 \times 10^{-5} \text{ eV K}^{-1}$).

The electron distribution in a semiconductor material is best expressed with Fermi statistics. According to Fermi statistics, at 0 K, the *Fermi level*, E_F , is defined as the energy at which the probability of finding an electron is 1/2. When dealing with electrochemical systems with different phases, it is better to explain the Fermi level through thermodynamics,

which defines the Fermi level of a given phase as the electrochemical potential of an electron, μ_e^α , in a phase α .

$$E_F^\alpha = \mu_e^\alpha = \mu_{e,c}^\alpha - e\phi^\alpha \quad (1.2)$$

where $\mu_{e,c}^\alpha$ is the chemical potential of an electron in phase α , e is the electron charge and ϕ^α is the absolute electrostatic potential in phase α . It is commonly agreed that the value of E_F is taken zero for the free electron in vacuum expressed in eV.^{22,23}

In an intrinsic semiconductor, the Fermi level lies in the middle of the band gap due to the dynamic equilibrium of charge carriers. It means that all the energy levels below the Fermi energy are occupied and the energy levels above it are most likely to be vacant. To increase the charge carrier concentration in an intrinsic semiconductor to thereby increase its electrical conductivity and change the optoelectronic properties, impurities are introduced into the material to create additional energy levels and perturb the dynamic equilibrium of charge carriers, so that $n_i \neq p_i$. This process is called semiconductor doping and it is usually conducted by introducing altermultivalent impurities into the intrinsic semiconductor crystal lattice to either increase the concentration of electrons or holes. In case of increasing the electron concentration, impurity atoms with higher number of valence electrons than the intrinsic semiconductor atoms are introduced. The classical example is the doping of Si with P. Si has four valence electrons, P has five, and one electron per atom is then left unbound, free to be donated. This perturbs the dynamic equilibrium of charge carriers so that $n \gg p$, additional energy level, E_D , is created below the conduction band edge, E_{CB} , and the Fermi level is shifted close to the E_{CB} . This type of doping is called *n-type doping* and the doped semiconductor is stated to be *n-type semiconductor*, where electrons are now the *majority charge carriers* and holes are the *minority charge carriers*. The reverse process takes place when creating a p-type semiconductor. When Si is substituted with Ga in a Si crystal lattice, which has three valence electrons, an acceptor energy level, E_A , just above the valence band edge, E_{VB} , is created. Electrons from the VB are then thermally excited to this acceptor energy level leaving behind mobile holes in the VB. This substantially increases the concentration of holes resulting in $p \gg n$ and Fermi level shifts to the top of the VB. This material is then called *p-type*, where the holes are the majority charge carriers. The schematic explanation of the different types of semiconductors is presented on Figure 1.2.^{22,23}

Semiconductor doping can also be achieved through other ways than introducing impurity atoms into the lattice. Inducing nonstoichiometry in compound semiconductors like CdTe or CuInGaSe can be a viable strategy to increase the charge carrier concentration. In

addition, naturally occurring n- or p-type conductivity in oxides like TiO₂ or NiO can be efficiently used when designing devices where specific conductivity types are needed. This naturally occurring conduction type in oxides originates at least partly from the oxygen vacancies in the lattice creating non-stoichiometry between metal and oxygen ions and can be altered through various strategies. For example, the non-stoichiometry can be influenced by using different synthesis routes, surface treatments and thermal treatments of material under different conditions.^{22,23}

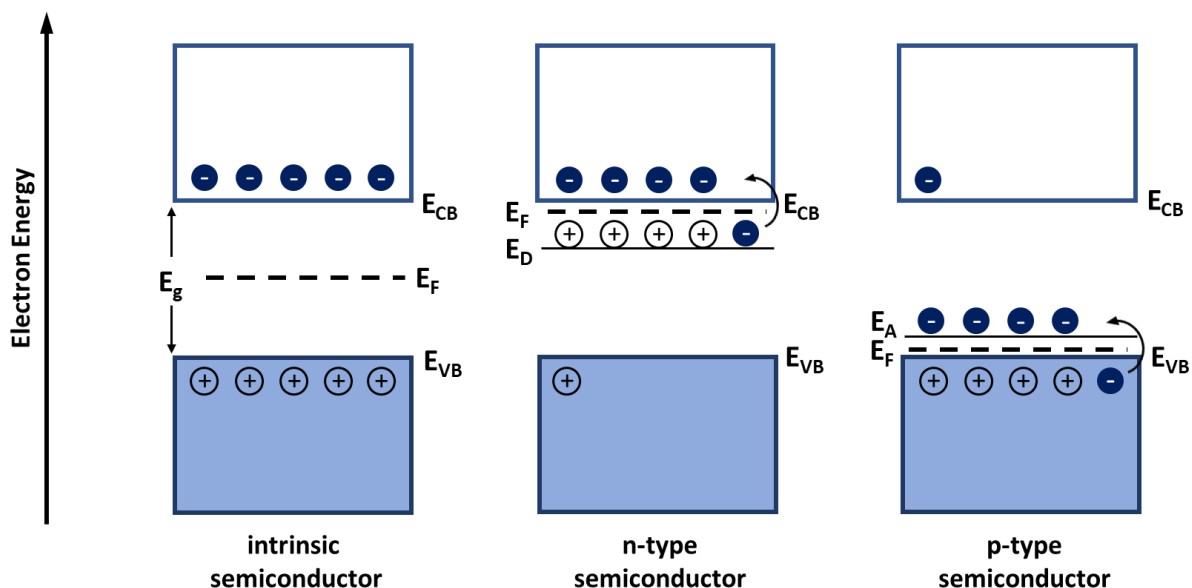


Figure 1.2. Schematic explanation of intrinsic semiconductor (left), n-type semiconductor (middle) and p-type semiconductor (right) showing the Fermi level, E_F , position in different types of semiconductors, donor energy level, E_D , position in n-type semiconductor and acceptor energy level, E_A , position in p-type semiconductor.^{22,23}

1.5.2. The semiconductor-electrolyte interface

In a PEC device, the chemical reactions are taking place on the semiconductor surface which is in contact with the electrolyte. The contact area between the semiconductor and the electrolyte is called the *semiconductor-electrolyte interface* and the chemical reactions are governed by the properties of that interface and the physical processes happening there.²³

In Chapter 1.6.1 the Fermi level was defined as the electrochemical potential of electrons in a given phase, μ_e^α , expressed in eV vs. the vacuum level. In a redox electrolyte, the potential of electrons can be calculated using the Nernst equation

$$E_{redox} = E_{redox}^o + \frac{RT}{nF} \ln \left[\frac{c_{ox}}{c_{red}} \right] \quad (1.3)$$

where E_{redox}^o is the formal potential of the redox couple, R is the universal gas constant ($R = 8.314 \text{ J K}^{-1} \text{ mol}^{-1}$), n is the number of electrons transferred, F is the Faraday constant ($F = 9.6485 \times 10^4 \text{ C mol}^{-1}$) and c_{ox} and c_{red} are the concentrations of oxidised and reduced species in the electrolyte. The E_{redox} is usually expressed in volts (V) against the normal hydrogen electrode (NHE) and according to the definition of the Fermi level, is also the potential of the Fermi level in the redox electrolyte, $E_{F, redox}$. However, because Fermi level is usually expressed against the vacuum reference, it is useful to introduce a conversion between the vacuum level and the NHE.^{22,23}

$$E_{F, redox} = -4.5 \text{ eV} - E_{redox} \quad (1.4)$$

When the contact between the semiconductor and the electrolyte is established and the semiconductor-liquid interface is formed, the different electrochemical potentials, i. e. Fermi levels, in the two phases will equilibrate and $E_{F, eq}$ is formed. This process takes place via charge transfer between the semiconductor and electrolyte. The majority charge carriers, either electrons or holes, transfer from the semiconductor to the electrolyte and a potential difference is formed between the two phases. The process is explained further using p-type semiconductor as an example (see Figure 1.3, a and b). When a p-type semiconductor is brought into contact with the electrolyte, the Fermi levels of the two phases are equilibrated through a transfer of positively charged holes from the semiconductor to the electrolyte. The excess positive charge inside the semiconductor is distributed near the interface forming a space-charge region (Figure 1.3, a). Because the potential difference between the semiconductor and the electrolyte is distributed across the space-charge region, the band positions at the semiconductor-electrolyte interface do not change. However, the accumulation of positive charge in the space-charge region makes the band energies inside the bulk semiconductor more negative shifting the bands up. As a result, the energy of the Fermi level also becomes more negative inside the p-type semiconductor after the equilibration and a downward band bending takes place in the space-charge region. At the same time, the electrolyte becomes positively charged forming a diffuse double layer near the semiconductor surface.²³

Similar process takes place in a n-type semiconductor, but in that case the electrons as majority charge carriers flow from the semiconductor to the electrolyte creating a negatively charged space-charge region near the interface compared to the bulk semiconductor (Figure 1.3, d). The band energies inside the bulk semiconductor become more positive due to the electron flow from the bulk to the interface, moving the Fermi level to more positive energies and inducing an upward band bending in the space-charge region.²³

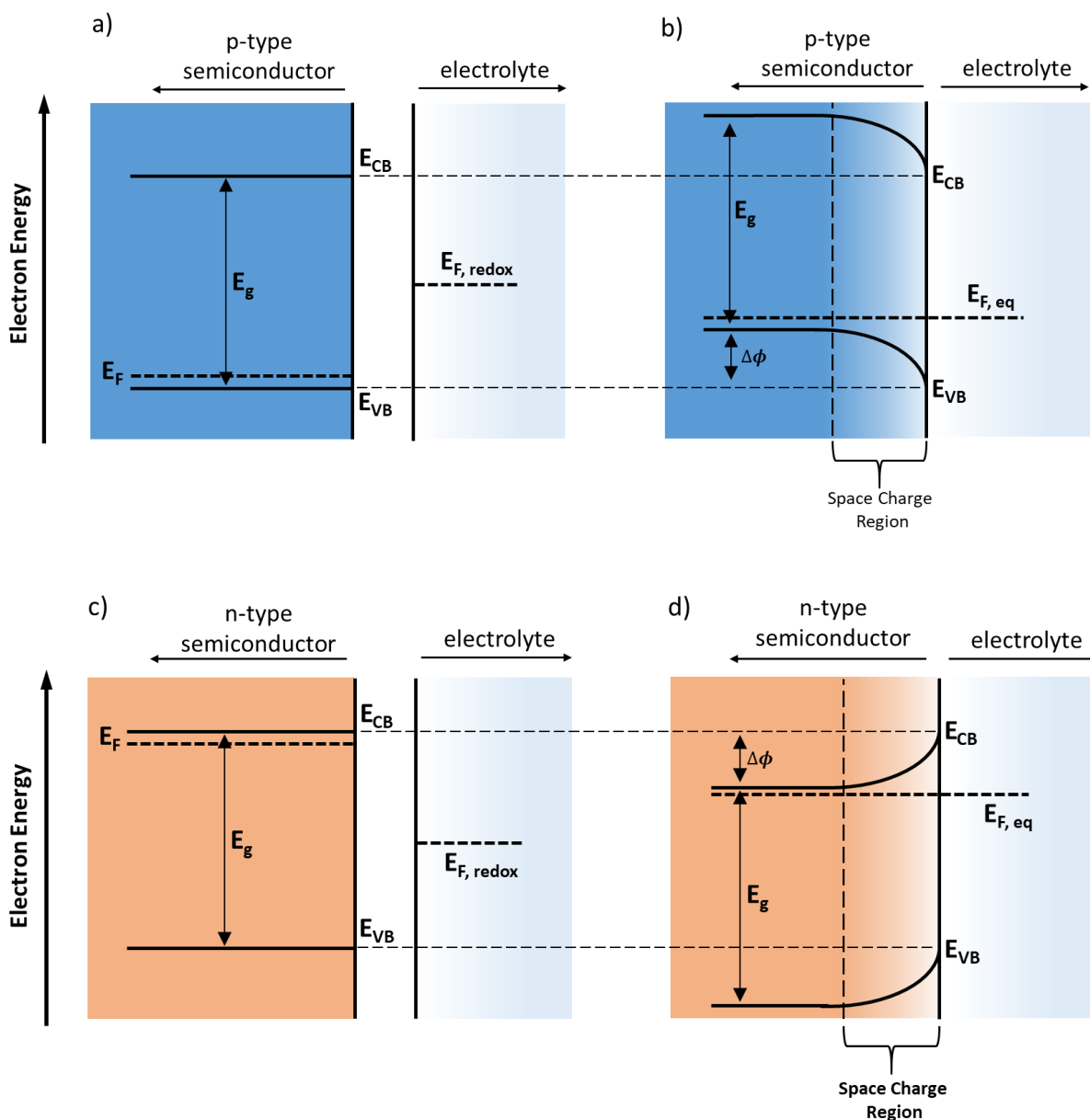


Figure 1.3. Schematic representation of the semiconductor-electrolyte interface for p-type (a and b) and n-type (c and d) semiconductors before the two phases are in depletion (a and c) and after equilibration when the contact between the phases is established (b and d) showing the corresponding energy levels, band bending near the interface, Fermi level shift due to the equilibration and the space charge region. $\Delta\phi$ represents the potential difference between the semiconductor surface at the interface and the bulk of the semiconductor where the energy bands are flat.^{22,23}

The potential at which there is no band bending in the semiconductor, i. e. there is no space-charge region formed, is called a flat-band potential, E_{fb} . As the name says, the energy bands in semiconductor are perfectly flat at this potential and no excess charge exists. E_{fb} is a useful parameter to know especially when external potential, E_{appl} is applied to the semiconductor electrode during electrochemical or photoelectrochemical measurements. In

case of p-type semiconductor, when E_{appl} is more positive than the E_{fb} , then holes start to accumulate at the semiconductor surface and so-called accumulation layer is formed. Under these conditions the electrode starts to behave more as a metal and is said to be become degenerate.²³

A similar process takes place in the n-type semiconductor when E_{appl} is more negative than the E_{fb} . Only in that case electrons accumulate on the electrode surface. E_{fb} can be determined experimentally, for example using photocurrent measurements (photocurrent onset potential) or electrochemical impedance spectroscopy.²³

In a situation, where an additional potential is applied to the semiconductor electrode, E_{appl} , the equilibrium between the chemical potential of electrons in the semiconductor and in the electrolyte is disturbed. This is because the externally applied potential changes the electron energy in the semiconductor.

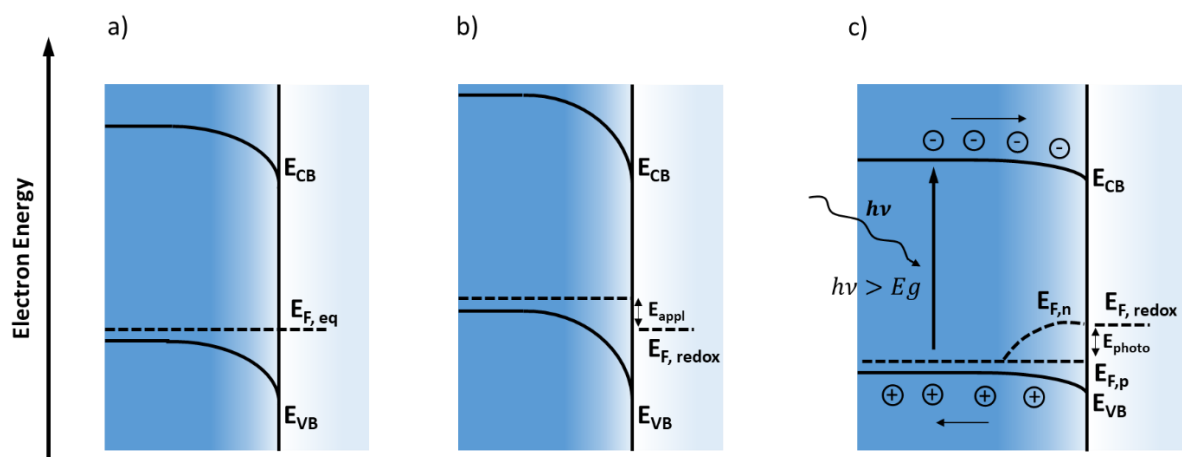


Figure 1.4. Schematic representation of the semiconductor-electrolyte interface and corresponding energy levels for a p-type semiconductor after equilibration when there is no applied bias or light illumination applied (a), under applied negative bias (b) and when light illumination is applied to the semiconductor (c). E_{appl} is the external potential applied to the semiconductor electrode using a potentiostat, E_{photo} is the photopotential created by the applied illumination between the Fermi level of the majority charge carriers, $E_{F,p}$, in this case holes, and the Fermi level of the electrolyte, $E_{F,redox}$.¹⁹

In the case of a p-type semiconductor, where additional negative potential is applied, the energy of the electrons in the semiconductor electrode is increased. As a result, the band energies in the semiconductor is increased increasing also the band bending in the space-charge region and increasing the energy of the Fermi level shifting it up by the value of the E_{appl} (Figure 1.4, b).^{19,23}

The opposite takes place when applying additional positive potential to the n-type semiconductor electrode (Figure 1.5, b). The energy of the electrons in the semiconductor is decreased lowering the band energies, which in turn increases the upward band bending in the space-charge region. Since the band energies are decreased, the energy of the Fermi level is also decreased by the extent of the E_{appl} .¹⁹

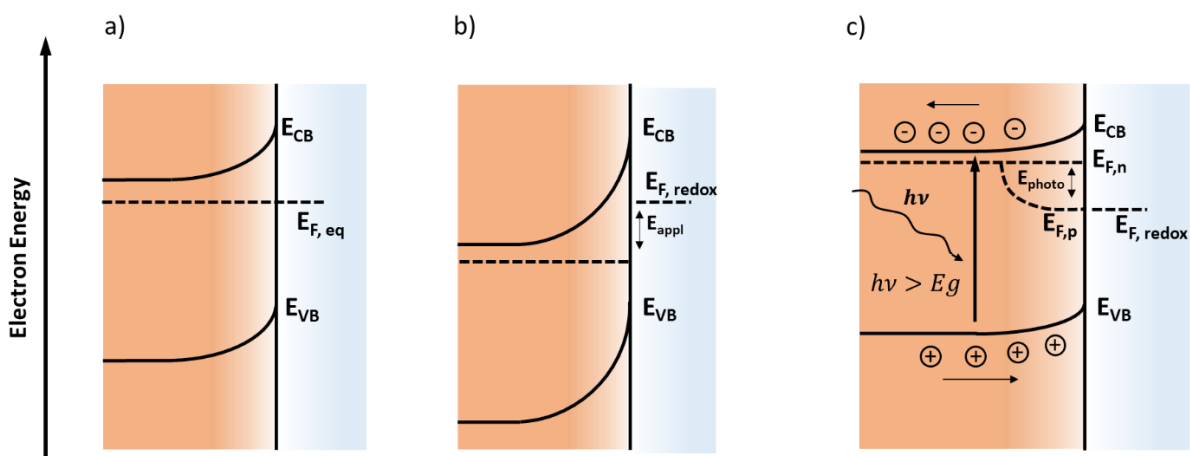


Figure 1.5. Schematic representation of the semiconductor-electrolyte interface and corresponding energy levels for a n-type semiconductor after equilibration when there is no applied bias or light illumination applied (a), under applied negative bias (b) and when light illumination is applied to the semiconductor (c). E_{appl} is the external potential applied to the semiconductor electrode using a potentiostat, E_{photo} is the photopotential created by the applied illumination between the Fermi level of the majority charge carriers, $E_{F,n}$, in this case electrons, and the Fermi level of the electrolyte, $E_{F,redox}$.¹⁹

A different process takes place at the semiconductor-electrolyte interface when the external energy is applied to the semiconductor through light illumination. When the semiconductor absorbs light with energy larger than the band gap of the material, $h\nu > E_g$ ($h\nu$ is the photon energy), an electron is excited from the VB to the CB and an electron-hole pair is created in the semiconductor (Figure 1.4.c and 1.5.c).¹⁹

Therefore, excitation through light illumination creates a delocalised electron in the CB and leaves behind a delocalised hole in the VB. Electron-hole pairs are created both in the space-charge region and also in the bulk of the semiconductor where there is no electric field. Some of the pairs will recombine and these recombination processes will be discussed later. Because the population of electrons in the CB and the population of holes in the VB at the semiconductor-electrolyte interface is increased due to the electron-hole pair generation, the

band bending in the space-charge region is decreased and the band energies are lowered. New steady-state is reached where the semiconductor-electrolyte interface is in steady-state with the photon flux. Therefore, two Fermi levels are said to exist in the space-charge region, one for electrons ($E_{F,n}$) and one for holes ($E_{F,p}$) (Figure 1.4.c and 1.5.c). The space-charge region supports the separation of the electron-hole pairs and directs the charge carriers to opposite directions. In case of a p-type semiconductor, the excited delocalised electrons in the CB are directed to the semiconductor surface due to the downward band bending in the space-charge region (Figure 1.4.c). At the same time, delocalised holes left in the VB are directed away from the semiconductor surface. The electrons transferred to the semiconductor surface can then reduce the oxidised species in the electrolyte given that the reduction potential of the oxidised species in the redox electrolyte is lower than the E_{CB} . The opposite process takes place in case of an n-type semiconductor. Due to the upward band bending in the space-charge region the excited delocalised electrons in the CB are directed away from the surface and the delocalised holes in the VB are directed towards the surface. The holes transferred to the surface are then able to oxidise the reduced species in the electrolyte given that the oxidation potential of the reduced species in the electrolyte is higher than the E_{VB} .^{19,23}

Photopotential generated under light illumination corresponds to the difference between the $E_{F,p}$ and $E_{F,redox}$ the overpotential required to drive the electrochemical reaction on the electrode surface. The photopotential is also expressed on Figures 1.4.c and 1.5.c. without the additional overpotential, for simplification. The photopotential for p-type semiconductor can be expressed with the following equation.

$$E_{photo} = |E_{F,p} - E_{F,n}| = |E_{F,p} - E_{F,redox}| - \eta \quad (1.5)$$

The equation is analogous for the n-type semiconductor, with an important distinction that the photocurrent is equivalent to the difference between $E_{F,n}$ and $E_{F,redox}$ minus overpotential.

The photocurrent, J_{photo} , generated by the semiconductor electrode under light illumination is, in ideal situation, equal to the rate of charge generation, G , and to the photon flux absorbed by the semiconductor. However, the photocurrent is reduced by various charge recombination processes taking place at the semiconductor and in the bulk of the semiconductor. These processes are visualised on Figure 1.6. for both p-type and n-type semiconductors under light illumination. To explain these recombination processes, a p-type semiconductor is taken as an example, for which the semiconductor-electrolyte interface under light illumination is presented on Figure 1.6.a. When light with energy higher than the E_g of the material is absorbed by the p-type semiconductor, electron-hole pairs are created and

the generation of the charges is expressed by the rate of charge generation, G . J_{photo} can be expressed as the current generated by excited electrons transferred from the CB to the semiconductor surface where they reduce the oxidised species in the electrolyte (for example driving proton reduction in case of photoelectrochemical water splitting). The recombination processes decreasing the J_{photo} are following: the recombination of excited electrons in the CB and holes in the VB in the bulk of the semiconductor, J_{br} , the recombination of excited electrons in the CB and holes in the VB in the space-charge region, J_{sr} , tunnelling of charges through the semiconductor-electrolyte interface, J_t , thermally induced transfer of charges through the semiconductor-electrolyte interface, J_{te} , and the recombination of electrons and holes at surface states in the band gap, J_{SS} (Figure 1.6.a). The real photocurrent can then be expressed by the following equation, which takes into account all the losses due to recombination processes.^{19,23}

$$J_{photo} = G - J_{br} - J_{sr} - J_t - J_{te} - J_{SS} \quad (1.6)$$

For an n-type semiconductor the recombination processes taking place are analogous, with the difference that the photocurrent is expressed as the current generated by delocalised holes in the VB transferred to the semiconductor surface where they oxidise the reduced species in the electrolyte (Figure 1.6.b).

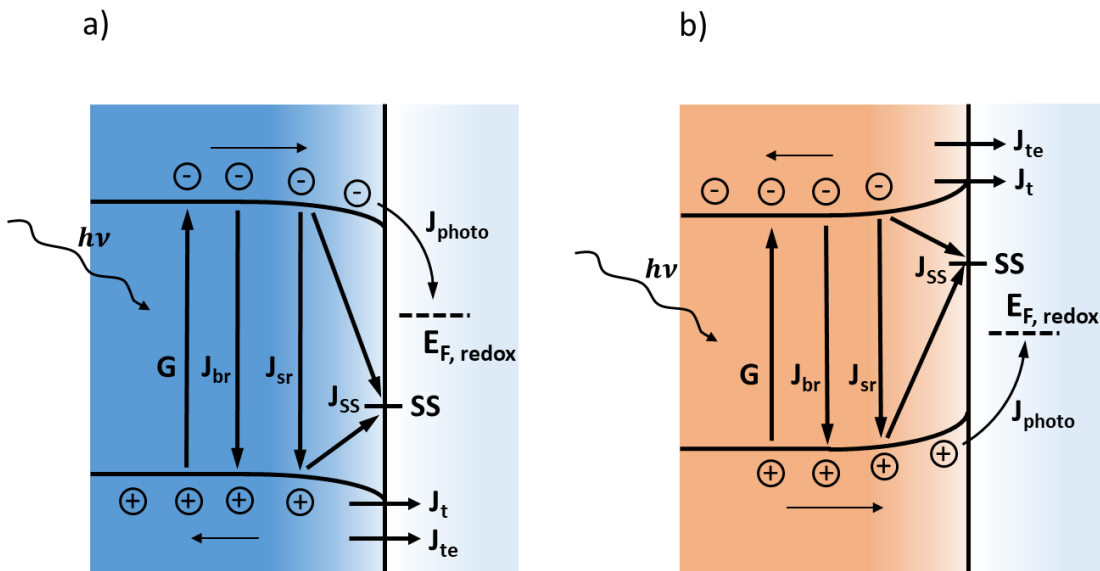


Figure 1.6. Photocurrent generation and recombination processes taking place in a p-type (a) and n-type (b) semiconductor electrodes. J_{br} – bulk recombination, J_{sr} – recombination in the space-charge region, J_t – tunnelling of charges through the semiconductor-electrolyte interface, J_{te} – thermionic emission, J_{SS} – recombination of charges with surface states. G is the rate of charge generation and J_{photo} is the photocurrent.^{19,23}

The excitation process during which the electron-hole pair is created is called a band-to-band transition and depending on the semiconductor material the transition can be either direct or indirect. In case of direct transition, the bottom of the CB and top of the VB are precisely opposite to each other (the electron wave vector, k_{ew} , for both CB and VB, is 0). This is not the case for an indirect transition. Therefore, the absorption coefficient, α , is also different for materials with different transition types. The absorption coefficient is a measure of the distance of light penetration into the material before it is absorbed. It is expressed as absorption depth written as $1/\alpha$. There is a large difference in absorption depth between materials with direct transition and indirect transition. The absorption depth for direct transition, can be in the range of 100 to 1000 nm, while for indirect transition, it can be in the range of 10^4 nm. The absorption coefficient, which determines the absorption depth is expressed as follows for the two transition types.²²

Direct transition:

$$\alpha = A'(hv - E_g)^{1/2} \quad (1.7)$$

Indirect transition:

$$\alpha = A'(hv - E_g)^2 \quad (1.8)$$

In equations 1.7 and 1.8, A' is the proportionality constant.²²

The existence of surface states in the band gap of the semiconductor at the semiconductor-electrolyte interface, causing the reduction of photocurrent due to recombination with the charge carriers, can be explained by the nature of the semiconductor-electrolyte interface. The instantaneous termination of the crystal lattice at the interface means that the bonding between the atoms at the surface is different from the bonding between the atoms in the bulk of the semiconductor material. For example, depending of the crystal structure, some of the bonds may become unsaturated which is compensated by the slightly different atomic structure at the surface or bonding with the species in the electrolyte. Consequently, the electronic structure of the surface is also different than in the bulk of the semiconductor. If the energies of the orbitals of these surface atoms lie in the band gap, recombination of these surface states with the charge carriers can take place. This would be the situation if the semiconductor is a perfect single crystal. In reality, the entropy of the crystal is increased since there may be additional defects in the semiconductor crystal lattice,

which may also create additional energy levels. In case of nanostructured semiconductor films, the situation is even more complex. Every semiconductor particle in the nanostructured film has the surface termination induced surface states and defects induced surface states. In addition, the connections between particles are not ideal and will in turn create even more recombination pathways. This is important to take into consideration when working with nanostructured films which is a widely used approach applied in catalysis and photocatalysis, since the nanostructured nature of the film yields a large surface area for the chemical reactions to take place. It is especially important in photoelectrochemistry for water splitting, because quite often different materials are combined in the photoelectrochemical devices. This is further discussed in the next chapter.²²

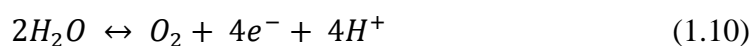
1.5.3 Photoelectrochemical water splitting

Photoelectrochemical water splitting is based on natural photosynthesis, where solar energy is stored in simple chemical bonds. The key is to mimic this process and store the solar energy in the form of electrons in covalent bonds between light elements (i.e. H-H, C-H and N-H), and do it much more efficiently. Of these bonds, H₂ has the largest energy density by mass, which is 143 MJ/kg.¹⁸ The drawback of H₂ is that it is a gas and needs appropriate storage or additional energy to store it as a liquid. The hydrocarbon fuels however are in liquid form and therefore have the optimum energy density by volume. Both options are considered as the candidates for the best solar fuel of the future and extensive research is ongoing in this field.¹⁸

The solar fuels generation in nature is run by two processes: the water splitting process and the carbohydrate formation process. It is shown that the main process which stores the solar energy is the water splitting one.³



Which in turn consist of two half reactions (under acidic conditions):



The water oxidation half reaction (Eq. 1.2) is the most challenging one. In order to form the O-O double bond, four O-H bonds in two water molecules must be broken. Then two H₂ molecules are formed from the electrons and protons released from the first reaction. When different fuel is the aim, the electrons and protons from water oxidation can also be combined with CO₂ to form liquid alcohol like methanol or other hydrocarbon fuels.¹⁸

To convert one molecule of H₂O to H₂ and ½ O₂ the free energy change under standard conditions is ΔG = 235.2 kJ/mol. This corresponds to thermodynamic reversible potential ΔE° = 1.23 V according to the Nernst equation.³ It means that the water oxidation runs at high anodic potential potentials:

$$E_{anodic} = 1.23 V - 0.059(pH) \text{ vs NHE} \quad (\text{Eq. 1.12})$$

To run the hydrogen evolution reaction, the corresponding cathodic potential is:

$$E_{cathodic} = 0 V - 0.059(pH) \text{ vs NHE} \quad (\text{Eq. 1.13})$$

The electrode which facilitates the oxidation reaction is called an *anode*, which is an n-type semiconductor, because the energy bands in the material are bent upwards and electrons are transferred away from the electrode surface due to the electric field in the space charge region at the semiconductor-electrolyte interface.^{18,19}

The electrode on which the reduction takes place is called a *cathode*, which is a p-type semiconductor, because the energy bands in the material are bent downwards and electrons are transferred to the electrode surface. In case of PEC water splitting, either anode or cathode or both are photoactive materials, and, in that case, they are called *photoanode* and *photocathode*.^{18,19}

In photoelectrochemical (PEC) water splitting, the idea is to use a semiconductor material(s) or a semiconductor-chromophore assembly to absorb light with photon energies larger than the 1.23 eV to run the water splitting reaction (Eq. 1.9). In practice, there are also additional losses in voltage due to kinetic and concentration overpotentials which are caused by charge carrier separation, charge carrier transport and catalysis. Therefore, to account for these losses, the energy needed to run the photoelectrocatalysis in practice is larger than 1.23 eV per one electron-hole pair and depending on the losses can be from 1.6 eV to 2.4 eV.¹⁹

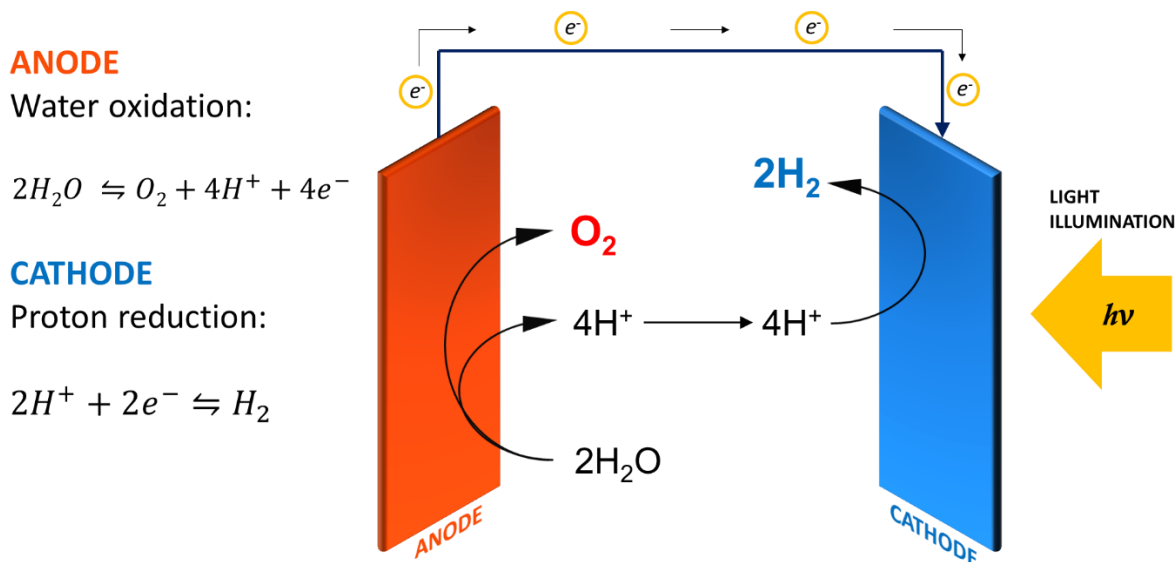


Figure 1.7. The schematics of the working principle of water splitting in a photoelectrochemical (PEC) cell. Water oxidation half-reaction is facilitated on the surface of the anode, the electrons released from the reaction transfer through an external circuit to the cathode side and are used to drive the proton reduction half-reaction takes on the surface of the cathode. In this case, process is driven by the light illumination from the cathode side where the cathode is photoactive.^{18,19}

There is an overpotential due to ohmic resistance originating from the resistivity in the system, η_{ohm} , there is an overpotential due to mass transport of ions in the electrolyte, η_{mt} , and then there is the overpotential needed to run the chemical reactions on both electrodes.

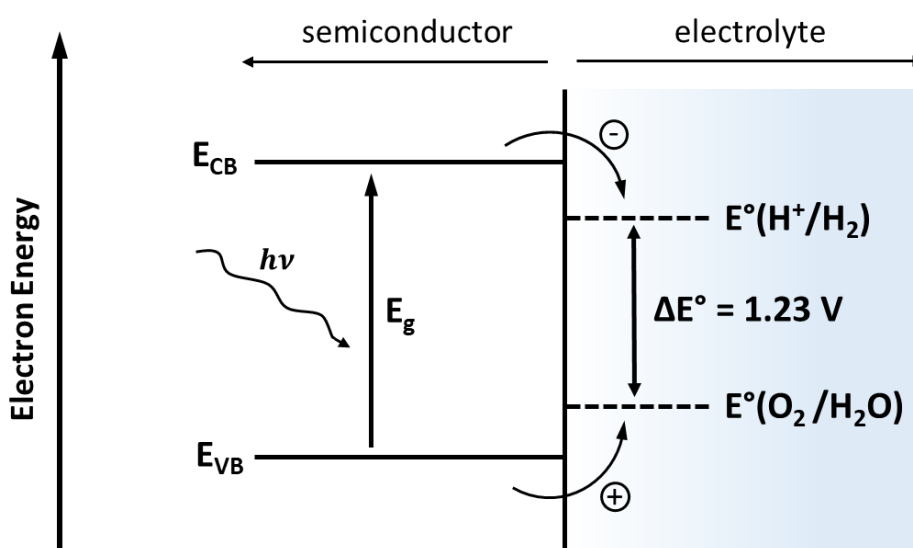


Figure 1.8. Schematic representation of the ideal semiconductor material for overall water splitting facilitating both water oxidation, $E^0(O_2/H_2O)$, and proton reduction, $E^0(H^+/H_2)$, half

reactions on its surface, E^0 is the reduction potential for both redox couples. E_{VB} of the semiconductor needs to be more positive than the $E^0(\text{O}_2/\text{H}_2\text{O})$ and E_{CB} needs to be more negative than the $E^0(\text{H}^+/\text{H}_2)$.¹⁹

The last can be divided into anodic overpotential, η_a , needed to be applied to the anode, and cathodic overpotential, η_c , which is applied to the cathode. The overall potential, ΔE , needed to be applied to the PEC cell is then expressed by the following equation.

$$\Delta E = \Delta E^0 + \eta_{ohm} + \eta_{mt} + \eta_a + \eta_c \quad (1.14)$$

To run the water splitting reaction efficiently the semiconductor photoelectrode must have optimal E_g for solar absorption. To have thermodynamic stability, the semiconductor's reductive decomposition potential for the proton reduction must be more negative than the semiconductor's conduction band edge (E_{cb}) and the oxidative decomposition potential for water oxidation must be more positive than the semiconductor's valence band edge (E_{vb}).³ The ideal material would satisfy both requirements and would be able to drive full water splitting reaction on its surface (Figure 1.8). In practice this material is hard to find and there are limited number of materials which meet these criteria.^{29,30,32,33} However, these materials have additional limitations, like high cost of fabrication and low stability, or they require additional co-catalysts to work.^{29,30,31,33} Therefore, the common practice is to use different semiconductors for the two half reactions, which significantly expands the choice of materials available.¹⁹

1.5.4 Photoelectrochemical cell

Photoelectrochemical cells can be divided into three categories depending on what is produced in the cell and if the reactions are spontaneous or not. If the reaction at the anode is just a reversal of the reaction happening on the cathode and no chemicals are produced in the process, then it is called a *regenerative PEC cell*. The best example of that type of PEC cell is a dye-sensitised solar cell (DSSC), where a redox couple facilitates the charge transfer between electrodes (for example iodide/triiodide couple). The function of the cell is to produce electricity from light, like a conventional solar cell, but this is achieved through chemical reactions at the semiconductor-electrolyte interfaces the in the cell. Another type of PEC cell is the one where different chemical reaction takes place on anode compared to cathode resulting in the production of chemicals and a change in the chemical composition of the electrolyte. This type of PEC cell is called a *photoelectrosynthetic cell*. In a

photoelectrosynthetic cell the net chemical reaction is nonspontaneous, $\Delta G > 0$, and the energy from the absorbed light is used to drive the reactions which would not run in the dark. This means that the energy from the light is stored as chemical energy as a result of the process. The example of this cell is the PEC cell for water splitting producing H_2 on the cathode and O_2 on the anode. There is also a third type of PEC cell which is quite similar to the photoelectrosynthetic cell, but there is an important difference. The chemical reactions in the cell are in this case spontaneous, $\Delta G < 0$, and the energy from the absorbed light is used to speed up the reaction which would otherwise take place also in the dark. This type of PEC cell is called a *photocatalytic cell*.^{20,23} An example of a photocatalytic cell is the reduction of N_2 to ammonia on p-GaP when light illumination is applied using Al as the reducing agent.²⁶ This process is called photoassisted nitrogen fixation.

The photoelectrosynthetic cell can also have several different variations depending on the architecture of the cell and the number of solid-solid interfaces in the cell. Generally, there are two main architecture types. In first type the electrodes are separated by electrolyte and connected through external wiring which facilitates the electron transfer from one electrode to another. In this case either only one electrode is photoactive and the other one is acting as the dark electrode, or both are photoactive. For example, photocathode is coupled with a dark anode (for example Pt) or vice versa. If both electrodes are photoactive, when photocathode is coupled with a photoanode, this is called a tandem configuration. The second type of photoelectrosynthetic PEC cell architecture is the one where anode and cathode are put together forming a monolithic structure with ohmic contact between the anode and cathode facilitating the electron transfer. The advantage of the first type of device is that the sides of the electrodes where the reactions take place are positioned face-to-face and therefore there is a direct and short path for ion transfer between the electrodes (for example proton transfer from anode to cathode). However, the limitation is the need for an external wiring between electrodes, the requirement to have two separate substrates where the electrodes are usually deposited and a potential need for a separation membrane between the electrodes which would prevent the mixing of the chemicals produced on the electrodes. In case of water splitting, proton exchange membrane (PEM) is often used. In case of the second monolithic architecture the wiring between the electrodes is not necessary and also there is no need for the separation membrane, because products are produced on the separate sides of the same electrode. However, the limitation is the transfer of ions between electrodes and also the fabrication of the electrode depending on the system, because active materials need to be deposited on both sides of the same substrate (for example photoactive layer with catalyst on anode side and catalyst on the cathode side).²⁰

In this thesis the focus is on the photoelectrosynthetic PEC cell and the proton reduction half reaction on the photocathode using the cell architecture where the light absorption, charge carrier generation and proton reduction is facilitated. The water oxidation half reaction is facilitated on the dark anode for which a platinised fluorine doped tin oxide (FTO) is used. The cathode and anode are separated from each other by aqueous electrolyte and connected through external wiring. Therefore, an introduction is provided for different parts of this type of PEC cell explaining their functions and requirements.

The most important part of this type of PEC cell is the photocathode. Photocathodes can be made of only one photoactive semiconductor material which facilitates electron-hole pair creation through light absorption and proton reduction on the surface. It can also be a material system where different materials have different functions.³⁴ Quite often a separate co-catalyst is used on the photoactive semiconductor surface which accelerates the proton reduction.³⁵ It can also be that a separate light absorber called photosensitiser is applied to the semiconductor surface which facilitates the charge carrier generation instead of the semiconductor (dye or a different type of photosensitiser).^{36,37} This type of cell is discussed in the next chapter under dye-sensitised PEC cell. The conditions for a good photocathode material for water splitting applications are that it has to be stable in water, resistant to photocorrosion, it has to have good conductivity to provide the sufficient cathodic current and the E_{CB} has to be more negative than the redox potential of the proton reduction.¹⁹

The anode in this case facilitates the water oxidation half reaction. Therefore, the overpotential, η_a , for this reaction needs to be as low as possible and the conductivity of the material has to be high. In the case of a photoactive anode, i. e. photoanode, the main requirement is that the E_{VB} is more positive than the oxidation potential of water. As for the photocathode, the photoanode needs to be stable in water and resistant to photocorrosion.¹⁹

PEM is needed for the separation of the H_2 and O_2 to prevent the formation of explosive mixtures and recombination of H_2 and O_2 . Therefore, it is a very important part of the device design. It is also one of the most expensive parts of the cell due to the deficiency of the suitable products on the market while the available ones have very high price (for example Nafion).³⁸

Another important property which has become a standard for PEC applications is the nanostructuring of the electrodes. This is due to the large active surface area this creates, meaning that the surface, where the fuel forming chemical reactions can take place, is considerably larger than for electrodes with smooth surface. There is a large number of

methods to fabricate nanostructured electrodes which all create electrodes with different surface areas and morphologies. The main aim is to have a large surface area but also a good contact between individual particles of the electrode to facilitate charge transfer.⁴⁰

Finally, to facilitate efficient H₂ evolution on photocathode or water oxidation on photoanode, an additional catalyst is usually needed to drive the half reactions. Often, noble metal catalysts like Pt, Pd or Ru are used when testing the new photocathode material to benchmark the system. This was also the purpose of using electrodeposited Pt in Chapter 3 in this thesis. However, keeping in mind the sustainability and possible upscaling of the system, earth-abundant catalysts are needed to keep the costs down. Number of different earth-abundant catalysts have been reported for photoelectrochemical H₂ evolution. The highest performing systems with co-catalyst have been based on p-Si photocathodes operating in acidic conditions, but using CoS as a co-catalyst, good results have been also shown in neutral water.⁴¹

1.5.5 Dye-sensitised photoelectrochemical cell

The dye-sensitised PEC cell is a subcategory of the photoelectrosynthetic cell. It evolved out of the dye-sensitised solar cell (DSSC), a device which instead of a p-n junction uses a semiconductor-electrolyte junction to separate charge carriers upon light illumination producing electrical current as a result. The first working DSSC based on nanostructured materials with reasonable efficiency was developed by O'Regan and Grätzel.²⁴ It had a working electrode with a layer of wide band gap nanostructured n-type semiconductor titanium dioxide (TiO₂) coated with a monolayer of Ru-based dye working as a photoanode and a Pt coated counter electrode which worked as a dark cathode. The dye on the TiO₂ surface facilitated the light absorption and electron-hole pair generation. The excited electron was injected from the photo-excited dye to the conduction band of the TiO₂. The electrodes were separated by a redox electrolyte containing an iodide-triiodide redox couple whose function was to act as a charge transfer shuttle between the electrodes. The device has several advantages compared to conventional solar cells. It uses cheap materials, production is low-cost and simple, and the reasonable efficiencies reported for the devices have enabled the technology to be commercialised.²⁵

The key to the success of the DSSC technology has been the high surface area n-TiO₂ electrode, which enabled the adsorption of enough light-absorbing dye to produce reasonable photocurrents. The p-type DSSC has also been under development for a considerable amount

of time with most devices based on nanostructured dye-sensitised NiO acting as the photocathode.⁴²⁻⁴⁷ These devices however have not achieved comparable efficiencies to TiO₂ based DSSCs, which are also much more common for that reason. This is mostly due to the limitations of the NiO, which are a poor hole conductivity and the non-ideal position of the valence band.⁴⁸

The concept of the DSSC was used to develop the dye-sensitised photoelectrosynthetic cell (referred in this thesis as dye-sensitised PEC cell). It is based on the same idea of using a high surface area nanostructured wide band gap semiconductor to act as a conductive support for photoabsorbing dye which would facilitate the charge carrier generation upon light absorption. However, in the case of the dye-sensitised PEC cell there is also a catalyst adsorbed on the dye or in the electrolyte, which would drive the chemical reactions on the electrode surface. The working principle of the dye-sensitised PEC cell is presented on Figure 1.9.

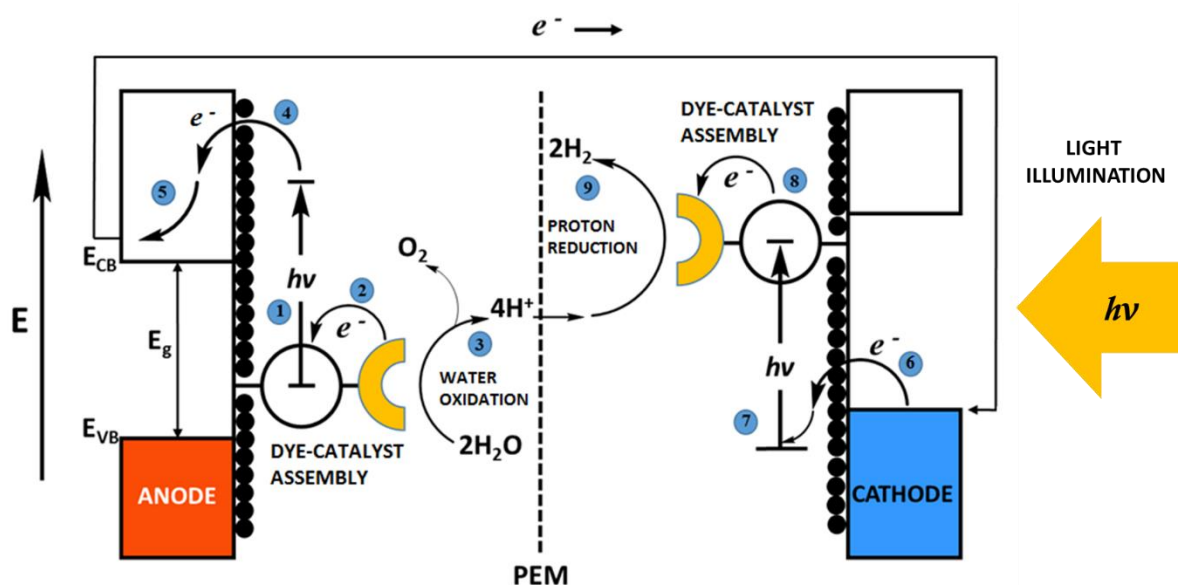


Figure 1.9. Schematic working principle of a hybrid dye-sensitised PEC cell, where both anode and cathode are dye-sensitised (tandem configuration) and functionalised with catalysts. 1, 7 – electron is excited to a higher energy state in the dye through light absorption, 2 – electron from the catalyst reduces the oxidised dye molecule after which the catalyst can oxidise water to O₂ and protons (3), 4 - excited electron is injected from the dye to the conduction band of the anode where it is transferred to the back contact (5) and from there through the external circuit to the cathode, 6 – electron is injected from the valence band of the cathode to the oxidised dye, 8 – excited electron in the dye on the cathode surface is transferred to the catalyst where it reduces protons in the electrolyte to H₂ (9).²⁷

In the dye-sensitised PEC cell (Figure 1.9) for water splitting the photoanode and photocathode are separated by the aqueous electrolyte so that the protons generated through water oxidation reaction diffuse through the electrolyte and proton exchange membrane (PEM) to the photocathode. In this figure both the photoanode and photocathode have dye and catalyst on the surface which facilitate the excited state electron transfer when photon is absorbed (1, 7). On the photoanode this is followed by the intramolecular electron transfer from the catalyst to the dye (2) and thereby catalyst is activated to perform water oxidation reaction (3). The excited electron is injected into the conduction band of the photoanode (4) from where it migrates through the material (5) and is transferred to the photocathode via the external circuit. On the photocathode, followed by the photon absorption, the hole is injected into the valence band of the photocathode (6) and proton reduction occurs (9) when hydrogen evolution catalyst is activated through the intramolecular electron transfer from the dye (8).²⁷

In the dye-sensitised PEC cell, when dye is adsorbed on the semiconductor, the band gap of the semiconductor, E_g , must be sufficiently wide to allow the photons to be transmitted and the dye to absorb the light of different wavelength. For example, if the dye absorbs photons with a wavelength of 600 nm (photon energy ~ 2 eV), then E_g of the semiconductor must be larger than 2 eV. Therefore, when designing a dye-sensitised photocathode, semiconductor band gap with and VB and CB positions must be taken into consideration when choosing suitable dye or dyes to be used with the specific material.

In this thesis the focus is on the study and development of the dye-sensitised photocathode and its application for hydrogen production coupled with a dark anode. The dye sensitised photocathode consists of a wide band gap nanostructured p-type semiconductor film on which a layer of light-absorbing dye is deposited and a catalyst which is either deposited on the surface of the dye-sensitised semiconductor nanoparticles or dissolved in the electrolyte. The working principle of the dye-sensitised photocathode is presented in Figure 1.10. The valence band of the semiconductor has to be more negative than the HOMO of the dye (HOMO – highest occupied molecular orbital) for the hole injection from the dye to the valence band to occur (2) when the electrons in the dye molecule are excited to an excited state in LUMO of the dye (LUMO – lowest unoccupied molecular orbital) (1). For the hydrogen to be evolved, a catalyst is used with reduction potential more positive than the LUMO of the dye so that electrons would have enough driving force to be transferred to the surface of the catalyst (3) where they accumulate and drive the proton reduction (4).²⁷ NiO is the most widely reported wide-band gap photocathode material used in dye-sensitised PEC cells.⁴⁹⁻⁶⁰ The dye-sensitised PEC cells based on NiO are discussed further in Chapter 3 and 4.

The structure of the dye molecule is also important so that the charge transfer could take place from the semiconductor, through the dye to the catalyst. Common practice is to use donor- π -acceptor structure, also known as push-pull structure, where charge transfer would occur from one part of the dye (donor moiety) to another (acceptor moiety) upon light absorption and electron excitation. The donor part of the dye would be connected to the dye surface through an “anchor” unit and the acceptor unit would be positioned close to the catalyst so that there would be optimal conditions for electron transfer from the semiconductor to the catalyst. The dye also needs to have a very long-lived excited state, so that recombination would not occur before the electron transfer to the catalyst. There are several recombination mechanisms that can take place on the dye-sensitised photocathode.

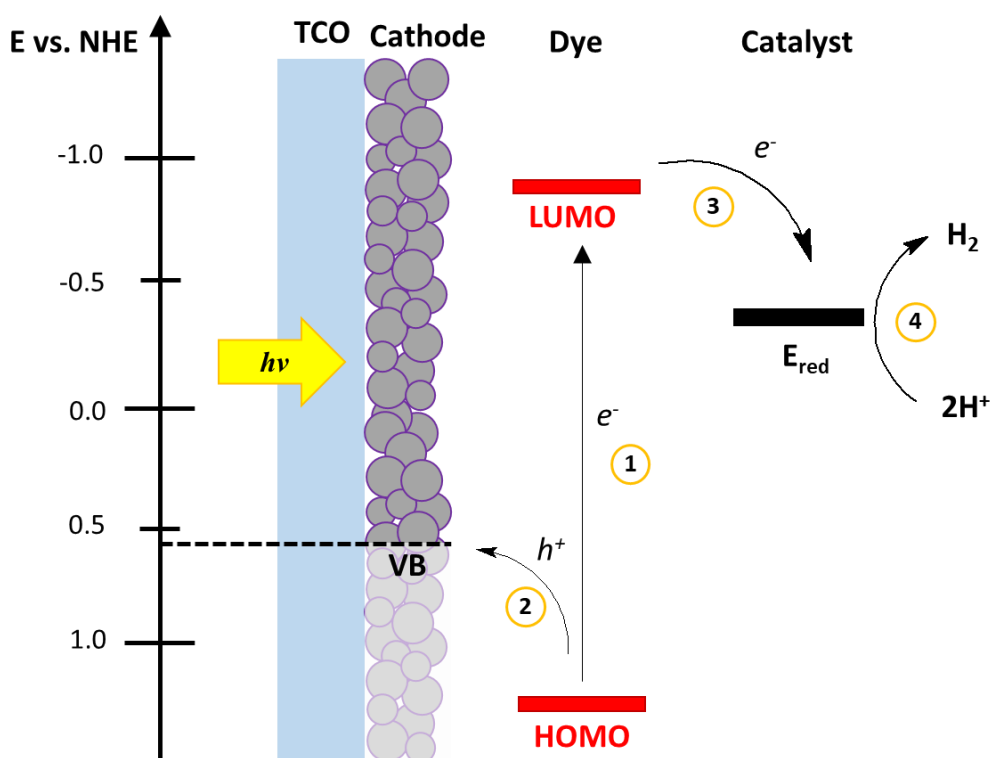


Figure 1.10. The working principle of a dye-sensitized photocathode for proton reduction. Upon light absorption by the dye, the electron is excited from the HOMO of the dye to the LUMO of the dye (excited state potential) (1), the same time the hole injection to the valence band of the semiconductor occurs regenerating the dye (2). The excited electron is transferred to the surface of the catalyst (3) which catalyzes the proton reduction (4).

The excited electron can recombine with the hole in the HOMO of the dye or with the holes in the valence band of the semiconductor. Also, the electron transferred to the catalyst can

recombine with the hole in the HOMO or with the hole in the valence band of the semiconductor.^{27,28}

The driving force for electron transfer, ΔG_{et} , from the dye to the catalyst is an important parameter to take into consideration when designing a dye-sensitised PEC cell. It can be calculated as the potential difference between the LUMO of the dye and the reduction potential of the catalyst.³⁶ Or in case of using electron acceptor in the solution, the driving force can be calculated as the potential difference between the LUMO of the dye and the reduction potential of the electron acceptor.

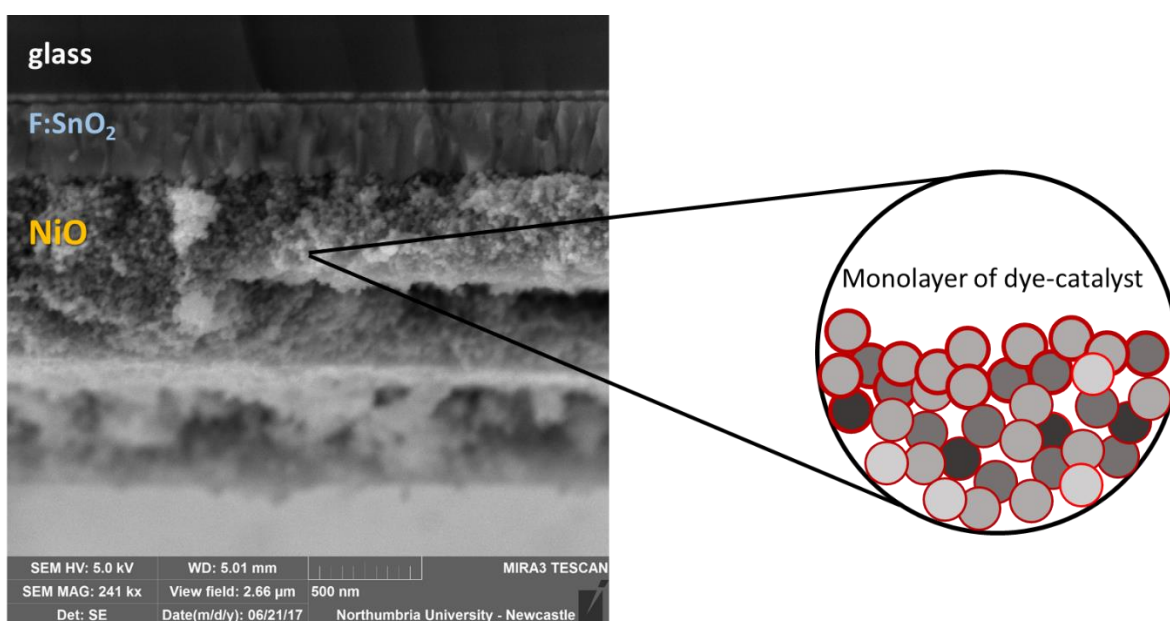


Figure 1.11. SEM image of the cross-section of the dye-sensitised NiO photocathode which is deposited on the FTO transparent conductive oxide on glass substrate. On the right the schematic picture of the nanostructured NiO is presented showing the dye-catalyst monolayer on the NiO nanoparticles. *The SEM image was taken by P. Maiello in Northumbria University.*

Finally, for the maximum light absorption it is important to have a high surface area on the cathode which would enable to adsorb the maximum number of dye molecules on the semiconductor surface. A similar strategy is used here as for the semiconductors in regular PEC cells where high active surface is sought for semiconductor electrodes. In dye-sensitised photocathode cell the high surface area serves two functions: maximum dye adsorption and maximum active surface area for proton reduction. An example of this type of high surface

area photocathode is presented on Figure 1.11, where SEM image of the dye-sensitised nanostructured NiO photocathode is presented with a schematic drawing of the nanoparticle film with dye adsorbed on every particle. The same NiO photocathodes were also used in this thesis with different dyes (Chapter 3) and integrated photocatalysts (Chapter 4).

1.7 Aims

The first aim of this project was to benchmark NiO based dye-sensitised photocathodes to understand the effect of the experimental environment on the photoelectrochemical performance of the dye-sensitised NiO photocathode and to study how the performance is influenced by each different parameter. The purpose was to understand what is limiting the current in dye-sensitised NiO photocathodes and what would be the optimal conditions to obtain highest photocurrents.

Further on, the second aim was to study the H₂ evolution on the dye-sensitised NiO photocathode in the optimal conditions and see how different catalysts perform. Especially, the focus was to see if the hydrogen evolution efficiency is increased if the dye and the catalyst are integrated into one molecule, instead of using separate catalyst.

In addition, it was reasoned that if NiO would be replaced with a different material, the performance and the H₂ evolution would be increased. CuCrO₂ was chosen as a candidate material and the results of this study are presented in Chapter 5.

Finally, it was reasoned that a multiphysics model of a PEC cell would be a useful tool to predict the performance of a PEC cell. A proof-of-concept modelling study of a PEC cell was performed using experimental parameters obtained during studies discussed in Chapters 3 and 4 and results are presented in Chapter 6.

References

- 1 United Nations, Department of Economic and Social Affairs, Population Division. World Population Prospects 2019. <https://population.un.org/wpp> (accessed 27.07.2019)
- 2 U.S. Energy Information Administration. International Energy Outlook 2018. <https://www.eia.gov/outlooks/ieo/>
- 3 BP Statistical Review of the World, 68th edition, 2019.
- 4 Edenhofer, O., R. Pichs-Madruga, Y. Sokona, E. Farahani, S. Kadner, K. Seyboth, A. Adler, I. Baum, S. Brunner, P. Eickemeier, B. Kriemann, J. Savolainen, S. Schlömer, C. von Stechow, T. Zwickel and J.C. Minx (eds.) IPCC, 2014: Summary for Policymakers. In: Climate Change 2014: Mitigation of Climate Change. Contribution of Working Group III to the Fifth Assessment Report of the Intergovernmental Panel on Climate Change. Cambridge University Press, Cambridge, United Kingdom and New York, NY, USA.
- 5 J. Cook, N. Oreskes, P. T. Doran, W. R. L. Anderegg, B. Verheggen, E. W. Maibach, J. S. Carlton, S. Lewandowsky, A. G. Skuce, S. A. Green, D. Nuccitelli, P. Jacobs, M. Richardson, B. Winkler, R. Painting, K. Rice, Environ. Res. Lett., 2016, 11, 048002.
- 6 Levitus, S.; Antonov, J.; Boyer, T.; Baranova, O.; Garcia, H.; Locarnini, R.; Mishonov, A.; Reagan, J.; Seidov, D.; Yarosh, E.; Zweng, M. (2017). NCEI ocean heat content, temperature anomalies, salinity anomalies, thermosteric sea level anomalies, halosteric sea level anomalies, and total steric sea level anomalies from 1955 to present calculated from in situ oceanographic subsurface profile data (NCEI Accession 0164586). Version 4.4. NOAA National Centers for Environmental Information. Dataset.
- 7 R. S. Nerem, B. D. Beckley, J. T. Fasullo, B. D. Hamlington, D. Masters and G. T. Mitchum. Climate-change–driven accelerated sea-level rise detected in the altimeter era. PNAS, 2018.
- 8 The Paris Agreement. <https://unfccc.int/process-and-meetings/the-paris-agreement/the-paris-agreement> (accessed 28.07.2019)

- 9 V. Masson-Delmotte, P. Zhai, H.-O. Pörtner, D. Roberts, J. Skea, P.R. Shukla, A. Pirani, W. Moufouma-Okia, C. Péan, R. Pidcock, S. Connors, J.B.R. Matthews, Y. Chen, X. Zhou, M.I. Gomis, E. Lonnoy, T. Maycock, M. Tignor, and T. Waterfield (eds.) IPCC, 2018: Summary for Policymakers. In: Global Warming of 1.5°C. An IPCC Special Report on the impacts of global warming of 1.5°C above pre-industrial levels and related global greenhouse gas emission pathways, in the context of strengthening the global response to the threat of climate change, sustainable development, and efforts to eradicate poverty. In Press.
- 10 WEO-2017, Special Report: Energy Access Outlook, International Energy Agency. 2017.
- 11 Renewables 2018: Analysis and Forecasts to 2023. International Energy Agency. 2019.
- 12 Office of Energy Efficiency and Renewable Energy, Wind Energy Technologies Office. <https://www.energy.gov/eere/wind/how-do-wind-turbines-work> (accessed 28.07.2019).
- 13 N. S. Lewis, G. Crabtree, Eds.; Basic Research Needs for Solar Energy Utilization; Office of Science, U. S. Department of Energy: Washington, DC, 2005.
- 14 IRENA (2019), Renewable Power Generation Costs in 2018, International Renewable Energy Agency, Abu Dhabi.
- 15 J. A. Moulijn, M. Makkee, A. Van Diepen, Chemical Process Technology, 2nd revised edition, 2013.
- 16 IRENA, Hydrogen from renewable power: Technology outlook for the energy transition, 2018, International Renewable Energy Agency, Abu Dhabi.
- 17 Solar Fuels and Artificial Photosynthesis: Science and innovation to change our future energy options. 2012. RSC publishing. www.rsc.org/solar-fuels. (accessed 20.07.2019).
- 18 T. R. Cook, D. K. Dogutan, S. Y. Reece, Y. Surendranath, T. S. Teets, D. Nocera, Chem. Rev., 2010, 110, 6474-6502.
- 19 M. G. Walter, E. L. Warren, J. R. McKone, S. W. Boettcher, Q. Mi, E. A. Santori and N. S. Lewis, Chem. Rev., 2010, 110, 6446-6473.

- 20 A. C. Nielander, M. R. Shaner, K. M. Papadantonakis, S. A. Francis, N. S. Lewis, *Energy Environ. Sci.*, 2015, 8, 16.
- 21 A. J. Bard, *J. Photochem.*, 1979, 10, 59.
- 22 K. Rajeshwar, *Fundamentals of Semiconductor Electrochemistry and Photoelectrochemistry*, 2007, 1-45.
- 23 A. J. Bard, L. R. Faulkner, *Electrochemical Methods: Fundamentals and Applications*, 2nd Ed., 2001, 746-760.
- 24 B. O'Regan, M. Grätzel, *Nature*, 1991, 353, 737-740.
- 25 M. Grätzel. *J. Photochemistry and Photobiology C: Photochemistry Reviews*, 2003, 4, 145–153.
- 26 C. R. Dickson and A. J. Nozik, *J Am. Chem. Soc*, 1978, 100, 8007.
- 27 W. Song, Zuofeng Chen, C. R. K. Glasson, K. Hanson, H. Luo, M. R. Norris, D. L. Ashford, J. J. Concepcion, M. K. Brennaman, T. J. Meyer, *ChemPhysChem*, 2012, 13, 2882 – 2890.
- 28 J. Willkomm, K. L. Orchard, A. Reynal, E. Pastor, J. R. Durrant, E. Reisner, *Chem. Soc. Rev.*, 2016, 45, 9.
- 29 A. Kudo, Y. Miseki. *Chem. Soc. Rev.*, 2009, 38, 253–278.
- 30 S. Chen, T. Takata, K. Domen. *Nat. Rev. Mat.*, 2017, 17050.
- 31 T. K. Townsend, N. D. Browning, F. E. Osterloh. *ACS Nano*, 2012, 6, 8, 7420-7426.
- 32 Y. Yan, B. Y. Xia, B. Zhao, X. Wang, *J. Mater. Chem. A*, 2016, 4, 17587.
- 33 J. H. Montoya, L. C. Seitz, P. Chakthranont, A. Vojvodic, T. F. Jaramillo, J. K. Nørskov.
- 34 W. Yang, J. Moon, *ChemSusChem* 2018, 11, 1–12.
- 35 A. Paracchino, V. Laporte, K. Sivula, M. Grätzel, E. Thimsen, *Nat. Mat.* 2011, 10, 456-461.
- 36 S. Yun, N. Vlachopoulos, A. Qurashi, S. Ahmad, A. Hagfeldt, *Chem. Soc. Rev.*, 2019, 48, 3705.
- 37 E. A. Gibson, *Chem. Soc. Rev.*, 2017, 46, 6194.

- 38 A. S. Aricò, M. Girolamo, S. Siracusano, D. Sebastian, V. Baglio, M. Schuster, *Membranes*, 2017, 7, 25.
- 39 A. Kirubakaran, S. Jain, R. K. Nema, *Ren. Sus. En. Rev.*, 2009, 13, 2430–2440.
- 40 S. C. Warren, K. Voitchovsky, H. Dotan, C. M. Leroy, M. Cornuz, F. Stellacci, C. Hébert, A. Rothschild, M. Grätzel, *Nat. Mat.*, 2013, 12, 842–849.
- 41 I. Roger, M. A. Shipman, M. D. Symes, *Nat. Rev. Chem.*, 2017, 1, 0003.
- 42 J. He, H. Lindström, A. Hagfeldt and S. Lindquist, *J. Phys. Chem. B*, 1999, 103, 8940–8943.
- 43 J. He, H. Lindström, A. Hagfeldt and S.-E. Lindquist, *Sol. Energy Mater. Sol. Cells*, 2000, 62, 265–273.
- 44 C. Y. Lee, H. S. Park, J. C. Fontecilla-Camps and E. Reisner, *Angew. Chem., Int. Ed.*, 2016, 55, 5971–5974.
- 45 D. Mersch, C. Y. Lee, J. Z. Zhang, K. Brinkert, J. C. Fontecilla-Camps, A. W. Rutherford and E. Reisner, *J. Am. Chem. Soc.*, 2015, 137, 8541–8549.
- 46 B. Shan, A. K. Das, S. Marquard, B. H. Farnum, D. Wang, R. M. Bullock and T. J. Meyer, *En. Env. Sci.*, 2016, 9, 3693–3697.
- 47 J. J. Leung, J. Warnan, D. H. Nam, J. Z. Zhang, J. Willkomm, E. Reisner, *Chem. Sci.*, 2017, 56, 510–514.
- 48 G. Boschloo and A. Hagfeldt, *J. Phys. Chem. B*, 2001, 105, 3039–3044.
- 49 K. Fan, F. Li, L. Wang, Q. Daniel, E. Gabrielsson and L. Sun, *Phys. Chem. Chem. Phys.*, 2014, 16, 25234–25240.
- 50 L. Li, L. Duan, F. Wen, C. Li, M. Wang, A. Hagfeldt and L. Sun, *Chem. Commun.*, 2012, 48, 988–990.
- 51 L. Tong, A. Iwase, A. Nattestad, U. Bach, M. Weidelener, G. Götz, A. Mishra, P. Bäuerle, R. Amal, G. G. Wallace and A. J. Mozer, *Energy Environ. Sci.*, 2012, 5, 9472.
- 52 Z. Ji, M. He, Z. Huang, U. Ozkan and Y. Wu, *J. Am. Chem. Soc.*, 2013, 135, 11696–11699.

- 53 P. B. Pati, L. Zhang, B. Philippe, R. Fern'andez-Ter'an, Ahmadi, L. Tian, H. Rensmo, L. Hammarström and H. Tian, *ChemSusChem*, 2017, 10, 2480–2495.
- 54 M. A. Gross, C. E. Creissen, K. L. Orchard and E. Reisner, *Chem. Sci.*, 2016, 7, 242–247.
- 55 R. J. Kamire, M. B. Majewski, W. L. Hoffeditz, B. T. Phelan, O. K. Farha, J. T. Hupp and M. R. Wasielewski, *Chem. Sci.*, 2017, 8, 541–549.
- 56 N. Pöldme, L. O'reilly, I. Fletcher, J. Portoles, I. V. Sazanovich, M. Towrie, C. Long, J. G. Vos, M. T. Pryce, E. A. Gibson. *Chem. Sci.*, 2019, 10, 99.
- 57 N. Kaeffer, J. Massin, C. Lebrun, O. Renault, M. Chavarot-Kerlidou and V. Artero, *J. Am. Chem. Soc.*, 2016, 138, 38, 12308-12311.
- 58 G. H. Summers, J-F Lefebvre, F. A. Black, E. S. Davies, E. A. Gibson, T. Pullerits, C. J. Wood, K. Zidek. *Phys. Chem. Chem. Phys.*, 2016, 18, 1059.
- 59 C. J. Wood, G. H. Summers, C. A. Clark, N. Kaeffer, M. Braeutigam, L. R. Carbone, L. D'Amario, K. Fan, Y. Farre', S. Narbey, F. Oswald, L. A. Stevens, C. D. J. Parmenter, M. W. Fay, A. L. Torre, C. E. Snape, B. Dietzek, D. Dini, L. Hammarström, Y. Pellegrin, F. Odobel, L. Sun, V. Artero, E. A. Gibson. *Phys. Chem. Chem. Phys.* 2016, 18, 10727.
- 60 N. Kaeffer, C. D. Windle, R. Brisse, C. Gablin, D. Leonard, B. Jusselme, M. Chavarot-Kerlidou and V. Artero, *Chem. Sci.*, 2018, 9, 6721–6738.

Chapter 2. Experimental procedures and methodology

2.1 General Methods

All reagents (analytical grade) were purchased from Sigma-Aldrich and used without further purification unless stated otherwise. Solvents were purchased from Fisher Scientific (analytical grade) and used without further purification unless stated otherwise. De-ionised (DI) water used for all analytical and (photo)electrochemical measurements was purified with Milli-Q purification system (water resistivity > 18.2 MΩ cm). Acetonitrile was purchased from Fischer Scientific (HPLC grade) and dried over molecular sieves. Dye D1 was available from previous study and was synthesised by G. Summers.¹ Dye D2 was synthesised and provided by A. Cullen in M. Pryce group in Dublin City University. Dye D3 was synthesised by Z. Han according to the literature (Chapter 3).² Dye-catalyst assemblies studied in Chapter 4 were synthesised and provided by L. O'Reilly in M. Pryce group in Dublin City University.³ CuCrO₂ and CuCr_{0.5}Fe_{0.5}O powder synthesis and paste preparation was carried out by K. Sardar in E. A. Gibson group in Newcastle University (Chapter 5). Chloropentaamminecobalt chloride, [Co(NH₃)₅Cl]Cl₂, was synthesised by G. Summers according to the literature.⁶ Tris(ethylenediamine)cobalt(III) tetrafluoroborate, [Co(en)₃](BF₄)₃, was synthesised by F. Black according to the literature.^{7,8}

2.2 Chemical Methods

2.2.1 NiO photocathode fabrication

Mesoporous NiO photocathodes were prepared by following a reported procedure.⁴ A NiCl₂ precursor solution was prepared by dissolving anhydrous NiCl₂ (1 g) and the tri-block co-polymer F108 (poly (ethylene glycol)-block-poly (propylene glycol)-blockpoly(ethylene glycol)) (1 g) in ethanol (6 g) and DI water (3 g). The precursor solution described above was spread onto fluorine doped tin oxide (FTO) conducting glass substrates (Pilkington TEC15, sheet resistance 15 Ω cm⁻²) using Scotch tape as a spacer (0.79 cm²), followed by sintering in an oven at 450 °C for 30 min. Undyed NiO films were prepared to a thickness of 1.5 μm, measured using a Bruker DektakXT stylus profilometer and averaged over 5 samples.

2.2.2 Synthesis of CuCrO₂

Synthesis of CuCrO₂ polycrystalline powder was carried out by K. Sardar according to the following method. An equimolar proportion of Cu(NO₃)₂ · 3H₂O and NH₄CrO₄ was ground

using a mortar and pestle. The mixture turned to a highly viscous paste having dark brown colour. Few drops of ethanol were added to ensure sufficient mixing of the paste. The formed brown paste was dried to form a dark brown powder. The powder was further ground and then used as a precursor for the synthesis of CuCrO_2 . The precursor powder was heated in N_2 atmosphere at 900°C and evolution of crystalline phases was examined by powder X-ray diffraction (pXRD) analysis (Figure 5.2, Chapter 5). For control measurements, the precursor powder was heated in air at 900°C to form second batch of CuCrO_2 powder.

2.2.3 Synthesis of $\text{CuCr}_{0.5}\text{Fe}_{0.5}\text{O}_2$

Synthesis of $\text{CuCr}_{0.5}\text{Fe}_{0.5}\text{O}_2$ polycrystalline powder was carried out by K. Sardar according to the following method. $\text{Cu}(\text{NO}_3)_2 \cdot 3\text{H}_2\text{O}$, $\text{FeCl}_3 \cdot 3\text{H}_2\text{O}$, $\text{Cr}(\text{NO}_3)_3 \cdot 9\text{H}_2\text{O}$ and citric acid mono hydrate were dissolved in DI water with molar ratio of 1:0.5:0.5:4 using 4 mmol of $\text{Cu}(\text{NO}_3)_2 \cdot 3\text{H}_2\text{O}$. The solution was then placed in an oil bath and heated to 90°C till it formed a dark blue viscous gel. This gel was dried in a hot air oven at 125°C overnight. The obtained solid was ground thoroughly in a mortar with a pestle to obtain a fine powder. The obtained powder was calcined under N_2 at 900°C for 10 h and evolution of crystalline phases was examined by powder X-ray diffraction (pXRD) analysis (Figure 5.18, Chapter 5).

2.2.4 Paste preparation and thin film deposition

CuCrO_2 and $\text{CuCr}_{0.5}\text{Fe}_{0.5}\text{O}_2$ pastes for electrode deposition were prepared according to the following procedure by K. Sardar. First, 80 mg of CuCrO_2 or $\text{CuCr}_{0.5}\text{Fe}_{0.5}\text{O}_2$ powder were first ground with 80 μl of oleic acid for 15 minutes. To it, 560 mg of terpineol was added and ground thoroughly for 15 minutes. This mixture was added to a clear solution containing 160 mg of ethyl cellulose in 5 ml of ethanol and continued grinding until almost all of the ethanol had evaporated, leaving behind a highly viscous paste.

The as-prepared paste was subsequently deposited onto FTO conducting substrates (Pilkington TEC15, sheet resistance $15 \Omega \text{ cm}^{-2}$) using doctor-blading technique. The as-deposited films with planar surface area of 0.79 cm^{-2} were annealed in air at 500°C for 3 h. For CuCrO_2 , half of the films were subsequently annealed in N_2 at 500°C for 3 h.

2.2.5 Dye-sensitisation of photocathodes

Dye sensitization was carried out on NiO electrodes (NiO deposited on FTO described in Chapter 2.2.1) to obtain D1|NiO, D2|NiO, D3|NiO discussed in Chapter 3, and 1|NiO and 2|NiO discussed in Chapter 4, and on CuCrO₂ electrode (CuCrO₂ deposited on FTO) to make D1|CuCrO₂ discussed in Chapter 5. The dye sensitization was conducted by soaking the bare electrodes in acetonitrile solutions (0.3 mM) of the corresponding dye or dye-catalyst assemblies for 16 h at room temperature. After this, the sensitised electrodes were removed from the solutions, rinsed with acetonitrile to remove any excess dye on the surface and left to dry in air.

2.2.6 Synthesis of C1 catalyst

The C1 inorganic catalyst ([Co(bdt)₂]TBA (where bdt = 1,2-benzenedithiolate)) synthesis was carried out according to the following modified literature method.⁵

Materials:

Co(BF₄)₂ · xH₂O (cobalt tetrafluoroborate hydrate), KOtBu (potassium tert-butoxide), benzene-1,2-dithiol, NBu₄Br (tetrabutylammonium bromide), dry methanol (MeOH).

Procedure:

MeOH was dried over molecular sieves prior to synthesis.

1. In a three-neck round bottom flask, Co(BF₄)₂ · 6H₂O (289.5 mg, 0.85 mmol) and KOtBu (384.5 mg, 3.42 mmol) were dissolved in 30 mL of dry MeOH under an N₂ atmosphere and allowed to stir at room temperature for 30 minutes.
2. To this solution, a degassed mixture of benzene-1,2-dithiol (237.1 mg, 1.67 mmol) in dry MeOH (5 mL) was added dropwise. The solution was allowed to stir for 4 h at room temperature while the colour darkened to deep blue.
3. To this solution, a solution of NBu₄Br (275.2 mg, 0.85 mmol) in 3 mL of dry MeOH was added, and the solution was allowed to stir at room temperature overnight.
4. The solvent volume was reduced under vacuum to ~10 mL, and a dark blue precipitate was formed.

5. The solid was collected and recrystallized from a dichloromethane / diethyl ether mixture to yield C1 as a blue crystalline solid (417 mg, 0.72 mmol, 85% yield).

6. Crystals for single crystal X-ray diffraction were grown subsequently by inserting a small vial with C1 in dichloromethane into a larger vial filled with diethyl ether to induce a slow diffusion crystallisation in the smaller vial. This method yielded large C1 crystals.

The obtained crystals of C1 were characterised using single crystal X-ray diffraction performed by Dr. P. Waddell. The crystal structure obtained from the single crystal X-ray diffraction is presented on Figure 2.1 below.

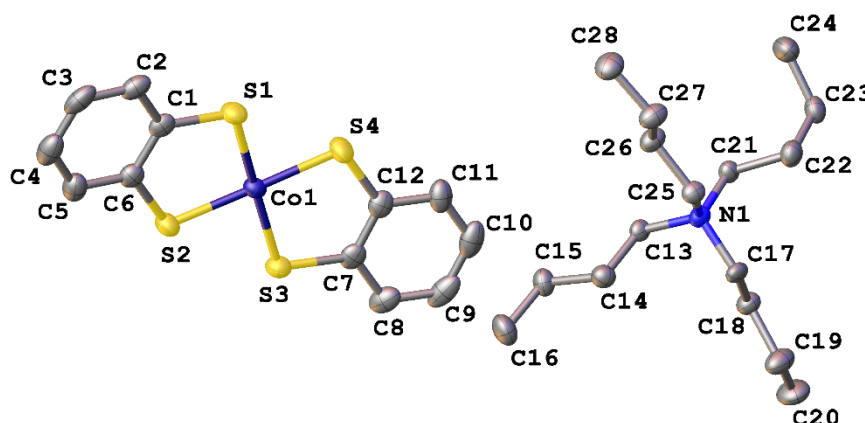


Figure 2.1. Molecular structure of C1 from Single Crystal XRD showing the $[\text{Co}(\text{bdt})_2]^-$ and TBA^+ counterion.

2.2.7 Electrolyte preparation

Aqueous electrolytes for photoelectrochemical measurements were prepared according to the following methods. Acetate buffer (pH 5) was prepared by mixing 35.7 ml of 0.1 M acetic acid (Sigma Aldrich, $\geq 99.8\%$) with 64.3 ml 0.1 M sodium acetate (Sigma Aldrich, $\geq 99.5\%$). Phthalate buffer (pH 3) was prepared by making a 0.1 M solution of potassium hydrogen phthalate (Sigma-Aldrich, 99.99%) and adjusting the pH to pH 3 with the addition of HCl. Phosphate buffer (pH 7) was prepared by mixing 1 M monosodium phosphate monohydrate solution (57.7 ml) with 1 M disodium phosphate heptahydrate solution (42.3 ml)

and diluting it to 0.1 M by the addition of DI water. Electrolyte solutions with electron acceptors were prepared by dissolving the corresponding reagents in 0.1 M buffer solutions.

Potassium hexacyanoferrate(III) (potassium ferricyanide) (Sigma-Aldrich, $\geq 99\%$) and 4,4'-Dithiodipyridine (DTDP) (Sigma-Aldrich, $\geq 98\%$) were recrystallised from warm water. Tris(ethylenediamine)cobalt(III) chloride, $[\text{Co}(\text{en})_3]\text{Cl}_3$, (Sigma-Aldrich, $\geq 99\%$) was recrystallised from warm water-acetonitrile mixture. Tris(acetylacetonato)iron(III), $\text{Fe}(\text{acac})_3$, (Sigma-Aldrich, $\geq 99\%$) was recrystallised from the mixture of warm water and MeOH.

2.2.8 Electrodeposition of catalysts

Electrodeposition of Pt and NiMo_xS ($x = ca. 0.05$) catalyst on dye sensitised NiO photocathodes was carried out using the Differential Pulse Amperometry (DPA) technique described in detail in the work of Shan et al.⁹ Briefly, during a DPA electrodeposition a forward pulse negative bias is applied for a short period of time after which a reverse pulse positive bias is applied. These forward and reverse pulses are cycled an arbitrary number of times in order to achieve a suitable deposition of desired material. During the forward pulse negative bias an electron percolation is induced during which electrons are transferred from FTO substrate to the corresponding dye molecules adsorbed on NiO (either D1, D2 or D3), from where they are further transferred between dye molecules through a lateral electron hopping mechanism. The applied negative bias has to be more negative than the reduction potential of the corresponding dye to facilitate the electron hopping process. The metal ions in solution are then reduced at the electrode surface by the electrons transferred from the FTO substrate via dye molecules.⁹

For NiMo_xS ($x = ca. 0.05$) electrodeposition a following formulation was used for the deposition solution. A solution of 50 mM NiCl_2 , 2.1 mM Na_2MoO_4 and 1.0 M thiourea in deionised (DI) water was prepared and degassed under N_2 for at least 30 minutes.⁹ For Pt deposition, a solution of 50 mM H_2PtCl_6 (chloroplatinic acid) in DI water was prepared.

DPA electrodeposition was carried out for Pt and NiMo_xS deposition on dye sensitised NiO photocathodes according to the following procedure. The deposition solution was placed in a three-electrode cell with the dye|NiO|FTO photocathode as the working electrode, Pt wire as the counter electrode and Ag/AgCl as the reference electrode. The electrodes were connected to a potentiostat and forward pulsed bias of -1 V was applied for 5 s followed by a reversed pulsed bias of 0.2 V for 5 s. This cycle was repeated for 15 times. After the procedure the working electrode was removed from the cell and rinsed with DI water.

2.3 Physical characterisation methods

2.3.1 *UV-visible spectroscopy*

The UV-visible absorption measurements were carried out with the Shimadzu 1800 UV-vis spectrophotometer (Chapters 3 and 4). The absorption spectra of dye and dye-catalyst samples in solution were measured using a quartz cuvette. The absorption of the dye and dye-catalyst on NiO was obtained by measuring the absorption of the dye sensitised NiO photocathode and subtracting the bare NiO|FTO absorption.

The diffuse-reflectance measurements were carried out on CuCrO₂ photocathodes using the Shimadzu 3600 UV-vis spectrophotometer with an ISR-603 integrating sphere using barium sulphate for baseline calibration (Chapter 5).

2.3.2 *Scanning electron microscopy*

The SEM measurements were carried on CuCrO₂ and CuCr_{0.5}Fe_{0.5}O₂ samples using TESCAN MIRA 3 instrument using different energy resolutions noted on the SEM images in Chapter 5. The SEM was also equipped with lithium-drifted silicon detector which enabled the measurement of Energy Dispersive Spectroscopy (EDS) data for the CuCr_{0.5}Fe_{0.5}O₂ samples presented in Chapter 5. The measurements were conducted by P. Maiello in Northumbria University.

2.3.3 *Powder X-ray diffraction*

The powder X-ray diffraction measurements were performed on Bruker 2D Phaser with copper radiation (Cu K α , $\lambda = 1,5419 \text{ \AA}$) on CuCrO₂ and FeCu_{0.5}Cr_{0.5}O₂ powder and film samples. The measurements presented in in Chapter 5 were performed by K. Sardar, data analysis and figures were made by N. Pöldme.

2.3.4 *X-ray photoelectron spectroscopy*

X-ray photoelectron spectroscopy (XPS) was carried out on Kratos Axis Nova XPS spectrometer using a monochromatic Al K α source. The samples were mounted on a clean aluminium platen and immobilised using double sided adhesive tape. The largest analysis area

available in this spectrometer (300 mm x 700 mm) was used. All the measurements were repeated on three different analysis positions with non-overlapping analysis areas. Charge compensation was used throughout the measurements. Spectra were analysed using CasaXPS software (version 2.3.16). Gaussian (70%) Lorentzian (30%), defined in CasaXPS as GL(30), profiles were used for each component.¹⁴ Spectra have been calibrated to obtain the adventitious C 1s spectral component binding energy of 284.7 eV. The measurements were performed by J. Portoles in NEXUS National EPSRC XPS Centre, data analysis and figures were made by N. Pöldme.

2.3.5 *Time-of-flight secondary ion mass spectrometry*

ToF-SIMS analyses were carried out using an ION-TOF 'TOFSIMS IV – 200' instrument (ION-TOF GmbH, Münster, Germany) of single-stage reflectron design.¹⁸ Positive and negative ion spectra and images of the samples were obtained using a Bi₃²⁺ focused liquid metal ion gun at 25 keV energy, incident at 45° to the surface normal and operated in 'bunched' mode for high mass resolution. This mode used 20 ns wide ion pulses at 6.7 kHz repetition rate. Charge compensation was affected by low-energy (*ca.* 20 eV) electrons provided by a flood gun. The total ion dose density was less than 1 x 10¹⁶ ions per m². The topography of the sample surface and the ion gun mode of operation limited the mass resolution in this work to *ca.* $m/\Delta m = 5000$. Positive and negative ion static SIMS spectra and images were recorded from the samples at room temperature. Raw data containing the secondary ions recorded at each pixel was acquired with a 128 x 128 pixel raster and a field of view of 200 mm x 200 mm. The samples for ToF-SIMS analysis were mounted directly onto a sample holder using small pieces of silicone-free double-sided tape (3M grade 665). The measurements were performed by I. Fletcher in NEXUS National EPSRC XPS Centre, data analysis and figures were made by N. Pöldme.

2.3.6 *Electrochemical and photoelectrochemical characterisation methods*

Electrochemical (EC) and photoelectrochemical (PEC) measurements were carried out using an IviumStat potentiostat connected to an electrochemical or photoelectrochemical cells. Cells used in this study were: BASi low volume solution cell for measurements of solutions in the dark, a custom-made three-electrode PEC cell (Figure 2.1) and a custom made two compartment PEC cell (Figure 2.2). For the counter electrode, a Pt coated FTO-coated glass slide (Chapters 3 and 5) or a platinum wire (Chapter 4) was used. Ag/AgCl (3.0 M

NaCl) was used as the reference electrode for the measurements in aqueous solutions, and Ag/AgNO₃ was used for measurements with non-aqueous solvents.

All potentials were reported vs Ag/AgCl reference electrode. For conversion to NHE, the following equation was used: $E_{\text{NHE}} = E_{\text{Ag/AgCl}} + E^{\circ}_{\text{Ag/AgCl}}$. For conversion to RHE, the Nernst equation was used ($E_{\text{RHE}} = E_{\text{Ag/AgCl}} + 0.059 \text{ pH} + E^{\circ}_{\text{Ag/AgCl}}$).

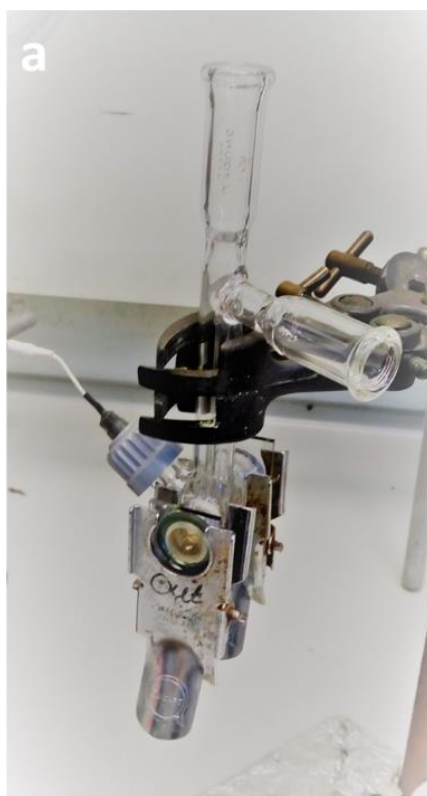


Figure 2.2. Custom built one compartment PEC cell used in studies throughout this thesis (Chapters 3, 4 and 5). WE and CE are clamped to the cell in a way, that they are in vertical position facing each other and in contact with the electrolyte inside the main compartment of the cell. Reference electrode is inserted into the cell from the side and the gas samples are taken through the top outlet of the cell either in the end of the measurement or continuously as described in Chapter 2.2.7.2.

During the PEC experiments, irradiation was provided by a 300 W Xe lamp (Oriel) fitted with an AM1.5 filter (Newport). This was calibrated using a calibrated reference Si solar cell (Newport) to give a power density of 100 mW cm⁻² (1 sun) at the photocathode surface with the irradiated area of 0.79 cm². During the IPCE measurements, a monochromator (Cornerstone) was used to apply monochromatic light illumination from the

white light illumination provided by the 300 W Xe lamp (Oriel) and the calibration was carried out against a certified reference Si photodiode.

The PEC cells were degassed with Ar or N₂ for at least 15 minutes prior to each measurement. The pH was measured using a pH mV⁻¹ Benchtop Meter (Hanna instruments). During chronoamperometry measurement chopped light illumination was first applied with 30 s intervals (1 cycle: 30 s light on/30 s light off), which was followed by constant light illumination. Before every PEC measurement, the working electrode (WE) was held 30 s to 1 min under the potential applied during the measurement, E_{appt} , in the dark to stabilise the background current.

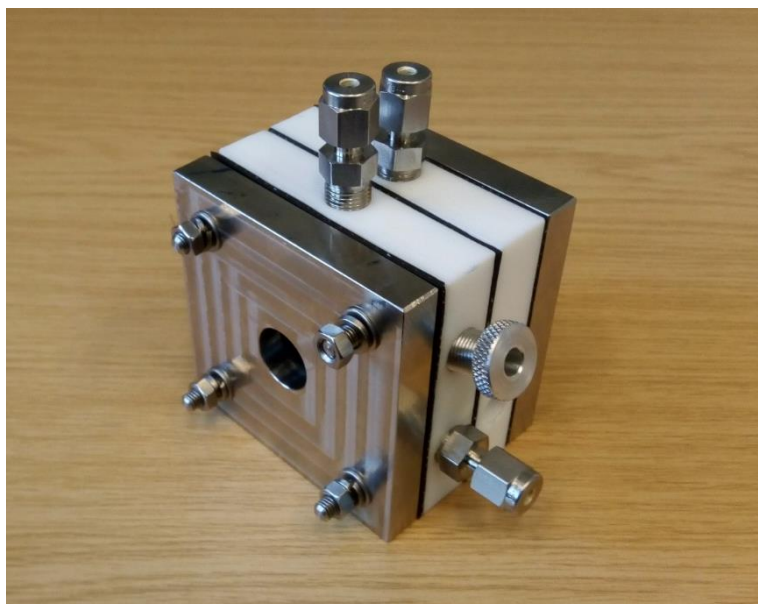


Figure 2.3. Custom built two compartment PEC cell. The cell's two compartments holding the electrolyte are made out of Teflon (white on the Figure), the WE and CE are in contact with electrolyte in the main compartments and are fixed in place by the stainless-steel sides, which hold the electrodes pushed against the Teflon compartments. The light illumination is applied through the hole in the stainless-steel side and the reference electrode is inserted into the cell from the side.

The faradaic efficiency, η_{Far} , was calculated by dividing the amount of H₂ produced experimentally (mol) with the theoretical H₂ production (mol) according to the charge generated from the photocurrent.

2.3.7 Gas chromatography

Gas chromatography (GC) measurements were carried out using a Shimadzu GC2014 chromatograph with the thermal conductivity detector (TCD) operating at 80 °C and fitted with a ShinCarbon ST Micropacked column (Restek) using Ar as a carrier gas. The experimental setup for the in-line, continuous gas sampling and analysis method is described in full by Summers et al.²² Briefly, Ar was continuously flowed through the electrolyte solution in a PEC cell to a 6-port, 2-position switch (VICI) through a cold trap at a constant flow (typically 10 cm³ min⁻¹). The switch injected a gas samples to the GC at three-minute intervals, maintained using a mass flow controller (Bronkhorst, E-Flow series). A 200 ml sample was analysed automatically every 3 min. The calibration of the amount of H₂ detected was carried out by varying the flow rate of H₂ (mol min⁻¹) into the system using the second 6-port, 2-position switch, which doses H₂ into the stream of carrier gas. The H₂ peak area varied linearly with the flow rate and the peak area was plotted against the flow rate on a calibration plot. The gradient of the line was used to calculate the H₂ production rate (mol min⁻¹) and to get the total amount of H₂ produced during an experiment, the production rate was integrated with respect to time.

The headspace analysis method was carried out as follows. A gas sample of specific volume (200 µl) was taken from the PEC cell after the measurement through a rubber seal on the cell. The sample was injected to the GC column through the injection port and the analysis was started manually. The area of the H₂ peak on the chromatogram was integrated obtaining the volume of H₂ produced during the measurement. Three gas samples were usually taken, and the average production was calculated for each measurement. Calibration for headspace analysis was carried out by injecting gas samples with known concentration of H₂ into the GC and taking the calibration number from the calibration graph.

2.4 Theoretical background

The basics of the theory behind the physical characterisation techniques used in this thesis are briefly explained in this chapter. The literature sources used are listed in References in the end of Chapter 2 and corresponding references are also provided in the end of every paragraph.

2.4.1 UV-visible spectroscopy

UV-visible spectroscopy is a measurement technique to measure the absorption of light in ultraviolet and visible regions of electromagnetic spectrum, at 190–400 and 400–700 nm, respectively.¹⁰ When photons are incident with a semiconductor material there are three possible scenarios of what will happen. Photon can be scattered from the material, transmitted through the material or absorbed in the material. The latter happens only when the energy of a photon, E_{ph} , is equal or greater than the band gap, E_g , of the semiconductor material. E_g is the difference in energy between the highest occupied molecular orbital (HOMO) and the lowest unoccupied molecular orbital (LUMO) or in another words, the energy amount needed to excite an electron from the valence band to the conduction band. When a photon is absorbed in a semiconductor material then charge carriers are created in the form of an electron-hole pair. This electronic transition occurs in the UV-visible range and the UV-visible spectroscopy is used to detect and quantify those transitions.^{10,11}

The measure of absorbance of light into material is the absorption coefficient, α , which determines how deep into the material the light with specific wavelength will reach before it is absorbed. It depends on the wavelength and the properties of the material. The absorption coefficient dependence on the wavelength is plotted on a graph. A low absorption coefficient shows that the material is not absorbing light very well at a given wavelength or there are forbidden electronic transitions, which result in low absorbance.¹⁰

The value for E_g of the material can be determined from UV-visible data using a Tauc plot (Figure 2.4).¹² In a Tauc plot, the absorption spectrum of a material is displayed in a way that the band gap of the material can be extrapolated. On the y-axis the quantity $(\alpha h\nu)^r$ is given, where α is the absorption coefficient, r is a constant, depending on the nature of the band gap transition ($r = 1/2$ for indirect transition, $r = 2$ for direct transition), and $h\nu$ is the photon energy (h – Planck's constant, ν – frequency of a photon) calculated using the following equation

$$E_{ph} = hc / \lambda \quad (2.1)$$

And the band gap of the material, E_g , can be calculated as follows

$$E_g = h\nu / \lambda \quad (2.2)$$

where h is the Planck's constant equal to 6.626×10^{-34} J s, c is the speed of light equal to 2.998×10^8 m s⁻¹ and λ is the wavelength.¹¹

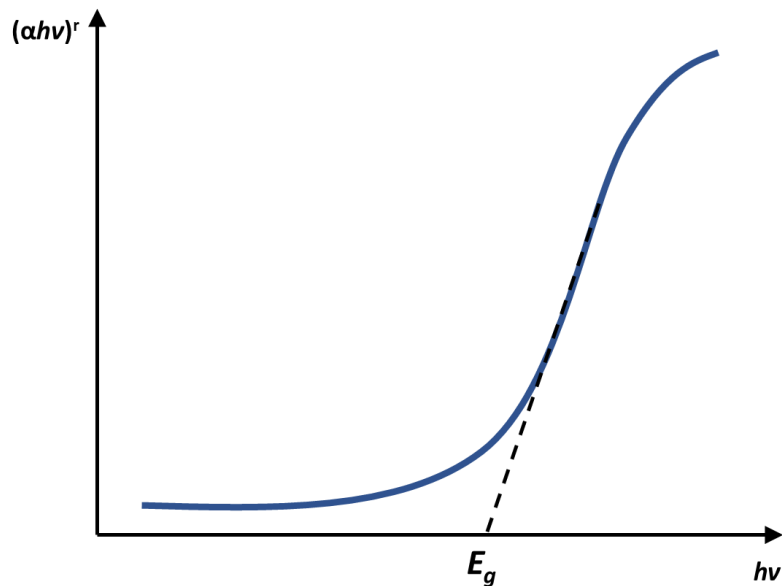


Figure 2.4. Schematic representation of a Tauc plot used to determine the band gap, E_g , of the material.

2.4.2 Scanning Electron Microscopy

Scanning Electron Microscopy (SEM) is a material characterization technique which uses a focused beam of high-energy electrons to probe the sample and to create a high magnification image. When an electron beam interacts with the atoms in various depths in the sample, electrons and radiation are emitted as a result, which give information about the sample material and surface morphology. These include secondary electrons, back-scattered electrons, photons (characteristic X-rays), visible light and heat. Secondary electrons and back-scattered electrons are the ones used for creating an image of the sample. Secondary electrons are emitted from the top surface layer of the sample and are, therefore, especially useful to give information about the morphology and topography. Back-scattered electrons are reflected from the sample through elastic scattering. They are most valuable for multiphase samples by enhancing the contrast in sample composition. Characteristic X-rays are generated when electrons collide inelastically with inner shell electrons in sample atoms resulting in creation of excited state electron (and also a core hole) which releases energy (X-ray with specific wavelength) when returning to the lower energy state. These characteristic X-rays

correspond to specific element and, therefore, the composition of the sample can be determined.¹⁰

SEM technique can be applied to various different sample materials, like semiconductors, alloys, polymers, organic tissue and even microorganisms. Achievable resolution can be even better than 1 nm and samples can be studied in different conditions: high temperatures, low temperatures, high and low vacuum and even in wet conditions. When using conventional imaging in SEM then the sample should be conductive and electrically grounded, otherwise electrostatic charge can accumulate on the sample surface and ruin the image. When sample has low conductivity or is insulating then it is usually coated with thin layer of conducting material like gold, silver, platinum and graphite.¹⁰

2.4.3 Powder X-ray Diffraction

X-ray diffraction is one of the most common and powerful techniques to determine the structure of materials. It is based on the interference created by an object in the path of waves. The general condition for the interference to occur is that wavelength of the radiation must be in the same magnitude as the dimensions of the object. The interference can be either destructive, decreasing the amplitude of the wave, or constructive, increasing the amplitude of the wave. The areas of constructive and destructive interference can be seen and regions of higher or lower intensities. The pattern formed by the interference of different intensities is called the diffraction pattern. In the case of X-rays, the wavelength is in the order of 10^{-10} m which is the same magnitude as the separation of lattice planes in a crystal.¹⁰

For analysis of the diffraction pattern, the simplest way is to visualize the lattice planes as parallel semi-transparent mirrors reflecting the X-ray beams. Using this quite simple model, the angle of the incident beam for the constructive interference can be calculated. According to Bragg's law the reflected waves are in phase and therefore interfere constructively when the glancing angle of the X-ray beam satisfies the following relation:

$$n\lambda = 2d\sin\theta \quad (2.3)$$

where θ is the glancing angle, d is the separation of the planes, λ is the wavelength and n is the integer number of the wavelength. When the incident angle is determined, the separation of planes, d , can be calculated. This is also one of the main applications of the Bragg's law.¹⁰

The X-ray diffraction can be either applied to a single-crystal sample, a powder sample or a film sample. For the last two sample types a powder X-ray diffractometer is used, and the

diffraction pattern obtained is referred to as the powder diffraction pattern. Both in a powder and a film sample there is a larger amount of small crystals oriented in random directions. However, some of those crystals will be oriented in a way that constructive interference can result when the sample is irradiated. In a powder diffractometer the intensities of the reflections are collected electronically by a detector rotating around the sample stage. The result is the powder diffraction pattern giving a relation between reflection intensity and the glancing angle θ . The powder diffraction technique is mainly used for identification of the solid substances when the created diffraction pattern is compared with a database of stored diffraction patterns. It can also be useful to determine different phases since the diffraction patterns of different phases of the same substance vary. Also, the amounts of different phases can be determined and initial determination of the parameters of the unit cell.¹⁰

The diffraction peak width also varies with the scattering angle 2θ as $\cos\theta$. At large angles the crystallite size broadening is most pronounced. However, at large angles the instrumental profile width and microstrain broadening have also larger effect. In addition, the peak's intensity decreases at larger angles. Hence, it is better to use peaks between angles 30° and 50° 2θ to get the most reliable result.¹³

2.4.4 X-ray photoelectron spectroscopy

X-ray photoelectron spectroscopy (XPS) is a powerful surface characterisation technique widely used to obtain information about the electronic structure and ionisation energies of atoms and, therefore, the chemical composition of surfaces.¹⁴ The technique is based on the photoelectric effect first observed by H. Hertz in 1887 and explained by A. Einstein in 1921, for which he received a Nobel Prize in physics. Using photoemission as an analytical tool was further developed by K. Siegbahn. In 1954 his research group recorded the first XPS spectrum on sodium chloride and 1981 he received a Nobel Prize in physics for his work which was of crucial importance in developing XPS to the analysis technique it is today.

The basic principle of XPS is explained as follows. X-ray photons with defined specific energy are used to irradiate the surface of the sample thereby exciting the core level electrons of surface atoms which are then emitted from the surface as photoelectrons. Emitted photoelectrons with different energies are filtered using a hemispherical analyser after which the intensities of photoelectrons with defined energies are recorded by the detector. Because the core level electrons of atoms in solid-state have defined energetic values, i. e. binding energies, a photoelectron spectrum with peaks characterising the electronic structure of atoms

and the sample surface can be generated as a result of the measurement. Since each core-level electron has a defined binding energy, E_b , and X-ray energy is constant throughout the measurement, each emitted photoelectron has a defined kinetic energy, E_k , which is expressed by the following equation:

$$E_k = h\nu - E_b - \phi_{analyser} \quad (2.5)$$

Where E_b is the binding energy of the core level electron, $h\nu$ is the X-ray photon energy (for example for Al $K\alpha$ radiation source, $h\nu = 1486.6$ eV) and $\phi_{analyser}$ is the work function, which is produced by the analyser and is usually around 4-5 eV.¹⁴

The XPS spectra shows the binding energies specific to electronic states of atoms on the sample surface. In addition, the chemical environment of the surface atoms can be established from the shifts of the photoelectric lines which are well defined and characteristic to a specific chemical species. For example, different oxide species can be identified from the shifts of photoelectric lines. In addition, even larger organic molecules deposited on the surface can be identified from XPS data, since different chemical bonding can be correlated to specific chemical shifts.¹⁴

2.4.5 Time-of-flight secondary ion mass spectrometry

Time-of-flight secondary ion mass spectrometry (ToF-SIMS) is a highly sensitive analytical surface characterisation technique, which enables the detection and identification of particles with a mass resolution as fine as 0.001 atomic mass units (amu). It is used for surface analysis across different scientific disciplines to find answers to wide variety of questions and different levels of complexity.¹⁵

In ToF-SIMS analysis, a focused pulsed primary ion beam is used to bombard the surface of the sample (which can be solid or liquid), thereby removing secondary ions from the top first or second monolayer of the sample material. The removal of the ions takes place through a so-called collision cascade effect, where the energy of the primary ions is transferred to the targeted surface allowing the atoms or molecules in top surface layers to overcome the surface binding energy. The ionised particles (both positive and negative ions) are accelerated to a common kinetic energy along the flight path directing them to the time-of-flight mass analyser. Since the accelerated ions possess the same kinetic energy, the velocity and time-of-flight is different for ions with different masses. The lighter ions gain higher velocities and have shorter time-of-flight, reaching the analyser sooner. Therefore, the mass of

different ions can be determined according to their flight time from the time of collision to the time they reach the detector. This enables also to achieve a very high resolution, because the time-of-flight of the secondary ions can be measured in nanoseconds.¹⁵

The ToF-SIMS apparatus consists of several essential components. The ion gun generates the high-energy primary ion beam (keV) using a source material, which is usually Cs or Ga. Samples are mounted on a sample target and the sample chamber and ultrahigh vacuum is applied to the whole system to remove anything from the measurement atmosphere that can interfere with the primary ion beam and secondary ions extracted from the sample surface. The purpose of the flight path is to direct the secondary ions to the detector while separating the ions according to their mass using a mass analyser. The detector usually consists of a Faraday cup, which catches the charged particles, and an electron multiplier, which generates a pulse of electron upon ion impact with the cup which is directly measured by a computer.^{16,17}

The high resolution provides the opportunity to detect trace elements on the surface even down to the levels of ppm and ppb. It also provides the possibility to analyse insulating materials because, during the flight time of the secondary ions, the extraction field can be switched off. This allows the low energy electrons to be used to compensate any surface charging occurring on the sample. Due to the nature of the measurement, using an ion beam for surface analysis, it can also be used for depth profiling with high precision. During depth profiling an ion beam is used to remove individual atomic layers from the surface and measuring the mass spectra after the removal of each layer. In addition, one of the most powerful features of the technique is the possibility to conduct retrospective analysis of the surface, which means that for every surface particle registered by the detector, a full mass spectra and location on the surface is stored. This, however, results in a very large sets of data to be generated during the measurement, which needs to be taken account when planning an extensive study.^{16,17}

With the ToF-SIMS measurement, detailed and concise elemental and molecular information can be acquired about the sample surface. Samples can be inorganic and organic, because the soft nature of the primary ion collision with the sample allows even large molecules to be removed from the surface with minimal fragmentation. This enables the analysis of surfaces of very different materials. It is used for the analysis of different semiconductor materials, ceramics, metals, polymers, biomaterials and even organic tissue. Therefore, it is not surprising that the technique is also applied in very different scientific fields. For example, ToF-SIMS analysis is becoming increasingly common technique to be

used in materials science, but it is also applied in the study of pharmaceuticals, geological materials and even in astrophysics.^{16,17}

2.4.6 *Electrochemical and photoelectrochemical methods*

2.4.6.1 *Electrochemical system and (photo)electrochemical cell*

Any system, which can be connected to at least two electrodes enabling the application of potential between the electrodes and inducing an electron flow from one electrode to another through an external circuit, can be described as an electrochemical system. It can be a lithium ion battery in an electrical car, an industrial electrolyser producing chlorine, a fuel cell producing electricity or a biological system which can be studied when connecting electrodes to it. An electrochemical system can consist of several electrochemical cells. An electrochemical cell however is a more specific term describing an electrochemical system with two or three electrodes connected to it. Electrochemical cells can be galvanic cells, where spontaneous redox reactions on electrodes create electrical current, and electrolytic cells, in which electric current is used to catalyse chemical reactions on the electrodes to produce useful chemicals. Fuel cells, for example, are galvanic cells and best example of an electrolysis cell is an electrolyser. Photoelectrochemical (PEC) cells are also electrolysis cells, but energetic free carriers (electrons and holes) in a PEC cell are provided by electronic excitation of the material by sunlight. Ideally zero bias is applied to the cell, but in practice low applied bias is used to promote charge extraction and prevent charge recombination.^{19,20}

An electrochemical cell consists of either two or three electrodes. A two-electrode electrochemical cell has a working electrode (WE) and a counter electrode (CE). In three electrode electrochemical cell, a reference electrode is also used. When the potential of the WE is measured in a two electrode cell, it is measured against the CE. But in three-electrode configuration, it is measured against the reference electrode. The reference electrode keeps a constant potential during the experiment. The controlling of the potential of the working electrode with respect to the reference electrode means that the potential energy of the electrons in the working electrode is controlled. When the potential of the working electrode is made more negative with respect to the reference electrode then the energy of the electrons is increased, and they can start to move from the electrode to the solution species with vacant electronic states. This flow of electrons from the electrode to the solution is called cathodic current (reduction current). However, when the potential is made more positive, then the energy of the electrons in the working electrode is decreased and electrons of the solution species may start to transfer to the working electrode with energetically lower electronic

states. The electron flow from solution to the working electrode is called anodic current (oxidation current).^{19,20}

2.4.6.2 *Cyclic and Linear Sweep Voltammetry*

Voltammetry is an electroanalytical method with the purpose of studying the current density dependence on the applied potential. The applied potential is varied over time and the current response is measured. The scan rate in voltammetry measurement determines how fast the applied potential is varied, usually mV s^{-1} .^{19,20}

Cyclic Voltammetry (CV) is a popular electrochemical technique to conduct studies on electrochemical systems and it has proven to be very useful for obtaining information about complex electrode reactions. In the CV measurement the potential of the working electrode is cycled and resulting current is measured. When potential is swept to the positive direction (anodic scan) then the oxidation of solution species occurs, and the process is represented by a peak in current profile. This process gives us the anodic peak current (i_{pa}) and anodic peak potential (E_{pa}) of the oxidation process. When the potential is switched and swept to the negative direction (cathodic scan) then at sufficiently negative potentials reduction of solution species occurs represented by peak in current profile. This gives us the cathodic peak current (i_{pc}) and cathodic peak potential (E_{pc}) for the reduction process.^{19,20}

The ratio of the peak currents, $i_{\text{pa}}/i_{\text{pc}}$, and the separation of the peak potentials, $E_{\text{pa}} - E_{\text{pc}}$ can tell us several things about the process under study. For a reversible redox process, the $i_{\text{pa}}/i_{\text{pc}} = 1$ at all scan rates and $\Delta E_{\text{p}} = E_{\text{pa}} - E_{\text{pc}} = 59.2 / n$ (mV) at 298 K (n = number of electrons transferred). For a quasi-reversible process, the value of ΔE_{p} is larger than $59.2 / n$ and increases with the scan rate. In addition, if the process is not reversible, then the value of $i_{\text{pa}} / i_{\text{pc}}$ is less than 1 due to additional chemical reactions of oxidised and reduced species, meaning that oxidised and reduced species are not stable during the CV experiment.^{19,20}

Linear Sweep Voltammetry (LSV) follows the same basic principles and experimental procedures as the Cyclic Voltammetry with the difference that potential is swept only in one direction. It is useful when only reduction or oxidation is of interest or when conducting photocurrent measurement where photocurrent generation dependence on applied potential is studied or the photocurrent onset potential needs to be determined. It is also widely used for determining the overpotentials for different chemical reactions taking place on the WE.^{19,20}

2.4.6.3 Chronoamperometry

During a chronoamperometry (CA) measurement the potential of the WE is held at constant value and the current density profile dependence on time is studied. It is a very useful experiment when studying the long-term efficiency and stability of the WE and overall electrochemical system. For example, it is a crucial technique to assess the photocurrent generation efficiency and stability over time and it also gives a valuable insight into the various additional processes which can occur on the electrode during a long-term operation. For example, during the CA under light illumination measurements, the photocurrent response profile after the light is applied can give indications about charge transfer limiting processes on the electrode.^{19,20}

2.4.6.4 Incident photon-to-electron conversion efficiency

The quantum efficiency of a photoactive system is also known as the incident photon-to-electron conversion efficiency (IPCE). It quantifies how much light is converted into electricity for a given photoactive system (e. g. photoelectrode like photocathode) at a specific wavelength and is calculated using the following equation:

$$IPCE(\%) = \frac{J_{ph}(\lambda)}{\Phi(\lambda)} \cdot 100\% = \frac{J_{ph}(\lambda) [A\ cm^{-2}] \cdot hv [J]}{P_{in}(\lambda) [W\ cm^{-2}] \cdot e [C]} \cdot 100\% \quad (2.6)$$

Where $J_{ph}(\lambda)$ is the photocurrent density at a given wavelength, $\Phi(\lambda)$ is the incident photon flux at a given wavelength, $P_{in}(\lambda)$ is the intensity of the incident light, $hv [J]$ is the photon energy and $e [C]$ is the elementary charge.²¹

2.4.6.5 Electrochemical and photoelectrochemical impedance spectroscopy

Electrochemical impedance spectroscopy (EIS) is an electroanalytical technique where oscillating potential is applied to the WE and the frequency and amplitude of the oscillation (sinusoidal wave) is controlled. The applied potential difference between the WE and CE induces an ion migration to the electrodes of opposite charge to the migrating ions forming a double layer on both electrodes. When potential is applied to the WE, the double layer on the surface will charge and discharge as a capacitor would (Figure 2.5), allowing the flow of alternating current (AC) through the system without the need of charge transfer between WE

and CE. This in turn allows the study of the electrode-electrolyte interface enabling to determine several important parameters of the system.^{19,20}

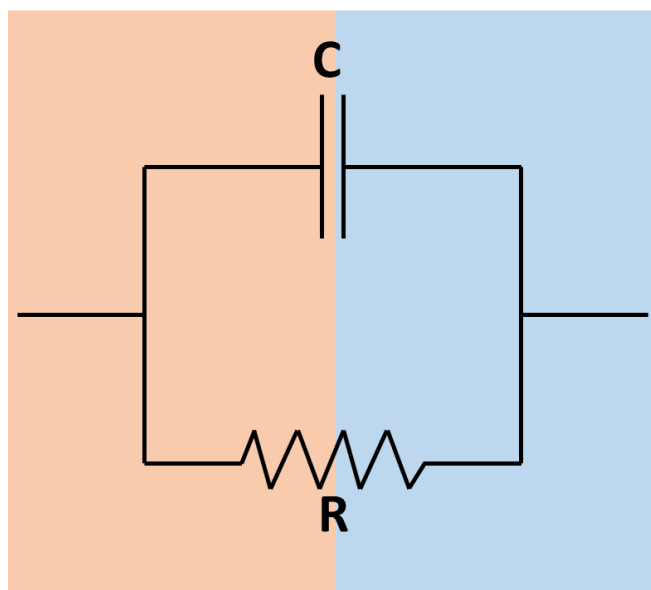


Figure 2.5. Schematic presentation of the equivalent circuit formed at the semiconductor-electrolyte interface when oscillating potential is applied to the electrode. The semiconductor-electrolyte interface can be rationalised as a capacitor (C) which is in parallel with a resistor (R).

Impedance of an electrochemical system can be expressed using Ohm's law. In a direct current measurement, an equation $E = I \cdot R$ applies, showing that a constant potential, E , between two points in a conductor is directly proportional to the current times the resistance (IR). During an AC measurement, the potential can then be expressed as follows

$$E_{AC}(t) = \Delta E e^{i(\omega t + \phi E)} \quad (2.7)$$

Where ΔE is the amplitude of the applied potential, ω is the frequency of the oscillation, t is the time, i is the imaginary unit and the ϕE is the phase shift of the oscillation.

When the ΔE is small, ≤ 10 mV, then the response of the electrode to modulation can be considered linear and the current that is created by the oscillation across the circuit is expressed as follows:

$$I_{AC}(t) = \Delta I e^{i(\omega t + \phi I)} \quad (2.8)$$

where the definitions of the variables in the equation are analogous to the variables in Eq. 2.8.

The Ohm's law is then under alternating current conditions written as $E = Z \cdot I$ (2.9), where Z is the impedance. The impedance of the circuit can then be written as follows:

$$Z = \frac{\Delta E e^{i(\omega t + \phi_E)}}{\Delta I e^{i(\omega t + \phi_I)}} = \Delta Z e^{i(\phi_E - \phi_I)} = \Delta Z e^{i\theta} \quad (2.10)$$

Where $\theta = \phi_E - \phi_I$.

By determining the potential amplitude and measuring the phase shift of the current, the impedance of the system can be determined.^{19,20}

The impedance of an electrochemical system is most commonly visualised either using a Nyquist plot or a Bode plot. In Nyquist plot the measured impedances of a system are plotted on a complex plane (Figure 2.6), while in Bode plot the phase shift is plotted against the applied frequency.^{19,20}

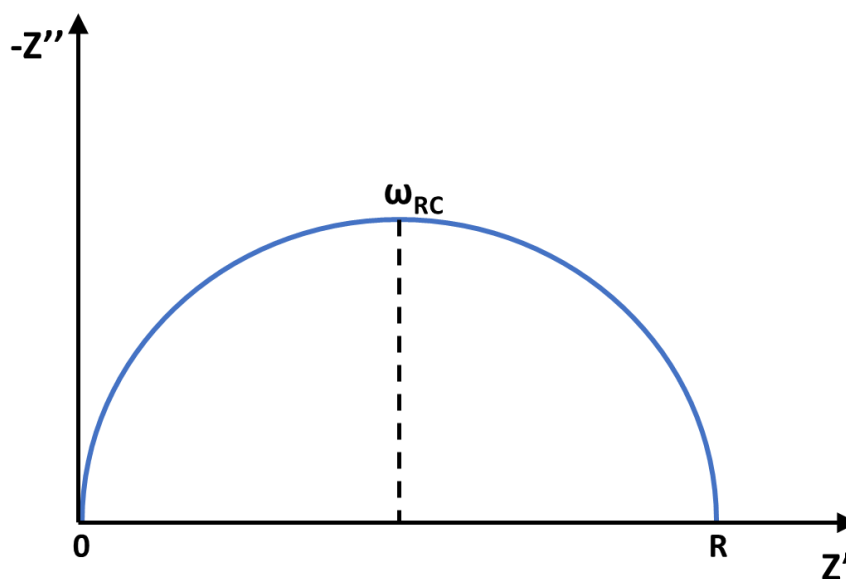


Figure 2.6. Schematic presentation of the Nyquist plot of an ideal system where real part of the complex impedance is plotted on the x-axis and the negative of the imaginary part is plotted on the y-axis forming a perfect semicircle. When frequencies are really high the impedance is 0 because the current passes through the capacitor unhindered. At very low frequencies the impedance is equal to the resistance, R , at the semiconductor-electrolyte interface (Figure 2.5). At intermittent frequencies between the extremes, the impedance obtains a semi-circular shape. The frequency at the top of the semicircle is called the *characteristic frequency* of the system and is expressed as $\omega_{RC} = 1/RC$.

2.4.7 Gas Chromatography

Gas Chromatography (GC) is a chemical analysis technique used to analyse complex samples with different compounds mixed together by vaporising them and separating them into known compounds in a chromatographic column which can then be identified according to their retention time and quantified according to the peak area on the chromatogram. Additional uses can be an identification of an unknown compound or checking the purity of a known compound. The chromatographic column is filled with a stationary medium through which a carrier gas, usually Ar or N₂, is passed. When the sample is injected into the GC through an injection port, it is then pushed through the column by the carrier gas. Samples can be in gas or (volatile) liquid form. In case of a liquid sample, the liquid is vaporised upon injection. Different chemicals interact differently with the stationary phase in the column and therefore they also have a different retention time, the time they exit the column and are transferred through a detector. The method for quantification depends on the detector the GC is equipped with. In this work a thermal conductivity detector (TCD) was used, which method of detection is based on the measurement of the thermal conductivity of the compound. The compound passes through the detector, which is equipped usually with a tungsten-rhenium filament. When compound molecules interact with the filament, the temperature and voltage of the filament changes giving the response which is associated with a specific known compound.¹⁰

References

- 1 G. H. Summers, J.-F. Lefebvre, F. A. Black, E. Stephen Davies, E. A. Gibson, T. Pullerits, C. J. Wood and K. Zidek, *Phys. Chem. Chem. Phys.*, 2016, 18, 1059–1070.
- 2 P. Qin, H. Zhu, T. Edvinsson, G. Boschloo, A. Hagfeldt, L. Sun, *J. Am. Chem. Soc.*, 2008, 130, 8570-8571.
- 3 N. Pöldme, L. O'reilly, I. Fletcher, J. Portoles, I. V. Sazanovich, M. Towrie, C. Long, J. G. Vos, M. T. Pryce, E. A. Gibson. *Chem. Sci.*, 2019, 10, 99-112.
- 4 S. Sumikura, S. Mori, S. Shimizu, H. Usami and E. Suzuki, *J. Photochem. Photobiol., A*, 2008, 199, 1–7.
- 5 W. N. McNamara, Z. Han, P. J. Alperin, W. W. Brennessel, P. L. Hollan, R. Eisenberg. *J. Am. Chem. Soc.* 2011, 133, 15368–15371.
- 6 J. Massin, M. Brautigam, N. Kaeffer, N. Queyriaux, M. J. Field, F. H. Schacher, J. Popp, M. Chavarot-Kerlidou, B. Dietzek and V. Artero, *Interface Focus*, 2015, 5, 20140083.
- 7 S. Powar, T. Daeneke, M. T. Ma, D. Fu, N. W. Duffy, G. Götz, M. Weideler, A. Mishra, P. Bäuerle, L. Spiccia and U. Bach, *Angew. Chem. Int. Ed. Engl.*, 2013, 52, 602–5.
- 8 J. A. Broomhead, F. P. Dwyer, J. W. Hogarth and R. E. Sievers, in *Inorganic Syntheses Volume 6*, ed. E. G. Rochow, John Wiley & Sons Ltd., 1960, pp. 183–186.
- 9 B. Shan, A. Nayak, R. N. Sampaio, M. S. Eberhart, L. Troian-Gautier, M. K. Brennaman, G. J. Meyer, T. J. Meyer. *Energy Environ. Sci.*, 2018, 11, 447.
- 10 P. Atkins, J. de Paula, *Atkins' Physical Chemistry*, 8th edition. New York : W. H. Freeman and Company, 2006.
- 11 K. Rajeshwar, *Fundamentals of Semiconductor Electrochemistry and Photoelectrochemistry*, 2007,
- 12 *Optical properties and electronic structure of amorphous Ge and Si*. Tauc, J. 1, s.l. : Elsevier, 1968, *Materials Research Bulletin*, Vol. 3, pp. 37-46.
- 13 S. A. Speakman, 'Estimating Crystallite Size Using XRD', *Mit Centre for Materials Science and Engineering*, 2014.

- 14 N. Fairley, <http://www.casaxps.com>, © Casa software Ltd, 2005.
- 15 Benninghoven, A., 1994, *Angewandte Chemie International (in English)*, 33, 10, 1023-1043.
- 16 VanVaeck, L., Adriaens, A., and Gijbels, R., 1999, *Mass Spectrometry Reviews*, 18, 1-47.
- 17 Adriaens, A., VanVaeck, L., and Adams, F., 1999, *Mass Spectrometry Reviews*, 18, 48-81.
- 18 J. Schwieters, H. G. Cramer, T. Heller, U. Jürgens, E. Niehuis, J. Zehnpfenning, A. Benninghoven and U. Jurgens, *J. Vac. Sci. Technol., A*, 1991, 9, 2864–2871.
- 19 A. J. Bard, L. R. Faulkner, *Electrochemical Methods: Fundamentals and Applications*, 2nd Ed., 2001.
- 20 C. H. Hamann, A. Hamnett, W. Vielstich, *Electrochemistry*, 2nd Ed., 2007.
- 21 M. G. Walter, E. L. Warren, J. R. McKone, S. W. Boettcher, Q. Mi, E. A. Santori, N. S. Lewis, *Chem. Rev.* 2010, 110, 6446–6473.
- 22 P. A. Summers, J. Dawson, F. Ghiotto, M. W. D. Hanson-Heine, K. Q. Vuong, E. Stephen Davies, X. Z. Sun, N. A. Besley, J. McMaster, M. W. George and M. Schroder, *Inorg. Chem.*, 2014, 53, 4430–4439.

Chapter 3. Benchmarking dye-sensitised NiO photocathodes for photoelectrochemical H₂ evolution

Abstract

The focus in this chapter is to study the effect of the experimental environment to the photoelectrochemical performance of the dye sensitised NiO photocathode. For that, an optimal electron acceptor (EA) for photocurrent generation was chosen and applied in all experiments, while changing the experimental conditions. The effect of electrolyte composition, the pH of the electrolyte and the concentration of the EA were studied. It was observed that the highest photocurrent was obtained with 4,4'-dithiodipyridine (DTDP) electron acceptor with 5 mM concentration in pH 3 aqueous electrolyte. After determining the optimal conditions for photocurrent generation using the most robust dye available, D1, the NiO-based system was tested for H₂ evolution with electrodeposited Pt catalyst. In addition, NiO photocathode was tested with another dye with a polymeric structure and with a commercially available benchmark organic dye. Both systems were studied photoelectrochemically under the optimal conditions determined in the first part of the study with NiO and also tested for H₂ evolution with electrodeposited catalysts on the surface. The highest photocurrents were observed with the commercially available benchmark organic dye D3 with 5 mM DTDP electron acceptor and the highest efficiency for H₂ evolution was produced on the same system with electrodeposited Pt catalyst on the surface.

3.1 Introduction

Mesoporous NiO has been used in p-DSCs and tandem cells since the late 1990's. It is one of the few stable p-type semiconductors with a wide band-gap and, consequently, the electrode film does not compete with the dye for visible light absorption.²⁻⁷ Recently, it has been used in a dye-sensitised PEC to reduce H⁺ to H₂.^{1,8-13} Nanostructured NiO films can be produced at reasonably low temperatures in a cost-efficient manner, making them ideal for large-scale applications. NiO is also stable in the mildly acidic aqueous environments required for H₂ production. Excitation of a photosensitiser adsorbed on NiO can result in extraction of an electron from the NiO (hole injection) reducing the sensitiser and initiating the photocatalytic reaction.^{14,15} The exact mechanism for H₂ evolution, which requires two electrons, is unclear at this stage.^{13,16-18}

3.2 Properties of NiO

Nanostructured NiO is a wide band-gap semiconductor with an indirect bandgap of 3.55 eV reported in literature.¹⁴ For the NiO electrode used in this thesis, a value of 3.4 eV was estimated from the UV-vis data (Figure A.1 in Appendix). It has reasonable transparency which means that NiO films do not absorb the light in the same spectral region as the dye. It has a face-centred cubic crystal structure with Ni²⁺ and O²⁻ at the octahedral sites and the conduction originates mostly from Ni vacancies in the crystal lattice.¹⁹ The Hall mobility has been measured to be approximately 0.5 cm² V⁻¹ s⁻¹ at 200 K; with the positive sign indicating p-type conductivity.¹⁹ In addition, nanostructured NiO films can be made easily at sufficiently low temperatures in a cost-efficient manner making the process potentially feasible for scale-up and applicable in industry.²⁰ Nanostructured NiO films are also stable in the mildly acidic aqueous environment which is required for H₂ production. The valence band of NiO (VB) is approximately 0.4 V vs. NHE in pH 6.8 phosphate buffer.¹⁴ Therefore, when the dye is photoexcited on the NiO surface, hole injection from the dye to the NiO valence band takes place (Figure 1.13 in Chapter 1.6.5). The main differences between the PEC devices employing nanostructured NiO lie in the photosensitizer (dye) used for photon absorption and the catalyst used for proton reduction.

3.3 Previous studies on NiO

He *et al.* reported the first p-type DSSC using NiO as the photocathode.² Soon after that the same group demonstrated that a tandem DSSC can be fabricated using NiO as the photocathode and TiO₂ as the photoanode.³ It took some time until in 2012 dye-sensitized NiO was successfully used in a water splitting device to reduce H⁺ to H₂.⁸ Soon after that the dye-sensitized NiO photocathode was combined with a dye-sensitized TiO₂ photoanode in a tandem PEC device, where H₂ was produced on the photocathode and O₂ was produced on the photoanode.¹

Dye-sensitized PEC cells, where H₂ evolution is catalysed photoelectrochemically using the molecular photosensitizer-catalyst assemblies adsorbed on a nanostructured p-type semiconductor electrode (p-SC), have several advantages when compared to other water splitting systems. Firstly, the use of sacrificial electron donors is not needed compared to homogeneous systems where proton reduction is carried out by molecular or colloidal photocatalysts in solution, because the electrons for H⁺ reduction are provided by the water

oxidation reaction on the photoanode and delivered to the photocathode through the circuit.^{3,8} Secondly, combining a molecular photosensitizer with a molecular or colloidal catalyst on a semiconductor surface enables the separate optimisation of the photon absorption, charge transfer and catalyst activity. This would ideally avoid the trade-off between higher efficiency and lower cost leading to more efficient systems with the benefit on having cheaper materials and more cost-efficient processing.^{1,21} Thirdly, using a molecular photosensitizer creates the opportunity to finely tune the absorption properties of the system and thereby combine the dye-sensitized photocathode with a dye-sensitized photoanode in a tandem configuration enabling the absorption of lower energy photons on one electrode as well as the higher energy photons which are absorbed on the other electrode.² Thus, more light is utilised in the device and this should theoretically lead to higher overall efficiency compared to the single junction devices.

The photoelectrochemical process is initiated when dyes adsorbed on the NiO surface absorb light, stimulating hole injection into the NiO material and reduction of the dye.²² Research into suitable molecular catalysts for sensitizing p-SC is pertinent to progress in this area as NiO films and other such p-DSCs are stunted in their photocatalytic efficiency due to rapid recombination between the reduced dye and the hole of the valence band of the NiO.²³ Therefore, a notable requirement for an efficient p-type dye-sensitized photocathode is down to the dye's dynamic processes. A long-lived (μs) photoinduced charge-separated state decelerates this charge recombination and the rival process of the dye regeneration (Figure 1.13 in Chapter 1.6.5), allowing for enough time for catalysis.

Over the recent years, several proof-of-concept examples of PEC cells producing H_2 on dye-sensitized photocathodes have been published by various groups and most of them have used nanostructured NiO in their devices with few exceptions.^{1,8-13,24,25} The reason that NiO has been chosen as one of the most suitable candidate materials is that it satisfies the main requirements for a dye-sensitized photocathode (discussed in Chapter 1.6.5). In the first PEC device reported by Li et al. in 2012, the P1 dye (Dye D3 in this thesis) was used with CoI molecular catalyst generating maximum photocurrent density under the applied potential of $-0.4\text{ V vs. Ag/AgCl}$ of *ca.* $25\ \mu\text{A cm}^{-2}$ in pH 7 phosphate buffer.⁸ The same year Tong et al. demonstrated solar-driven H_2 generation with donor-acceptor dye PMI-6T-TPA without using a catalyst.⁹ Several additional device fabrication techniques have been reported lately which improve the device performance and stability. It has been reported by Kamire et al. that by depositing a thin insulating layer of Al_2O_3 between the NiO and the dye, the recombination between the NiO and the dye is hindered.¹³ Gross et al. reported another strategy to increase

the performance and stability of their dye-sensitised NiO photocathodes.¹² They performed a layer-by-layer deposition of dye and catalyst using Zr^{4+} to spatially separate the catalyst from the NiO. This resulted in increased photocurrents due to slower recombination between the catalyst and the NiO.¹² Alternative approach would be to have the photosensitizer and catalyst covalently linked. This should enhance the charge transfer between the photosensitizer and the catalyst. An example of this design was published by Kaeffer and co-workers when they demonstrated light-driven H_2 generation on dye-sensitised NiO using a covalently linked dye-catalyst assembly based on cobalt diimine-dioxime catalyst.²⁶ They were able to show photocurrents up to $15 \mu A cm^{-2}$ in pH 5.5 aqueous electrolyte under applied potential of 0.14 V vs RHE and light driven H_2 generation with 10% Faradaic efficiency.²⁶

3.4 Motivation and aims of the project

The aim of this project was to first understand the effect of the experimental environment to the photoelectrochemical performance of the dye-sensitised NiO photocathode and to study how the performance is influenced by each different parameter. To do that, an optimal electron acceptor (EA) for photocurrent generation was chosen which could be used in all experiments, while changing the experimental conditions. Then, the effect of different experimental conditions was studied: the electrolyte composition, the pH of the electrolyte and the concentration of the electron acceptor. After determining the optimal conditions using the most robust dye available, the dye was changed to the best performing commercially available dye, which has been shown to also evolve H_2 when combined with the right catalyst. The optimal conditions were tested, and the photocathode was thereafter tested with different catalysts, to see if these conditions also have an effect on H_2 production.

3.5 Results and discussion

3.5.1 *Dye-sensitised NiO photocathode with BODIPY dye*

To carry out the study of understanding the effect of the experimental environment to the photoelectrochemical performance of the dye-sensitised NiO photocathode, a robust organic push-pull BODIPY dye D1 was chosen (Figure 3.1), which was synthesised in our group and has been previously reported as an efficient dye in DSSCs.²⁷ The dye has a donor-acceptor character containing a BODIPY (boron-dipyrromethene) acceptor units connected to

diaminoethane)cobalt(II/III) complex ($[\text{Co}(\text{en})_3]^{2+/3+}$) as a redox mediator in a p-type NiO-based DSSC and achieved a two-fold increase in the cell efficiency.²⁹ In addition to Co-based redox mediators, Perera et al. reported a Fe-based redox mediator, $[\text{Fe}(\text{acac})_3]^{0/1-}$, and applied it in DSSC achieving energy conversion efficiency of *ca.* 2.5 % which was the highest reported at the time.³⁰

In this thesis the highest photocurrents of $440 \pm 30 \mu\text{A cm}^{-2}$ generated with D1|NiO were obtained using DTDP (4,4'-dithiodipyridine) EA under $E_{\text{appl}} = -0.2 \text{ V}$ during a chronoamperometry (CA) measurement (Figure 3.2, right) and increasing up to $670 \mu\text{A cm}^{-2}$ (at $E_{\text{appl}} = -0.5 \text{ V}$ vs. Ag/AgCl) when measuring the potential dependence during LSV measurement under chopped light (Figure 3.2, left). The second highest photocurrent values under same conditions and same E_{appl} were obtained with $[\text{Co}(\text{NH}_3)_5\text{Cl}]\text{Cl}_2$ (chloropentaamminecobalt chloride) generating a photocurrent density of *ca.* $83 \mu\text{A cm}^{-2}$ (Figure 3.2.right). The third highest photocurrent values were obtained with $[\text{Co}(\text{en})_3]\text{Cl}_3$ (tris(ethylenediamine)cobalt(III) chloride) EA with recorded photocurrents *ca.* $39 \mu\text{A cm}^{-2}$ (Figure 3.2.right).

Other EAs tested were $\text{Fe}(\text{acac})_3$ (tris(acetylacetonato)iron(III)), MV (methyl viologen) and $\text{K}_3[\text{Fe}(\text{CN})_6]$ (potassium ferricyanide(III)). Of these, $\text{Fe}(\text{acac})_3$ and MV generated negligible photocurrents (Figure 3.2.left, Figure 3.5.B) and $\text{K}_3[\text{Fe}(\text{CN})_6]$ showed to be unstable under the experimental conditions corroding the photocathode (Figure 3.5.A and C). The results from CA measurements along with respective redox potentials for different EAs are presented in Table 3.1.

In addition, in case of $\text{K}_3[\text{Fe}(\text{CN})_6]$ and MV, spikes in the photocurrent were observed under chopped light, which implies that charge accumulates at the surface of the electrode because transfer to the electron acceptor is inefficient. This was not the case for the EAs presented in Figure 3.2, which complements their superior performance with the exception of $\text{Fe}(\text{acac})_3$. Either current flows until all the dyes are reduced and then stabilises, or electrons are subsequently transferred to the EA until the rate of charge transfer to the EA equals the rate of recombination between the holes in the NiO and either the reduced dye or the reduced EA. Increasing the concentration of EA should increase the current if the rate of dye regeneration is limiting.

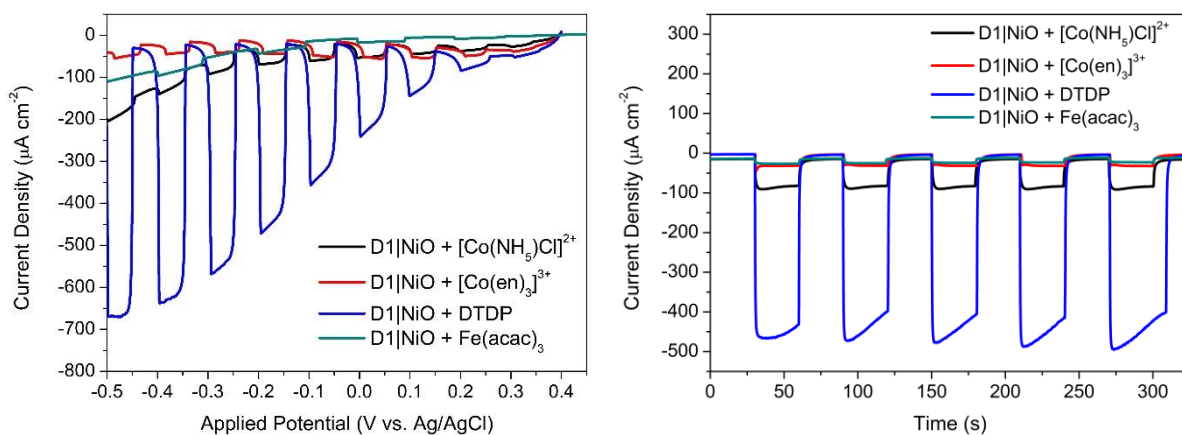


Figure 3.2. Left - LSV on D1|NiO with 5 mM EA in 0.1 M acetate buffer (pH 5). Light illumination was applied with 5 s intervals (5 s in the dark / 5 s under illumination). Right - CA under $E_{appl} = -0.2$ V vs. Ag/AgCl on D1|NiO with 5 mM EA in 0.1 M acetate buffer (pH 5). Light illumination was applied with 30 s intervals (30 s in the dark / 30 s under illumination). Light illumination intensity was 1 sun (100 mW cm⁻²). The electrolyte was degassed for 15 min under N₂ before measurement.

Table 3.1. Results from PEC measurements with different EAs.

EA	J_{photo} (μA cm ⁻²)	E_{redox} (V vs. Ag/AgCl)	Stable (yes / no)
[Co(NH ₃) ₅ Cl] ^{2+/+}	83 ± 4	-0.44	yes
[Co(en) ₃] ^{3+/2+}	39 ± 6	-0.55	yes
DTDP ^{0/1-}	440 ± 30	-0.26	yes
[Fe(acac) ₃] ^{0/1-}	12 ± 1	-0.37	no
MV ^{2+/+}	7 ± 4	-0.48	yes
[Fe(CN) ₆] ^{3-/4-}	110 ± 40	0.04	no

The photocurrents, J_{photo} , generated on D1|NiO with different EAs ($c = 5$ mM) under 100 mW cm⁻² light illumination in pH 5 0.1 M acetate buffer are presented, along with corresponding redox potentials measured experimentally, E_{redox} , for EA redox couples and the assessment of stability during the measurement. The photocurrents were measured by taking the average between the first and the last photocurrent measured during the chopped light CA measurement (Figures 3.2, right and 3.5.A and B).

On Figure 3.3 the working mechanism of the D1|NiO photocathode with different EA in solution is presented. An important parameter that can be also derived from that working mechanism is the driving force for electron transfer, ΔG_{et} , from the excited dye D1 to the EA. The ΔG_{et} depends on the reduction potential of the EA and the LUMO of the D1 and was introduced in Chapter 1.6.5. Essentially, the higher the ΔG_{et} the faster the electrons reduce the EA on the photocathode surface resulting in higher photocurrents.

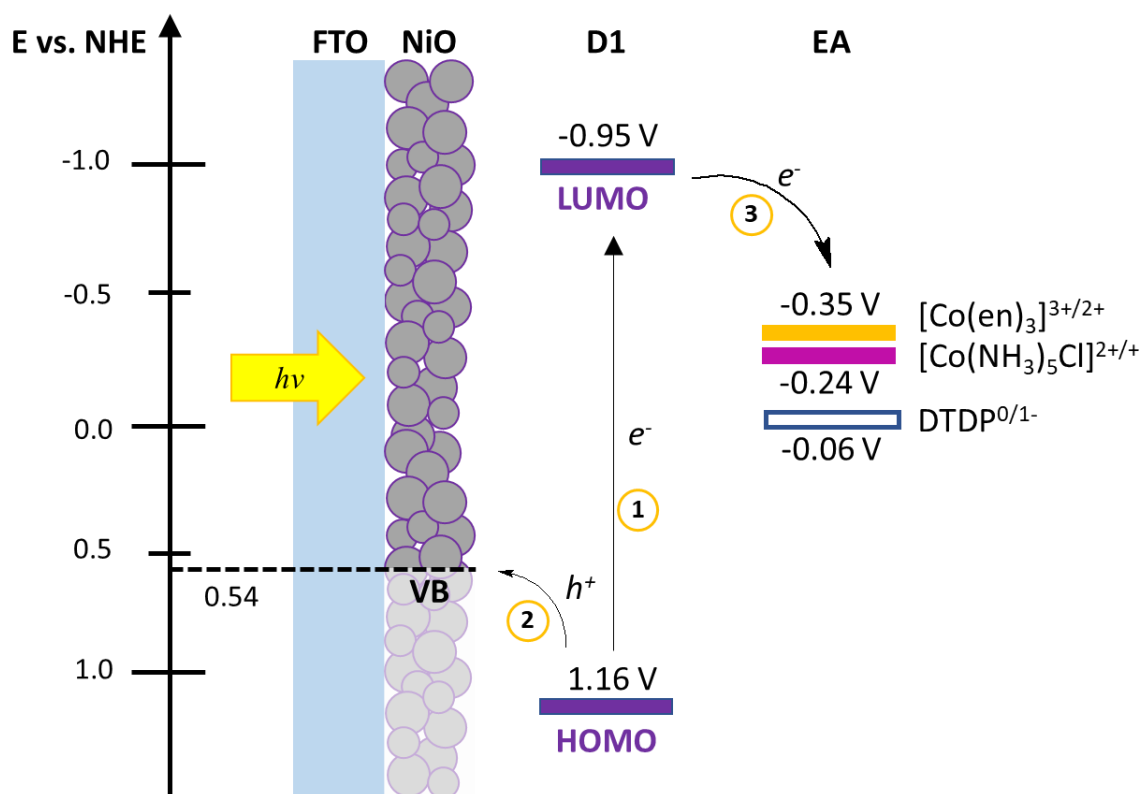


Figure 3.3. Schematics of the D1|NiO photocathode working principle with EAs in solution. When light illumination is applied to the dye-sensitised photocathode, electron is excited from its ground state in HOMO to an excited state in LUMO (1), this leaves a positively charged hole, h^+ , which is then injected from the dye to the valence band, VB, of NiO (2). Excited electrons with higher energy in LUMO of the dye can then reduce the EA (3). Values for HOMO and LUMO of D3 are reported previously in literature.²⁷

The photocurrent dependence on ΔG_{et} for different stable EA used with D1|NiO is presented on Figure 3.4 and it clearly shows the correlation between increasing ΔG_{et} and higher photocurrents, with the exception of MV, which has the third highest ΔG_{et} (Figure 3.4) but shows negligible photocurrent (Table 3.1). The highest driving force of 0.89 eV was determined for DTDP EA producing $440 \mu\text{A cm}^{-2}$ as already mentioned before and presented in Table 3.1 and the second highest driving force was determined for $[\text{Co}(\text{NH}_3)_5\text{Cl}]\text{Cl}_2$ showing also second highest photocurrents. The negligible photocurrents shown with MV could be due to additional factors like diffusion coefficient of MV in water or electrostatic interactions between the MV and the D1, which hinder the electron transfer compared to other EAs.

To continue with studying the effect of the concentration of EA, electrolyte composition and the pH, an optimal EA must be chosen that can be used in all subsequent experiments. That way the effect of the EA on the results can be excluded. The $\text{K}_3[\text{Fe}(\text{CN})_6]$

was excluded due to its instability, and MV due to the negligible photocurrents it generated under experimental conditions.

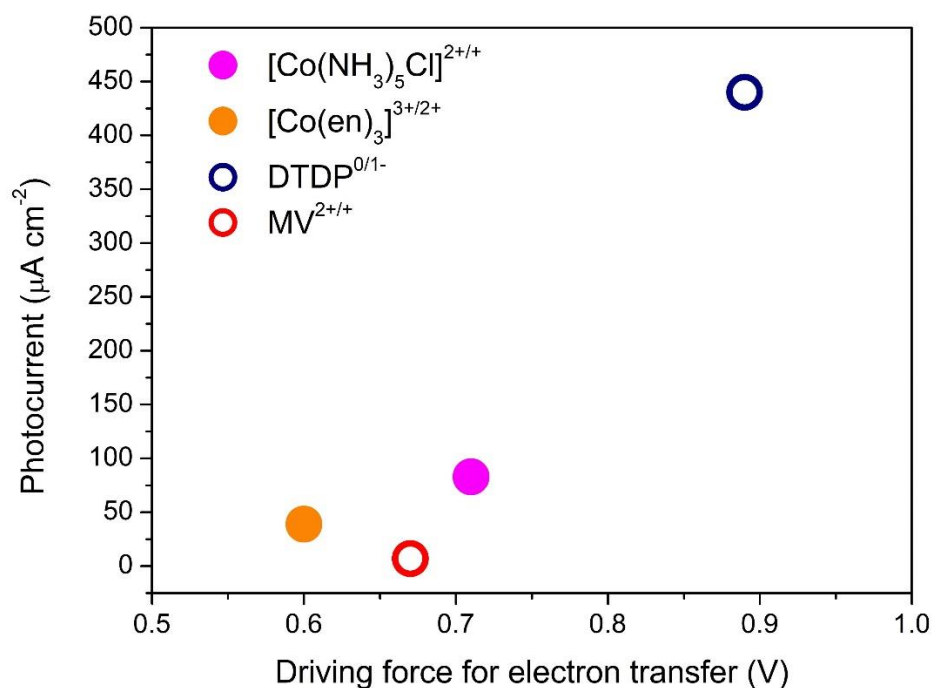


Figure 3.4. Driving force for electron transfer, ΔG_{et} , from the excited dye D1 to the EA for different stable electron acceptors used with D1|NiO photocathode.

The drawback of using the $\text{Fe}(\text{acac})_3$ was its low solubility in water which limited the concentration we could use to 5 mM. In addition, we observed deterioration of photocathode after the measurements. Of the three best performing EAs, DTDP solubility is also limited to 5 mM and the $[\text{Co}(\text{NH}_3)_5\text{Cl}]^{2+}$ is only soluble in water, which leaves us with $[\text{Co}(\text{en})_3]^{3+}$. The solubility of $[\text{Co}(\text{en})_3]^{3+}$ was tested to be at least 50 mM in water, the pH stability was observed to be from pH 1 to pH 13, and when changing the counter ion from Cl^- to BF_4^- , the EA was also soluble in acetonitrile, which enabled its use in the measurement where electrolyte composition effects were studied.

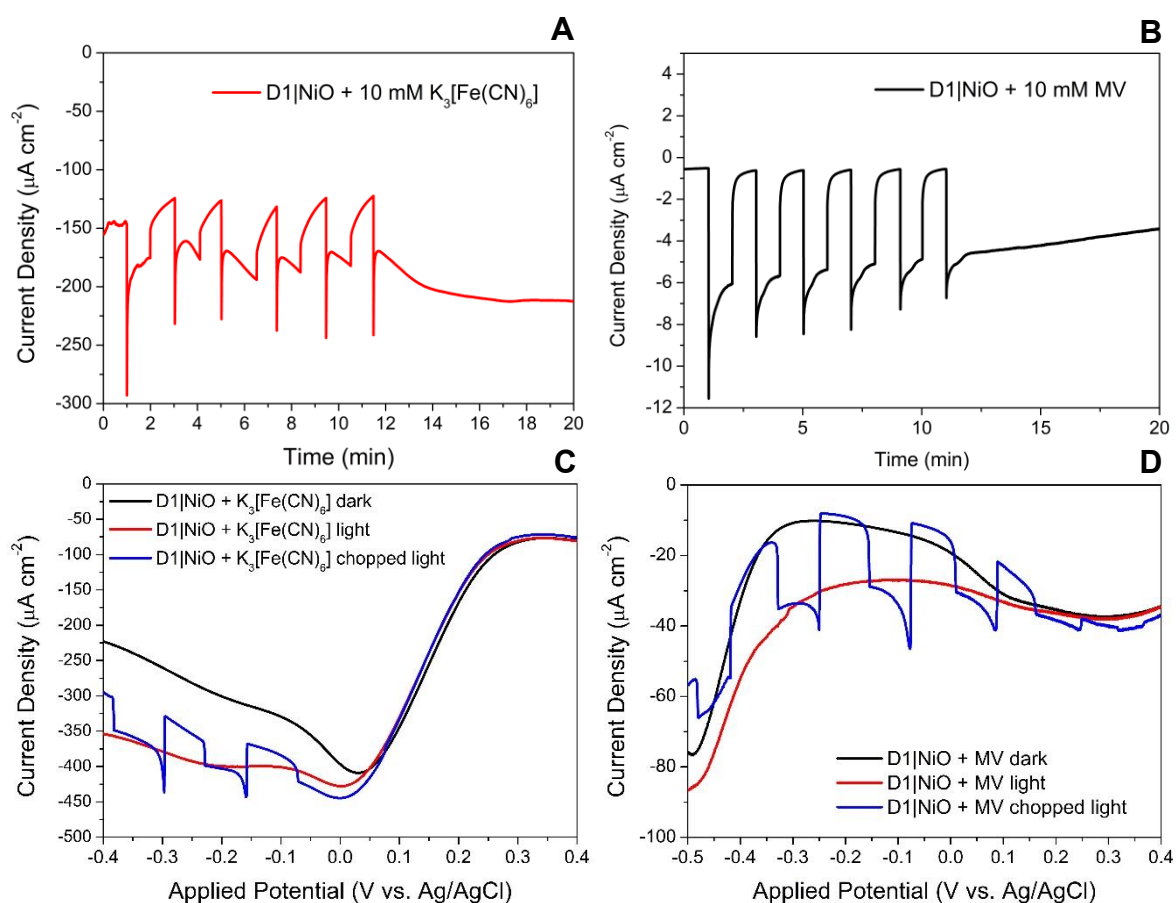


Figure 3.5. CA on D1|NiO under $E_{appl} = -0.2$ V vs Ag/AgCl and chopped light illumination (A and B) and LSV (C and D) on D1|NiO with 10 mVs^{-1} scan rate under chopped light irradiation with 10 mM potassium ferricyanide (A and C) and 10 mM MV (B and D) in 0.1 M acetate buffer (pH 5). Light illumination intensity was 1 sun (100 mW cm^{-2}). In CA the light was chopped with 1 min intervals and in LSV 10 s intervals. Electrolyte was degassed for 15 min with N_2 before the measurement

3.5.1.2 Photocurrent dependence of electron acceptor concentration

The next step in the study was to understand if the current is limited by diffusion of the acceptor out of the pore or it is limited by the rate of dye regeneration. In order to find an answer to this question, LSV and CA measurements were carried out on the D1|NiO photocathodes with varying the concentration of the EA, for which $[\text{Co}(\text{en})_3]\text{Cl}_3$ was used due to its high solubility in water. Concentration of the EA was varied from 1 mM to 50 mM and what was observed was that photocurrents increased when increasing the concentration of the EA (Figure 3.6). The photocurrents measured for 1 mM $[\text{Co}(\text{en})_3]\text{Cl}_3$ in solution was *ca.* $20 \mu\text{A cm}^{-2}$ increasing to *ca.* $75 \mu\text{A cm}^{-2}$ with 50 mM $[\text{Co}(\text{en})_3]\text{Cl}_3$. In addition, with the increase of the concentration increased also the transient photocurrent spikes both in LSV and CA

measurements (Figure 3.6). This indicates that the charge accumulation on the electrode surface increases with the increase in EA concentration. However, the stabilised current was still increasing with increasing the concentration meaning that the charge transfer is not yet limited by the diffusion of the EA out of the pores of NiO, but rather by the rate of dye regeneration. This result gives us also a good indication of the catalyst concentration in solution which could be used to optimise the system.

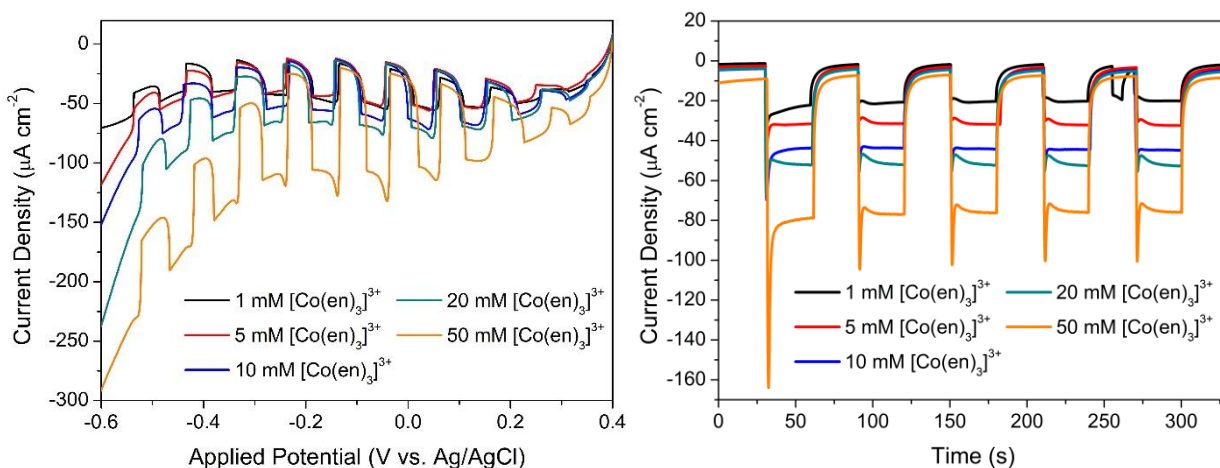


Figure 3.6. Left - LSV on D1|NiO with increasing concentrations of [Co(en)₃]Cl₂ in 0.1 M acetate buffer (pH 5) with scan rate of 10 mVs⁻¹. Light illumination was applied with 5 s intervals (5 s in the dark / 5 s under illumination); Right - CA on D1|NiO under E_{appl} = -0.21 V vs. Ag/AgCl applied potential with 5 mM EA in 0.1 M acetate buffer (pH 5). Light illumination was applied with 30 s intervals (30 s in the dark / 30 s under illumination). Light illumination intensity was 1 sun (100 mW cm⁻²) and electrolyte was degassed under N₂ for 15 min. before measurement.

3.5.1.3 Photocurrent dependence of electrolyte composition

The third part of the study was to test the dye-sensitised D1|NiO photocathode in different electrolytes to understand how the photocurrent is influenced by the chemical environment of the electrolyte. For that, the D1|NiO photocathode was measured in aqueous electrolyte, in acetonitrile and in the mixture of those two with various amounts of acetonitrile in 0.1 M acetate buffer. In this study, a robust EA [Co(en)₃](BF₄)₃ was used, soluble both in water and acetonitrile as previously discussed. First, the reduction potential of the [Co(en)₃]³⁺ was determined in acetonitrile by cyclic voltammetry (Figure 3.7, left) and found to be -0.13 V vs. Ag/AgCl. With dye-sensitised D1|NiO as the working electrode, an irreversible wave at -0.53 V vs. Ag/AgCl was observed in aqueous solution (0.1 M NaCl, pH 7) (Figure 3.7,

right). When light was applied, there was a positive shift in the potential and an increase in the photocurrent density. This indicates that irradiation of the dye leads to an increase in the rate of electron transfer from the electrode to the acceptor.

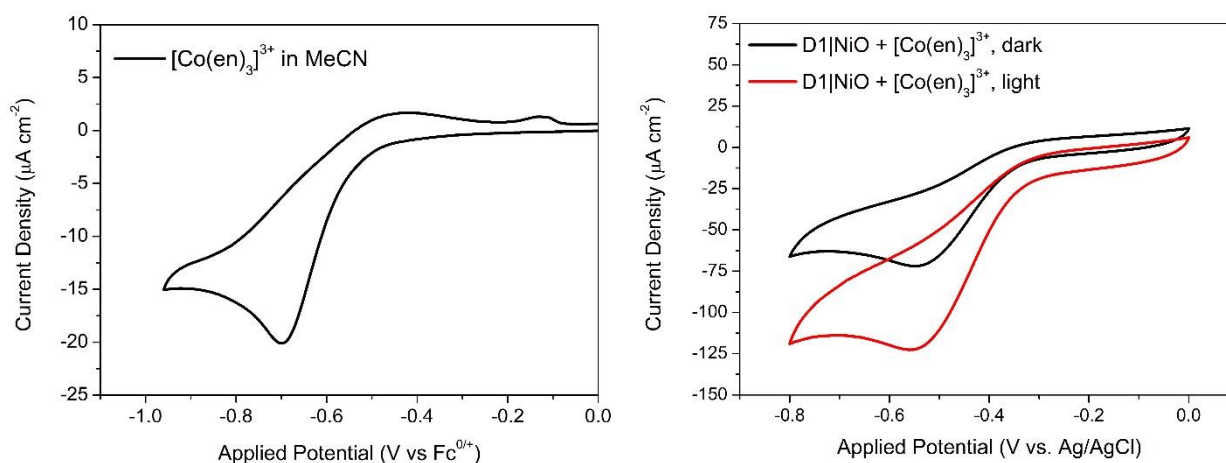


Figure 3.7. Left - Cyclic voltammetry of 1 mM $[\text{Co}(\text{en})_3](\text{BF}_4)_3$ in acetonitrile containing 0.1 M LiClO_4 using a glassy carbon working electrode; Right - cyclic voltammetry of 1 mM $[\text{Co}(\text{en})_3](\text{BF}_4)_3$ aqueous 0.1 M NaCl solution (pH 7) with D1|NiO as the working electrode in the dark (black) and under illumination (red). In all three cases a 10 mV s^{-1} scan rate was used. The electrolyte was degassed for 15 min under N_2 before the measurement.

Figure 3.8 shows the difference between the current measured from a D1|NiO photocathode immersed in a dry acetonitrile solution (left) and an aqueous solution (right) containing $[\text{Co}(\text{en})_3](\text{BF}_4)_3$ as an electron acceptor. The films were irradiated with AM 1.5 light at 100 mW cm^{-2} and the applied bias was swept from 0.5 to $-0.5 \text{ V vs. Ag/AgCl}$. To enable comparable conductivity, the ionic strength of the solution was increased by adding 0.1 M LiClO_4 . Under aqueous conditions, increasing photocurrent was observed until -0.3 V without any increase in the dark current. When the potential was held at 0 and $-0.2 \text{ V vs. Ag/AgCl}$, stable photocurrents were observed for both potentials (Figure 3.9). However, the photocurrent was approximately three times higher when -0.2 V was applied, compared to 0 V. The photocurrent observed, when the electrode was immersed in acetonitrile electrolyte, was considerably higher than the ones recorded in aqueous electrolyte. Photocurrents over $300 \text{ } \mu\text{A cm}^{-2}$ and $400 \text{ } \mu\text{A cm}^{-2}$ were recorded when the electrode was immersed in an electrolyte solution with dry acetonitrile and held at potentials of 0 V vs. Ag/AgCl (ca. 0.2 V vs. NHE) and $-0.2 \text{ V vs. Ag/AgCl}$ (Figure 3.8, left). The conversion between Ag/AgCl and NHE is presented in Chapter 2.3.6.

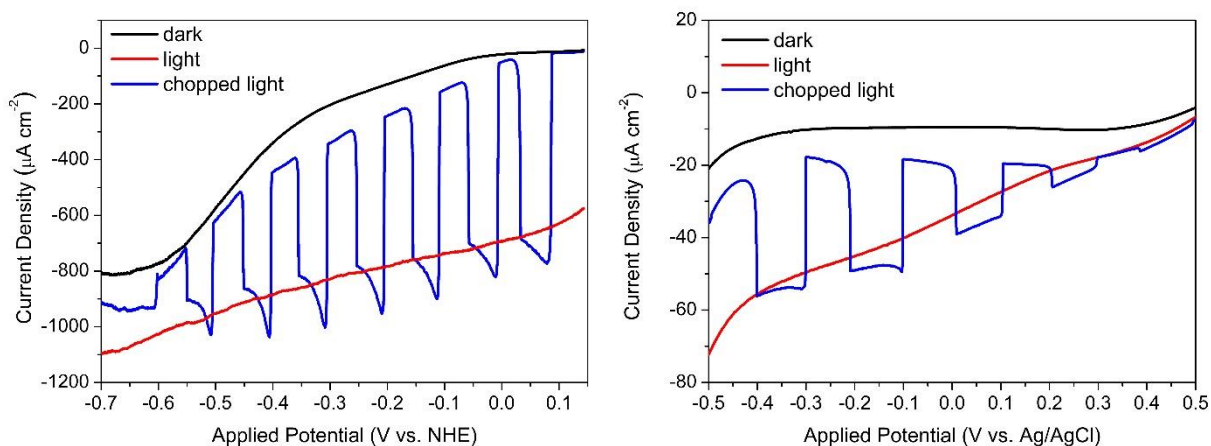


Figure 3.8. Left - LSV of D1|NiO immersed in a solution of 10 mM $[\text{Co}(\text{en})_3](\text{BF}_4)_3$ and 0.1 M LiClO_4 in dry acetonitrile, in the dark (black), under illumination (red) and under chopped light illumination (blue). The scan rate was 10 mV s^{-1} potential was swept towards negative potentials (cathodic scan) and the reference electrode was Ag/AgNO_3 ($-0.04 \text{ V vs. FeCp}_2^{+/0}$); Right - LSV of D1|NiO immersed in a solution of 10 mM $[\text{Co}(\text{en})_3](\text{BF}_4)_3$ in 0.1 M aqueous acetate buffer (pH 5) in the dark (black), under continuous illumination (red) and chopped slight illumination (blue) at scan rate 10 mV s^{-1} . The electrolyte was degassed for 15 min under N_2 before the measurement.

The mean photocurrent recorded during the CA experiment measurement in acetonitrile with an applied bias of 0 V vs. NHE (Figure 3.9, left) was approximately $540 \mu\text{A cm}^{-2}$. The current recorded at the same potential, when the electrode was immersed in the aqueous electrolyte, was less than 10 times smaller, approximately $45 \mu\text{A cm}^{-2}$ (Figure 3.9, right).

Figure 3.10 shows an overlay of the chronoamperometry measurements, recorded at $-0.2 \text{ V vs. Ag}/\text{AgCl}$ (ca. 0 V vs. NHE) in water and in acetonitrile. It was observed that when the electrode is immersed in the acetonitrile solution, the photocurrents are more than ten times higher than in aqueous conditions. In both measurements transient current spikes can be observed when the light is switched on, but the spikes are considerably more pronounced for the measurement in acetonitrile showing much more rapid rate of photocurrent decay which indicates higher recombination between the excited electrons and holes in NiO. As above, either current flows until all the dyes are reduced and then plateaus or electrons are subsequently transferred to $[\text{Co}(\text{en})_3](\text{BF}_4)_3$ until the rate of charge transfer to the acceptor equals the rate of recombination between the holes in the NiO and either the reduced dye or the reduced acceptor.

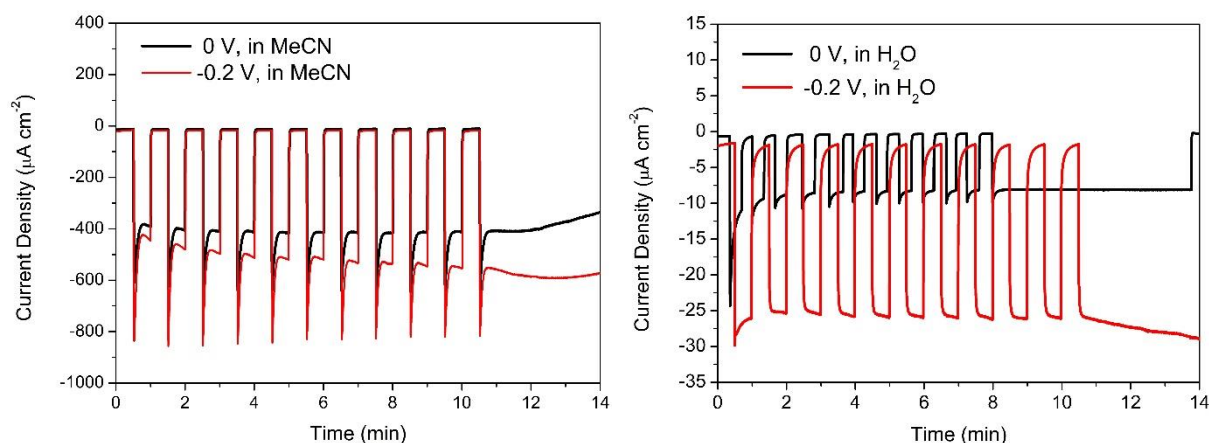


Figure 3.9. Left - CA of D1|NiO immersed in a solution of 10 mM $[\text{Co}(\text{en})_3](\text{BF}_4)_3$ and 0.1 M LiClO_4 in dry acetonitrile, under $E_{\text{appl}} = 0 \text{ V}$ vs. Ag/AgCl (black) and under $E_{\text{appl}} = -0.2 \text{ V}$ vs. Ag/AgCl (red). The scan rate was 10 mV s^{-1} and the reference electrode was Ag/AgNO_3 (-0.04 V vs. $\text{FeCp}_2^{+/0}$); Right - CA of D1|NiO immersed in a solution of 10 mM $[\text{Co}(\text{en})_3](\text{BF}_4)_3$ and 0.1 M acetate buffer in DI H_2O , under $E_{\text{appl}} = 0 \text{ V}$ vs. Ag/AgCl (black) and under $E_{\text{appl}} = -0.2 \text{ V}$ vs. Ag/AgCl (red). The scan rate was 10 mV s^{-1} and the reference electrode was Ag/AgCl (3.0 M NaCl). The electrolytes were degassed for 15 min under N_2 before the measurement.

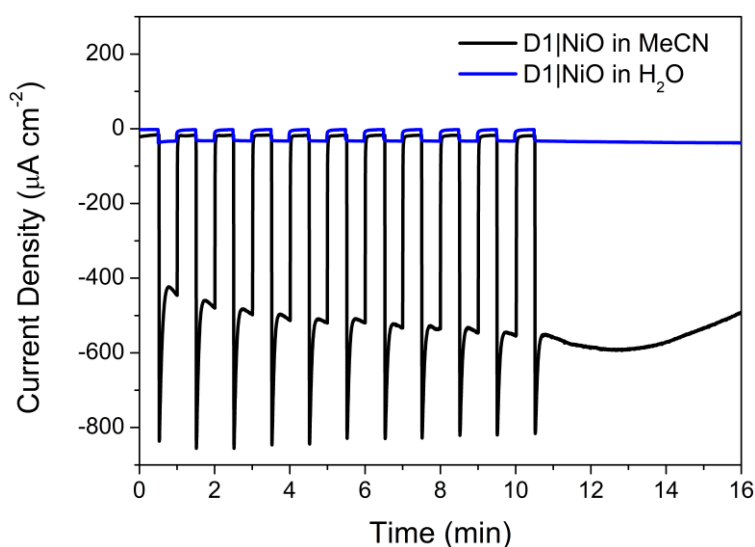


Figure 3.10. CA of D1|NiO immersed in a solution of 10 mM $[\text{Co}(\text{en})_3](\text{BF}_4)_3$ in DI H_2O (blue) and in acetonitrile (black) under $E_{\text{appl}} = -0.2 \text{ V}$ vs. Ag/AgCl (*ca.* 0 V vs. NHE). The electrolyte was degassed for 15 min under N_2 before the measurement.

To probe this solvent dependence further, photoelectrochemical measurements were performed using water/acetonitrile mixtures during which the LSV and CA were recorded. Solutions of 10 mM $[\text{Co}(\text{en})_3](\text{BF}_4)_3$ and 100 mM LiClO_4 in and deionised water were combined to yield mixtures with 10% , 50%, and 90% (v/v) deionised water in acetonitrile. Ag/AgCl was used as a reference electrode. The results are shown on Figure 3.11 and Figure 3.12. Both experiments show a clear dependence of the photocurrent density on the volume of

water in the solution. The higher the percentage of water, the lower the photocurrent density. The highest photocurrent was observed at both 0 V and -0.2 V vs. Ag/AgCl for mixtures with 10% water, while the lowest photocurrents were recorded for mixtures with 90% water. Interestingly, the photocurrents observed for 50% DI H₂O: 50% acetonitrile mixtures during the CA measurements under $E_{appl} = 0$ V and $E_{appl} = -0.2$ V vs. Ag/AgCl vary greatly in magnitude while the photocurrents for 10% DI H₂O and 90% DI H₂O increase slightly with the increase in negative E_{appl} (Figure 3.12). During the CA under $E_{appl} = 0$ V vs Ag/AgCl the photocurrents were *ca.* 110 $\mu\text{A cm}^{-2}$, but under $E_{appl} = -0.2$ V vs Ag/AgCl they were *ca.* 230 $\mu\text{A cm}^{-2}$, which is a considerable increase compared to the other mixtures. The same behaviour was less evident during the LSV measurements with the same DI H₂O: acetonitrile mixtures (Figure 3.11), but still observable, with faster increase in photocurrent density for 50% DI H₂O mixture during potential scan than for the other two mixtures. In addition, during the chopped light LSV (Figure 3.10, right) it can be observed that the transient photocurrent spikes are present when measuring the 10% and 90% DI H₂O mixtures, but not for the 50% DI H₂O mixture.

The diffusion coefficient of water is considerably lower than for acetonitrile and it increases over 2 times when going from pure water to pure acetonitrile, according to work by Siouffi and co-workers.³¹ This could also contribute to the considerably higher photocurrents measured for mixtures with higher acetonitrile content (Figure 3.12). In addition, the differences in the shape of the LSV of DI H₂O: acetonitrile mixtures in the dark and especially in the light shows a difference in redox processes when observing the higher acetonitrile content in mixtures. This difference is even more pronounced when light illumination is applied which indicates that there is a light-activated reduction of the EA at more positive potentials for mixtures with 50 and 90 % of acetonitrile. Also, the LSV shape might also be influenced by the difference between the H⁺ and Li⁺ intercalation when increasing the acetonitrile content.

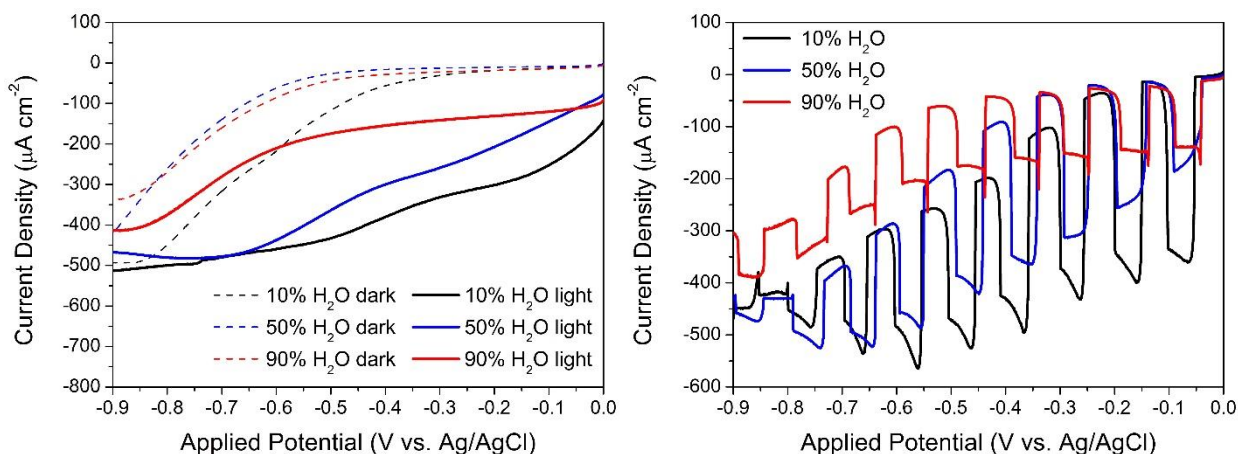


Figure 3.11. LSV of D1|NiO immersed in a solution of 10 mM $[\text{Co}(\text{en})_3](\text{BF}_4)_3$ and 0.1 M LiClO_4 in mixtures of acetonitrile and DI H₂O under light illumination and in the dark (Left) and under chopped light illumination (right). The scan rate was 10 mV s^{-1} . The dashed lines represent the currents in the dark (10% water – black, 50% water – blue, 90% water – red) and the solid lines represent the currents generated under illumination (10% water – black, 50% water – blue, 90% water – red) (Right) The same experiment but with chopped light illumination at 5 second intervals (10% water – black, 50% water – blue, 90% water – red). The electrolyte was degassed for 15 min under N₂ before the measurement.

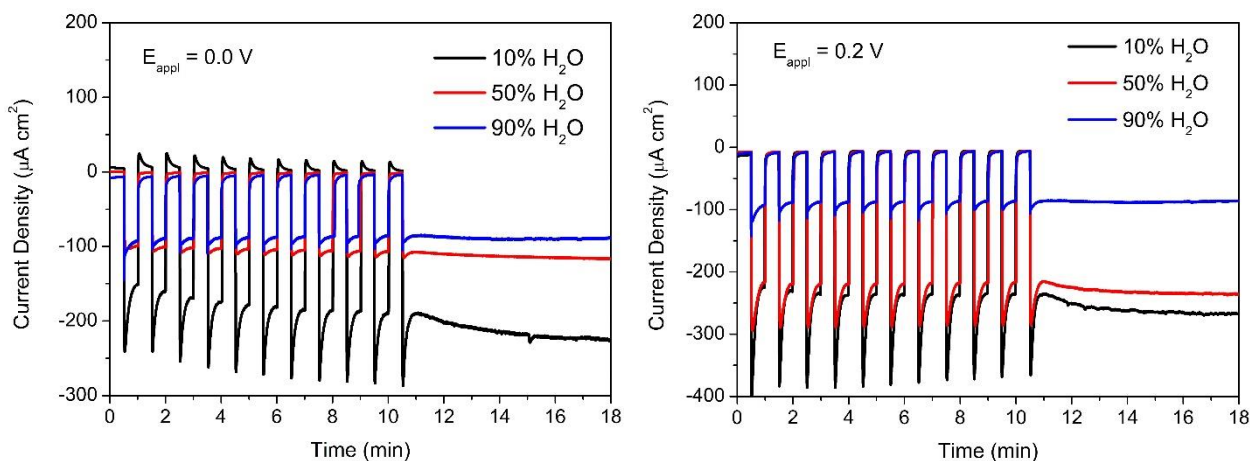


Figure 3.12. CA of D1|NiO immersed in 10 mM $[\text{Co}(\text{en})_3](\text{BF}_4)_3$ and 0.1 M LiClO_4 solutions in mixtures of acetonitrile and DI H₂O under light illumination and in the dark and held under $E_{\text{appl}} = 0 \text{ V}$ vs. Ag/AgCl (Left) and $E_{\text{appl}} = -0.2 \text{ V}$ vs. Ag/AgCl (Right). The electrolyte was degassed for 15 min under N₂ before the measurement.

3.5.1.4 Photocurrent dependence of pH of the electrolyte

The final part of the study to understand the effect of electrolyte on the photocathode performance was focused on the photocurrent dependence of the electrolyte pH. This was carried out by measuring photocurrents in 0.1 M KCl electrolytes with different pH ranging from pH1 to pH13 and in the presence of EA. For the EA, $[\text{Co}(\text{en})_3]^{3+}$ was used as in previous parts of the overall study to be able to compare the results. The electrolytes were made up of 10 mM $[\text{Co}(\text{en})_3]\text{Cl}_3$ with the addition of either HCl to decrease the pH, or KOH to increase the pH. The UV-visible spectroscopy and CV of the 10 mM $[\text{Co}(\text{en})_3]\text{Cl}_3$ solutions were additionally measured to check the pH stability of the $[\text{Co}(\text{en})_3]^{3+}$. This was carried out for solutions with pH1, pH5 and pH 13. (Figure A2 in Appendix). The ionic strength was kept constant by the addition of EA where necessary, making sure that the concentration of $[\text{Co}(\text{en})_3]^{3+}$ would be the same in all pH solutions when adding acid or base.

In Figure 3.13 the LSV of D1|NiO in different pH 0.1 M KCl with 10 mM $[\text{Co}(\text{en})_3]^{3+}$ is presented. It can be observed, that when decreasing the pH from 7 to 1 (Figure 3.13, left), then the photocurrents increase substantially from *ca.* 40 $\mu\text{A cm}^{-2}$ at pH 5 to *ca.* 275 $\mu\text{A cm}^{-2}$ at pH 4 further on up to *ca.* 320 $\mu\text{A cm}^{-2}$ at pH 3. But at pH 2 the photocurrents diminish down to *ca.* 50 $\mu\text{A cm}^{-2}$. On the other hand, when increasing the pH from 7 to 13, a steady increase in photocurrents can be observed right up to *ca.* 200 $\mu\text{A cm}^{-2}$ pH 12, after which the photocurrent spikes to *ca.* 350 $\mu\text{A cm}^{-2}$.

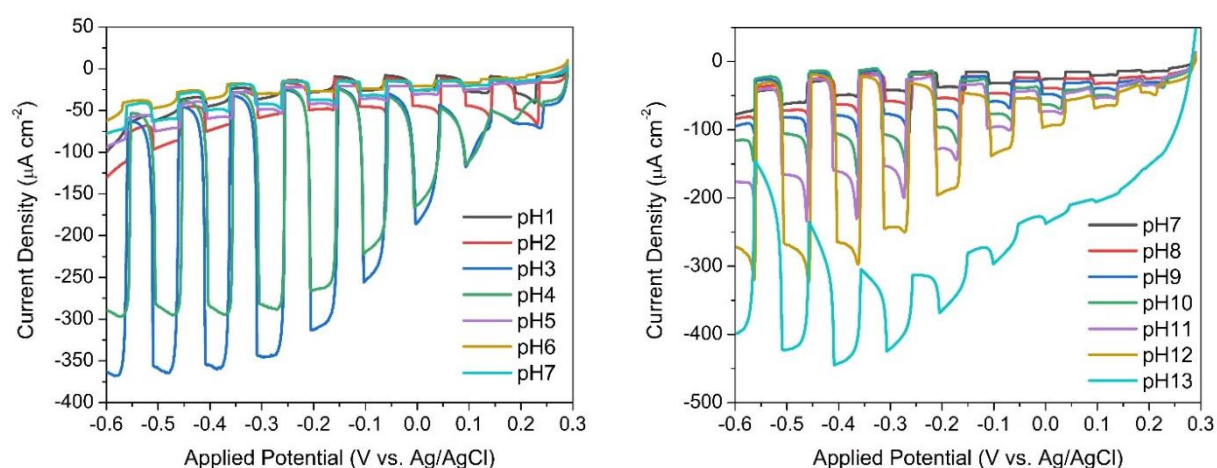


Figure 3.13. LSV of D1|NiO under chopped light illumination in 0.1 M KCl electrolytes with different pH and 10 mM $[\text{Co}(\text{en})_3]\text{Cl}_3$ as EA. Left – pH2 to pH7, right – pH7 to pH13. For pH13, 0.1 M KOH was used. pH of the electrolytes was modified either with additions of 0.1 M HCl to decrease the pH, or 0.1 M KOH to increase the pH, while keeping the ion

concentration unchanged. The electrolyte was degassed for 15 min under N₂ before the measurement.

The photocurrent onset change is also observed when changing the pH. The photocurrent onset of 0.33 V vs. Ag/AgCl is recorded in pH 3 electrolyte, in pH 5 the photocurrent onset is 0.28 V vs. Ag/AgCl and in pH 13, the onset of 0.15 V vs. Ag/AgCl is recorded.

Contrasting results when changing the pH have been reported in the literature. Castillo et al. observed a decrease in the photocurrent as the pH was decreased, which they reasoned was due to the shift in the flat band potential of NiO to more positive potentials as the H⁺ concentration was increased.¹⁶ Accumulating H⁺ at the NiO surface could lower the driving force for electron transfer, ΔG_{et} , from the NiO valence band to the photoexcited dye (see Chapter 1.6.5). However, Click et al. observed an increase in photocurrent at lower pH values which they attributed to an increase in the rate of hydrogen production.³² They reasoned that the hydrophobic substituents on their dye shielded the NiO surface from H₃O⁺. This can also explain the high photocurrents observed at pH 3 and pH 4 in this study. The shielding from H₃O⁺ by tert-butylbenzene functional groups of the D1 dye on the NiO surface could have the similar effect, but when decreasing the pH lower, the effect of H⁺ accumulation on the NiO surface takes over, lowering the driving force for electron transfer substantially and resulting in a rapid decrease in photocurrent. In addition, changes in other factors, like surface wetting and electrostatic forces, may also contribute to the differences in photocurrent in different pH.

The cyclic voltammetry measurements conducted on the solutions with different pH to observe the change in redox peak potentials and photocurrent density can give us information about the impact on any change in NiO valence band edge on the photocurrent density arising from e.g. a change in the rate of photoinduced electron transfer from the NiO to the dye. We have included the electrochemical behaviour of the bare NiO electrodes in water, shown on Figure 3.14, to highlight the activity of the electrode itself. The features are consistent with those previously described by Boschloo and Hagfeldt and materials prepared by other groups.^{14,33} It is well known that the peaks shift slightly when dye is adsorbed to the NiO surface.³² A Nernstian shift in the NiO valence band edge is also observed when pH is increased, as expected (Figure 3.14).

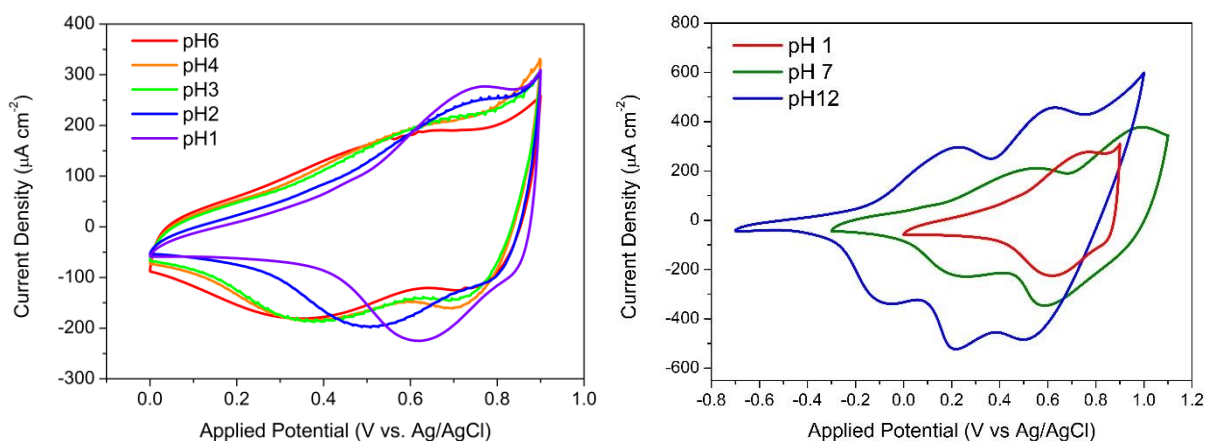


Figure 3.14. Left - CV on bare NiO electrode with decreasing pH in 0.1 M NaCl with 50 mV s^{-1} . Purple – pH 1, blue – pH 2, green – pH 3, orange – pH 4, red – pH 6. Right – CV of bare NiO in pH 1 0.1 M NaCl + HCl (red), pH 7 0.1 M phosphate buffer, pH 12 0.1 M NaCl + NaOH. Measured in a three-electrode electrochemical cell with a Pt wire counter electrode and Ag/AgCl (3.0 M NaCl) reference electrode. The electrolyte was degassed for 15 min under N_2 before the measurement.

3.5.1.5 H_2 evolution on Pt|D1|NiO photocathode

The final part of the study was to test the dye-sensitised photocathode for H_2 evolution using the best experimental conditions determined in the previous steps of the study. This time, instead of the EA we used an electrodeposited Pt catalyst on the D1|NiO to drive the proton reduction half reaction. Catalyst deposition was carried according to the instructions in Chapter 2.2.8. Hydrogen evolution was quantified using Gas Chromatography (GC) during which the gas from the headspace of the PEC cell was analysed after the CA measurement. The CA was measured under $E_{\text{appl}} = -0.3 \text{ V vs. Ag/AgCl}$ and under constant 1 sun (100 mW cm^{-2}) light illumination for 1 h (Figure 3.15). The PEC cell used was a one compartment custom made glass cell, with Pt|D1|NiO|FTO working electrode (WE), Pt|FTO counter electrode (CE) and Ag/AgCl reference electrode (3.0 M NaCl). In addition, control measurements were carried under same conditions for the same electrode but without illumination to determine if the H_2 evolution is really driven by the light, not electrochemically, and also for Pt|FTO electrode under illumination to show that the H_2 evolution only occurs due to dye interaction with the photons through which the excited state electrons are created and followed by charge transfer to the surface of the catalyst, where the proton reduction occurs. The working principle of the H_2 on the D1|NiO photocathode with Pt catalyst on the surface is presented on Figure 3.16.

After 1 h of CA measurement, the gas from the PEC cell's headspace was analysed with GC and H₂ evolution was detected only when Pt|D1|NiO was measured under constant light illumination. The photocurrent measured during the experiment was *ca.* 25 $\mu\text{A cm}^{-2}$, volume of H₂ evolved was $1.34 \pm 0.22 \mu\text{mol}$ and Faradaic efficiency of $20 \pm 2 \%$ was calculated. The low Faradaic efficiency indicates that there are significant losses in the system. The low efficiency could be due to the recombination of H₂ and O₂ in the cell since there was no membrane between the anode and the cathode. It could also be due to the analysis technique, which enables loss of gas during the injection and transport of gas in a GC syringe.

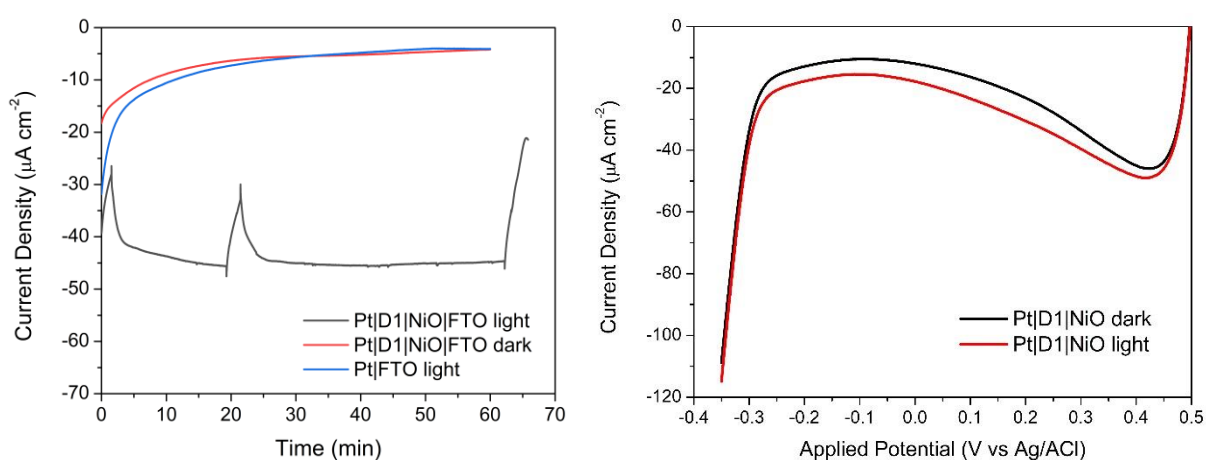


Figure 3.15. Left - CA of Pt|D1|NiO in pH 3 0.1 M phthalate buffer in the dark (red) and under 1 sun illumination (black). The CA was measured under $E_{appl} = -0.3 \text{ V vs. Ag/AgCl}$. CA of Pt on FTO under 1 sun illumination is included as a control measurement. The measurement was carried out in a three electrode PEC cell with Ag/AgCl reference electrode (3.0 M NaCl) and the gas in the headspace of the cell was analysed after the measurement using Gas Chromatography (GC). Right - LSV of Pt|D1|NiO in 0.1 M phthalate buffer (pH 3) under constant light illumination (red) and in the dark (black) with scan rate of 10 mVs^{-1} . Light illumination intensity was 1 sun (100 mW cm^{-2}) and electrolyte was degassed under N₂ for 15 min. before measurement.

It is also probable that part of the losses happens due to the decomposition of the dye on the surface of the photocathode, because the charge transport process of excited electrons from the dye to the catalyst is not efficient enough. This process is further studied and dye decomposition under light illumination is shown in Chapter 3.5.3.3. Interestingly, the photocurrent increased slowly when the light illumination was applied and also decreased slowly when the light was cut off. Since this was not observed when EA was used with the same photocathode, the reason of this behaviour must be the Pt catalyst on the surface of the electrode.

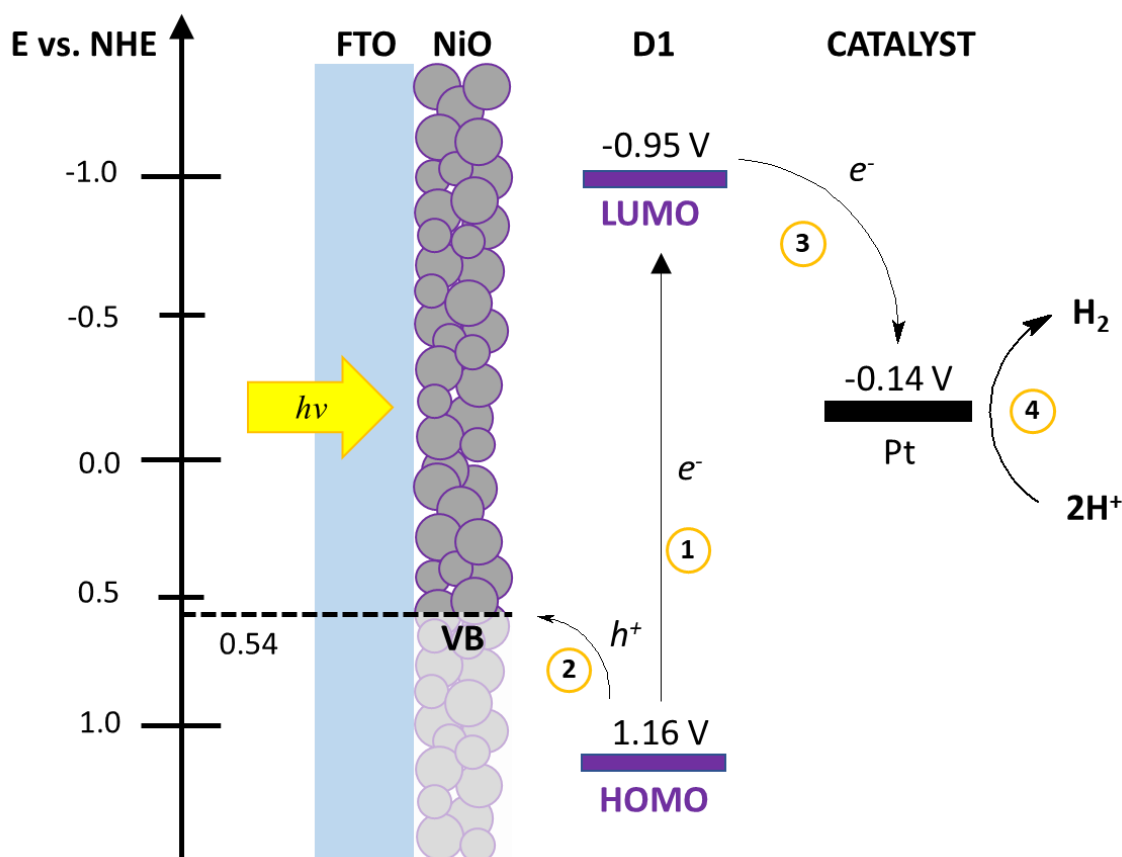


Figure 3.16. Schematics of the Pt|D1|NiO photocathode working principle. When light illumination is applied to the dye-sensitised photocathode, electron is excited from its ground state in HOMO to an excited state in LUMO (1), this leaves a positively charged hole, h^+ , which is then injected from the dye to the valence band, VB, of NiO (2). Excited electrons with higher energy in LUMO of the dye are then transferred to the surface of the Pt catalyst (3) where the H_2 evolution is catalysed (4). Values for HOMO and LUMO of D3 are reported previously in literature.²⁷ Value for overpotential required for the Pt catalyst to drive H_2 evolution reaction was estimated from Figure 3.40 (left) from the point where the $J = 100 \mu\text{A cm}^{-2}$.

3.5.2 Photoelectrochemistry of D2 BODIPY polymer dye on NiO

To understand the effect of the dye on the photoelectrochemical performance of dye-sensitised NiO photocathode, we carried out similar experiments with a different dye, which was also a BODIPY but with a polymeric structure (Figure 3.17). The dye, D1, was synthesised by our collaborator A. Cullen in M. Pryce group in Dublin City University.

LSV and CA measurements were carried out in the dark and under illumination (1.5 AM, 100 mW cm^{-2}) in aqueous electrolyte solutions with and without the EA. In addition, using UV-vis spectroscopy, the dye stability in acetonitrile solution was studied along with measurements on the NiO, which enabled to determine the dye loading on the NiO electrode.

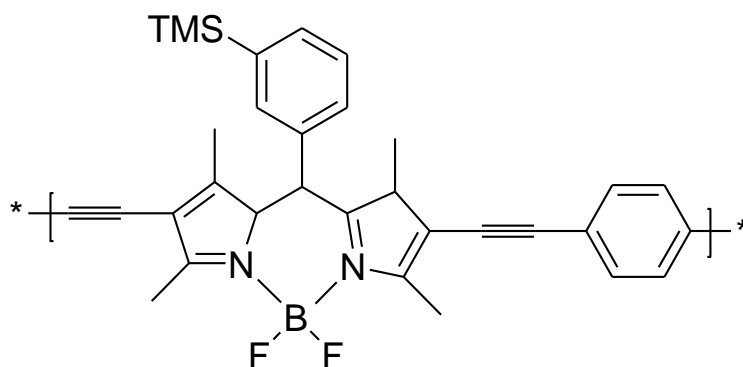


Figure 3.17. D2 dye: BODIPY 3-TMS-Aryl Polymer with phenyl link.

PEC measurements were carried out on D2|NiO thin film samples deposited on FTO conductive substrates. D2 was adsorbed on nanostructured NiO in a 0.3 mM D2 dye bath using acetonitrile as a solvent. First, the UV-vis spectra of D2 in acetonitrile was measured after periods of time to assess the stability of the dye in solution and to optimise the time for dye adsorption without decomposing the dye (Figure 3.18, left). This was followed by UV-vis spectroscopy on D2|NiO samples to measure the dye absorption on the electrode and calculate the dye loading. To do that, an extinction coefficient for the D2 had to be determined. This was achieved by UV-vis measurements of solutions of D2 in acetonitrile with different concentration and constructing a Beer-Lambert plot with the obtained data. The slope of the plot enables to determine the extinction coefficient, ϵ , of the dye. For our dye D2, the extinction coefficient ϵ was determined to be $9000 \text{ L mol}^{-1} \text{ cm}^{-1}$. The dye loading was estimated according to literature using the absorption on the NiO (Figure 3.18, right) and the extinction coefficient

and was calculated to be $13 \text{ nmol}\cdot\text{cm}^{-2}$.³⁴ This value is in similar order of magnitude with other dye-sensitised photocathodes reported elsewhere.²⁶

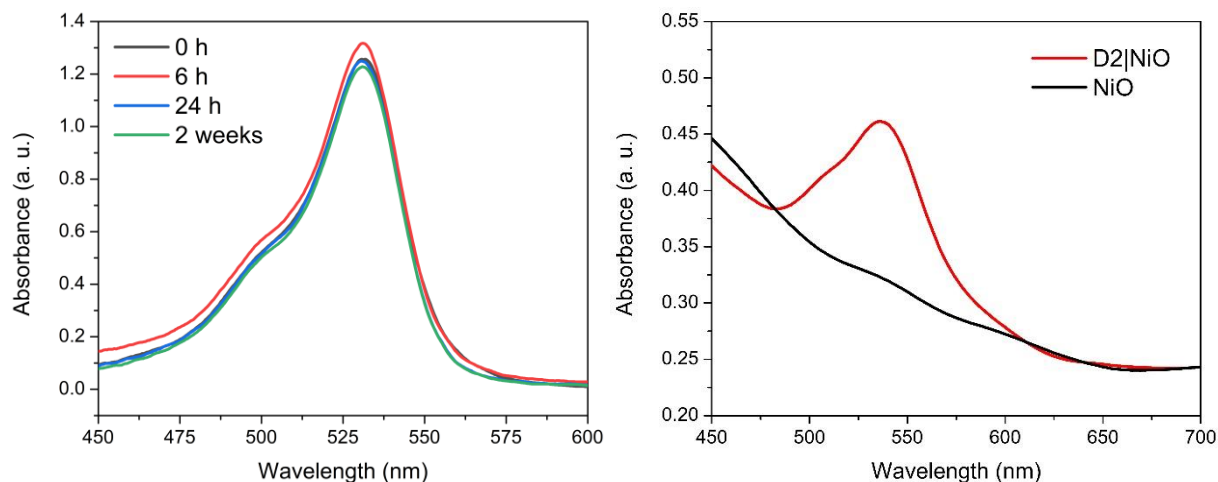


Figure 3.18. Left - UV-vis spectra of D2 in acetonitrile (0.3 mM) after preparation (black), after 6 h (red), after 24 h (blue) and after 2 weeks (green). The NiO films were taken out from the dye bath after 24 h. Right - UV-vis spectra of D2|NiO (red) and NiO (black). The NiO films were taken out from the dye bath after 24 h.

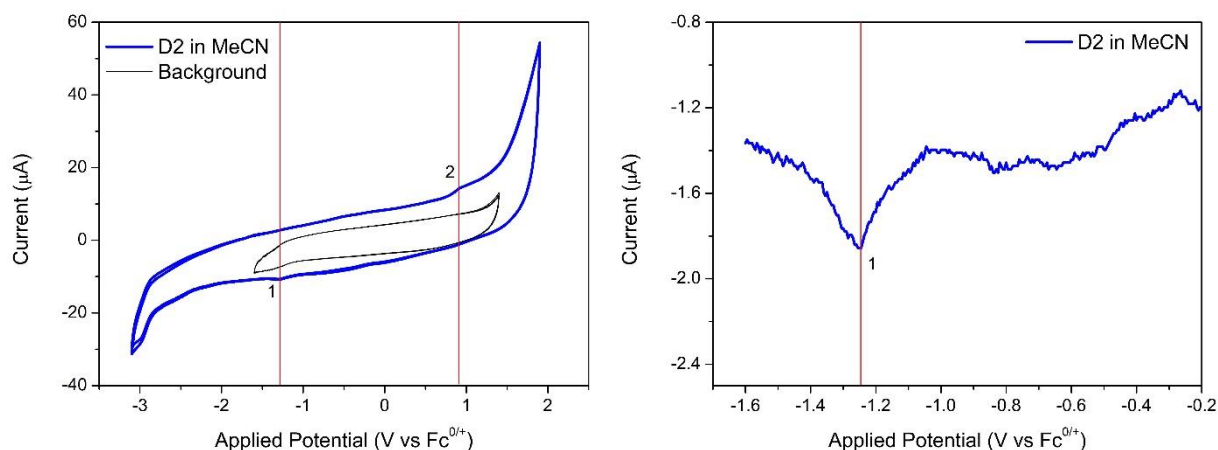


Figure 3.19. Left – CV of 0.2 mM D2 in MeCN with 0.1 M TBAPF₆ supporting electrolyte (blue). Reduction potential, E_{red} , and oxidation potential, E_{ox} , if D2 are marked (1) and (2), respectively. The CV of the background, 0.1 M TBAPF₆ in MeCN is added as a reference (black). Right – Differential Pulse (DP) measurement of 2 mM D2 in MeCN with 0.1 M TBAPF₆ supporting electrolyte. Ag/AgNO₃ reference electrode was used and the potentials are referenced to a ferrocene/ferrocenium ($\text{Fc}^{0/+}$) redox couple, which was used for calibration. The solution was degassed for 15 min under N₂ before the measurement.

To determine the HOMO and LUMO potentials of the D2 dye, a CV and Differential Pulse Voltammetry (DPV) measurements were carried out on the dye solution in acetonitrile (Figure 3.19). Since the amount of dye available was very small, only 0.2 mM solutions were used, and therefore the redox processes are hardly visible. But still, the reduction, E_{red} , and

oxidation, E_{ox} , potentials for the dye were determined and the values were $E_{red} = -0.68$ V vs. Ag/AgCl (-0.48 V vs. NHE) and $E_{ox} = 1.48$ V vs. Ag/AgCl (1.68 V vs NHE). These values are presented also on the Figure 3.20, where the working principle of the D2|NiO photocathode with EAs under illumination is shown.

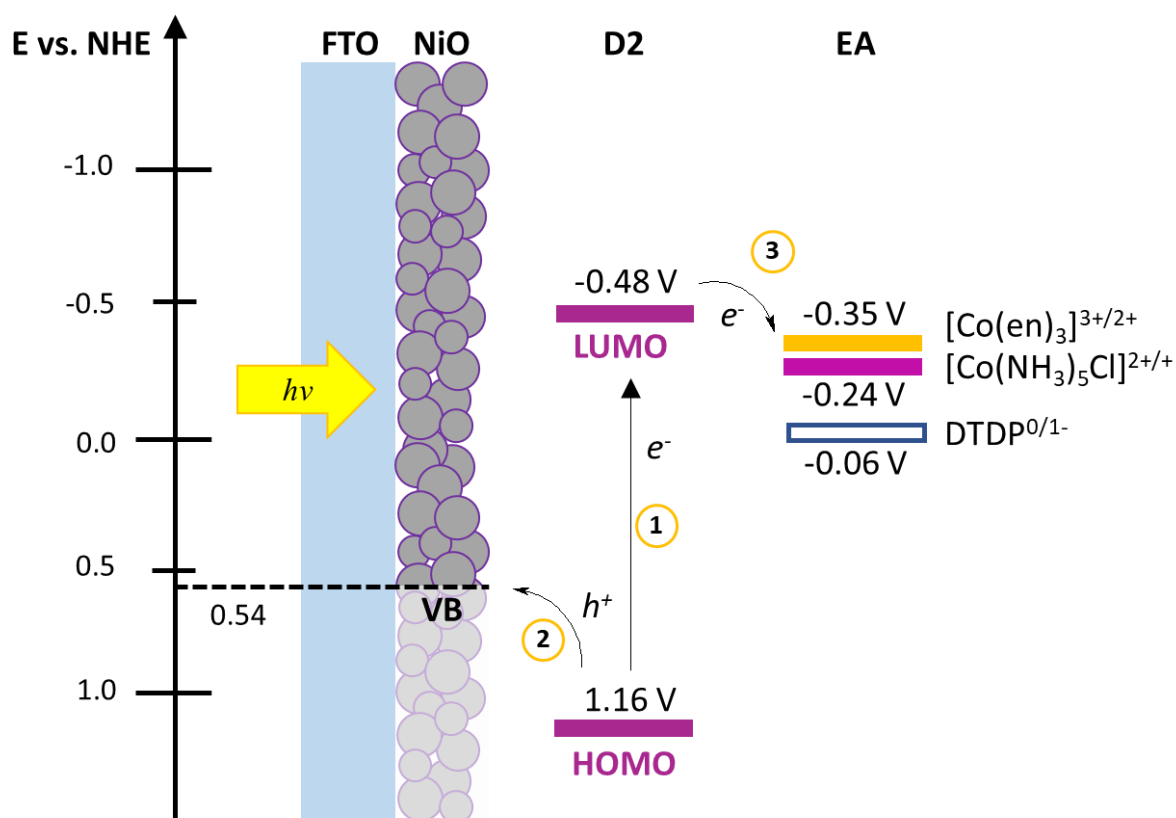


Figure 3.20. Schematics of the D2|NiO photocathode working principle with EAs in solution. When light illumination is applied to the dye-sensitised photocathode, electron is excited from its ground state in HOMO to an excited state in LUMO (1), this leaves a positively charged hole, h^+ , which is then injected from the dye to the valence band, VB, of NiO (2). Excited electrons with higher energy in LUMO of the dye can then reduce the EA (3). The values for HOMO and LUMO of D2 were estimated from CV measurement on Figure 3.18, left.

PEC measurements were carried out on D2|NiO films in a three-electrode cell with Ag/AgCl reference electrode and Pt|FTO counter electrode. LSV, CV and CA were performed under simulated light illumination (1.5 AM, 100 mW cm^2) and in the dark in 0.1 M aqueous buffers with different pH. Initially, the LSV and CA measurements were conducted in 0.1 M acetate buffer (pH 5) with D2|NiO to see if there is any photocurrent generated without EA or catalyst. Thereafter, the same measurements were repeated with 10 mM $[\text{Co}(\text{NH}_3)\text{Cl}]\text{Cl}_2$ and 10 mM $[\text{Co}(\text{en})_3]\text{Cl}_3$ dissolved in electrolyte solution to compare the results obtained without the EA. These EAs were chosen due to their suitable reduction potential, which is lower than the LUMO of the dye, and high photocurrents achieved with D1|NiO system.

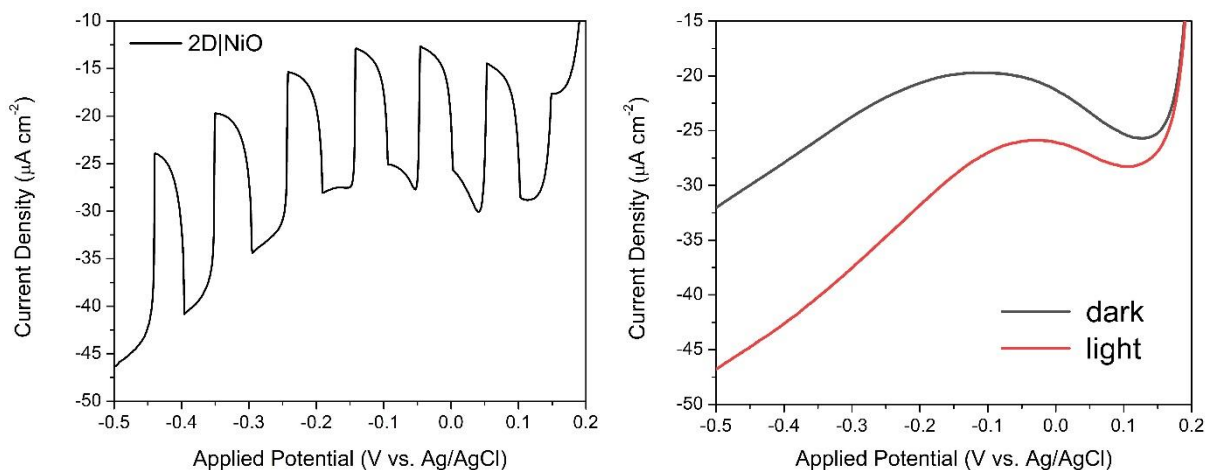


Figure 3.21. Left - LSV of D2|NiO in pH 5 0.1 M acetate buffer under chopped light illumination (5 s in the dark, 5 s under light). Right - LSV of D2|NiO in pH 5 0.1 M acetate buffer under simulated light illumination (1.5 AM, 100 mW/cm²) (red) and in the dark (black). Scan rate was 10 mV s⁻¹. Scan speed was 10 mV s⁻¹. Electrolyte was degassed under N₂ for 15 min. before measurement.

The LSV measurements were carried out on D2|NiO without EA in the dark and under light illumination (Figure 3.21). Since there is no pathway for the electrons to go after they are excited to higher energy level in the dye, the most probable result would be that the dye would be decomposed over time, since the excited electrons would reduce the dye over time. This hypothesis is further studied and proved in Chapter 3.5.3.3. during the stability study with a different dye. Photocurrent generation of *ca.* 20 $\mu\text{A cm}^{-2}$ was achieved without the EA, which was almost independent from the applied potential when negative potential was increased during the LSV cathodic scan (Figure 3.21). The dark current however was increasing, which is most probably due to dye reduction which starts already from approximately -0.1 V vs. Ag/AgCl. The dye reduction potential was estimated to be -0.68 V vs. Ag/AgCl (Figure 3.19), which is considerably lower than for dye D1, which has reduction potential of -0.95 V vs NHE (*ca.* -1.15 V vs. Ag/AgCl) (Figure 3.3).

CA measurements were also carried out on D2|NiO without EA under chopped light illumination and under different E_{appl} . The measurements showed that the photocurrent increases until $E_{\text{appl}} = -0.1$ V vs. Ag/AgCl and then stays the same even when the E_{appl} is increased. These results are in good correlation with the results from LSV measurements. The highest photocurrent densities measured without an EA on D2|NiO were 10 $\mu\text{A/cm}^2$ under an applied potential of -0.1 and -0.2 V vs. Ag/AgCl. (Figure 3.22).

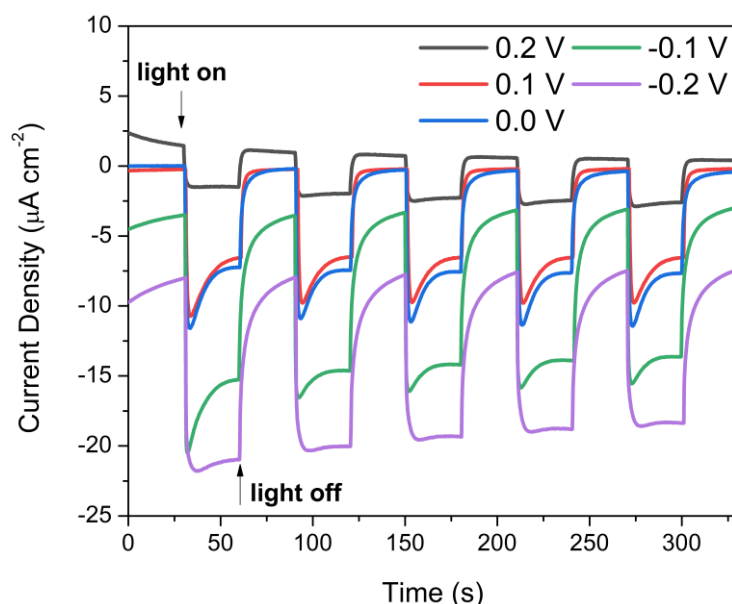


Figure 3.22. CA under different applied potentials on D2/NiO in pH 5 0.1 M acetate buffer. Light illumination was applied with 30 s intervals (30 s in the dark, 30 s under light, 5 cycles). Light illumination intensity was 1 sun (100 mW cm^{-2}) and electrolyte was degassed under N_2 for 15 min. before measurement.

To study the photocurrents obtainable with EA in solution, 10 mM $[\text{Co}(\text{NH}_3)\text{Cl}]\text{Cl}_2$ and $[\text{Co}(\text{en})_3]\text{Cl}_3$ were added to the electrolyte solution to harvest the photoexcited electrons through reduction of the acceptor. LSV and CA measurements were carried out and they showed considerable increase in photocurrents compared to the system without EA, which was expected. With $[\text{Co}(\text{NH}_3)\text{Cl}]\text{Cl}_2$ photocurrent densities up to $60 \mu\text{A cm}^{-2}$ were recorded under both applied potentials during the CA measurement (Figure 3.23). The CA measurements with 10 mM $[\text{Co}(\text{en})_3]\text{Cl}_3$ in solution showed a little bit lower photocurrents, with the best result of ca. $40 \mu\text{A cm}^{-2}$ obtained at $E_{\text{appl}} = 0.0 \text{ V}$ vs Ag/AgCl (Figure 3.24). The lower photocurrents for $[\text{Co}(\text{en})_3]\text{Cl}_3$ can be explained by the lower driving force, ΔG_{et} , for electron transfer from the reduced dye to the $[\text{Co}(\text{en})_3]^{3+}$ (see Chapter 1.6.5). The results from CA were in good agreement with the LSV measurements (Figure 3.25), which showed similar photocurrents. What was also shown, was the increase in dark current with increase in negative applied potential as for the LSV measurements without EA (Figure 3.21). However, the photocurrent is also increasing with potential, which can be explained by the reduction of the $[\text{Co}(\text{en})_3]^{3+}$ which has the $E_{\text{red}} = -0.55 \text{ V}$ vs. Ag/AgCl (-0.35 V vs. NHE, Figure 3.20). Therefore, there are two processes occurring at the same time visible on the LSV, the reduction of the dye D2 and the reduction of the EA, giving the shape of the LSV as seen on Figure 3.25.

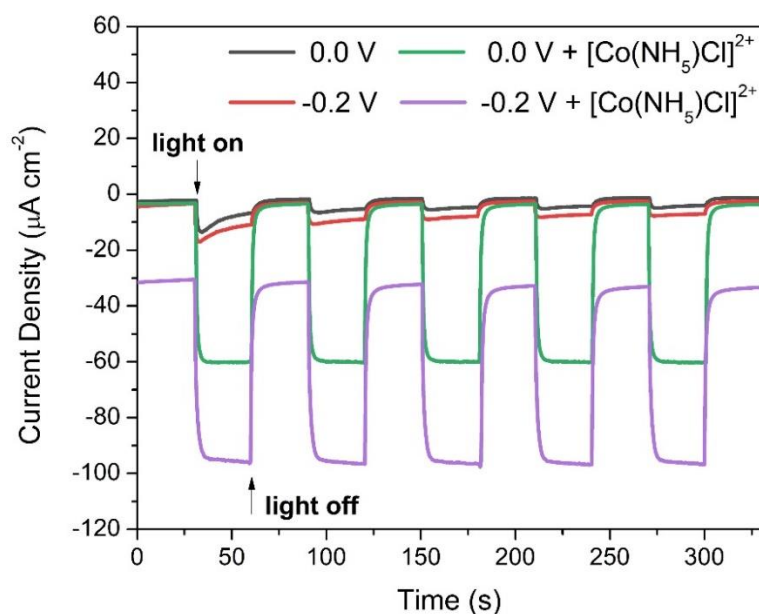


Figure 3.23. CA under 0 V and -0.2 V vs. Ag/AgCl E_{appl} with and without 10mM $[\text{Co}(\text{NH}_3)\text{Cl}]\text{Cl}_2$ as EA on D2|NiO in pH 5 0.1 M acetate buffer. Black and red – without EA, green and purple – with 10 mM $[\text{Co}(\text{NH}_3)\text{Cl}]\text{Cl}_2$ in electrolyte solution. Light illumination was applied with 30 s intervals (30 s in the dark, 30 s under light, 5 cycles). Light illumination intensity was 1 sun (100 mW cm^{-2}) and electrolyte was degassed under N_2 for 15 min. before measurement.

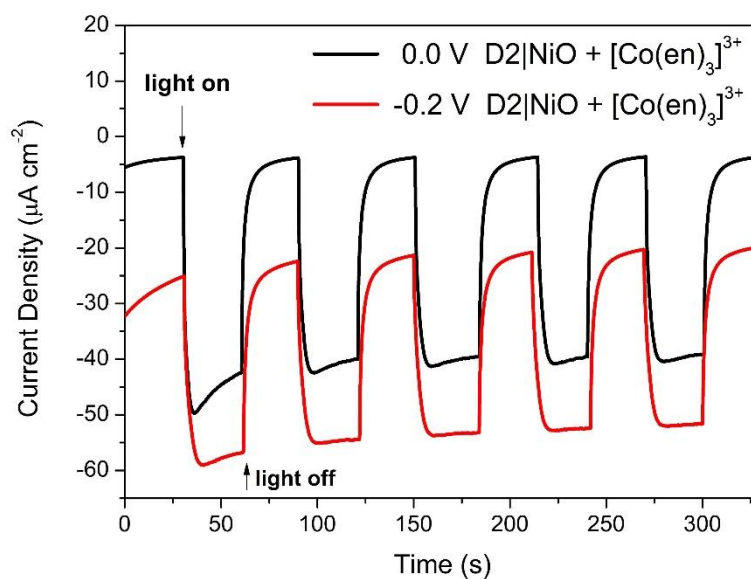


Figure 3.24. CA of D2|NiO under $E_{appl} = 0.0 \text{ V}$ and $E_{appl} = -0.2 \text{ V}$ vs. Ag/AgCl with 10 mM $[\text{Co}(\text{en})_3]\text{Cl}_3$ in 0.1 M acetate buffer (pH 5) under chopped light illumination. Light illumination was applied with 30 s intervals (30 s in the dark, 30 s under light, 5 cycles). Light illumination intensity was 1 sun (100 mW cm^{-2}) and electrolyte was degassed under N_2 for 15 min. before measurement.

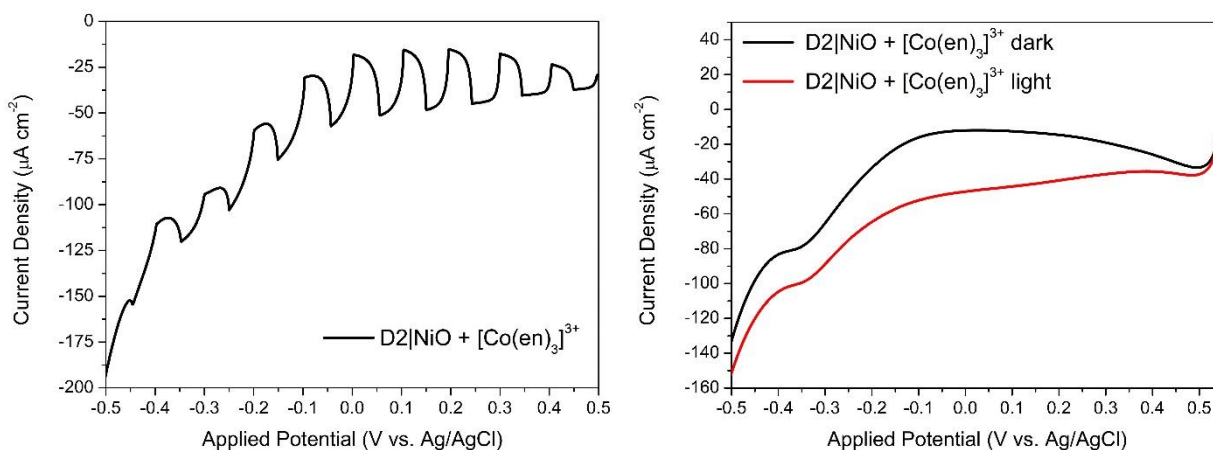


Figure 3.25. Left - LSV of D2|NiO with 10 mM $[\text{Co}(\text{en})_3]\text{Cl}_3$ in 0.1 M acetate buffer (pH 5) under chopped light illumination with scan rate of 10 mVs^{-1} . Light illumination was applied with 5 s intervals (5 s in the dark / 5 s under illumination); Right - LSV of D2|NiO with 10 mM $[\text{Co}(\text{en})_3]\text{Cl}_3$ in 0.1 M acetate buffer (pH 5) under constant light illumination (red) and in the dark (black) with scan rate of 10 mVs^{-1} . Light illumination intensity was 1 sun (100 mW cm^{-2}) and electrolyte was degassed under N_2 for 15 min. before measurement.

Then, the same measurements were carried out with the best performing EA, DTDP, in pH 3 0.1 M phthalate buffer, to observe the photocurrent generation under the optimal conditions determined in first part of the NiO-based photocathodes study with dye D1. This would also give a good indication of the photocurrents that could be obtained with the best suitable catalyst under the same conditions. The LSV measurements presented on Figure 3.26 showed considerably higher photocurrents with DTDP than with the $[\text{Co}(\text{NH}_3)\text{Cl}]\text{Cl}_2$ and $[\text{Co}(\text{en})_3]\text{Cl}_3$ with *ca.* $100 \mu\text{A cm}^2$ at $-0.2 \text{ V vs. Ag/AgCl}$ on the cathodic sweep under illumination (Figure 3.26, right) and a steady increase in photocurrent from the photocurrent onset at $0.4 \text{ V vs. Ag/AgCl}$ until the dye reduction becomes a dominant process at approximately $E_{\text{appl}} = -0.45 \text{ V vs. Ag/AgCl}$.

The CA measurements under same conditions are in good agreement with the results from the LSV measurements. Under $E_{\text{appl}} = -0.2 \text{ V vs. Ag/AgCl}$ photocurrents of *ca.* $90 \mu\text{A cm}^2$ were obtained (Figure 3.27). It is important to also note, that the DTDP concentration in electrolyte was 5 mM due to its low solubility in water, compared to the 10 mM for $[\text{Co}(\text{NH}_3)\text{Cl}]\text{Cl}_2$ and $[\text{Co}(\text{en})_3]\text{Cl}_3$. The driving force for the electron transfer, ΔG_{et} , from the reduced D2 to the DTDP is considerably higher than it was with $[\text{Co}(\text{NH}_3)\text{Cl}]\text{Cl}_2$ or $[\text{Co}(\text{en})_3]\text{Cl}_3$, which explains the considerably higher photocurrents we see during the LSV and CA measurements.

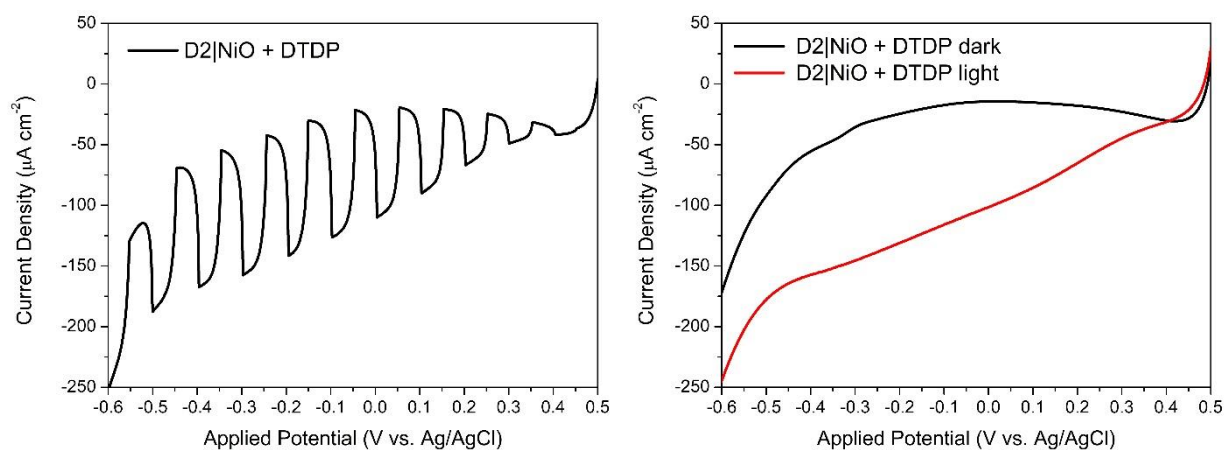


Figure 3.26. Left - LSV of D2|NiO with 5 mM DTDP in 0.1 M phthalate buffer (pH 3) under chopped light illumination with scan rate of 10 mVs^{-1} . Light illumination was applied with 5 s intervals (5 s in the dark / 5 s under illumination); Right - LSV of D2|NiO with 5 mM DTDP in 0.1 M phthalate buffer (pH 3) under constant light illumination (red) and in the dark (black) with scan rate of 10 mVs^{-1} . Light illumination intensity was 1 sun (100 mW cm^{-2}) and electrolyte was degassed under N_2 for 15 min. before measurement.

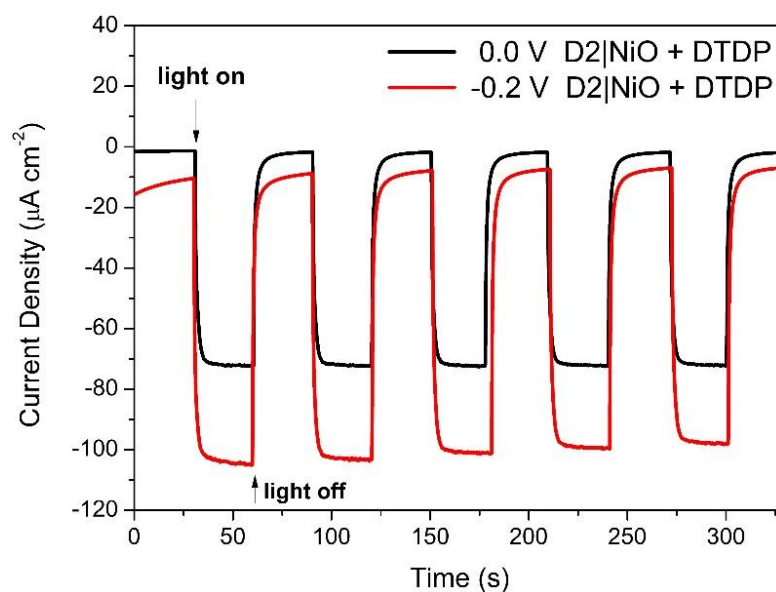


Figure 3.27. CA of D2|NiO under $E_{\text{appl}} = 0.0 \text{ V}$ and $E_{\text{appl}} = -0.2 \text{ V}$ vs Ag/AgCl with 5 mM DTDP in 0.1 M phthalate buffer (pH 3) under chopped light illumination. Light illumination was applied with 30 s intervals (30 s in the dark, 30 s under light, 5 cycles). Light illumination intensity was 1 sun (100 mW cm^{-2}) and electrolyte was degassed under N_2 for 15 min. before measurement.

The final part of the study with D2|NiO was to test the dye-sensitised photocathode for H_2 evolution using the best experimental conditions determined in the previous steps of the

study. This time, instead of the EA we used an electrodeposited Pt catalyst on the D2|NiO to drive the proton reduction half reaction. Catalyst deposition was carried according to the instructions in Chapter 2.2.8. First, the LSV of the Pt|D2|NiO under chopped and constant light was measured, to see if any photocurrent is generated at all.

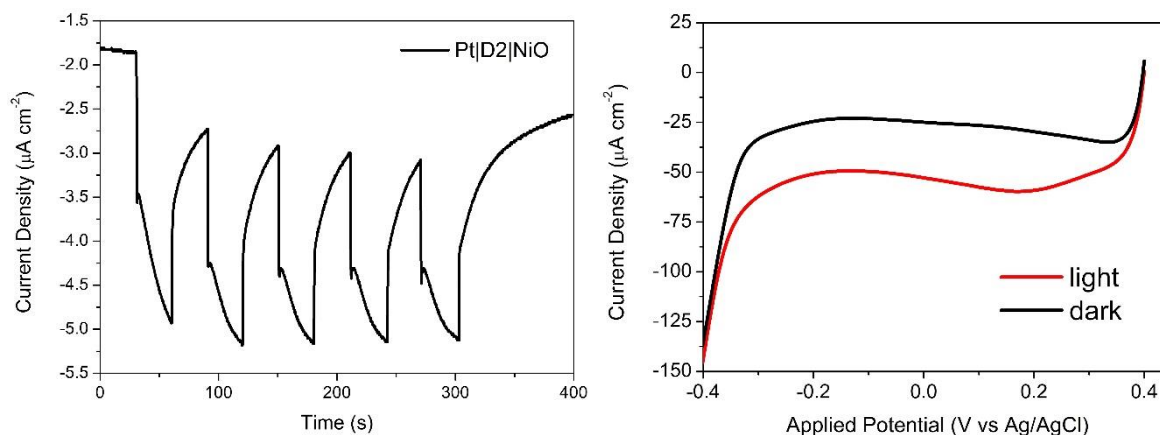


Figure 3.28. Left - CA of Pt|D2|NiO under $E_{appl} = -0.3$ V vs Ag/AgCl in 0.1 M phthalate buffer (pH 3) under chopped light illumination (30 s dark / 30 s light). Right - LSV of Pt|D2|NiO in 0.1 M phthalate buffer (pH 3) under constant light illumination (red) and in the dark (black) with scan rate of 10 mVs^{-1} . Light illumination intensity was 1 sun (100 mW cm^{-2}) and electrolyte was degassed under N_2 for 15 min. before measurement.

The LSV under light illumination on Figure 3.28 (right) gave photocurrent onset potential of 0.4 V vs Ag/AgCl, which is in good agreement with the measurements with DTDP EA. It also shows photocurrents of *ca.* $25 \mu\text{A cm}^2$ until there is a rapid increase in dark current. This is an indication of the overpotential of Pt for H_2 evolution in this system, which is approximately -0.35 V vs Ag/AgCl, determined from Figure 2.28 (right), black line. However, the photocurrent measured under chopped light illumination during CA measurement (Figure 3.28, left) showed negligible photocurrents of *ca.* $3 \mu\text{A cm}^2$ with a considerable increase in photocurrent during the light illumination, which could be an indication of a photocorrosion process.

To measure and quantify the H_2 evolution of the Pt|D2|NiO photocathode, the CA measurement was carried out over a longer period of time under constant light illumination. H_2 evolution was detected and quantified using Gas Chromatography (GC) during which the gas from the headspace of the PEC cell was analysed after the CA measurement. The CA was measured under $E_{appl} = -0.3$ V vs Ag/AgCl and under constant 1 sun (100 mW cm^{-2}) light illumination for 1 h. The PEC cell used was a one compartment custom made glass cell, with

Pt|D1|NiO|FTO working electrode (WE), Pt|FTO counter electrode (CE) and Ag/AgCl reference electrode (3.0 M NaCl).

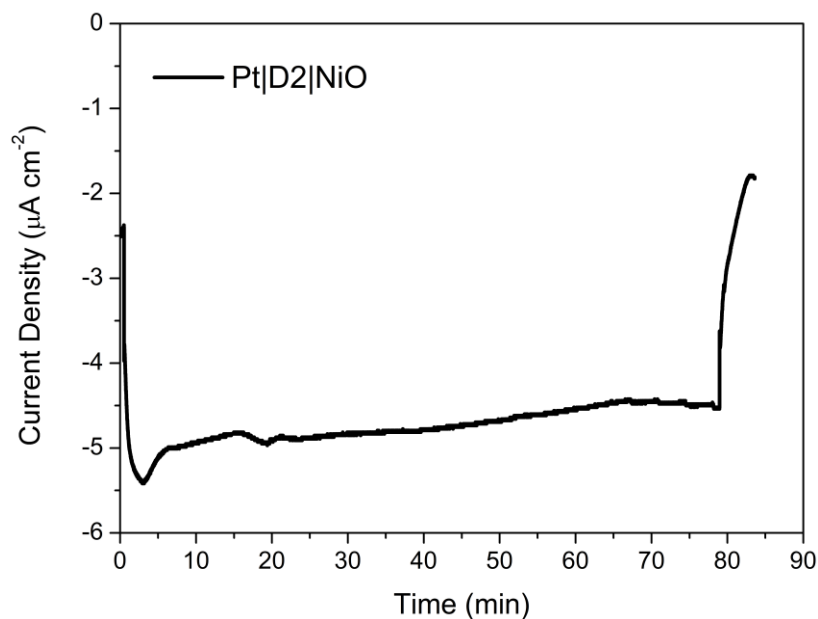


Figure 3.29. CA of Pt|D2|NiO in 0.1 M phthalate buffer (pH 3) under $E_{\text{appl}} = -0.3$ V constant light illumination. Light illumination intensity was 1 sun (100 mW cm^{-2}) and electrolyte was degassed under N_2 for 15 min. before measurement.

The photocurrent measured during the experiment was *ca.* $3 \mu\text{A cm}^{-2}$ (Figure 3.29), volume of H_2 evolved was 1.10 ± 0.08 nmol and Faradaic efficiency of 1.2 ± 0.2 % was calculated. Since the amount of H_2 detected with the GC was negligible, it is important to note that large error comes in from the integration of the peak on chromatogram. The overall conclusion is, that the small current generated during the light illumination is most probably due to the photocorrosion of the electrode of which a large part is most probably the decomposition of the dye during the process. This was also visible seen from the electrode after the measurement, showing large discoloration.

3.5.3 Dye-sensitised NiO photocathode with a benchmark donor-acceptor organic dye

In this part of the study on NiO-based photocathodes, a commercially available benchmark p-type dye D3, also known as P1 in the literature³⁵, was used to sensitise NiO electrodes to study the photocurrent generation with electron acceptors (EAs) and discuss the results comparing them to the previously studied systems D1|NiO and D2|NiO. In addition, the D3|NiO system was tested for H₂ evolution with electrodeposited Pt and nickel molybdenum sulphide (NiMoS) catalyst. Photoelectrochemical measurements were carried out with the D3|NiO photocathodes using the optimised conditions from Chapter 3.5.1 measuring photocurrent generation with [Co(en)₃]Cl₃ EA and best performing EA DTDP (Chapter 3.5.1). In addition, a stability study was conducted by conducting a CA measurement under constant light illumination on D3|NiO photocathode and taking UV-vis spectrum before and after the measurement to see if the photocurrent generation is connected to dye decomposition during the measurement. Finally, a catalyst layer was deposited on the dye-sensitised photocathode surface and H₂ evolution was measured with GC to see, if, how much and under which conditions H₂ is produced with this photocathode.

3.5.3.1 Properties and previous studies with D3 dye and D3-sensitised photocathodes

Synthesis of the organic dye D3, 4-(Bis-{4-[5-(2,2-dicyano-vinyl)-thiophene-2-yl]-phenyl}-amino)-benzoic acid, was first reported by L. Sun and co-workers along with performance in a DSSC.³⁵ The dye has a push-pull structure where the triphenylamine

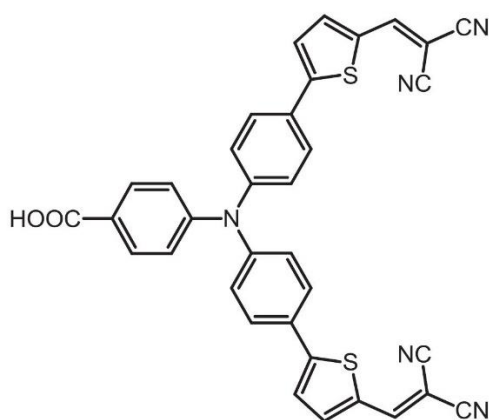


Figure 3.30. Structure of the benchmark organic dye D3.

moiety acts as an electron donor, thiophene unit is the conjugated chain facilitating the charge transport and malononitrile moiety is the electron acceptor part (Figure 3.30).³⁵ After the first report, D3 was successfully applied in NiO-based DSSC an IPCE of 64% was reported, which was the record value for a p-type DSSC at the time.³⁶ Soon after that, D3 was used in a PEC cell and light-driven H₂ evolution was shown on D3|NiO photocathode using an inorganic cobalt catalyst in solution.⁸ The D3 dye for this study was synthesised in our lab by Z. Han.

3.5.3.2 Photocurrent generation with electron acceptor

First, the photocurrent generation on D3|NiO was monitored using the [Co(en)₃]Cl₃ electron acceptor. LSV was carried out on D3|NiO in a three electrode PEC cell used also for previous measurements with D1|NiO and D2|NiO photocathodes (Chapters 3.5.1 and 3.5.2) in pH 3 0.1 M phthalate buffer. The pH was chosen according to the best results from Chapter 3.5.1 and concentration was chosen to be 10 mM to be able to compare the results obtained with the D1|NiO and D2|NiO with the same EA. The results showed high photocurrents up *ca.* 470 $\mu\text{A cm}^{-2}$ at -0.2 V vs. Ag/AgCl (Figure 3.31). As a comparison, the chopped light LSV (Figure 3.31, left) and CA (Figure 3.32) of D3|NiO is presented to show that without the EA a negligible photocurrent is produced.

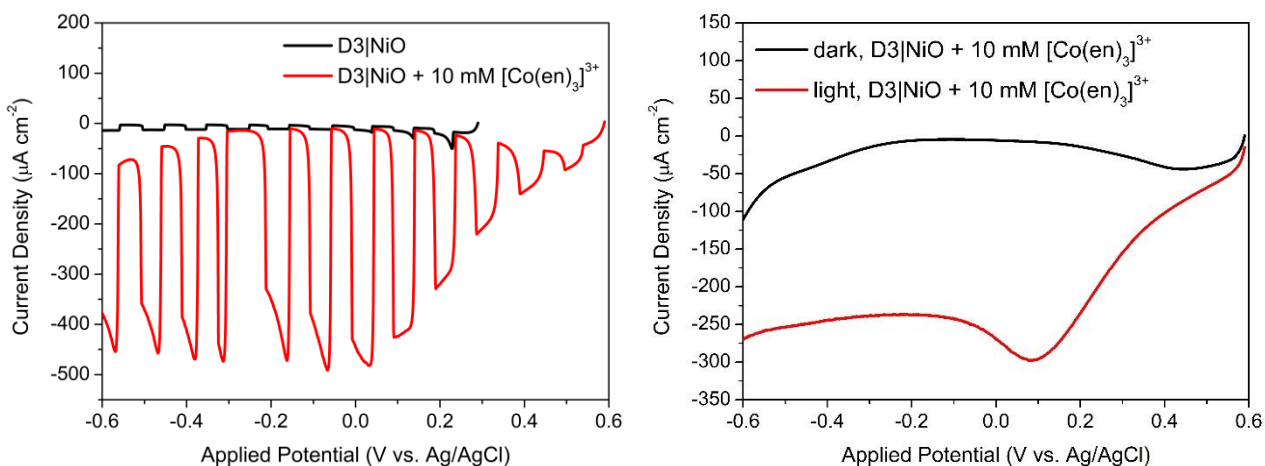


Figure 3.31. Left - LSV of D3|NiO with 10 mM [Co(en)₃]Cl₃ in 0.1 M phthalate buffer (pH 3) under chopped light illumination with scan rate of 10 mVs⁻¹. Light illumination was applied with 5 s intervals (5 s in the dark / 5 s under illumination); Right - LSV of D3|NiO with 10 mM [Co(en)₃]Cl₃ in 0.1 M phthalate buffer (pH 3) under constant light illumination (red) and in the dark (black) with scan rate of 10 mVs⁻¹. Light illumination intensity was 1 sun (100 mW cm⁻²) and electrolyte was degassed under N₂ for 15 min. before measurement.

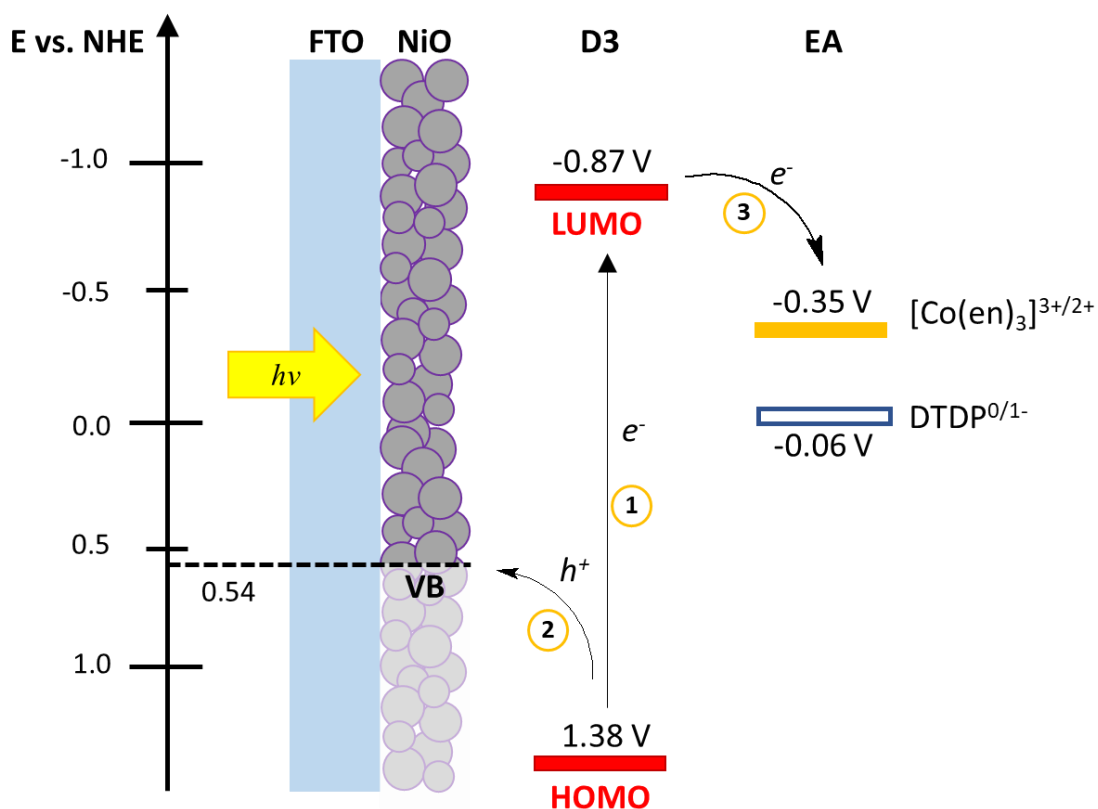


Figure 3.32. Schematics of the D3|NiO photocathode working principle with EAs in solution. When light illumination is applied to the dye-sensitised photocathode, electron is excited from its ground state in HOMO to an excited state in LUMO (1), this leaves a positively charged hole, h^+ , which is then injected from the dye to the valence band, VB, of NiO (2). Excited electrons with higher energy in LUMO of the dye can then reduce the EA (3). Values for HOMO and LUMO of D3 were taken from literature.³⁵

When observing the results of the CA with $[\text{Co}(\text{en})_3]\text{Cl}_3$ on Figure 3.33, strong transient photocurrent was produced decreasing to approximately $200 \mu\text{A cm}^{-2}$ during the 30 s light illumination. This is an indication of charge accumulation at the surface of the electrode due to an inefficient charge transfer to the $[\text{Co}(\text{en})_3]^{3+}$. This phenomenon was also observed for D1|NiO system with $[\text{Co}(\text{en})_3]\text{Cl}_3$ (Figure 3.5), but the transient spikes were less pronounced. However, with the D2|NiO, this was not observed indicating a more efficient charge transfer from the dye to the EA.

After PEC measurements with $[\text{Co}(\text{en})_3]\text{Cl}_3$, EA was changed to DTDP (5 mM), which was the best performing EA with D1|NiO and D2|NiO pH 3 0.1 M phthalate buffer. During the LSV under chopped light illumination (Figure 3.34, left) and constant light illumination (Figure 3.34, right), photocurrents of *ca.* $400 \mu\text{A cm}^{-2}$ were measured at -0.2 V vs. Ag/AgCl. During the measurement, the photocurrent increased with potential up until

approximately $E_{appl} = -0.0$ V, after which the photocurrent stabilised and was not affected by the further increase of the negative bias.

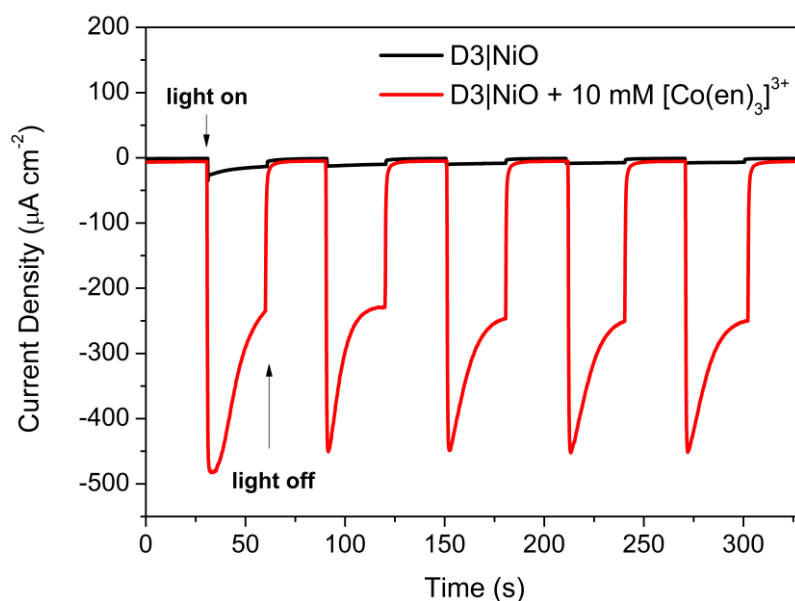


Figure 3.33. CA on D3|NiO under $E_{appl} = -0.2$ V vs. Ag/AgCl applied potential with 10 mM $[\text{Co}(\text{en})_3]\text{Cl}_3$ in 0.1 M phthalate buffer (pH 3). Light illumination was applied with 30 s intervals (30 s in the dark / 30 s under illumination). Light illumination intensity was 1 sun (100 mW cm^{-2}) and electrolyte was degassed under N_2 for 15 min. before measurement.

After the LSV, a CA measurement was carried out under same conditions and it also showed a transient photocurrent during the 30 s light illumination (Figure 3.35). However, with DTDP EA, the transient photocurrent decay was smaller and during the 30 s light illumination the photocurrent decreased approximately $50 \mu\text{A cm}^{-2}$ to $350 \mu\text{A cm}^{-2}$. It indicates that the rate of recombination is lower with DTDP EA with D3|NiO resulting in higher overall photocurrent and showing that the DTDP EA is more compatible with the D3|NiO photocathode. The working principle of the D3|NiO photocathode with EAs is presented on Figure 3.32 and it shows that the driving force for electron transfer from the excited D3 dye to the EA is higher for DTDP, which would also explain the higher photocurrent. The stabilisation of the photocurrent after approximately $E_{appl} = -0.0$ V vs Ag/AgCl indicates, that at that applied potential the rate of charge transfer to the EA equals the rate of recombination between the holes in the NiO and either the reduced dye or the reduced EA.

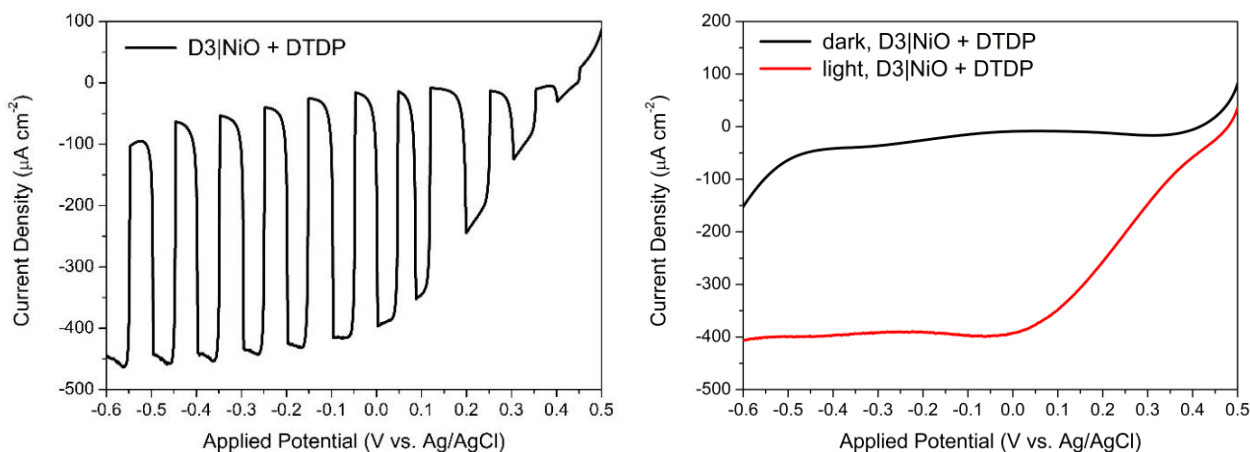


Figure 3.34. Left - LSV of D3|NiO with 5 mM DTDP in 0.1 M phthalate buffer (pH 3) under chopped light illumination with scan rate of 10 mVs^{-1} . Light illumination was applied with 5 s intervals (5 s in the dark / 5 s under illumination); Right - LSV of D3|NiO with 5 mM DTDP in 0.1 M phthalate buffer (pH 3) under constant light illumination (red) and in the dark (black) with scan rate of 10 mVs^{-1} . Light illumination intensity was 1 sun (100 mW cm^{-2}) and electrolyte was degassed under N_2 for 15 min. before measurement.

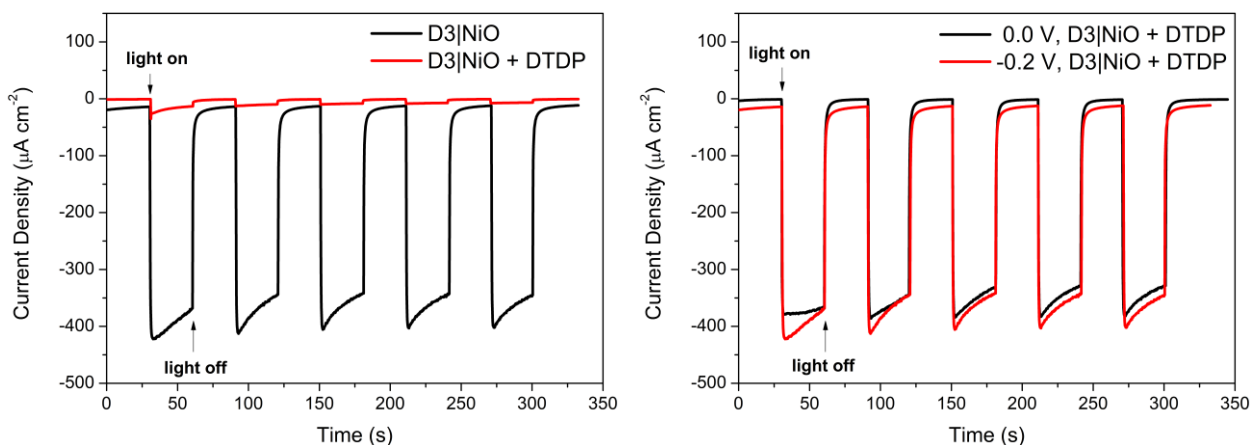


Figure 3.35. Left - CA on D3|NiO with 5 mM DTDP vs. D3|NiO without EA in 0.1 M phthalate buffer (pH 3) and under $E_{appl} = -0.2 \text{ V vs. Ag/AgCl}$. Right - CA on D3|NiO with 5 mM DTDP under $E_{appl} = -0.2 \text{ V}$ and $E_{appl} = 0.0 \text{ V vs. Ag/AgCl}$. Light illumination was applied with 30 s intervals (30 s in the dark / 30 s under illumination). Light illumination intensity was 1 sun (100 mW cm^{-2}) and electrolyte was degassed under N_2 for 15 min. before measurement.

The concentration dependence study with $[\text{Co}(\text{en})_3]\text{Cl}_3$ in Chapter 3.5.1.2. showed that the photocurrent generation is not limited by the EA concentration even when the concentration of the $[\text{Co}(\text{en})_3]\text{Cl}_3$ was increased to 50 mM. In case of DTDP EA, this could not be checked due to the low solubility of the EA, which is limited to 5 mM in aqueous

electrolyte. However, it can be hypothesised, that with an EA with similar structure and reduction potential but a higher solubility in water, considerably higher photocurrents could be achieved with higher concentrations of the EA. In addition, this knowledge is useful when choosing a suitable H_2 evolution catalyst which could be able to drive an efficient H^+ reduction reaction under similar experimental conditions.

3.5.3.3 Stability study of D3|NiO

During PEC measurements it was observed that even if there is no EA or catalyst in the system and the photocathode has just dye adsorbed on it, there is still a small photocurrent produced during LSV and CA measurements. In a system with EA or catalyst, when the dye-sensitised photocathode is illuminated by the light and the electrons are excited to an excited state then these electrons are either reducing the EA or catalyst, or recombine with the holes in the NiO. When there is no EA or catalyst, then the electrons can only recombine, but this should not give a photocurrent response during the PEC measurements. Therefore, the most probable reason for this photocurrent is the decomposition of the dye during light illumination. This has also been discussed previously in literature regarding dye-sensitised systems for photocatalysis.¹⁶ To understand the origin of this photocurrent when there is no EA or catalyst, a CA measurement was carried out on D3|NiO under constant light illumination (100 mW cm^{-2}) for 1 h and UV-vis spectra of the photocathode was collected before and after the measurement.

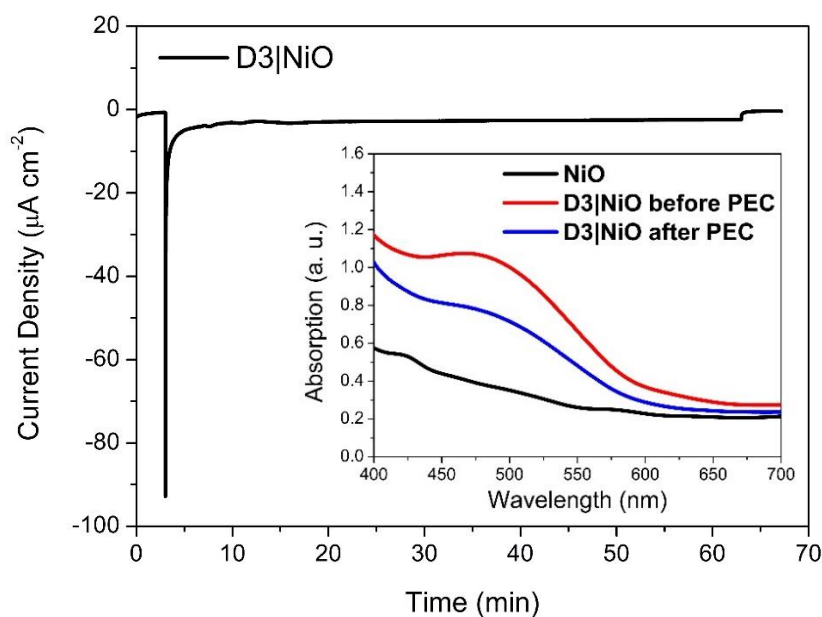


Figure 3.36. CA of D3|NiO under $E_{appl} = -0.2 \text{ V}$ vs. Ag/AgCl in pH 5 0.1 M acetate buffer under constant light illumination. Light illumination intensity was 1 sun (100 mW cm^{-2}) and

electrolyte was degassed under N₂ for 15 min. before measurement. Inset – UV-vis spectra of D3|NiO before CA (red) and after CA (blue), bare NiO UV-vis spectrum (black) is added for reference.

The results showed that in the beginning of the CA when light illumination was applied, there was a very high transient photocurrent of *ca.* 93 $\mu\text{A cm}^{-2}$ which reduced rapidly to *ca.* 3 $\mu\text{A cm}^{-2}$ and kept slowly decreasing during the whole measurement (Figure 3.36) The photocurrent recorded in the end of the measurement was *ca.* 2 $\mu\text{A cm}^{-2}$. More importantly the comparison of the UV-vis results of D3|NiO before and after the CA showed clearly a considerable decrease in D3 absorbance (Figure 3.36, Inset). This shows that the dye decomposes during the measurement and indicates that the photocurrent generated during the time the photocathode is under light illumination originates from the dye decomposition. This result can also be used to explain the photocurrents generated by other dye-sensitised photocathodes without EA or catalyst during light illumination, something we observed also for D2|NiO photocathode (Figure 3.21 in Chapter 3.5.2).

3.5.3.4 *H₂ evolution on D3|NiO photocathode with electrodeposited catalysts*

The final part of the study with D3|NiO photocathode was to test the system for H₂ evolution using the best experimental conditions determined in the previous steps of the study. This time, instead of the EA we used an electrodeposited Pt and NiMoS (nickel molybdenum sulphide) catalyst on the D3|NiO to drive the proton reduction half reaction. Catalyst deposition was carried out according to the instructions in Chapter 2.2.8. NiMoS catalyst deposition was adapted from the recent work from T. J. Meyer and co-workers, where they showed H₂ evolution on dye-sensitised NiO photocathode with NiMoS catalyst electrodeposited on the surface.³⁷

First, the chopped light CA (Figure 3.37, left) and LSV in the dark and under light illumination (Figure 3.37, right) was carried out on Pt|D3|NiO. The chopped light CA was conducted under $E_{\text{appl}} = -0.2$ V vs Ag/AgCl and it showed stable photocurrents of *ca.* 10 $\mu\text{A cm}^{-2}$ with small transient spikes when the light illumination was applied. The LSV of Pt|D3|NiO showed a steady photocurrent of approximately 15 $\mu\text{A cm}^{-2}$ during the cathodic sweep until *ca.* $E_{\text{appl}} = -0.35$ V, until there was a sharp increase in dark current related to the H₂ evolution on Pt (Figure 3.37, right and Figure 3.40, left).

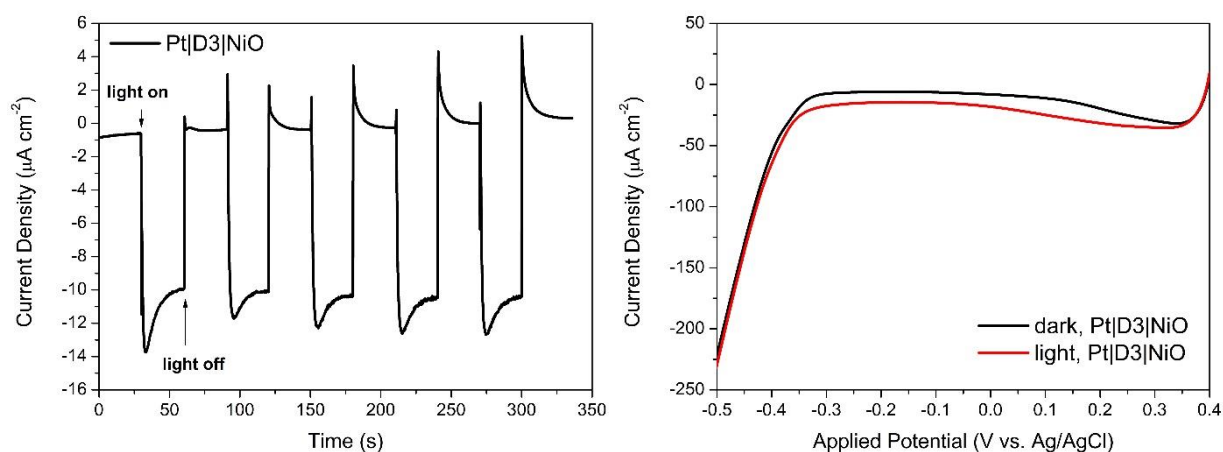


Figure 3.37. Left - CA of Pt|D3|NiO under $E_{appl} = -0.2$ V vs Ag/AgCl in 0.1 M phthalate buffer (pH 3). Right – LSV of Pt|D3|NiO in 0.1 M phthalate buffer (pH 3), scan rate 10 mV s^{-1} , under light illumination (red) and in the dark (black). Light illumination intensity was 1 sun (100 mW cm^{-2}) and electrolyte was degassed under N_2 for 15 min. before measurement.

The CA was measured under $E_{appl} = -0.2$ V vs. Ag/AgCl for Pt|D3|NiO and under $E_{appl} = -0.3$ V vs. Ag/AgCl for NiMoS|D3|NiO. Measurement was carried out under constant 1 sun (100 mW cm^{-2}) light illumination for 1 h. The PEC cell used was a one compartment custom made glass cell, with Pt|D3|NiO|FTO working electrode (WE), Pt|FTO counter electrode (CE) and Ag/AgCl reference electrode (3.0 M NaCl).

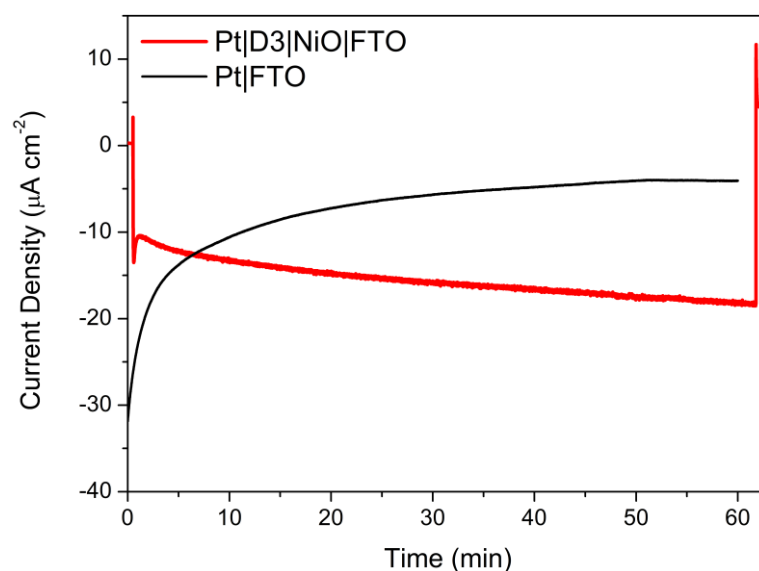


Figure 3.38. CA of Pt|D3|NiO (red) under constant light illumination and under $E_{appl} = -0.2$ V vs. Ag/AgCl in 0.1 M phthalate buffer (pH 3). CA of Pt on FTO under -0.3 V vs. Ag/AgCl (black) is added for reference. Light illumination intensity was 1 sun (100 mW cm^{-2}) and electrolyte was degassed under N_2 for 15 min. before measurement.

A control measurement was carried out under the same conditions for Pt|FTO electrode under illumination to show that the H₂ evolution only occurs due to dye interaction with the photons through which the excited state electrons are created and followed by charge transfer to the surface of the catalyst, where the proton reduction occurs. H₂ evolution was quantified using Gas Chromatography (GC) during which the gas from the headspace of the PEC cell was analysed after the CA measurement.

After 1 h of CA measurement, the gas from the PEC cell's headspace was analysed with GC and H₂ evolution was detected when Pt|D1|NiO was measured under constant light illumination. The photocurrent measured during the experiment was *ca.* 10 $\mu\text{A cm}^{-2}$ in the beginning of the measurement increasing to 20 $\mu\text{A cm}^{-2}$ after 1 h of light illumination (Figure 3.38). Volume of H₂ evolved was 87 ± 2 nmol and Faradaic efficiency of 39 ± 1 % was calculated. The low somewhat low Faradaic efficiency indicates that there are losses in the system. The low efficiency could be due to the recombination of H₂ and O₂ in the cell since there was no membrane between the anode and the cathode. It could also be due to the analysis technique, which enables loss of gas during the injection and transport of gas in a GC syringe.

It is also probable that part of the losses happens due to the decomposition of the dye on the surface of the photocathode, because the charge transport process of excited electrons from the dye to the catalyst is not efficient enough. The increasing current during the measurement is also an indication of another underlying process happening during the light illumination which could be related to photocorrosion. Since the increase in photocurrent was not observed when EA was used with the same photocathode, the reason of this behaviour must be the Pt catalyst on the surface of the electrode. It indicates that the charge transfer from the dye to the surface of the catalyst depends on the time the electrode is exposed to light. Most probable process happening is the dye decomposition during the light illumination and that was also shown during the stability study in Chapter 3.5.3.3.

Finally, the H₂ evolution was tested with a different catalyst, nickel molybdenum sulphide (NiMoS). First, the LSV was measured on the NiMoS|D3|NiO under light illumination and in the dark (Figure 3.39). It showed increasing photocurrent when negative applied potential was increased and also an increase in dark current starting from -0.35 V vs. Ag/AgCl.

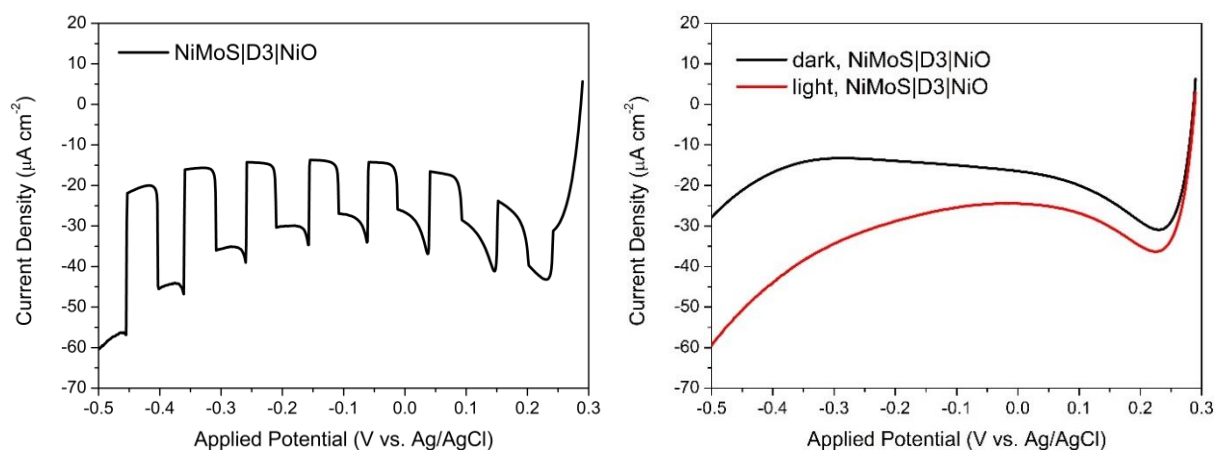


Figure 3.39. Left - LSV of NiMoS|D3|NiO in 0.1 M phthalate buffer (pH 3) under chopped light illumination with scan rate of 10 mVs^{-1} . Light illumination was applied with 5 s intervals (5 s in the dark / 5 s under illumination); Right - LSV of NiMoS|D3|NiO in 0.1 M phthalate buffer (pH 3) under constant light illumination (red) and in the dark (black) with scan rate of 10 mVs^{-1} . Light illumination intensity was 1 sun (100 mW cm^{-2}) and electrolyte was degassed under N_2 for 15 min. before measurement.

To detect and quantify H_2 evolution a CA measurement under constant light illumination was carried out under $E_{\text{appl}} = -0.3 \text{ V vs Ag/AgCl}$ (Figure 3.40). It showed a large transient spike in photocurrent in the beginning of the experiment, which then stabilised to *ca.* $10 \mu\text{A cm}^{-2}$. However, by the end of the measurement after approximately 80 min constant light illumination, the photocurrent had diminished to $5 \mu\text{A cm}^{-2}$. After the CA measurement, the gas from the PEC cell's headspace was analysed with GC and H_2 evolution was detected. Volume of H_2 evolved was $4.3 \pm 0.2 \text{ nmol}$ and Faradaic efficiency of $2.1 \pm 0.1 \%$ was calculated.

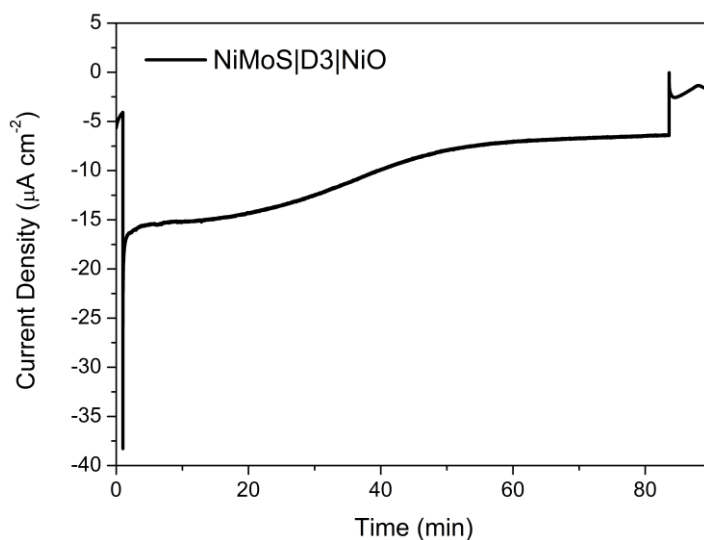


Figure 3.40. CA of NiMoS|D3|NiO (red) under constant light illumination and under $E_{\text{appl}} = -0.2 \text{ V vs Ag/AgCl}$ in 0.1 M phthalate buffer (pH 3). Light illumination intensity was 1 sun (100 mW cm^{-2}) and electrolyte was degassed under N_2 for 15 min. before measurement.

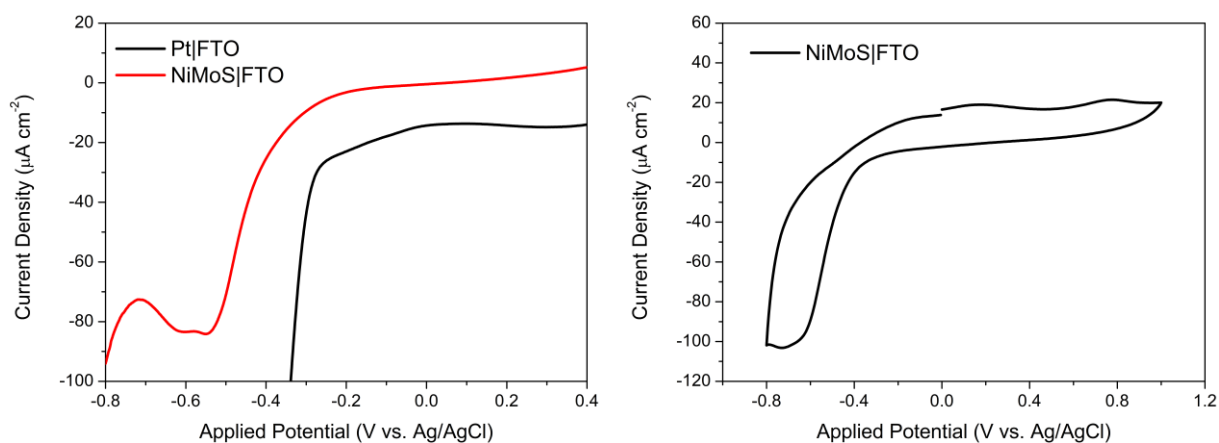


Figure 3.41. Left – LSV of Pt (black) and NiMoS (red) on FTO in 0.1 M phthalate buffer (pH 3), scan rate 10 mV s^{-1} . Right – CV of NiMoS on FTO, scan rate was 50 mV s^{-1} . Electrolytes were degassed under N_2 for 15 min. before measurement.

The very low Faradaic efficiency and H_2 yield is most probably due to photocorrosion of the photocathode of which part would be the decomposition of the dye and part the reduction of the catalyst. Since the NiMoS catalyst overpotential is *ca.* $-0.7 \text{ V vs. Ag/AgCl}$ (*ca.* -0.5 vs NHE , Figure 3.41, left, red), the driving force for electron transfer, ΔG_{et} , from the reduced dye D3 to the NiMoS catalyst should be sufficient for efficient charge transfer to occur (Figure 3.42). However, this is not reflected in the photocurrent. The modest photocurrent suggests that excited electrons, instead of being transferred to the catalyst, decompose the dye. This process was shown to happen in Chapter 3.5.3.3. when there is no EA or catalyst in solution or on the photocathode. In addition, there is a reduction process on the NiMoS at more positive potential than the H_2 evolution overpotential, which most probably consumes also the electrons which otherwise would be driving the H_2 evolution. These two processes combined would result in substantial losses in the system and the photocorrosion of the photocathode which is also evident in the CA profile in Figure 3.40, where the photocurrent considerably decreases during the measurement under light illumination.

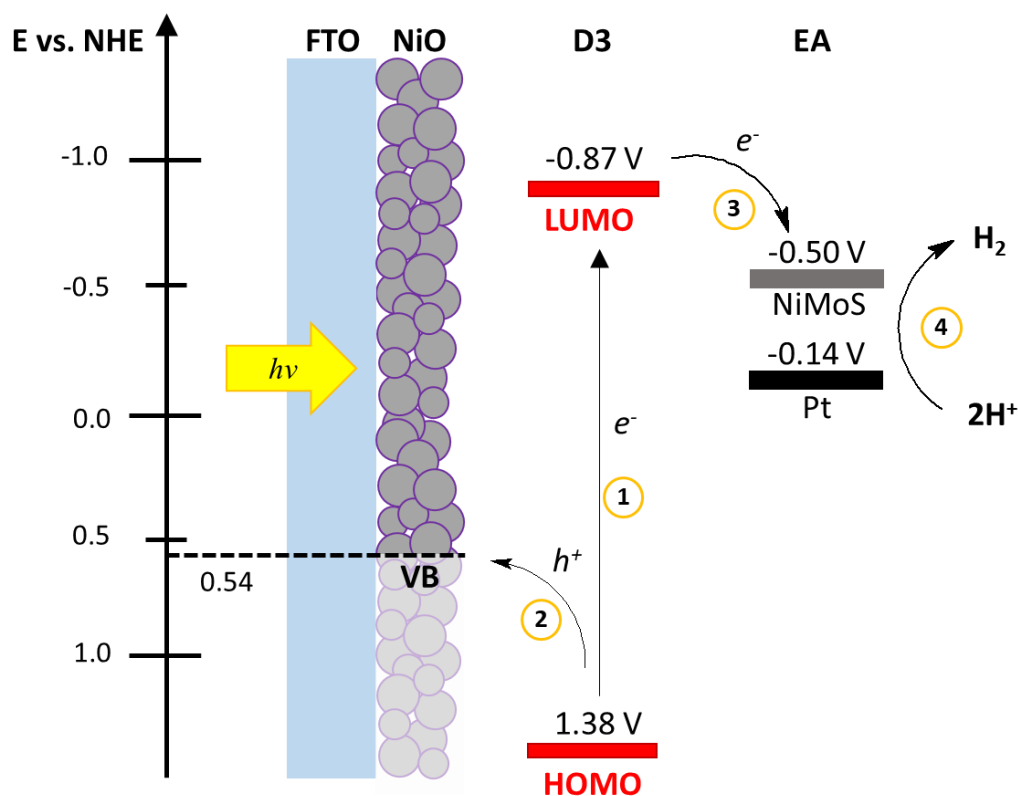


Figure 3.41. Schematics of the Pt|D3|NiO and NiMoS|D3|NiO photocathode working principle. When light illumination is applied to the dye-sensitised photocathode, electron is excited from its ground state in HOMO to an excited state in LUMO (1), this leaves a positively charged hole, h^+ , which is then injected from the dye to the valence band, VB, of NiO (2). Excited electrons with higher energy in LUMO of the dye are then transferred to the surface of the Pt catalyst (3) where the H_2 evolution is catalysed (4). Values for HOMO and LUMO of D3 are reported previously in literature.³⁵ Value for overpotential required for the Pt and NiMoS catalyst to drive H_2 evolution reaction was estimated from Figure 3.41 (left).

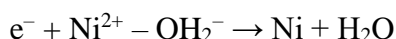
3.6 General discussion

Kaeffer et al. attributed the low yield of H_2 (8-10%) to the occurrence of NiO reduction to Ni^0 in the electrode.²⁶ In Chapter 4 of this thesis, the dye-sensitised NiO electrodes have been analysed post-catalysis using X-ray Photoelectron Spectroscopy (XPS) and no Ni^0 was detected. It is not surprising as NiO reduction by H_2 usually requires elevated temperatures and is hindered by the presence of water.^{38,39} Therefore, it is important to consider the mechanism at the electrode surface. Dare-Edwards et al. have presented the electrochemistry and photoelectrochemistry of NiO in detail.⁴⁰ A summary is as follows. As-prepared NiO is non-stoichiometric and Ni vacancies are present at 0.6 eV and 0.8 eV above the Ni 3d⁸ band, and these deep traps pin the Fermi level. The two features present in the

cyclic voltammetry of NiO (presented on Figure 3.14 for our electrode) at 0.6 V vs. Ag/AgCl and 1.2 V vs. Ag/AgCl at pH 0 are associated with oxidising Ni²⁺ to Ni³⁺ at the surface.



Two features are observed due to the different locations of the Ni²⁺ at the surface and the proximity to other Ni³⁺ sites. The onset for photoelectrochemical H₂ production in Li-doped NiO in 0.5 M H₂SO₄ occurs at -0.2 V vs. Ag/AgCl. This is associated with the tunnelling of holes from the surface to trap states in the bulk (which lie close to the Fermi level). Following excitation, electrons migrate to the surface where they can either reduce Ni²⁺ to Ni⁰ or reduce H⁺ to H₂.



(followed by dissolution of Ni in acidic solution, pH 1).

Or



The interpretation of the cathodic current at applied potentials more negative than 0.4 V vs. Ag/AgCl, is complicated by a slow process which is associated with the filling of the two sets of surface states. Between -0.4 and +0.5 V vs. Ag/AgCl, the photocurrent is limited by fast recombination between the electrons and holes mediated by the surface states. Below 0 V vs. NHE these states are intermediates in the H₂ evolution reaction. The reduced species can be re-oxidised by holes tunnelling to the valence band at the surface, thereby reducing the cathodic photocurrent. At more negative potentials than -0.4 V vs. Ag/AgCl the surface states are filled, and no parasitic recombination occurs.

The behaviour of NiO-based p-DSCs is consistent with this interpretation, but the working principle of the system is different. In the dye-sensitised NiO the electrons are promoted to a higher energy level within the dye, when the light illumination is applied to the photocathode and the NiO is oxidised via hole injection from the dye to the valence band of the NiO (Figure 3.41). Fill factors are typically low (0.3-0.4), which is consistent with a

parasitic recombination reaction.⁴¹ It has been shown that the reduction of iodide to triiodide is promoted at the surface of NiO and D'Amario et al. showed that there is a high density of trap states close to the Fermi level which are associated with charge-recombination.^{42,43} Annealing NiO to remove the defects, the Ni³⁺ impurities, increases the voltage but reduces the photocurrent.⁴⁴ Charge-recombination between the reduced dye molecules and holes in the NiO is known to be extremely fast in p-DSCs (charge lifetimes are on the order of ps for Dye⁻|NiO⁺ compared to μs for Dye⁺|TiO₂⁻). Unlike TiO₂ n-DSCs where the maximum photocurrent is at short-circuit, the photocurrent continues to rise when a negative bias is applied to NiO p-DSCs. This is consistent with filling the surface states and reducing charge-recombination. It has been observed that an increase in the charge-separated state lifetime occurs in the presence of I⁻/I₃⁻ where it would be expected to decrease as the charge on the dye is intercepted by the acceptor in the electrolyte.⁴⁵ This has been attributed to the I₂⁻ in the electrolyte reducing Ni³⁺ at the oxide surface.

The reported Faradaic efficiency of photocathodes for H₂ evolution vary from <10% to >100%, even though the photocurrent density tends to be within a similar order of magnitude. This discrepancy is intriguing, considering that two electrons are required in the catalytic step, provided by consecutive one-electron transfer steps from the dye. An alternative interpretation could be that the photocurrent recorded is not directly associated with catalysis. Rather than a mechanism which proceeds by electron transfer from NiO to the dye and then to the catalyst (or directly to H⁺ in the example by Tong et al.⁹), which is typically proposed in the field, there could be an alternative explanation.^{8,16,26,27,32} It is possible that rather than reducing the catalyst, some of the reduced dye molecules are rapidly re-oxidised by recombination with a surface state, consistent with spectroscopic measurements described by Smeigh et al. and D'Amario et al.^{42,46} The reduced species formed at the surface are responsible for the hydrogen evolution reaction, consistent with Dare-Edwards et al.'s mechanism for direct photoelectrochemical hydrogen evolution with NiO. This mechanism is consistent with the broad range of Faradaic efficiencies listed in the introduction. If the "missing" photocurrent was consumed in the formation of Ni⁰ and/or dissolution of the electrode, we would expect this to be a general limitation of NiO photocathodes.

In addition to this explanation for the low Faradaic efficiency, another explanation is the decomposition of the dye on the NiO surface when the electron transfer process from the reduced dye to the catalyst is inefficient. This was shown in Chapter 3.5.3.3., where the UV-vis of D3|NiO was taken before and after the CA measurement where there was no EA or catalyst in the system and it was clearly visible from the results that the dye had decomposed

on the surface resulting in a considerable reduction in the dye absorption. It can be reasoned that this process of dye decomposition would occur in a system with catalyst whenever the charge transfer to the catalyst is inefficient. Additional contributing factor to the dye decomposition could be the conversion of dissolved O₂ to peroxide, which would decompose the dye. In future studies, the electrolyte after PEC measurements could be tested to detect if peroxide has formed and membrane can be used to keep the formed peroxide from contact with the dye-sensitised photocathode.

Finally, the Faradaic efficiency of the H₂ evolution can also be lowered by the recombination of evolved H₂ with the O₂ in the cell produced on the anode. In our case, this is most probably one of the contributing processes to the lower efficiency since there was no membrane in the cell between the anode and the cathode, which would prevent the recombination.

3.7. Conclusions

In this Chapter, NiO as the benchmark p-type semiconductor for dye-sensitised PEC H₂ evolution was studied from the perspective of the experimental conditions and the experimental environment, the dye and the catalyst. Three different dye-sensitised NiO photocathodes were studied with different dyes using EAs in solution to measure the photocurrent generation or electrodeposited catalysts on the surface of the photocathode to test the systems for H₂ evolution.

During the first part of the study, the effect of the experimental environment to the photoelectrochemical performance of the dye-sensitised NiO photocathode with D1 robust organic dye was thoroughly studied. Different EAs, different concentration of the EA, changes to the electrolyte composition and changes to the pH of the electrolyte was used to understand the effect of those parameters to the photocurrent generation on the photocathode. It was derived from the results that the optimal conditions for photocurrent generation in aqueous electrolyte were achieved with highest photocurrents when the DTDP EA in in pH 3 0.1 M phthalate buffer was used. The DTDP has the most positive reduction potential of the stable EA used, which also results in the highest driving force for the electron transfer, ΔE_{et} , from the reduced dye to the EA (Figure 3.4). This is most probably one of the leading factors of the highest photocurrent achieved with the DTDP EA. It was also shown that there is a correlation between the ΔE_{et} and the photocurrent, showing higher photocurrents for EAs with

larger ΔE_{et} (Figure 3.4). The limitation of that system was the low solubility of DTDP in water. However, a concentration study with a different EA, with considerably higher solubility in water showed that the diffusion of the EA out of the pores of the nanostructured NiO is not a limiting factor for the system. This is an indication that considerably higher photocurrents can be expected for a system with a right catalyst. Studies with electrolyte mixtures of acetonitrile and water showed, that by increasing the acetonitrile concentration in the electrolyte, the photocurrents increase considerably. It was reasoned that this could be due to higher diffusion coefficient of acetonitrile and EA in acetonitrile. The studies with different pH of the electrolyte with EA showed that highest photocurrents with D1|NiO were obtained in electrolyte with pH 3. This condition was therefore chosen also for further studies with different photocathodes. Finally, H₂ evolution was confirmed from D1|NiO photocathode with electrodeposited Pt catalyst on the surface. The Faradaic efficiency was, however, low for the process and it was reasoned that this could be due to decomposition of the dye on the surface and also because of the recombination of evolved H₂ with dissolved O₂ in the cell since the PEC cell used in this study had no proton exchange membrane.

During the second and third part of the study, the NiO electrode was tested with two different dyes. One of which was an organic dye D2 with a polymeric structure and another one a benchmark commercially available organic dye D3, which has shown to work for H₂ evolution in dye-sensitised systems. The D2 dye produced reasonable photocurrents with EAs, but failed to give any serious results when H₂ evolution was measured with Pt catalyst. Negligible amounts of H₂ was detected, but the most of the photocurrent generated was attributed to the decomposition of the dye during the PEC measurement. It was reasoned that due to the positive LUMO level of the dye, the driving force for the electron transfer from the reduced dye to the catalyst was not efficient enough to overcome the dye decomposition process.

The D3 dye however, showed the highest photocurrents of all three systems with the DTDP EA and optimal conditions determined in the first part of the study (pH 3 electrolyte). In addition, H₂ evolution was confirmed with the Pt catalyst electrodeposited on the electrode surface and the Faradaic efficiency was calculated to be close to 40 %. Therefore, it can be concluded that of the three systems studied, the D3|NiO performed the best with highest photocurrents and also the highest efficiency for H₂ evolution. The Faradaic efficiency, however, was far from ideal and therefore it was reasoned that considerable losses still take place due to the poor electron transfer from the excited dye to the catalyst resulting in partial decomposition of the dye.

In the following chapter (Chapter 4) the dye-sensitised photocathodes for H₂ evolution were developed further using the knowledge learned from the projects discussed in this chapter. The main focus was to see, if the efficiency of the H₂ evolution is increased by using an integrated photocatalysts instead of separate dye and catalyst on the surface of the semiconductor nanoparticles. Two photocatalysts were tested with NiO under similar optimised conditions developed in this Chapter and extra care was put on the post-catalysis characterisation of the photocatalysts with advanced surface characterisation techniques. This was to understand if the photocatalysts decompose during the PEC measurements and if so, in what extent and what are the decomposition products.

References

- 1 K. Fan, F. Li, L. Wang, Q. Daniel, E. Gabrielsson and L. Sun, *Phys. Chem. Chem. Phys.*, 2014, 16, 25234–25240.
- 2 J. He, H. Lindström, A. Hagfeldt and S. Lindquist, *J. Phys. Chem. B*, 1999, 103, 8940–8943.
- 3 J. He, H. Lindström, A. Hagfeldt and S.-E. Lindquist, *Sol. Energy Mater. Sol. Cells*, 2000, 62, 265–273.
- 4 C. Y. Lee, H. S. Park, J. C. Fontecilla-Camps and E. Reisner, *Angew. Chem., Int. Ed.*, 2016, 55, 5971–5974.
- 5 D. Mersch, C. Y. Lee, J. Z. Zhang, K. Brinkert, J. C. Fontecilla-Camps, A. W. Rutherford and E. Reisner, *J. Am. Chem. Soc.*, 2015, 137, 8541–8549.
- 6 B. Shan, A. K. Das, S. Marquard, B. H. Farnum, D. Wang, R. M. Bullock and T. J. Meyer, *Energy Environ. Sci.*, 2016, 9, 3693–3697.
- 7 J. J. Leung, J. Warnan, D. H. Nam, J. Z. Zhang, J. Willkomm, E. Reisner, *Chem. Sci.*, 2017, 56, 510–514.
- 8 L. Li, L. Duan, F. Wen, C. Li, M. Wang, A. Hagfeldt and L. Sun, *Chem. Commun.*, 2012, 48, 988–990.
- 9 L. Tong, A. Iwase, A. Nattestad, U. Bach, M. Weidelener, G. Götz, A. Mishra, P. Bäuerle, R. Amal, G. G. Wallace and A. J. Mozer, *Energy Environ. Sci.*, 2012, 5, 9472.
- 10 Z. Ji, M. He, Z. Huang, U. Ozkan and Y. Wu, *J. Am. Chem. Soc.*, 2013, 135, 11696–11699.
- 11 P. B. Pati, L. Zhang, B. Philippe, R. Fernandez-Teran, Ahmadi, L. Tian, H. Rensmo, L. Hammarström and H. Tian, *ChemSusChem*, 2017, 10, 2480–2495.
- 12 M. A. Gross, C. E. Creissen, K. L. Orchard and E. Reisner, *Chem. Sci.*, 2016, 7, 242–247.
- 13 R. J. Kamire, M. B. Majewski, W. L. Hoffeditz, B. T. Phelan, O. K. Farha, J. T. Hupp and M. R. Wasielewski, *Chem. Sci.*, 2017, 8, 541–549.

- 14 G. Boschloo and A. Hagfeldt, *J. Phys. Chem. B*, 2001, 105, 3039–3044.
- 15 A. M. Brown, L. J. Antila, M. Mirmohades, S. Pullen, S. Ott and L. Hammarström, *J. Am. Chem. Soc.*, 2016, 138, 8060–8063.
- 16 C. E. Castillo, M. Gennari, T. Stoll, J. Fortage, A. Deronzier, M.-N. Collomb, M. Sandroni, F. Legalite, E. Blart, Y. Pellegrin, C. Delacote, M. Boujtita, F. Odobel, P. Rannou and S. Sadki, *J. Phys. Chem. C*, 2015, 119, 5806–5818.
- 17 A. M. Lapedes, B. D. Sherman, M. K. Brennaman, C. J. Dares, K. R. Skinner, J. L. Templeton and T. J. Meyer, *Chem. Sci.*, 2015, 6, 6398–6406.
- 18 D. W. Kim, S. C. Riha, E. J. DeMarco, A. B. F. Martinson, O. K. Farha and J. T. Hupp, *ACS Nano*, 2014, 8, 12199–12207.
- 19 D. Adler, J. Feinleib. *Phys. Rev. B*. 1970, 2, 3112-3134.
- 20 S. Sumikura, S. Mori, S. Shimizu, H. Usami and E. Suzuki, *J. Photochem. Photobiol. A Chem.*, 2008, 199, 1–7.
- 21 E. A. Gibson, *Chem. Soc. Rev.*, 2017, 46, 6194.
- 22 J. R. Swierk and T. E. Mallouk, *Chem. Soc. Rev.*, 2013, 42, 2357–2387.
- 23 L. Francas, C. Richmond, P. Garrido-Barros, N. Planas, S. Roeser, J. Benet-Buchholz, L. Escriche, X. Sala and A. Llobet, *Chem. - A Eur. J.*, 2016, 22, 5261–5268.
- 24 T. Kowacs, Q. Pan, P. Lang, L. O'Reilly, S. Rau, W. R. Browne, M. T. Pryce, A. Huijser and J. G. Vos, *Faraday Discuss.*, 185, 2015. DOI:10.1039/C5FD00068H.
- 25 C. Y. Lee, H. S. Park, J. C. Fontecilla-Camps and E. Reisner, *Angew. Chemie - Int. Ed.*, 2016, 55, 5971–5974.
- 26 N. Kaeffer, J. Massin, C. Lebrun, O. Renault, M. Chavarot-Kerlidou and V. Artero, *J. Am. Chem. Soc.*, 2016, 138, 38, 12308-12311.
- 27 G. H. Summers, J-F Lefebvre, F. A. Black, E. S. Davies, E. A. Gibson, T. Pullerits, C. J. Wood, K. Zidek. *Phys. Chem. Chem. Phys.*, 2016, 18, 1059.
- 28 J. Massin, M. Brautigam, N. Kaeffer, N. Queyriaux, M. J. Field, F. H. Schacher, J. Popp, M. Chavarot-Kerlidou, B. Dietzek and V. Artero, *Interface Focus*, 2015, 5, 20140083.

- 29 S. Powar, T. Daeneke, M. T. Ma, D. Fu, N. W. Duffy, G. Götz, M. Weidener, A. Mishra, P. Bäuerle, L. Spiccia, U. Bach. *Angew. Chem. Int. Ed.* 2013, 52, 602–605.
- 30 I. R. Perera, T. Daeneke, S. Makuta, Ze. Yu, Y. Tachibana, A. Mishra, P. Bäuerle, C. A. Ohlin, U. Bach, L. Spiccia. *Angew. Chem. Int. Ed.* 2015, 54, 3758–3762.
- 31 V. Huss, I. L. Chevalier and A. M. Siouffi, *Journal of Chromatography*, 500 (1990) 241-255.
- 32 K. A. Click, D. R. Beauchamp, Z. Huang, W. Chen and Y. Wu, *J. Am. Chem. Soc.*, 2016, 138, 1174–1179.
- 33 C. J. Wood, G. H. Summers, C. A. Clark, N. Kaeffer, M. Braeutigam, L. R. Carbone, L. D’Amario, K. Fan, Y. Farre’, S. Narbey, F. Oswald, L. A. Stevens, C. D. J. Parmenter, M. W. Fay, A. L. Torre, C. E. Snape, B. Dietzek, D. Dini, L. Hammarström, Y. Pellegrin, F. Odobel, L. Sun, V. Artero, E. A. Gibson. *Phys. Chem. Chem. Phys.* 2016, 18, 10727.
- 34 N. Kaeffer, C. D. Windle, R. Brisse, C. Gablin, D. Leonard, B. Jousset, M. Chavarot-Kerlidou and V. Artero, *Chem. Sci.*, 2018, 9, 6721–6738.
- 35 P. Qin, H. Zhu, T. Edvinsson, G. Boschloo, A. Hagfeldt, L. Sun, *J. Am. Chem. Soc.*, 2008, 130, 8570-8571.
- 36 L. Li, E. Gibson, P. Qin, G. Boschloo, M. Gorlov, A. Hagfeldt, L. Sun, *Adv. Mater.*, 2010, 22, 1759-1762.
- 37 B. Shan, A. Nayak, R. N. Sampaio, M. S. Eberhart, L. Troian-Gautier, M. K. Brennaman, G. J. Meyer, T. J. Meyer. *Energy Environ. Sci.*, 2018, 11, 447.
- 38 B. Janković, B. Adnađević and S. Mentus, *Chem. Eng. Sci.*, 2008, 63, 567–575.
- 39 A. F. Benton and P. H. Emmett, *J. Am. Chem. Soc.*, 1924, 46, 2728–2737.
- 40 B. Y. M. P. Dare-edwards, A. Hamnett and N. D. Nicholson, *Inorg. Chem.*, 1981, 6 43–661.
- 41 F. Odobel, Y. Pellegrin, E. A. Gibson, A. Hagfeldt, A. L. Smeigh and L. Hammarström, *Coord. Chem. Rev.*, 2012, 4, 2551–2564.
- 42 L. D’Amario, L. J. Antila, B. Pettersson Rimgard, G. Boschloo and L. Hammarström, *J. Phys. Chem. Lett.*, 2015, 6, 779–783.

- 43 L. D'Amario, G. Boschloo, A. Hagfeldt and L. Hammarström, *J. Phys. Chem. C*, 2014, 118, 19556–19564.
- 44 X. L. Zhang, F. Huang, A. Nattestad, K. Wang, D. Fu, A. Mishra, P. Bäuerle, U. Bach and Y.-B. Cheng, *Chem. Commun.*, 2011, 47, 4808–10.
- 45 J-F. Lefebvre, X-Z. Sun, J. A. Calladine, M. W. George, E. A. Gibson. *Chem. Commun.*, 2014, 50, 5258.
- 46 A. L. Smeigh, L. Le Pleux, J. Fortage, Y. Pellegrin, E. Blart, F. Odobel and L. Hammarström, *Chem. Commun.*, 2012, 48, 678–80.

Chapter 4. Photoelectrocatalytic H₂ evolution from integrated photocatalysts adsorbed on NiO

Abstract

A new approach to increasing the faradaic efficiency of dye-sensitised photocathodes for H₂ evolution from water, using integrated photocatalysts, furnished with ester groups on the peripheral ligands, [Ru(decb)₂(bpt)PdCl(H₂O)](PF₆)₂ (1) and [Ru(decb)₂(2,5-bpp)PtI(CH₃CN)](PF₆)₂ (2), (decb = 4,4'-diethylcarboxy-2,2'-bipyridine, bpp = 2,2':5',2''-terpyridine, bpt = 3,5-bis(2-pyridyl)-1,2,4-triazole) is described. Overall, 1|NiO is superior to previously reported photocathodes, producing photocurrent densities of 30–35 μA cm⁻² at an applied bias of -0.2 V vs. Ag/AgCl over 1 hour of continuous white light irradiation, resulting in the generation of 0.41 mmol h⁻¹ cm⁻² of H₂ with faradaic efficiencies of up to 90%. Furthermore, surface analysis of the photocathodes before and after photoelectrocatalysis revealed that the ruthenium bipyridyl chromophore and Pd catalytic centre (1) were photochemically stable, highlighting the benefits of the approach towards robust, hybrid solar-to-fuel devices.

4.1 Introduction

It was demonstrated in the previous chapter that dye-sensitised photocathodes can evolve H₂ under white light irradiation when using electrodeposited catalyst on the surface. But this approach has also several limitations which hinder efficient H₂ production over a longer period of time. One of the limitations of this approach is that when electrodepositing the catalyst on a dye sensitised electrode, the contact between the dye molecules and the catalyst particles might not be sufficient enough to facilitate fast charge transfer without losses due to recombination. NiO photocathodes are limited by the rapid recombination of the reduced dye and the hole in the NiO valence band which reduces the photocatalytic efficiency of these systems, and therefore, the contact between the dye and the catalyst needs to be good enough to facilitate efficient electron transfer from the dye to the catalyst to overcome this recombination process. Obviously, research into ways to increase the photosensitizer efficiency and reduce the non-productive back reaction will be of enormous benefit.^{1,2} In the previous chapter, several dye-sensitised systems were discussed which apply different strategies to overcome these limitations and to drive the H₂ evolution on dye-sensitised photocathodes.³⁻⁹ An alternative approach would be to have the photosensitizer and catalyst

covalently linked. This should enhance the charge transfer between the photosensitizer and the catalyst. An example of this design was published by Kaeffer and coworkers when they demonstrated light-driven H₂ generation on dye-sensitised NiO using a covalently linked dye-catalyst assembly based on cobalt diimine-dioxime catalyst.¹⁰ They were able to show photocurrents up to 15 $\mu\text{A cm}^{-2}$ in pH 5.5 aqueous electrolyte under applied potential of 0.14 V vs RHE and light driven H₂ generation with 10% faradaic efficiency.

As mentioned above, polypyridyl ruthenium(II) complexes have been explored as photosensitisers. The H₂ generating capability of compound 2 (Figure 4.1) has been previously studied by Vos and co-workers in solution (CH₃CN/TEA/H₂O), and a turnover number (TON) of 650 after 6 h irradiation at 470 nm was obtained.¹¹ Analysis of transient absorption (TA) data (Appendix, Article 1. *Work performed by E. A. Gibson*) indicated that the ester ligands on bipyridine lower the energy of the ³MLCT (metal-to-ligand charge transfer) state in which the unpaired spin is located on a peripheral carboxy-bipy ligand. She reasoned that the excited state is long-lived compared to the unsubstituted bipyridine complex perhaps explaining the high TONs achieved for this complex. In this project, H₂ production by 1|NiO and 2|NiO in dye-sensitised PEC's was confirmed under two different applied potentials, E_{appl} = -0.4 V and -0.2 V vs. Ag/AgCl, thereby avoiding the need for sacrificial agents. The performance and stability of the photocathodes are discussed below.

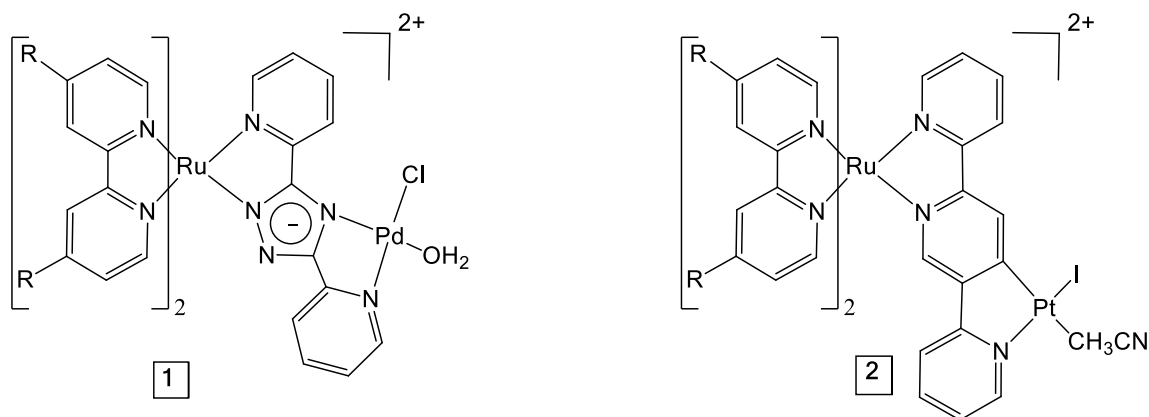


Figure 4.1. The structures of the dye-catalyst assemblies 1 and 2 (R = CO₂Et).

4.2 Results and discussion

4.2.1 Photocatalyst adsorption

The UV-visible absorption spectra of complexes 1 and 2 dissolved in acetonitrile solution and immobilised on NiO are provided in Fig. 4.2. The spectra are generally broader and blue shifted when compared to homogeneous solution ($I_{\max} = 490$ nm for 1 and 480 nm for 1|NiO, $I_{\max} = 480$ nm for 2 and *ca.* 470 nm for 2|NiO), which is consistent with an electronic interaction between the ground state of the dye and the NiO surface. Time-Dependent Density Functional calculations (TDDFT), conducted by our collaborators from Dublin City University, suggested that a Ru-to-carboxy-bipy charge-transfer transition is responsible for the low-energy absorption maximum (Appendix, Article 1).

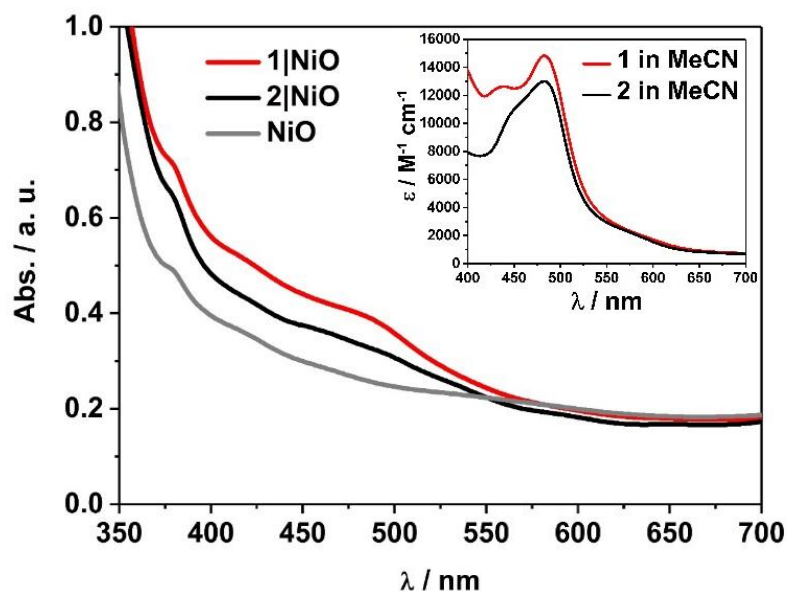


Figure 4.2. UV-vis absorption spectra of 1 (red) and 2 (black) adsorbed on NiO and bare NiO (gray). Inset: UV-vis absorption spectra of 1 (red) and 2 (black) in MeCN (0.028 mM and 0.032 mM, respectively).

The loading of the photocatalyst onto the NiO surface was quantified from the absorption of 1 and 2 on NiO (Fig. 4.2).¹² For 1, assuming that the absorption coefficient does not change substantially on grafting, the photocatalyst loading was 9 nmol cm⁻², and for 2, it was 5.3 nmol cm⁻². These values are reasonably similar, consistent with the similar anchoring system, and are a similar order of magnitude to dye-sensitised photocathodes reported elsewhere.¹⁰ The FTIR spectra (Appendix, Article 1. ESI, *Work performed by E. A. Gibson*) of complexes 1 and 2 in KBr have a carbonyl band at 1724 and 1726 cm⁻¹, respectively, and when the

complexes are immobilised on NiO, the carbonyl bands shift to 1720 cm^{-1} for both complexes. In both cases there is a marginal shift to lower frequency, which could indicate an interaction between the ester and NiO.

4.2.3 Photoelectrochemistry and H_2 evolution

All photoelectrochemical measurements were conducted on the dye-sensitised nanostructured NiO photocathodes using a custom-made three-electrode photoelectrochemical cell (see Figure 2.2 in Chapter 2.3.6). Linear sweep voltammetry (LSV) measurements were carried out on the 1|NiO and 2|NiO electrodes, immersed in aqueous electrolyte solution with 0.1 M KCl. The pH was adjusted with the addition of diluted HCl (pH 1 to pH 7). The potential was swept from $E_{appl} = 0\text{ V}$ to -0.6 V vs. Ag/AgCl for each pH value, under chopped light conditions, during which the samples were irradiated with white light (AM1.5, 100 mW cm^{-2}) over 10 s intervals, under steady-state illumination and in the dark (Figure 4.4). The photocurrent density increased slightly when the pH was raised. This is possibly due to slower charge injection and increased recombination at lower pH.¹³

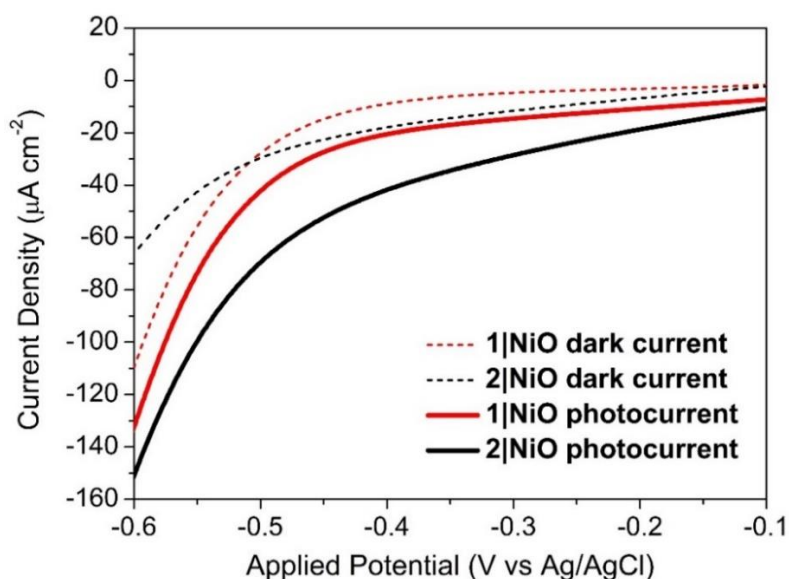


Figure 4.3. LSV of 1|NiO and 2|NiO immersed in aqueous 0.1 M KCl electrolyte (pH 3). The potential was swept from $E_{appl} = 0$ to -0.6 V vs. Ag/AgCl (3.0 M NaCl) in the dark and under simulated light illumination (AM1.5, 100 mW cm^{-2}).

The least acidic environment where H_2 was detected was pH 3 and this was chosen for further experiments. At pH 3, for both 1|NiO and 2|NiO, the photocurrent increased compared to the dark current until $E_{appl} = -0.4\text{ V}$ vs. Ag/AgCl (Figure 4.3). At more negative potentials,

the magnitude of both the dark current and photocurrent density increased considerably. Three potentials were chosen at which to monitor H₂ evolution, $E_{appl} = -0.4$ V vs. Ag/AgCl (ca. -0.01 V vs. RHE), where the photocurrent and dark current were most stable, $E_{appl} = -0.6$ V vs. Ag/AgCl (ca. -0.21 V vs. RHE), and $E_{appl} = -0.2$ V vs. Ag/AgCl (ca. 0.21 V vs. RHE), all of which are lower than the conduction band edge of TiO₂ (i.e. in a tandem PEC device, the bias which will be applied by the photoanode driving the overall water splitting), approximately -0.54 V vs. RHE.^{14,15}

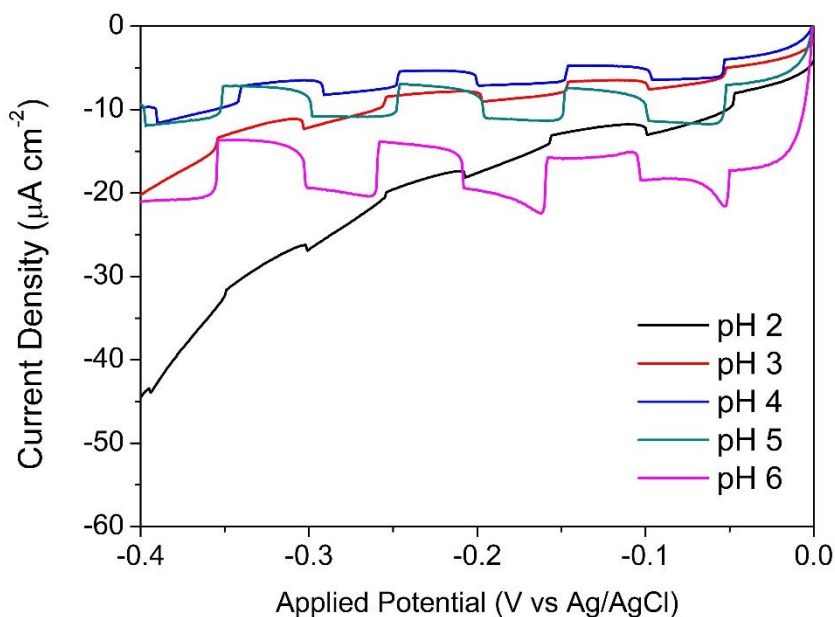


Figure 4.4. LSV measurements on 1|NiO in 0.1 M KCl aqueous electrolytes with additions of HCl to adjust the pH from pH1 to pH 7 under chopped light illumination.

E_{appl} was fixed while the current was measured and Ar was continuously flowed through the electrolyte solution and the exhaust was sampled by in-line GC analysis (see Chapter 2. Methodology). Control experiments were carried out on a bare fluorine-doped tin oxide (FTO) substrate and a non-sensitised NiO|FTO electrode under the same conditions (pH 3 aqueous electrolyte with 0.1 M potassium hydrogen phthalate) to distinguish between the activity of the substrate and the sensitised electrode and to check for any electrochemically active impurities (Figure 4.5). No H₂ or photocurrent was detected during the control measurements with FTO and the current density was considerably lower for the bare electrodes compared to the sensitised electrodes measured under same conditions. However, although no H₂ was detected, a steady increase in photocurrent was observed for the NiO|FTO

sample at $E_{appl} = -0.6$ V. The reason for the increase in photocurrent is possibly a reduction of some Ni^{3+} surface states during illumination with white light.¹⁶

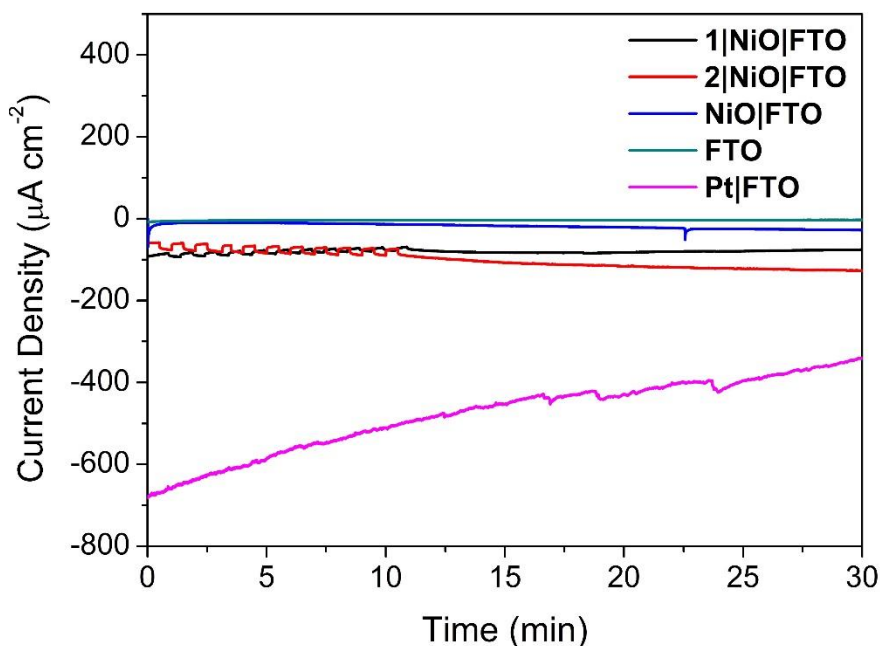


Figure 4.5. Chronoamperometry measurements of 1|NiO, 2|NiO, NiO|FTO, Pt|FTO and bare FTO in pH 3 0.1 M potassium hydrogen phthalate at applied potential of -0.6 V vs. Ag/AgCl reference electrode (3.0 M NaCl). For 1|NiO and 2|NiO chopped light illumination was applied during the first 10 min of the measurement (30 s dark current/30 s photocurrent) followed by constant light illumination.

The trends observed for the photoelectrodes 1|NiO and 2|NiO during the chronoamperometry experiments under chopped light irradiation (Figure 4.6) were consistent with the LSV experiments (Figure 4.3), which is representative of the good reproducibility of the system. For 1|NiO, stable cathodic photocurrents were recorded at $E_{appl} = -0.2$ V ($J_{photo} = ca. 37 \mu A cm^{-2}$) and $E_{appl} = -0.4$ V ($J_{photo} = ca. 44 \mu A cm^{-2}$), over 10 dark/light cycles (Figure 4.5). The dark current recorded during those measurements was negligible compared to the photocurrent and only increased slightly when the more negative potential was applied. For 2|NiO, a significant increase in photocurrent was observed at the more negative bias, $E_{appl} = -0.4$ V ($J_{photo} = ca. 53 \mu A cm^{-2}$) compared to $E_{appl} = -0.2$ V ($J_{photo} = ca. 31 \mu A cm^{-2}$) (Figure 4.6). As for 1|NiO, the dark current was very low compared to the photocurrent. An initial spike in the photocurrent was observed during the chronoamperometry of 2|NiO at $E_{appl} = -0.2$ V and -0.4 V. This rapidly decaying photocurrent is attributed to local capacitance effects, the reduction of the dye-catalyst assembly and/or Ni^{3+} on the surface.^{9,17} Another explanation

could be slow electron transfer from the catalyst to the H^+ or slow diffusion of the products from the pores leading to charge recombination.^{7,9,18} The spike in photocurrent was much less pronounced for 1|NiO which indicates that charge-transfer in the forward direction (e.g. from NiO to the catalyst, to the substrate) is faster than charge-recombination.^{9,17–19} After these initial spikes, the current was stable and the absence of capacitive features after the first on–off cycle suggests that the current is not diffusion limited. The chopped light illumination was followed by a constant white light illumination for up to a 1 h to test the electrode stability (Figure 4.7). A small, steady decrease in photocurrent was observed for both samples under almost all E_{appl} , due to the decrease in active surface area upon bubble formation on the electrode. This behaviour was also observed for a Pt-coated FTO electrode (Figure 4.5) and on shaking the cell, the current was restored. To remove the formed bubbles on the sample surface, the cell was manually shaken in the end of each measurement and additional samples of outlet gas were analysed with GC until no more H_2 was detected.

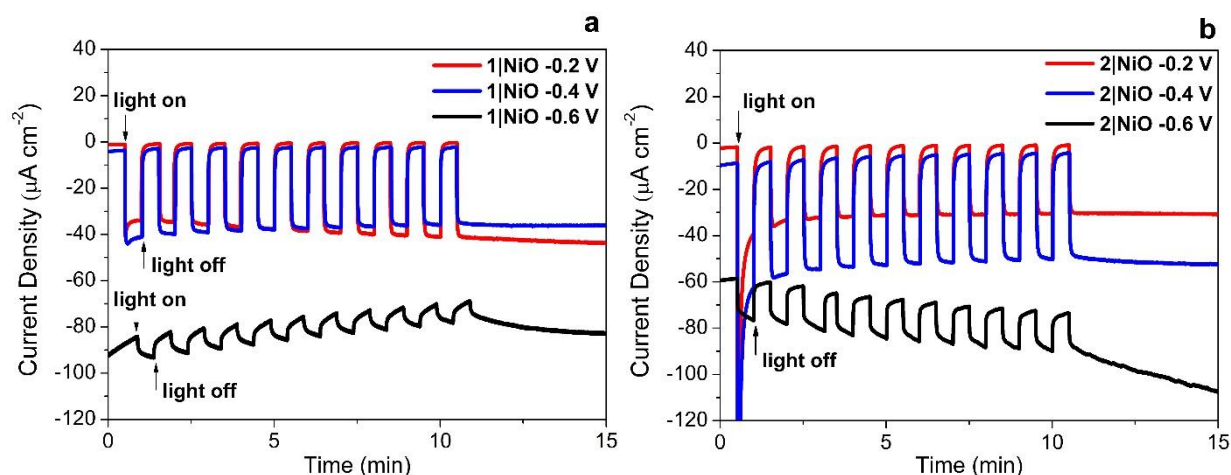


Figure 4.6. Chronoamperometry measurements of 1|NiO (a) and 2|NiO (b) immersed in pH 3 buffer containing 0.1 M potassium hydrogen phthalate. $E_{appl} = -0.2$ V, -0.4 V and -0.6 V vs. Ag/AgCl (3.0 M NaCl). Chopped light illumination was applied with 30 s intervals (10 cycles of dark current / photo-current).

Unlike the photocurrent, the dark current at $E_{appl} = -0.2$ V and $E_{appl} = -0.4$ V did not vary over the duration of the experiment and the magnitude was $< 10\%$ of the total current recorded. At more negative potentials than $E_{appl} = -0.6$ V, more significant changes in current vs. time were observed. A larger dark current ($J_{dark} = 78 \mu A cm^{-2}$) was recorded for 1|NiO (Figure 4.6.a) and 2|NiO (Figure 4.6.b), compared to the previous measurements, which decreased over time. In addition, for 2|NiO, the dark current decreased when the light was switched off and the photocurrent increased when light was turned on. This is an indication of changes occurring on the electrode surface during irradiation.

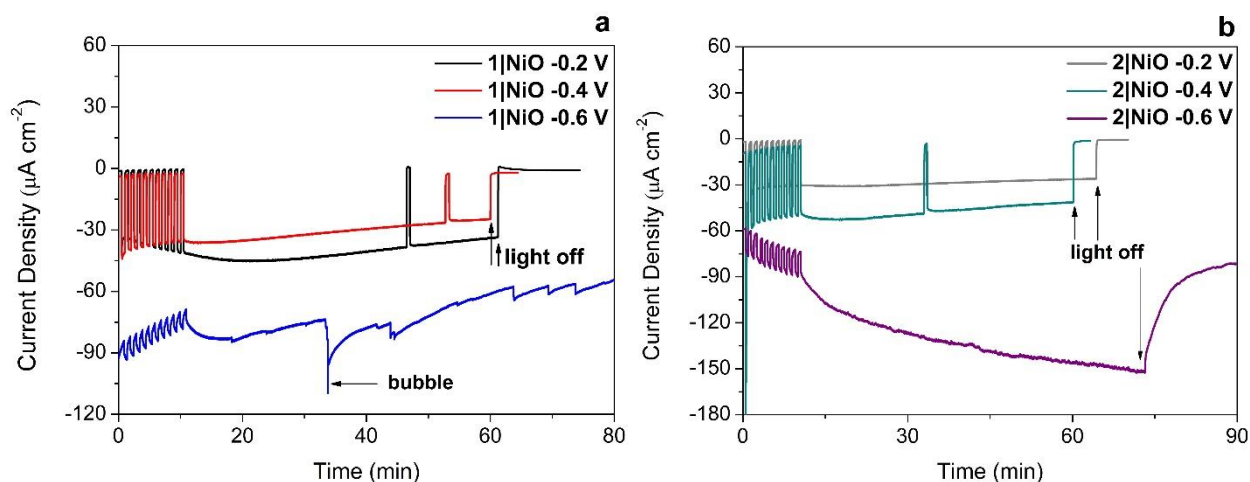


Figure 4.7. CA measurements of 1|NiO (a) and 2|NiO (b) in pH 3 aqueous electrolytes with 0.1 M potassium hydrogen phthalate. $E_{appl} = -0.2$ V, -0.4 V and -0.6 V vs. Ag/AgCl reference electrode (3.0 M NaCl). Chopped light illumination was applied with 30 s intervals (10 cycles of dark current/photocurrent).

H_2 was detected from both 1|NiO and 2|NiO under white light illumination at $E_{appl} = -0.2$ V to -0.6 V and the volume detected vs. time is presented in Figure 4.8 No H_2 was detected during the control measurements in the dark, except for 2|NiO under $E_{appl} = -0.6$ V, where the rate of H_2 evolution decreased after the light was switched off. The faradaic efficiencies (η_{Far}) calculated for 1|NiO and 2|NiO are presented in Table 4.1.

The efficiencies of both photocathodes decrease with the increase in applied potential. Reported values of η_{Far} for H_2 evolution elsewhere range from $<10\%$ to $>100\%$.²⁰ The values presented here are estimates as the peaks in the chromatogram corresponding to H_2 were small and integrated manually. The photocurrent density and volume of H_2 were affected by differences in film thickness and care was taken to ensure these were consistent between samples (average film thickness was *ca.* 2 mm). Turnover numbers (TONs) for the immobilised photocatalysts 1|NiO and 2|NiO were estimated from the number of dye molecules adsorbed and the quantity of H_2 produced at each E_{appl} during 1 hour and are included in Table 1. The best TON for 1 resulted from measurement under $E_{appl} = -0.2$ V vs. Ag/AgCl, which was 46 and increasing the potential resulted in lower TON. The estimated TONs for 2|NiO were higher than 1|NiO at all E_{appl} . However, as the photocatalyst was shown to be decomposing to Pt^0 during the post-catalysis characterisation of electrodes by XPS (Figure 4.15), the TON for 2 is not accurate.

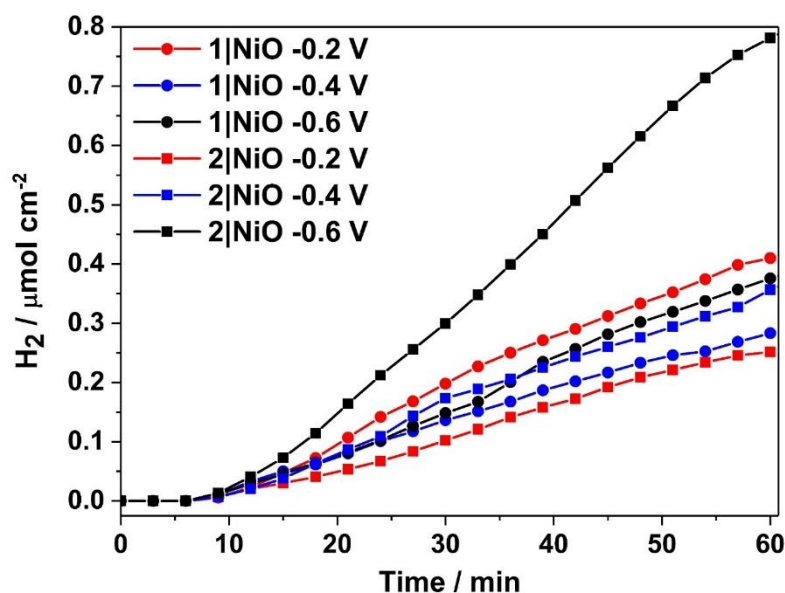


Figure 4.8. Cumulative photoelectrocatalytic H₂ production by 1|NiO and 2|NiO during the chronoamperometry measurements at different E_{appl} (Figure. 4.6 and 4.7). Chopped light illumination was applied during the first 10 min followed by constant light illumination until the end of the measurement (AM1.5, 100 mW cm⁻²).

Table 1. Photocurrent, Faradaic efficiencies and H₂ production during photoelectrocatalysis of 1|NiO and 2|NiO under AM1.5 illumination (100 mW cm⁻²).

E_{appl} / V vs. $Ag/AgCl$	1 NiO			2 NiO		
	-0.2	-0.4	-0.6	-0.2	-0.4	-0.6
$J_{photo} / \mu A cm^{-2}$	34.8 ± 1.4	31.2 ± 8.7	12.3 ± 1.9	31.8 ± 6.2	47.6 ± 7.5	43.7 ± 27.1
$J_{total} / \mu A cm^{-2}$	35.6 ± 1.8	34.2 ± 9.4	88.2 ± 4.9	33.2 ± 7.1	52.5 ± 12.0	114.7 ± 37.6
$P_{photo} / \%$	97.8	91.2	14	95.8	90.7	38.1
$\eta_{Far} / \%$	88.6	67.5	32.3*	59.1	56.9	44.4*
$[H_2] / \mu mol h^{-1} cm^{-2}$	0.41	0.28	0.37	0.25	0.36	0.78
TON	46	31	41	47	68	147

J_{photo} is the average photocurrent, J_{total} is the photocurrent plus dark current, P_{photo} is the percentage of photocurrent of the total current and η_{Far} is the Faradaic efficiency of H₂ production. η_{Far} was calculated using J_{photo} in case of $E_{appl} = -0.2$ V and $E_{appl} = -0.4$ V. * η_{Far} was calculated from the overall charge passed during the measurement (dark and photocurrent) in case of $E_{appl} = -0.6$ V vs. Ag/AgCl. TON calculated from the dye-loading (mol cm⁻²) and the [H₂] over 1 hour.

4.2.4 Electrode characterisation pre- and post-catalysis

The Time-of-Flight Secondary Ion Mass Spectrometry (ToF-SIMS) analysis was carried out on 1|NiO and 2|NiO pre- and post-catalysis (Figure 4.9 and Appendix, Figures A3-A10). Higher mass molecular ions corresponding to 1 and 2 were present in the SIMS spectra

of as-deposited 1|NiO and 2|NiO (pre-catalysis), respectively. This is consistent with the successful adsorption of photocatalysts 1 and 2 on the surface of the nanostructured NiO electrode.

The SIMS spectra, 1020–1140 mass per unit, of 1|NiO before and after photoelectrocatalysis are presented in Figure 4.9 and contain the higher mass molecular ions corresponding to dye-catalyst assembly 1. This indicates that 1 did not decompose during the experiment and is intact on the surface of the NiO during the photoelectrocatalysis under $E_{appl} = -0.4$ V vs. Ag/AgCl. The SIMS spectra for dye-catalyst assembly 2, also contain peaks corresponding to higher mass molecular ions in the post-catalysis samples (Appendix, Figure A10) The intensity of these peaks diminishes going from $E_{appl} = -0.2$ V to -0.6 V vs. Ag/AgCl. This indicates that 2 has partially detached or decomposed during photoelectrocatalysis. In Figure 4.9, several peaks are present in the range corresponding to dye-catalyst assembly 1. Inspection of the isotope patterns reveals that there is a combination of H₂O, Cl⁻ and CH₃CN coordinated to the Pd catalytic centre. Possible identities of these species are provided in the caption of Figure 4.9.

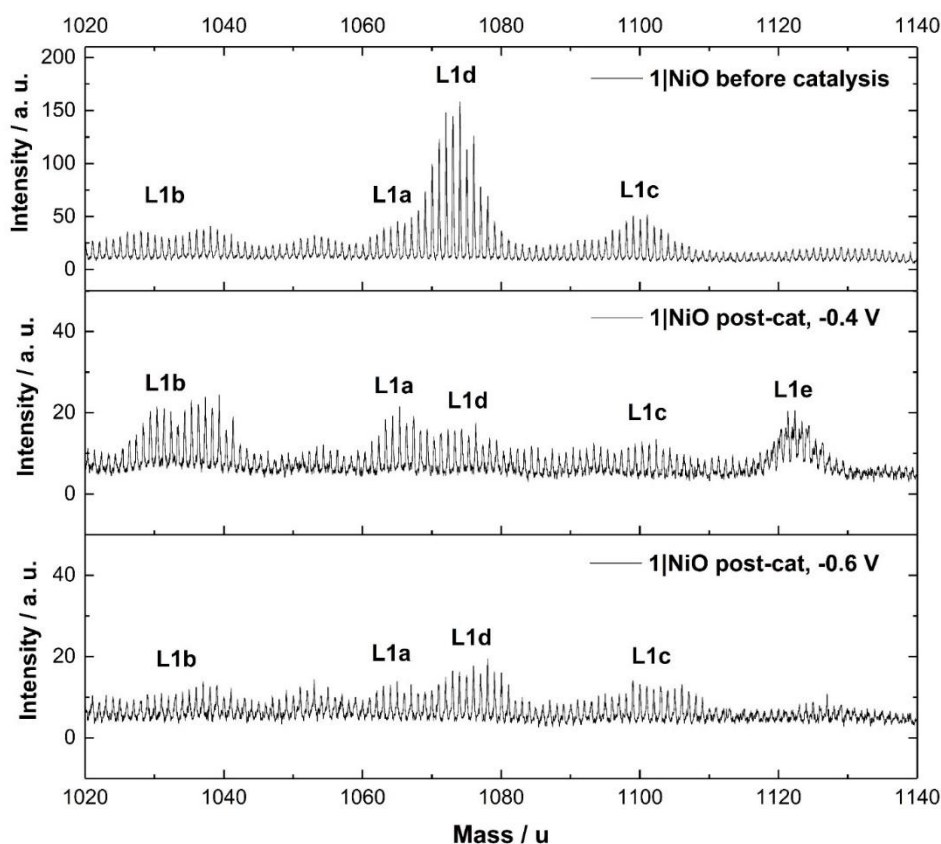


Figure 4.9. ToF-SIMS positive ion spectra of 1|NiO taken from three different samples: top: – pre-catalysis, middle: post-catalysis at -0.4 V vs. Ag/AgCl and bottom: post-catalysis -0.6 V

vs. Ag/AgCl. 1020 – 1140 mass/u range. Assignments are as follows: L1a - $[\text{Ru}(\text{decb})_2(\text{bpt})\text{PdCl}]^{2+}$ calcd. $m = 1065$, L1b - $[\text{Ru}(\text{decb})_2(\text{bpt})\text{Pd}]^{3+}$ calcd. $m = 1030$, L1c - $[\text{Ru}(\text{decb})_2(\text{bpt})\text{PdCl}(\text{H}_2\text{O})_2]^{2+}$ calcd. $m = 1101$, L1d - $[\text{Ru}(\text{decb})_2(\text{bpt})\text{Pd}(\text{CH}_3\text{CN})]^{3+}$ calcd. $m = 1071$, L1e $[\text{Ru}(\text{decb})_2(\text{bpt})\text{PdCl}(\text{H}_2\text{O})_3]^{2+}$ calcd. $m = 1119$.

Post-catalysis, there was some evidence for the presence of phthalate buffer residues with the detection of a fragment ion at $m/z = 121$ due to the PhCO_2^- species. No desorption of the photocatalyst was observed in the presence of the buffer (see above) but the results suggest that non-competitive co-adsorption of some phthalate is possible.

X-ray Photoelectron Spectroscopy (XPS) measurements were carried out on 1|NiO and 2|NiO pre- and post-catalysis ($E_{\text{appl}} = -0.4 \text{ V}$ and $E_{\text{appl}} = -0.6 \text{ V}$ vs. Ag/AgCl). The results are compared in Figures 4.10 – 4.15. There were no significant differences between the Ni 2p XPS spectra of pre- and post-catalysis samples (Figures 4.10 and 4.11), which indicates that there are no substantial changes to the NiO electrode during the experiments. In particular, the Ni^{3+} to Ni^{2+} ratio was similar and there was no visible Ni^0 peak at lower binding energy, which has been reported elsewhere for post-catalysis samples.²¹ The binding energy for Ni metal $2p_{3/2}$ peak on Ni and NiO samples has been reported at 852.6 eV.^{22,23}

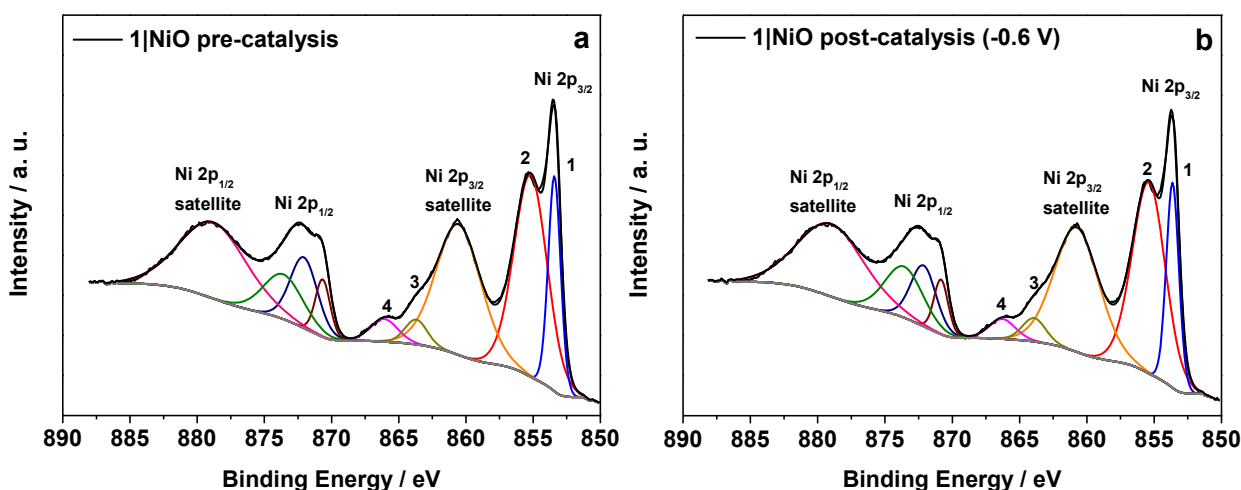


Figure 4.10. Ni 2p XPS spectrum of 1|NiO. (a) - Before photoelectrocatalysis, (b) – after photoelectrocatalysis under -0.6 V (vs. Ag/AgCl ref.) applied potential. (1) – Ni^{2+} ; (2) – Ni^{3+} ; (3, 4) – higher energy satellite peaks.²⁴

For 1|NiO, the C1s and Ru 3d regions (Figure 4.12) were largely unchanged, confirming that the dye-catalyst assembly 1 is present on NiO before and after photoelectrocatalysis. In both 1|NiO and 2|NiO samples, the binding energies for the Ru 3d

spin-orbit doublet peaks are situated at 281.1 eV and 285.3 eV for Ru 3d_{5/2} and Ru 3d_{3/2}, respectively, which is consistent with reported values for ruthenium tris(bipyridine) electrografted on boron doped diamond electrode (Ru 3d_{5/2}: 281.3 eV, Ru 3d_{3/2}: 285.5 eV).²⁶

There are no additional peaks present in the Ru 3d region to suggest that the Ru complex has decomposed. This is consistent with the presence of molecular ion fragments corresponding to [Ru(bpy)₂(L)]⁺ in the corresponding TOF-SIMS (Appendix, Figures A3 and A7). Therefore, we conclude that the photosensitiser part of both molecules is stable during the photoelectro-catalysis, even at potentials more negative than $E_{\text{appl}} = -0.6$ V vs. Ag/AgCl.

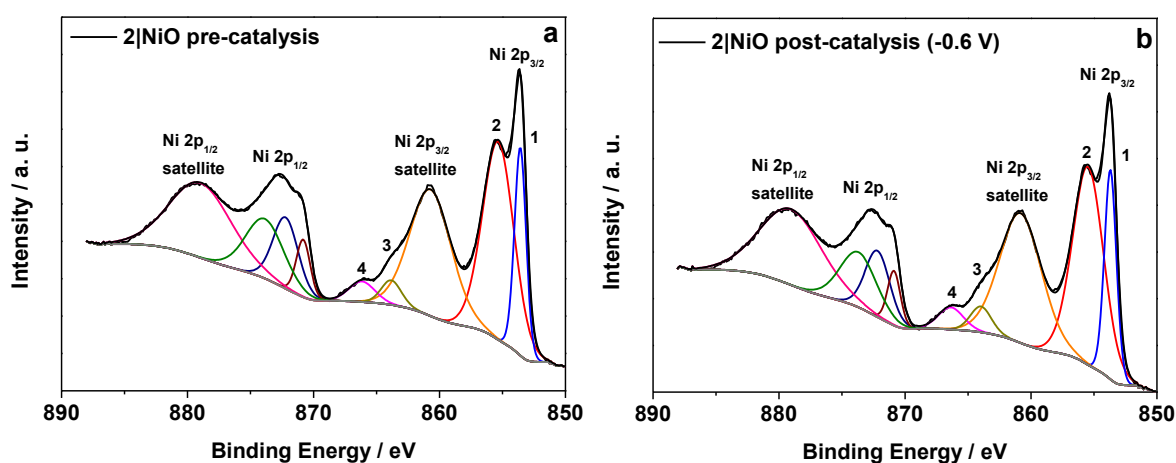


Figure 4.11. Ni 2p XPS spectrum of 2|NiO. (a) - Before photoelectrocatalysis, (b) – after photoelectrocatalysis under -0.6 V (vs. Ag/AgCl ref.) applied potential. (1) – Ni²⁺; (2) – Ni³⁺; (3, 4) – higher energy satellite peaks.²⁴

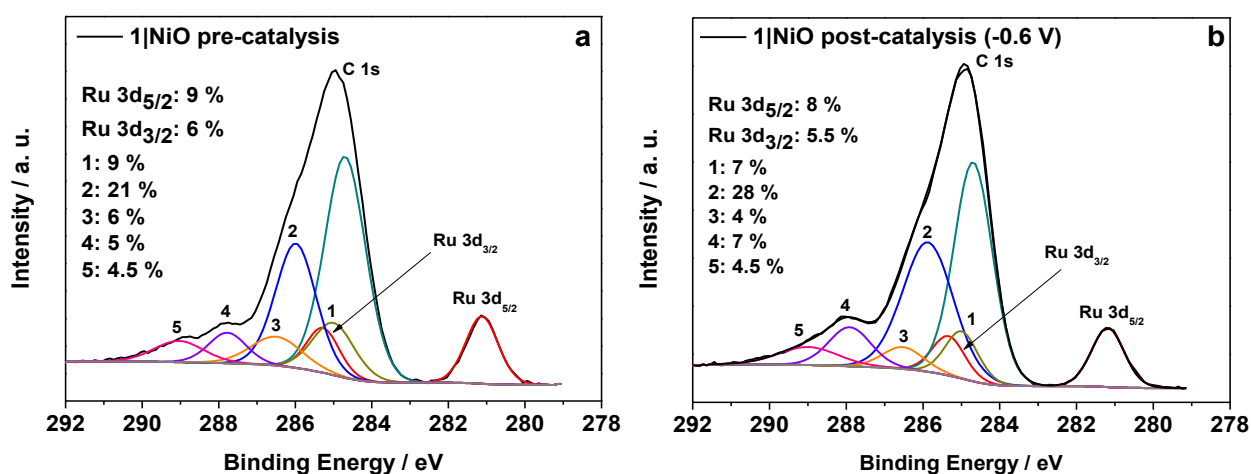


Figure 4.12. C 1s XPS spectrum of 1|NiO. (a) - Before photoelectrocatalysis, (b) – after photoelectro-catalysis under -0.6 V (vs. Ag/AgCl ref.) applied potential. The C1s is composed

of the following components: (1) – hydrocarbon; (2) – amine; (3) – alcohol, ether; (4) – carbonyl; (5) – ester, acid.²⁵ Differences between the Ru 3d doublet binding energies of as-deposited and post-catalysis samples are within the error margins (± 0.2 eV).

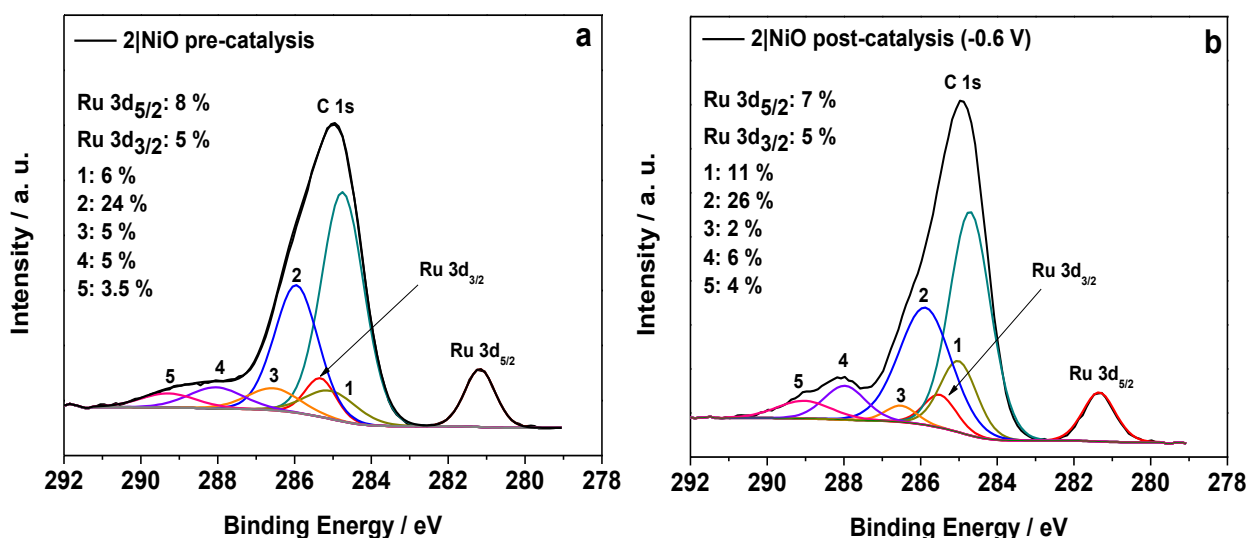


Figure 4.13. C 1s XPS spectrum of 2|NiO. (a) - Before photoelectrocatalysis, (b) – after photoelectro-catalysis under -0.6 V (vs. Ag/AgCl ref.) applied potential. (1) – hydrocarbon; (2) – amine; (3) – alcohol, ether; (4) – carbonyl; (5) – ester, acid.²⁵

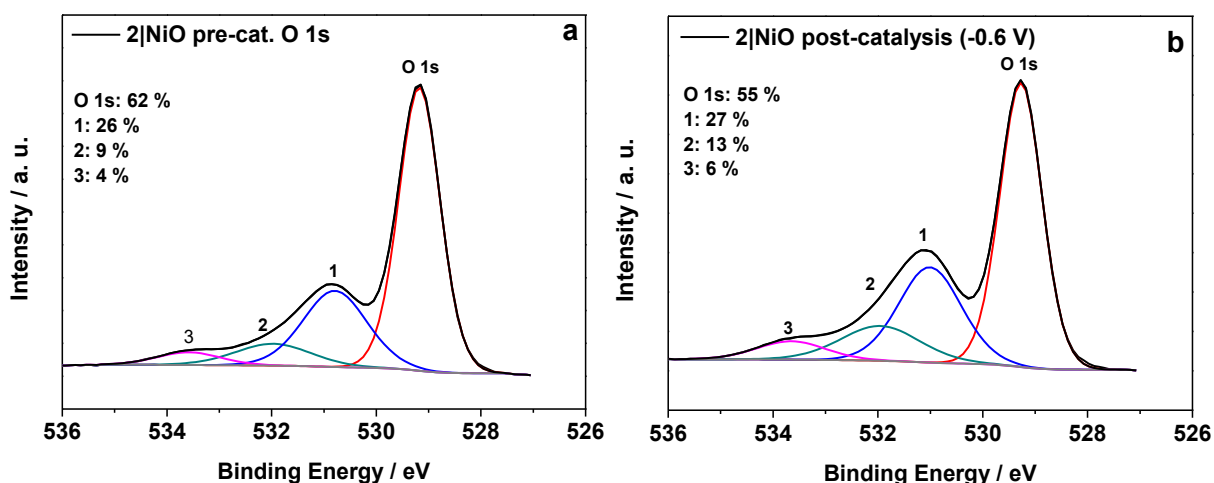


Figure 4.14. O 1s XPS spectrum of 2|NiO. (a) - Before photoelectrocatalysis, (b) – after photoelectro-catalysis under -0.6 V (vs. Ag/AgCl ref.) applied potential. (1) – oxide, hydroxide; (2) – carbonyl; (3) – ester.²⁵

The Pd 3d spin-orbit doublet in the spectra for 1|NiO, pre- and post-catalysis, (Figure 4.15 (a-c)) contain two major components in each band (1, 2, 3 and 4). Component 1 at 338.4

eV under Pd 3d_{5/2} peak is consistent with spectra reported previously for Pd(II) (PdCl₂²⁷ and bis(1,2-ethanediamine-N,N')dichloropalladium²⁸). The 3d_{5/2} binding energy for Pd(0) should lie between 334 eV and 336 eV, but component (3) has a maximum at 337.1 eV.²⁹ Therefore, components (3) and (4) are not attributed to Pd(0). Instead, (3) and (4) could correspond to a Cl-free complex, e.g. [Ru(decb)₂(bpt)Pd(CH₃CN)]³⁺ (L1d) identified in the ToF-SIMS spectrum in Figure 4.9.

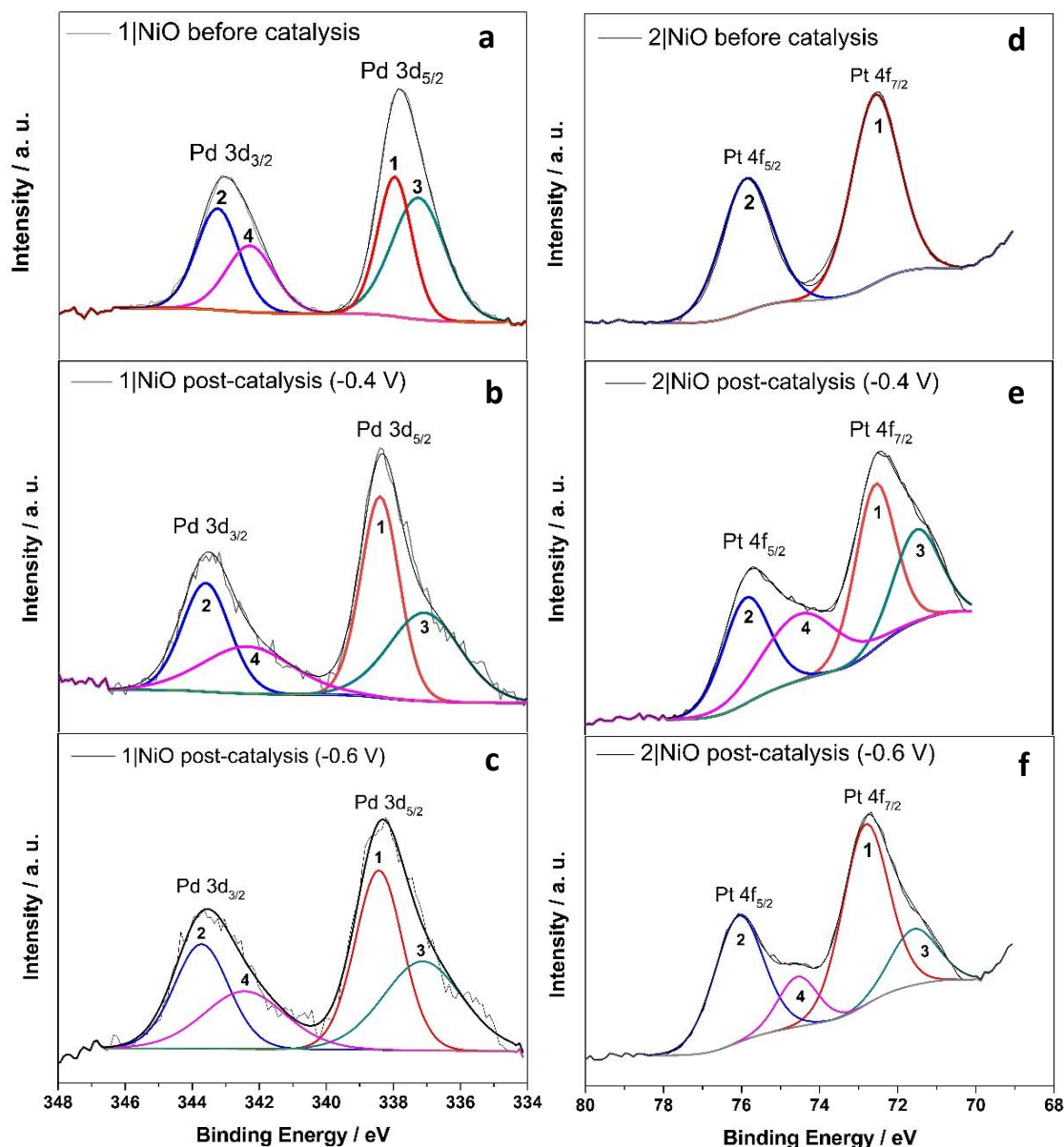


Figure 4.15. Pd 3d XPS spectrum of 1|NiO (a) before photoelectrocatalysis, after photoelectro-catalysis under (b) $E_{\text{appl}} = -0.4$ V and (c) $E_{\text{appl}} = -0.6$ V; Pt 4f XPS spectrum of 2|NiO (d) before photoelectrocatalysis, after photoelectrocatalysis under (e) $E_{\text{appl}} = -0.4$ V and (f) $E_{\text{appl}} = -0.6$ V vs. Ag/AgCl.

In contrast, each doublet peak in the Pt 4f spin-orbit doublet in the 2|NiO, pre-catalysis, spectrum (Figure 4.15 (d)) is composed of one component, with binding energies for (1) Pt 4f_{7/2} = 72.6 eV and (2) Pt 4f_{5/2} = 75.9 eV. These binding energies are consistent with those reported previously for Pt(II) iodo-complexes.^{30,31} Additional components (3 and 4) are present at lower binding energies in the spectrum for 2|NiO, post-catalysis, (Figure 4.15 (e) and (f)). The additional component (3) under Pt 4f_{7/2} doublet peak has the binding energy of 71.6 eV, which is consistent with Pt(0).^{32,33} This indicates that photocatalyst 2 decomposes during the photoelectrocatalysis and metallic Pt is formed on the NiO surface. These findings are consistent with the ToF-SIMS data, which showed the loss of higher mass species on post-catalysis samples of 2|NiO at $E_{\text{appl}} = -0.6$ V vs. Ag/AgCl (Appendix, Figure A8). From these results, it is reasoned that during the photoelectrochemical experiments, 2 decomposes to give Pt⁰ on the surface of the electrode and this could drive H₂ evolution in this system.

4.3 General discussion

The role of the photocathode in a dye-sensitised PEC is to use the electrons generated by water oxidation at a photocathode to drive reduction of H⁺ to H₂. The dye-sensitised photoelectrochemical devices reported previously used either co-adsorbed dyes and catalysts⁴ or covalently linked (but electronically de-coupled) metal ion coordination supramolecular dye-catalyst assemblies.^{8,21} High photocurrents have been reported elsewhere for an organic dye with an H₂-evolving catalyst in solution (however, pH 0 was used, which could be problematic when coupled with an oxygen-evolving photoanode).³⁴ The approach described here, instead, uses integrated photocatalysts.

The photocurrent densities for 1|NiO and 2|NiO are comparable with the best co-immobilised systems on NiO and ITO. However, 1|NiO is superior to previously reported photocathodes in terms of the Faradaic efficiency and stability of the photocurrent.^{35,36} The high faradaic efficiency of our photocathodes is attributed to the direct coupling of the photosensitiser with the catalyst. In the NiO systems reported previously, the dye and the catalyst have been either separate molecules (either co-deposited on the surface or a catalyst in solution) or tethered through non-conjugated linkers.²⁰ In such systems, the Faradaic yields reported are typically less than 70% and in some cases below 10%, possibly due to slow or inefficient charge-transfer to the catalyst (leading to charging and discharging of the electrode), the presence of side reactions (e.g. reduction of O₂) or the catalyst acting as a redox shuttle by diffusing from the cathode to the anode. Integrating the sensitiser and catalyst within one molecule permits rapid (i.e. not diffusion-limited) electron transfer to the catalytic

centre. While the precise mechanism for hydrogen evolution in the integrated photocatalyst system is not yet known, the transient spectroscopy confirms that electron transfer from NiO to the catalyst occurs rapidly upon excitation and the high Faradaic yield and stable photocurrents are consistent with catalysis out-competing charge-recombination.⁴⁰ Nonetheless, the system is far from optimum at this stage, for example, the light harvesting efficiency of both 1|NiO and 2|NiO is low. Thicker and more porous films may improve the performance,⁸ and chromophores with higher absorption coefficients could increase the photocurrent density.

The stability of the Ru chromophore on the NiO surface was encouraging as, rather than esters, carboxylic acid or phosphonic acid anchoring groups are generally used to adsorb the dye, which present challenges in synthesis and purification.^{3,4,5,8,9,36} Slight changes in the Pd and Pt catalyst structure during operation were anticipated, e.g. replacement of the halide ligands with solvent. Kaeffer *et al.*, for example, reported halide ligand substitution (Br^- for Cl^-) in cobalt-diimine-dioxime complexes post-catalysis in their co-immobilised system.¹⁰ These results are consistent with reactivity at the catalytic metal centre. The reduction of the Pd(II) centre is expected to be accompanied by dissociation of a chloride anion.^{37,38}

Initial inspection of the photocurrent density and volume of H_2 produced, suggested that 2, containing the Pt catalyst, outperformed 1, which contains the Pd catalyst. However, the increase in current observed (particularly at the most negative applied bias) during irradiation indicated that the electrode surface was changing during the experiment. The XPS and ToF-SIMS results confirm that the Pt complex is unstable in water, especially under irradiation at $E_{\text{appl}} = -0.6 \text{ V vs. Ag/AgCl}$, and the increasing current over time is attributed to the formation of electrocatalytically active Pt(0) on the NiO surface. It is also possible that the strong transient reductive photocurrents observed for NiO/Ru-Pt (Figure 4.6) correspond to the in-situ reduction of the Pt(II) complex, generating Pt(0) particles. Du *et al.* have previously reported the formation of colloidal platinum during photocatalytic H_2 evolution using a system containing platinum(II) bi- and terpyridyl chloro complexes, in the presence of a sacrificial electron donor (MeOH or triethanolamine) and an electron relay (TiO_2).³⁹ In contrast, the surface analysis experiments showed that 1, which contained the Pd centre, was present on the NiO surface after 1h PEC at potentials from $E_{\text{appl}} = -0.2$ to $-0.6 \text{ V vs. Ag/AgCl}$. These results highlight the importance of characterising the electrodes after the catalysis. Whilst in-situ characterisation of heterogenous catalysts is challenging, hybrid systems containing molecular catalysts furnished with spectroscopic handles present an opportunity to extract mechanistic information.⁴⁰

While the performance of the photocathodes is encouraging, it is anticipated that much higher yields are possible with some minor alterations to our experimental setup. Better device engineering is necessary to improve mass transport. The geometry of the custom-built PEC cell (Figure 2.2 in Chapter 2.3.6) is not optimised and bubble formation on the photocathode surface led to a drop in the active area. In this study, no membrane was used to separate the anode and photocathode, so the presence of oxygen formed at the Pt anode could provide a recombination pathway. While reasonable photocurrents were observed in pH 7 buffer, pH 3 was optimum for H₂ evolution. Raising this will be desirable for tandem devices.

4.4 Conclusions

Light driven H₂ production from water by two new photocathodes, comprised of integrated photocatalysts 1 and 2 adsorbed on NiO, has been described. Stable photocurrents and sustained H₂ production were observed for both photocathodes immersed in pH 3 buffer by PEC experiments with in-line gas chromatography, in the absence of sacrificial agents. The Faradaic efficiencies were estimated between 30 – 90%, depending on E_{appl} . Surface analysis experiments revealed that the Ru photosensitiser and the Pd catalyst are stable during photoelectrochemical H₂ evolution over a range of E_{appl} , whereas the Pt catalyst decomposed at more negative potentials. These findings were consistent with the observed photocurrent during PEC H₂ production, which was most stable for 1|NiO. These results are promising for the development of efficient photoelectrocatalytic devices for storing the energy from sunlight in chemical bonds. Future efforts will be directed towards increasing the absorptivity of the photocathodes and raising the optimum pH through modifications to the ligand structure.

References

- 1 A. L. Smeigh, L. Le Pleux, J. Fortage, Y. Pellegrin, E. Blart, F. Odobel and L. Hammarström, *Chem. Commun.*, 2012, 48, 678–80.
- 2 R. J. Dillon, L. Alibabaei, T. J. Meyer and J. M. Papanikolas, *ACS Appl. Mater. Interfaces*, 2017, 9, 26786–26796.
- 3 K. Fan, F. Li, L. Wang, Q. Daniel, E. Gabrielsson and L. Sun, *Phys. Chem. Chem. Phys.*, 2014, 16, 25234–25240.
- 4 L. Li, L. Duan, F. Wen, C. Li, M. Wang, A. Hagfeldt and L. Sun, *Chem. Commun.*, 2012, 48, 988–990.
- 5 L. Tong, A. Iwase, A. Nattestad, U. Bach, M. Weidelener, G. Götz, A. Mishra, P. Bäuerle, R. Amal, G. G. Wallace and A. J. Mozer, *Energy Environ. Sci.*, 2012, 5, 9472–9475.
- 6 Z. Ji, M. He, Z. Huang, U. Ozkan and Y. Wu, *J. Am. Chem. Soc.*, 2013, 135, 11696–11699.
- 7 P. B. Pati, L. Zhang, B. Philippe, R. Fernández-Terán, S. Ahmadi, L. Tian, H. Rensmo, L. Hammarström and H. Tian, *ChemSusChem*, 2017, 10, 2480–2495.
- 8 M. A. Gross, C. E. Creissen, K. L. Orchard and E. Reisner, *Chem. Sci.*, 2016, 7, 242–247.
- 9 R. J. Kamire, M. B. Majewski, W. L. Hoffeditz, B. T. Phelan, O. K. Farha, J. T. Hupp and M. R. Wasielewski, *Chem. Sci.*, 2017, 8, 541–549.
- 10 N. Kaeffer, C. D. Windle, R. Brisse, C. Gablin, D. Leonard, B. Jousset, M. Chavarot-Kerlidou and V. Artero, *Chem. Sci.*, 2018, 9, 6721–6738.
- 11 T. Kowacs, Q. Pan, P. Lang, L. O'Reilly, S. Rau, W. R. Browne, M. T. Pryce, A. Huijser and J. G. Vos, *Faraday Discuss.*, 2015, 185, 143–170.
- 12 L. A. Gallagher, S. A. Serron, X. Wen, B. J. Hornstein, D. M. Dattelbaum, J. R. Schoonover, T. J. Meyer, *Inorganic Chemistry*, 2005, 40, 2089–2097.
- 13 K. A. Click, B. M. Schockman, J. T. Dilenschneider, W. D. McCulloch, B. R. Garrett, Y. Yu, M. He, A. E. Curtze and Y. Wu, *J. Phys. Chem. C*, 2017, 121, 8787–8795.

- 14 L. Li, L. Duan, F. Wen, C. Li, M. Wang, A. Hagfeldt and L. Sun, *Chem. Commun.*, 2012, 48, 988–990.
- 15 G. Boschloo and D. Fitzmaurice, *J. Phys. Chem. B*, 1999, 103, 2228–2231.
- 16 L. D’Amario, R. Jiang, U. B. Cappel, E. A. Gibson, G. Boschloo, H. Rensmo, L. Sun, L. Hammarström and H. Tian, *ACS Appl. Mater. Interfaces*, 2017, 9, 33470–33477.
- 17 A. M. Lapedes, B. D. Sherman, M. K. Brennaman, C. J. Dares, K. R. Skinner, J. L. Templeton and T. J. Meyer, *Chem. Sci.*, 2015, 6, 6398–6406.
- 18 D. W. Kim, S. C. Riha, E. J. DeMarco, A. B. F. Martinson, O. K. Farha and J. T. Hupp, *ACS Nano*, 2014, 8, 12199–12207.
- 19 C. E. Castillo, M. Gennari, T. Stoll, J. Fortage, A. Deronzier, M.-N. Collomb, M. Sandroni, F. L’egalit’e, E. Blart, Y. Pellegrin, C. Delacote, M. Boujtita, F. Odobel, P. Rannou and S. Sadki, *J. Phys. Chem. C*, 2015, 119, 5806–5818.
- 20 E. A. Gibson, *Chem. Soc. Rev.*, 2017, 46, 6194–6209.
- 21 N. Kaeffer, J. Massin, C. Lebrun, O. Renault, M. Chavarot-Kerlidou and V. Artero, *J. Am. Chem. Soc.*, 2016, 138.
- 22 M. C. Biesinger, B. P. Payne, L. W. M. Lau, A. Gerson and R. S. C. Smart, *Surf. Interface Anal.*, 2009, 41, 324–332.
- 23 A. P. Grosvenor, M. C. Biesinger, R. S. C. Smart and N. S. McIntyre, *Surf. Sci.*, 2006, 600, 1771–1779.
- 24 M. C. Biesinger, B. P. Payne, L. W. M. Lau, A. Gerson and R. S. C. Smart, *Surf. Interface Anal.*, 2009, 41, 324–332.
- 25 G. Beamson and D. Briggs, *High Resolution XPS of Organic Polymers*, Wiley Interscience, 1992.
- 26 C. Agnès, J.-C. Arnault, F. Omnès, B. Jusselme, M. Billon, G. Bidan and P. Mailley, *Phys. Chem. Chem. Phys.*, 2009, 11, 11647.
- 27 C. Sleight, A. Pijpers, A. Jaspers, B. Coussens and R. J. Meier, *J. Electron Spectrosc. Relat. Phenom.*, 1996, 77, 41-57.
- 28 T. H. Fleisch and G. J. Mains, *J. Phys. Chem.*, 1986, 90, 5317-5320.
- 29 P. Brant, L. S. Benner and A. L. Balch, *Inorg. Chem.*, 1979, 18, 3422-3427.

- 30 M. C. Biesinger, B. P. Payne, L. W. M. Lau, A. Gerson and R. S. C. Smart, *Surf. Interface Anal.*, 2009, 41, 324–332.
- 31 D. T. Clark, D. B. Adams and D. Briggs, *J. Chem. Soc. Chem. Commun.*, 1971, 603.
- 32 A. P. Grosvenor, M. C. Biesinger, R. S. C. Smart and N. S. McIntyre, *Surf. Sci.*, 2006, 600, 1771–1779.
- 33 J. F. Moulder, *Handbook of X-ray Photoelectron Spectroscopy: A Reference Book of Standard Spectra for Identification and Interpretation of XPS Data*, Physical Electronics Division, Perkin-Elmer Corporation, 1992.
- 34 K. A. Click, D. R. Beauchamp, Z. Huang, W. Chen and Y. Wu, *J. Am. Chem. Soc.*, 2016, 138, 1174–1179.
- 35 F. Li, K. Fan, B. Xu, E. Gabrielsson, Q. Daniel, L. Li and L. Sun, *J. Am. Chem. Soc.*, 2015, 137, 9153–9159.
- 36 B. Shan, A. K. Das, S. Marquard, B. H. Farnum, D. Wang, R. M. Bullock and T. J. Meyer, *Energy Environ. Sci.*, 2016, 9, 3693–3697.
- 37 S. Rau, B. Schäfer, D. Gleich, E. Anders, M. Rudolph, M. Friedrich, H. Görls, W. Henry and J. G. Vos, *Angew. Chemie Int. Ed.*, 2006, 45, 6215–6218.
- 38 M. Karnahl, C. Kuhnt, F. Ma, A. Yartsev, M. Schmitt, B. Dietzek, S. Rau and J. Popp, *ChemPhysChem*, 2011, 12, 2101–2109.
- 39 P. Du, J. Schneider, F. Li, W. Zhao, U. Patel, F. N. Castellano and R. Eisenberg, *J. Am. Chem. Soc.*, 2008, 130, 5056–8.
- 40 N. Pöldme, L. O'Reilly, I. Fletcher, J. Portoles, I. V. Sazanovich, M. Towrie, C. Long, J. G. Vos, M. T. Pryce, E. A. Gibson. *Chem. Sci.*, 2019, 10, 99.

Chapter 5. CuCrO₂ as alternative photocathode material for photoelectrochemical H₂ evolution

Abstract

CuCrO₂ as an alternative material to NiO was studied as a photocathode for photoelectrochemical H₂ evolution. The aim was to show that the post-calcination annealing of the photocathodes under N₂ atmosphere changes the surface chemistry of the CuCrO₂ photocathodes which translates into superior stability and efficiency. The origin of these properties was discussed with the help of X-ray photoelectron spectroscopy surface analysis. Stable H₂ production on the CuCrO₂ photocathode from aqueous buffer solution was shown and the efficiency of the process was further increased with the use of inorganic cobalt co-catalyst in solution. In addition, successful sensitisation of the CuCrO₂ photocathode with an organic dye was demonstrated resulting in considerable increase in photocurrent when electron acceptor was added into the solution. An additional study was made where Fe was added to the CuCrO₂ to form CuCr_{0.5}Fe_{0.5}O₂ mixed metal delafossite. The aim of this study was to see how the Fe³⁺ addition to the delafossite crystal lattice influences the photoelectrochemical performance and stability of the material.

5.1 Introduction

Considerably fewer studies have been made on p-type materials than on n-type materials in the field of photoelectrochemical (PEC) water splitting.^{1,2,19} The n-type semiconductors are applied as photoanodes generating anodic photocurrents and driving the water oxidation half reaction. Two of the most notable examples of photoanodes are n-Fe₂O₃ and wide band gap TiO₂.^{1,2} p-type semiconductor materials on another hand are able to generate cathodic photocurrents and drive the photoelectrochemical hydrogen production.^{18,19} Several p-type binary oxides have been studied for photoelectrochemical (PEC) H₂ production, most notable examples being p-GaP, p-InP, p-GaInP₂, p-Si, Cu₂O, and wide band gap NiO. The latter one has been applied as hybrid photocathode functionalised with light-absorbing dye molecules (see Chapters 3 and 4).³⁻¹³ p-GaP, p-InP, p-GaInP₂, p-Si, have all shown high photocurrents and high efficiencies for H₂ production, but the materials are either rare and expensive, or unstable and hard to process, which makes them unsuitable for devices on an industrial scale.³⁻⁶

Cu₂O is probably the most notable of those materials which are easy to process and cheap. It is a versatile material and several studies concerning Cu₂O for different applications

like p-type thin film layer in PV devices, electrocatalyst, and photocathode for PEC H₂ evolution can be found when going through the corresponding literature.¹⁴⁻¹⁷ The high interest towards Cu₂O for PEC H₂ evolution comes from its favourable properties. It has a direct band gap of approximately 2 eV, which gives a theoretical photocurrent density of approximately 14.7 mA cm⁻² and a solar-to-hydrogen (STH) efficiency of 18 % (based on 1.5 AM spectrum), and the CB and VB energies straddle the electrochemical potentials of H₂ and O₂ evolution (see Chapter 1.6).¹⁸⁻²⁰ The properties and performance of Cu₂O have been studied for PEC water splitting as the H₂ evolution photocatalyst in several studies.⁷⁻¹¹ However, despite the favourable properties, it is not thermodynamically stable in water. The Cu₂O to Cu reduction potential lies in the band gap of the material and therefore, self-reduction takes place in aqueous environment (equation 5.1) resulting in corrosion and, in the end, destruction of the photocathode.^{18,20}



Strategies to protect the photocathode surface against the corrosion have been reported. Paracchino et al. used atomic layer deposition (ALD) method to deposit Al doped ZnO and TiO₂ on the Cu₂O to avoid the contact between the Cu₂O surface and water while providing electron transport from the CB of the Cu₂O to the surface of the photocathode. On top of the TiO₂ the Pt nanoparticles were deposited to drive the H₂ evolution half-reaction.²⁰ Other groups have used similar surface protection techniques with different catalysts to avoid the destruction of the Cu₂O photocathode.^{21,22}

However, the ALD process used in those studies to protect the Cu₂O surface is expensive and for industrial application a cheaper technology would be preferred.^{53,54} That is why there is growing pressure from the scientific community to find an alternative material which would be stable in the conditions for PEC water splitting. In search of these stable materials, mixed metal oxides based on Cu(I) could offer a promising alternative. The corrosion of Cu₂O takes place because upon light illumination, electron is excited and transfers from the Cu 3d¹⁰ atomic orbitals to the Cu 4s atomic orbitals and thereby reducing Cu(I).²³ But if another metal with unfilled d orbitals would be added, the electrons would transfer upon excitation to its atomic orbitals instead, avoiding the Cu(I) reduction on the photocathode surface.¹⁸

Of the different types of Cu(I) based mixed metal oxides, delafossites have recently gained a considerable amount of interest in the field of solar energy conversion, including the field of PEC water splitting. The Cu(I) delafossites show a range of band gap energies

depending on the specific material, which makes them applicable in different types of devices. CuFeO_2 has been reported with band gap energy, E_g , of approximately 1.36 eV.²⁴ In addition, CuFeO_2 , CuRhO_2 and $\beta\text{-CuGaO}_2$ also have a band gap in the visible region.¹⁸ Other types of Cu(I)-based delafossites are, conversely, wide band gap semiconductors, which makes them potential candidates for hybrid dye-sensitised devices like DSSCs and dye-sensitised PEC cells.

The application of several Cu(I)-based delafossites have been reported as materials used in p-type DSSCs. Compared to NiO, these materials have higher hole mobilities and a lower VB energy.²⁵ CuAlO_2 as a p-type semiconductor in DSSC was reported by Nattestad et al. They showed increased open-circuit potential compared to the same device with NiO as the p-type semiconductor and attributed it to the lower Cu 3d¹⁰ VB of CuAlO_2 .²⁶ CuGaO_2 has also been applied in DSSC devices. Yu et al. showed increased open-circuit potential when using a $\text{Co}^{2+/3+}$ redox couple in solution with hydrothermally grown nanoparticulate film of CuGaO_2 .²⁷ Xu et al. demonstrated CuGaO_2 platelet-like nanoparticle synthesis with sizes ranging from 100-200 nm in diameter and 10-30 nm in thickness.²⁸ By fabricating a thin nanostructured film using those synthesised particles, they showed high photocurrent density of approximately 2 mA cm⁻² and almost doubled the short-circuit current densities compared to the same devices made from NiO films.²⁸ They attributed their improved results compared to NiO to the high surface area of the nanostructured film and high conductivity of the delafossite material.²⁸

Of the different types of delafossite materials, CuCrO_2 has been reported on several occasions for its applicability in both DSSCs and in PEC water splitting cells.²⁹⁻³⁹ Most notable was the study made by Bach and co-workers, who demonstrated a CuCrO_2 based DSSC showing an open-circuit potential of 7.34 eV when using $[\text{Co}(\text{en})_3]^{2+/3+}$ redox couple.²⁹ That was the record open-circuit potential at a time in all p-type DSSCs and they attributed it to the lower VB of CuCrO_2 .²⁹

In the work presented in this chapter the focus is on CuCrO_2 . Partly because of the fascinating results in PEC H₂ evolution studies presented in literature and partly due to the promising results obtained in the lab during the initial studies with the material. The properties of CuCrO_2 and the results from previous studies with the material are discussed.

5.2 Properties of CuCrO₂

The pure delafossite phase has a rhombohedral structure with a space group of R3m. In the structure, the Cu atoms are forming O-Cu-O “dumbbells” through linear coordination with O atoms and are oriented in the c-direction. The O-Cu-O unit is, in turn, coordinated to three M(III) (M – metal) atoms on both sides forming an M(III)-centred octahedra which in turn creates a layer of M(III)O₂, which alternate with O-Cu-O “dumbbells” forming a layered structure (Figure 5.1). The top of the valence band is found to be dominated by the Cu d states and the p-type nature of the material comes from Cu vacancies in the crystal lattice.³² Therefore the hole formation takes place solely in the Cu sub-lattice and the conductivity in the material originates from a Cu(I)/Cu(II) hole transport mechanism as predicted by theory^{31,32} and reported experimentally³³.

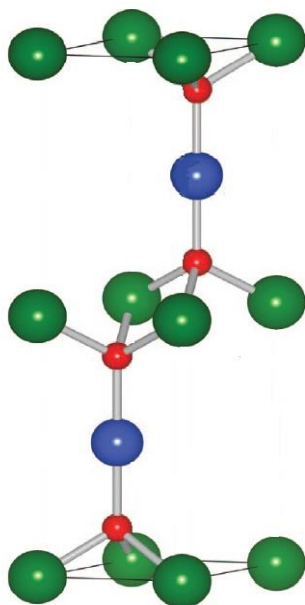


Figure 5.1. Structure of the CuCrO₂ unit cell. Green spheres – Cr, blue spheres – Cu, red spheres – O₂. Adapted from the paper of Scanlon et al.³¹

The conductivity of CuCrO₂ has been reported to be $3.36 \times 10^{-5} \Omega^{-1} \text{cm}^{-1}$ by Trari and co-workers.³⁴ In their theoretical study, Scanlon and co-workers also conclude that the Cr d and O 2p states in the valence band results in superior conductivities for CuCrO₂.^{31,32} They also found that the fundamental band gap (from modelling based on material properties) of CuCrO₂ is indirect.³¹ However, the optical band gap (experimentally obtained) of CuCrO₂ has been reported to be direct with values ranging from 2.95 eV to 3.30 eV.⁴⁵⁻⁵⁰ The VB of CuCrO₂ has been reported to be -5.3 eV vs vacuum level, which corresponds to 0.475 V vs NHE in pH 5 electrolyte.^{29,55} However, in measurements with high energy X-rays at Diamond

synchrotron light source, VB maxima of 0.5 eV vs Fermi level was observed (corresponding to 0.205 V vs NHE in pH 5 electrolyte).⁶⁰ In addition, the same VB maxima was observed also for NiO samples fabricated using the same synthesis route used also in this thesis (see Chapter 2.2.2). *The measurements at Diamond synchrotron light source were conducted by N. Potts, U. Cappel and E. A. Gibson. The CuCrO₂ samples were prepared by N. Pöldme and material was synthesised by K. Sardar.*

5.3 Previous studies on CuCrO₂

The photoelectrochemical activity of CuCrO₂ has previously been explored in several studies.³⁴⁻³⁹ H₂ production from water using a sacrificial agent was shown by Trari and co-workers with single crystal CuCrO₂, but the stability of the electrode was questionable as the H₂ production decreased considerably after half an hour light illumination.³⁴ Hensen and co-workers showed photoelectrochemical hydrogen production with CuCrO₂ powder in water/ethanol suspensions using various noble metal co-catalysts.³⁵ They showed photocurrents ca. 20 $\mu\text{A cm}^{-2}$ with ethanol as the sacrificial agent. A more detailed study of the photoelectrochemical performance of CuCrO₂ under illumination was performed by Diaz-Garcia et al. where they showed stable photocurrent generation of ca. 20 $\mu\text{A cm}^{-2}$ over time and described the pH and chemical stability of sol-gel synthesised CuCrO₂ thin films.³⁶ They did not, however, report H₂ production during their measurements. Recently, Janáky and co-workers showed that CO₂ reduction along with H₂ evolution is possible on almost phase-pure CuCrO₂ synthesised through solution combustion synthesis under high intensity UV-light 0.69 W cm⁻².³⁷ The stability of these electrodes was, however, problematic, showing a considerable decrease in photocurrent over time, which could be the results of photocorrosion of a Cu₂O impurity in the sample.³⁷

The previous reports on CuCrO₂ photoelectrochemistry show that it could be a very promising material for solar fuel production, but they also highlight that there are still several questions to be answered. First, the hydrogen production from pure water under 1 sun (1.5 AM, 100 mW·cm⁻²) illumination is yet to be confirmed, which would determine its applicability in actual real-life applications. Also, the stability of the material during PEC H₂ evolution is another issue which needs to be studied more in-depth. For that, the sample needs to be pure so that impurities can be excluded from being contributing factors to the photocorrosion and/or hydrogen production, because Cu₂O has been shown evolve H₂ as well.²⁰

Another strategy to improve the material is to modify the defects in the material. It is well known that defects, whether intrinsic or extrinsic, modify the (opto-)electronic properties of the semiconductor materials inducing changes in the band structure through, for example, creation of localised intra band-gap energy levels. In the case of CuCrO_2 , Jiang et al. used an oxygen getter, CaH_2 , to reduce CuCrO_2 nanoparticles synthesised via a hydrothermal route, and recorded the change in flat band potential as a result of the reduction.³⁸ They reasoned that the reduction of CuCrO_2 using CaH_2 decreases the concentration of holes at the top of the valence band and this in turn changes the Fermi level.³⁸

In addition, because of the large band gap of CuCrO_2 , functionalisation of the material with additional light absorbers and the use of earth-abundant co-catalysts are important methods to consider when optimising the system further. The first dye-sensitised CuCrO_2 photocathode was recently reported by Reisner and co-workers, showing hydrogen production with an additional Ni-based co-catalyst using a UV-filter.³⁹ They showed photocurrents of ca. $50 \mu\text{A cm}^{-2}$ with 5 mM DTDP EA at -0.38 V vs Ag/AgCl in pH 3 electrolyte, but during the CA measurement with Ni-based co-catalyst the photocurrent of $5 \mu\text{A cm}^{-2}$ was measured. During the CA measurement they reported a H_2 production of 35 nmol after 2 hours of light illumination and Faradaic efficiency of 31 %.³⁹

However, when the aim is to apply the photocathode in large-scale systems which could be industrially produced, it is important that the photocathode would be robust and stable also under the UV-light illumination because the applicability of additional UV cut-off filters to avoid semiconductor photocorrosion wouldn't be cost-efficient on industrial scale. In this study, the aim is to see if the dye-sensitised CuCrO_2 would be stable under light illumination which also includes UV component, and to determine, what is the dye contribution under these conditions, considering that CuCrO_2 is also photoactive in the UV-region.

5.4 Motivation

In this work, the focus is on studying the effects of post-calcination N_2 annealing on CuCrO_2 mesoporous photocathodes, which were fabricated from a CuCrO_2 powder, synthesised through a solid-state route and deposited on conducting substrates. The importance of inert atmosphere during synthesis is known, however in this study the aim is to study this effect further and show how it effects the device performance. It is shown that the post-calcination of the photocathodes under N_2 atmosphere changes the surface chemistry of

the CuCrO_2 photocathodes which translates into superior stability and efficiency of the device. The origin of these properties is discussed with the help of XPS surface analysis. Stable H_2 production on the CuCrO_2 photocathode from water is shown during 1 sun light illumination (1.5 AM , $100 \text{ mW} \cdot \text{cm}^{-2}$) and the efficiency of the process is further increased when inorganic cobalt co-catalyst is added to the electrolyte.

In addition, the successful sensitisation of the CuCrO_2 photocathode is shown using the D3 organic benchmark dye. As a result, considerable increase in photocurrent is shown when electron acceptor is added into the electrolyte and the contribution to the current from the dye is confirmed with IPCE measurement.

5.5 Results and discussion

5.5.1 Synthesis of CuCrO_2

An equimolar proportion of $\text{Cu}(\text{NO}_3)_2 \cdot 3\text{H}_2\text{O}$ and NH_4CrO_4 was ground using a mortar and pestle. The mixture turned to a highly viscous paste having dark brown colour. Few drops of ethanol were added to ensure sufficient mixing of the paste. The formed brown paste was dried to form a dark brown powder. The powder was further ground and then used as a precursor for the synthesis of CuCrO_2 . The precursor powder was heated in N_2 atmosphere at 900°C . For control measurements, the precursor powder was heated in air at 900°C to form second batch of CuCrO_2 powder.

5.5.2 Structural characterisation

Powder X-ray diffraction (pXRD) measurements were conducted on CuCrO_2 powder and thin film samples to determine the phase and purity of the material. Measurements were carried out using Bruker 2D Phaser diffractometer on powders synthesised in air and N_2 (See experimental section in Chapter 2.3.3). The experimental data was analysed using Rietveld refinement to obtain the lattice parameters.

The formation temperature of the phase-pure CuCrO_2 has been shown to be 800°C when using the solid-state route. Amrute et al. showed that the formation in air comprises of four steps while under nitrogen atmosphere it only takes one step.⁴⁰ The formation of phase-pure CuCrO_2 was shown from the solid-state synthesis route after 10 h heating under N_2 atmosphere (Figure 5.2, red). The same synthesis repeated under air also formed the pure CuCrO_2 phase (Figure 5.2, black).

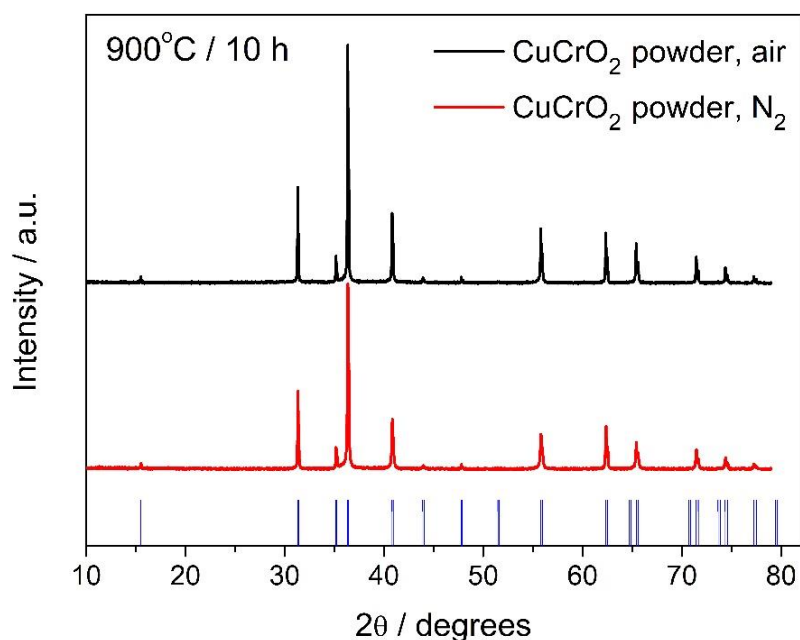


Figure 5.2. Powder X-ray diffraction pattern of CuCrO_2 synthesised in air (black) and under nitrogen (red) at 900°C during 10 h solid-state synthesis. Blue tick marks represent the CuCrO_2 reference pattern peak positions.

The only difference, which can be seen from the diffraction patterns, is the slightly lower relative intensity of the diffraction peaks for the CuCrO_2 powder formed under N_2 atmosphere compared to the diffraction peaks for powder formed in air (Figure 5.2.). The heating time of 10 h was chosen according to the literature results on solid-state synthesis of CuCrO_2 .⁴⁰ Amrute et al. showed that when solid-state synthesis was carried out by mixing $\text{Cu}_2\text{O} + \text{Cr}_2\text{O}_3$ the formation of pure CuCrO_2 phase was incomplete after 10 h of heating at 800°C .⁴⁰ Since solid-state synthesis in this study used different precursors, the 10 h heating time was chosen to observe if that would be sufficient for this synthesis route to form the pure phase. Initially the synthesis was carried out at 800°C according to the CuCrO_2 formation temperature stated in literature.⁴⁰ This, however, did not yield a pure phase, showing impurities on the diffraction pattern. Therefore the 900°C was chosen as the next temperature to test with the same 10 h heating time and as a result, the pure delafossite phase was obtained (Figure 5.2).

The pXRD pattern of CuCrO_2 was further processed using Rietveld refinement to see how the calculated pattern compares to the experimental data and obtain lattice parameters for the CuCrO_2 unit cell. The refinement of the CuCrO_2 pXRD data showed that the lattice parameters for CuCrO_2 unit cell did not differ considerably when comparing results for CuCrO_2 powder made in air and powder made in N_2 and were comparable with the literature values.⁴¹

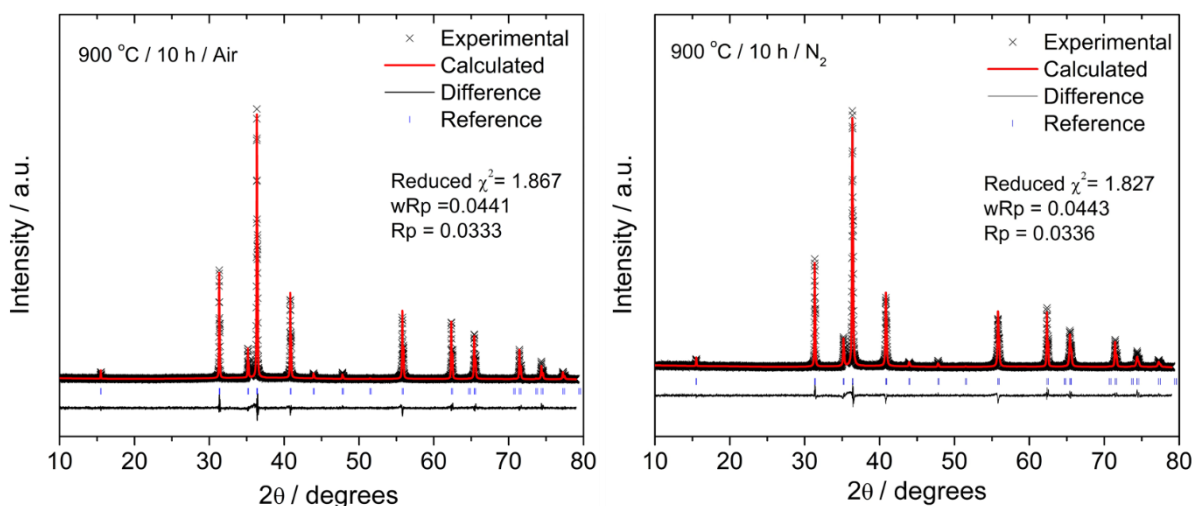


Figure 5.3. Rietveld refinement of powder X-ray diffraction patterns of CuCrO_2 synthesised under N_2 (left) and in air (right). *Made by K. Sardar in E. A. Gibson group, Newcastle University.*

Sample	$a = b$ [\AA]	c [\AA]	V [\AA^3]
CuCrO_2 powder, Air	2.974902(24)	17.10184(17)	131.0746(20)
CuCrO_2 powder, N_2	2.975023(15)	17.10247(15)	131.0902(15)
Literature values	2.9734(3)	17.1000(40)	130.93
Space group $R\bar{3}m$ $H(166)$, $\alpha=\beta=90^\circ$, $\gamma=120^\circ$			

Table 5.1. Lattice parameters of CuCrO_2 unit cell for CuCrO_2 powders made in air and N_2 . Literature values of CuCrO_2 unit cell are included for comparison¹⁹. *Calculated by K. Sardar in E. A. Gibson group, Newcastle University.*

Scanning electron microscopy was carried out on CuCrO_2 films to determine the differences in film morphology depending on the synthesis and treatment properties (see Chapter 2.2.2 for experimental procedure). The images of the films show inhomogeneous surface morphology with particles varying greatly in size (Figure 5.4).

When the films were made from the powder made in air, the particle size is considerable bigger than for the films which were made from the powder formed under N_2 atmosphere while using the same synthesis procedure and parameters. The particles have a platelet type of shape with triangular and hexagonal features. The size of the particles was determined to be from $0.5 \mu\text{m}$ to $2 \mu\text{m}$ on the longer side for the CuCrO_2 films made from powder made under N_2 (Figure 5.4). The post-calcination annealing of films under N_2 , however, did not affect the morphology notably, except for a slight increase in particle size. The thickness of the film was estimated from the SEM image of the cross-section of the film

and was measured to be $9 \pm 3 \mu\text{m}$. The surface of the film is very coarse, and thickness could vary quite a lot due to the nature of the deposition method, which in this case was doctor blading. During doctor blading deposition, the paste is spread on the conducting substrate using a smooth blade by applying stable force. This means that the thickness and uniformity of the film can vary depending on the force applied and human error.

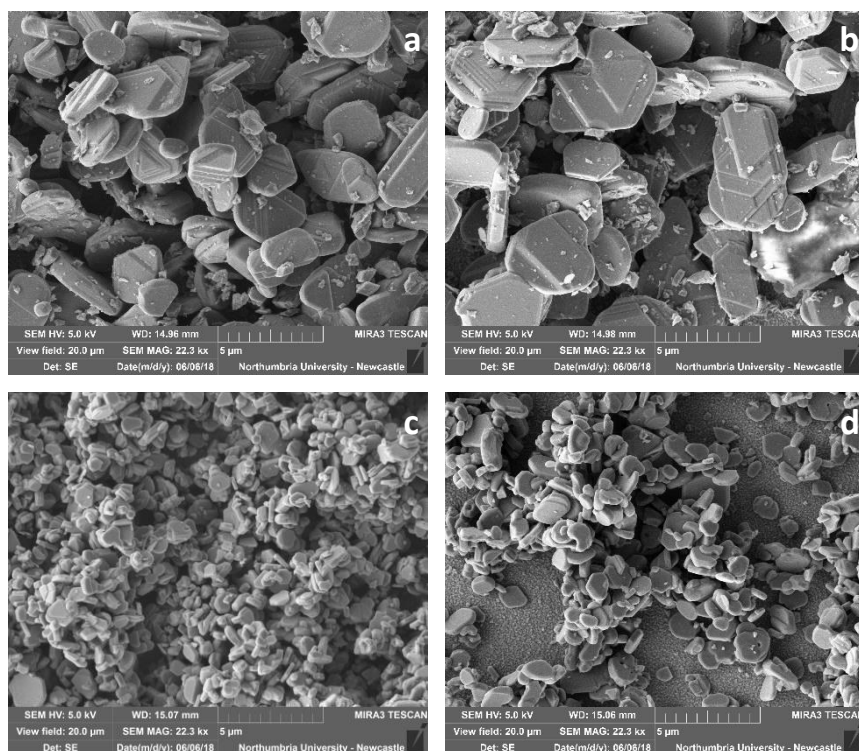


Figure 5.4. Scanning electron microscopy images of CuCrO₂ films: a) powder made in air, film calcined in air, b) powder made in air, film calcined in air + post-calcination annealing in N₂, c) powder made in N₂, film calcined in air, and d) powder made in N₂, film calcined in air + post-calcination annealing in N₂. *Measurement was performed by P. Maiello in Northumbria University.*

Data from pXRD did not show any substantial differences between CuCrO₂ powders made in air and in N₂ apart from the slight difference in peak intensities (Figure 5.2). However, from SEM images it was clearly seen that the particle size for powder made in air is considerably bigger which presumably also has an important effect on the active surface area of the samples and, as a result, on the photoelectrochemical performance. Preliminary PEC measurements were carried out on samples made from those two different powders and it was clearly observed, that the performance and stability of the films made from the powder made in air was considerably lower than the ones made from the powder made under N₂ (Figure

5.6). For this reason, during further studies, the focus was on CuCrO_2 powder made under N_2 and it was used for making samples for all the following experiments.

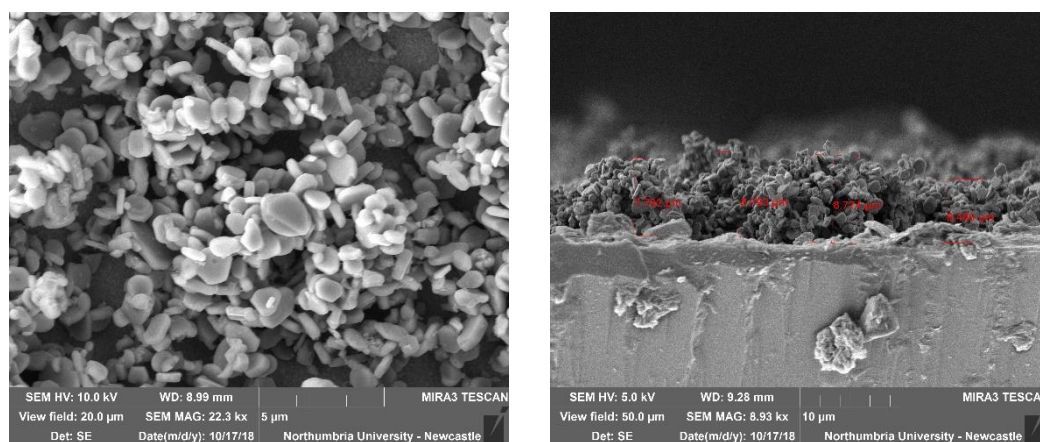


Figure 5.5. SEM images of the CuCrO_2 -N surface morphology (left) and the cross section of the CuCrO_2 -N film. *Measurement was performed by P. Maiello in Northumbria University.*

5.5.3 Electrochemical and photoelectrochemical characterisation

First, the photoelectrochemical performance of photocathodes made from powder made in air and from powder made in N_2 was compared. For that, the LSV and CA on both samples was carried out under chopped light illumination. The results of the CA measurement for both samples are presented below on Figure 5.6.

The CA shows photocurrent densities of $7 \pm 2 \mu\text{A cm}^{-2}$ for the CuCrO_2 photocathode made from powder made in air and $35 \pm 10 \mu\text{A cm}^{-2}$ for the photocathode made from powder made under N_2 . The mean photocurrent was determined by taking a value in the end of every 30 s light illumination period and calculating the average over the whole measurement. The photocurrent is less stable for the photocathode made from powder made under N_2 , but the results still clearly show that when CuCrO_2 powder is made under N_2 atmosphere, then the photocurrent is considerably enhanced. The lower photocurrent could partly be the reason of considerably larger particle size and thereby smaller active area for the CuCrO_2 made in air which can be observed in the SEM figures (Figure 5.4 a and b). Also, powder formation under N_2 atmosphere could also increase the oxygen vacancies in the CuCrO_2 crystal lattice which would effectively increase the hole mobility and conductivity of the material.

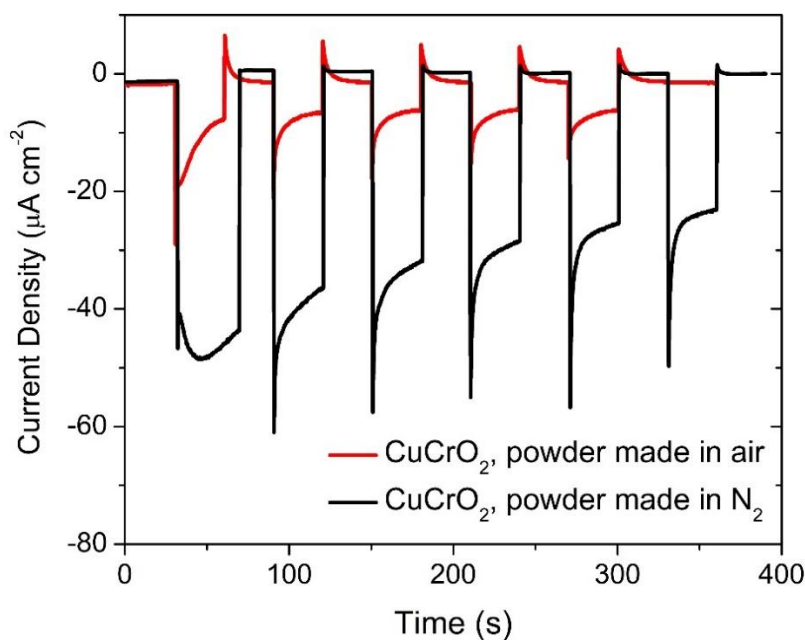


Figure 5.6. CA measurement on CuCrO_2 photocathodes under 0 V vs. Ag/AgCl applied potential and under chopped light illumination. Red - CuCrO_2 made from powder made in air and calcined in air, black – made from powder made in N_2 and calcined in air. Measurements were carried out in a three-electrode PEC cell in pH 5 0.1 M acetate buffer using Ag/AgCl reference electrode (3.0 M NaCl). The electrolyte was purged with N_2 for 15 min. before the measurement.

Xiong et al. reported a synthesis of CuCrO_2 nanocrystals with a size of 15 x 5 nm using a hydrothermal synthesis route. They fabricated high surface area photocathodes from that material and subsequently p-DSSCs, which showed an open circuit voltage, V_{OC} , of 102 mV and a short circuit density, J_{SC} , of 0.491 mA cm^{-2} using a coumarin 343 dye and I_3^-/T^- electrolyte. This result in V_{OC} was better than they achieved with their NiO DSSCs.³⁰ Using the same synthesis route as Xiong et al. Bach and co-workers demonstrated a CuCrO_2 based DSSC showing an V_{OC} of 734 mV and J_{SC} of 1.23 mA cm^{-2} when using $[\text{Co}(\text{en})_3]^{2+/3+}$ redox couple.²⁹ However, Xiong et al. also reported that the CuCrO_2 they synthesised is not thermally stable over 400°C, and they attributed this to the formation of CuCr_2O_4 spinel phase. This contradicts the results from study by Amrute et al. where they showed that pure-phase CuCrO_2 is thermally stable until 1100°C while all other delafossites decomposed at lower temperatures.⁴⁰ In addition, during their pXRD analysis with in-situ heating, they showed that CuCr_2O_4 spinel phase forms first at lower temperatures and then at 800°C the CuCrO_2 starts to form.⁴⁰ In their study CuCr_2O_4 spinel phase was formed from CuO and Cr_2O_3 as they used solid-state synthesis, but it indicates that either oxide or hydroxide impurities must be present in the sample to initiate the formation of the spinel since when the pure CuCrO_2 phase has formed, it is thermally stable.⁴⁰

Because the photocathodes from CuCrO_2 powder made under N_2 clearly showed better photoelectrochemical performance, then further optimisation of the photocathodes was continued using the powder synthesised through the N_2 route. To address the issue of stability, half of the CuCrO_2 photocathodes from powder made under N_2 and calcined in air ($\text{CuCrO}_2\text{-Air}$) were subsequently annealed under N_2 for 3 h at 500°C ($\text{CuCrO}_2\text{-N}_2$). This additional post-calcination annealing could reduce some of the non-stoichiometric species on the surface which might be the reason behind the photocorrosion of the photocathode. Electrochemical and photoelectrochemical characterisation was carried out on $\text{CuCrO}_2\text{-Air}$ and $\text{CuCrO}_2\text{-N}_2$ photocathodes to study the differences in electrochemical behaviour, photocurrent generation and photocurrent stability under light illumination.

Cyclic voltammetry showed that there are substantial differences in electrochemical behaviour between $\text{CuCrO}_2\text{-Air}$ and $\text{CuCrO}_2\text{-N}_2$ photocathodes (Figure 5.7). The $\text{CuCrO}_2\text{-Air}$ shows two reduction peaks at -0.1 and -0.3 V vs Ag/AgCl and an oxidation peak at 0.05 V vs. Ag/AgCl . The $E_{\text{red}} = -0.3$ V can be explained with the reduction of Cr^{6+} to Cr^{3+} .⁵⁵ The quasi-reversible redox process can be attributed to the reduction of Cu^{2+} impurities to Cu^+ ($E_{\text{red}} = -0.1$ V vs Ag/AgCl) on the cathodic sweep and the subsequent oxidation of Cu^+ to Cu^{2+} during the anodic sweep ($E_{\text{red}} = 0.05$ V vs. Ag/AgCl).⁵⁵ This means that the potential of the Cu^{2+} to Cu^+ redox process is within in the band gap of CuCrO_2 and self-reduction takes place in aqueous environment resulting in corrosion and, in the end, destruction of the photocathode (Eq. 5.1 in Chapter 5.1) like it is shown in literature for the $\text{Cu}(\text{I})\text{O}$.^{18,20}

Linear Sweep Voltammetry (LSV) was measured on $\text{CuCrO}_2\text{-Air}$ and $\text{CuCrO}_2\text{-N}_2$ in the dark and under illumination (Figure 5.8). The LSV of $\text{CuCrO}_2\text{-Air}$ shows similar behaviour as shown on the CV with clear reduction peak visible for both on the dark sweep and also under illumination (Figure 5.8, left, black solid and dashed line). These peaks are not observed on the LSV of $\text{CuCrO}_2\text{-N}_2$ (Figure 5.8, left, green solid and dashed line). More importantly, the photocurrent onset potential of $\text{CuCrO}_2\text{-N}_2$ is considerably more positive than the photocurrent onset potential of $\text{CuCrO}_2\text{-Air}$, 0.4 V vs Ag/AgCl for $\text{CuCrO}_2\text{-N}_2$ compared to 0.15 V vs Ag/AgCl for $\text{CuCrO}_2\text{-Air}$. Since the $J_{\text{ph.o}}$ is considered to be used as a reliable measure to determine the flat band potential, V_{fb} , of the semiconductor (un-doped), then it shows that the V_{fb} $\text{CuCrO}_2\text{-N}_2$ is more positive than for the $\text{CuCrO}_2\text{-Air}$ sample.^{58,59} One reason for that could be the removal of oxygen from the crystal lattice which increases the concentration of holes in the lattice.

The result is overall a good indication that the $\text{CuCrO}_2\text{-N}_2$ photocathode is much better candidate for a tandem PEC cell, because in addition to stability, higher photocurrent onset

potential makes it also easier to be coupled with a suitable photoanode to run the full water splitting reaction.¹⁹

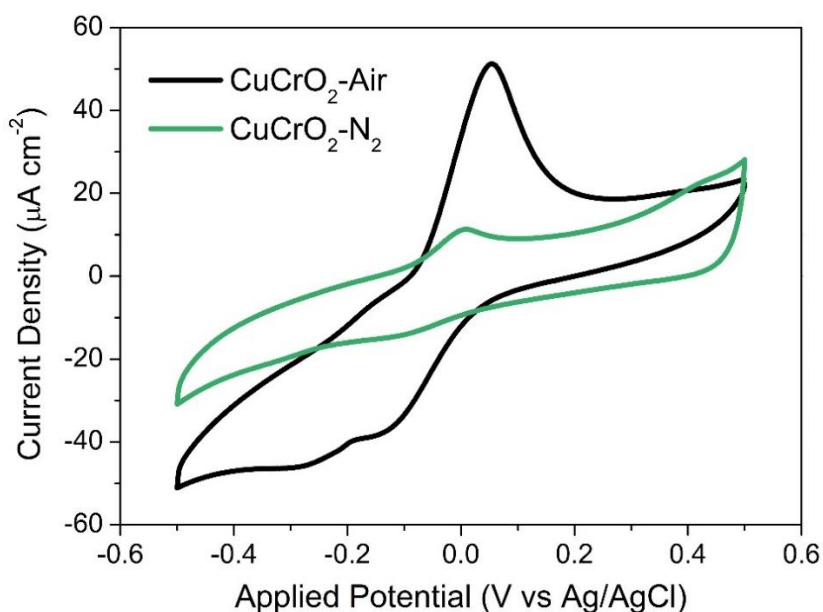


Figure 5.7. Cyclic Voltammetry of $\text{CuCrO}_2\text{-N}_2$ (green) and $\text{CuCrO}_2\text{-Air}$ (black) in the dark in pH 5 0.1 M acetate buffer measured in a three-electrode cell, scan rate 10 mV s^{-1} , with Ag/AgCl reference electrode (3.0 M NaCl). The electrolyte was purged with N_2 for 15 min. before the measurement.

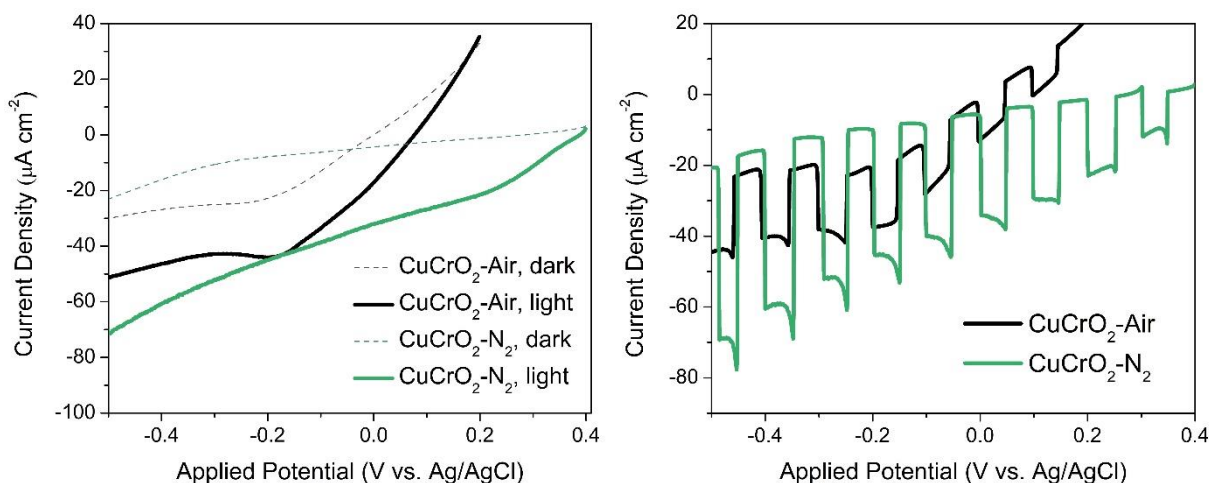


Figure 5.8. Left: LSV of $\text{CuCrO}_2\text{-N}_2$ (green) and $\text{CuCrO}_2\text{-Air}$ (black) in the dark (dashed line) and under 1 sun illumination (solid line). Right: LSV of $\text{CuCrO}_2\text{-N}_2$ (green) $\text{CuCrO}_2\text{-Air}$ (black) under chopped light 1 sun illumination. Measurements were carried out in a three-electrode PEC cell in pH 5 0.1 M acetate buffer using Ag/AgCl reference electrode (3.0 M NaCl). The electrolyte was purged with N_2 for 15 min. before the measurement.

To study and compare the stability of the $\text{CuCrO}_2\text{-Air}$ and $\text{CuCrO}_2\text{-N}_2$ the chronoamperometry measurements were conducted on both systems under chopped and constant light. The chopped light chronoamperometry measurement showed that for the $\text{CuCrO}_2\text{-Air}$ the photocurrent decreased considerably over time (Figure 5.8, black), and from the longer measurement during 1 h constant light, it was observed that the photocurrent was diminished to only few $\mu\text{A cm}^{-2}$ by the end of the measurement (Figure 5.18). This is a clear indication that the $\text{CuCrO}_2\text{-Air}$ photocathode is not stable under the experimental conditions and photocorrosion takes place due to the redox processes discussed previously presented on CV (Figure 5.7). The $\text{CuCrO}_2\text{-N}_2$, however, showed stable photocurrents over time under chopped light conditions (Figure 5.8, green). When light illumination was applied during CA on $\text{CuCrO}_2\text{-N}_2$, then a moderate transient spike was observed in the beginning on the photocurrent window, which indicated that there is a fast recombination process present in the system.¹³ When light illumination is applied on $\text{CuCrO}_2\text{-N}_2$ photocathode, the electrons are excited from the VB to the CB from where they transfer to the surface of the photocathode and drive the proton reduction half-reaction. On $\text{CuCrO}_2\text{-Air}$ photocathode, the same process takes place initially, however, the excited electrons on CB is, in large extent, reduce the photocathode.

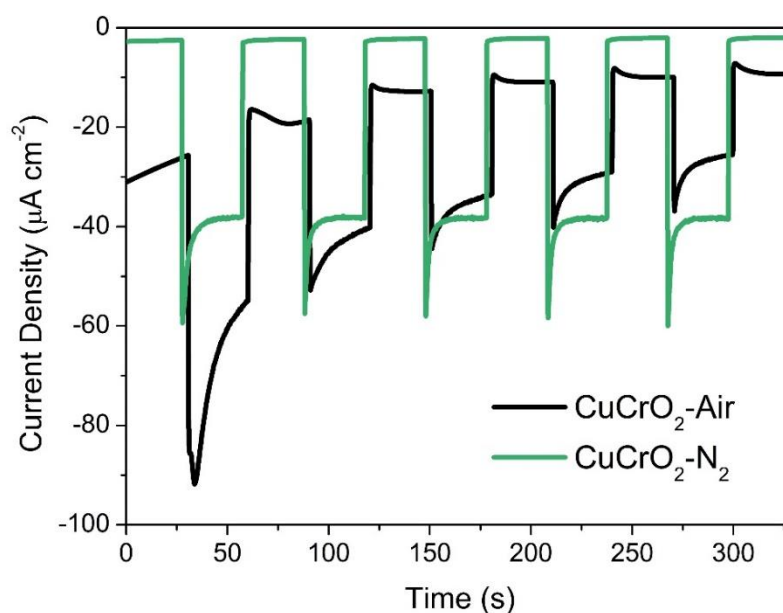


Figure 5.9. CA of $\text{CuCrO}_2\text{-N}_2$ (green) and $\text{CuCrO}_2\text{-Air}$ (black) under $E_{\text{appl}} = -0.2$ V vs. Ag/AgCl (0 V vs. NHE). Chopped light 1 sun illumination was applied with 30 s intervals (30 s in the dark / 30 s under illumination) in pH 5 0.1 M acetate buffer in a three electrode PEC cell using Ag/AgCl reference electrode (3.0 M NaCl). The electrolyte was purged with N_2 for 15 min. before the measurement.

The $\text{CuCrO}_2\text{-N}_2$ photocurrent-potential dependence was further studied with LSV when an electron acceptor was present in the solution (Figure 5.10). The main aim of that experiment was to see if the additional electron acceptor would decrease the recombination and increase photocurrents. As a result, when 5 mM DTDP (2,2'-dithiodipyridine) electron acceptor was added to the solution ($E_{\text{redox}} = -0.26 \text{ V vs Ag/AgCl}$, see Table 3.1 in Chapter 3.5.1.1), the photocurrent increased slightly during the LSV chopped light measurement (Figure 5.10, red line). More importantly, the transient spikes were not observed when DTDP was present which suggests that the recombination was hindered. Therefore, there is a possibility that when instead of EA we would have a suitable co-catalyst in solution, the efficiency of the catalyst- CuCrO_2 system could be increased.

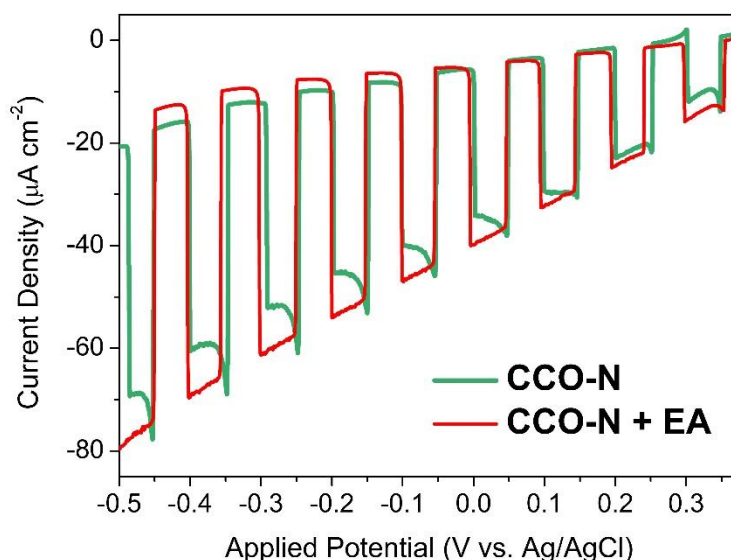


Figure 5.10. LSV of $\text{CuCrO}_2\text{-N}_2$ under chopped light illumination applied with 5 s intervals (5 s in the dark / 5 s under 1 sun illumination). Measurement was carried out in pH 5 0.1 M acetate buffer without electron acceptor (green) and with 5 mM DTDP (2,2'-dithiodipyridine) electron acceptor in solution (red). Measurement was conducted in a three-electrode custom made PEC cell using Ag/AgCl reference electrode (3.0 M NaCl). The electrolyte was purged with N_2 for 15 min. before the measurement.

The Incident Photon-to-Current Efficiency (IPCE) measurement was carried out on $\text{CuCrO}_2\text{-N}_2$ and $\text{CuCrO}_2\text{-Air}$ photocathodes to see the current generation dependence on the wavelength of the incident light (Figure 5.11). The measurement showed that almost all the current is generated by the light with the wavelength under 400 nm. This result shows that

there is great potential in functionalisation of the photocathodes with additional light absorbers to harvest the photons in the visible spectrum of the light.

The band gap, E_g , of the material was determined from the Tauc plot constructed using the IPCE data. The indirect band gap of CuCrO_2 was estimated from graph $(\text{IPCE} \cdot h\nu)^2$ vs E for both $\text{CuCrO}_2\text{-N}_2$ and $\text{CuCrO}_2\text{-Air}$ photocathodes. For $\text{CuCrO}_2\text{-Air}$ the band gap was estimated to be 3.14 eV and for $\text{CuCrO}_2\text{-N}_2$ 3.05 eV, which is in line with the previously reported values in literature using a similar method for the band gap determination.³⁶

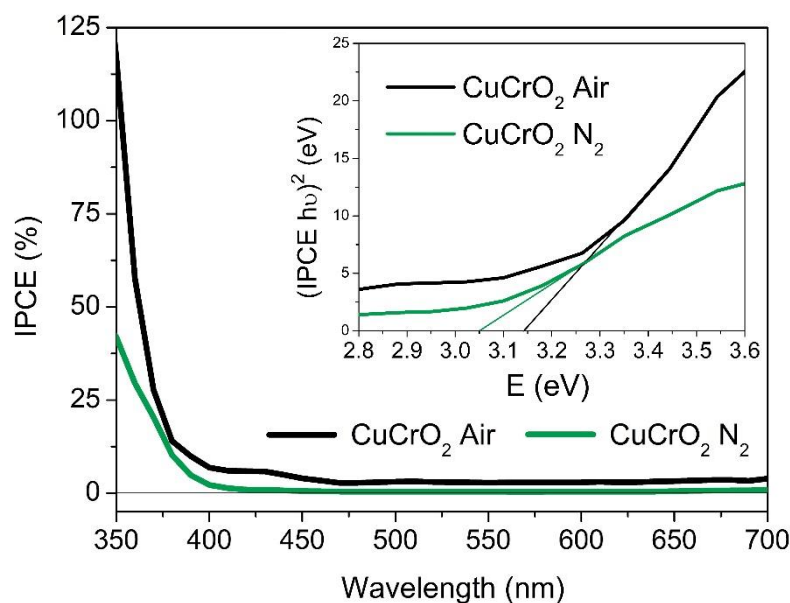


Figure 5.11. IPCE of $\text{CuCrO}_2\text{-N}_2$ (green) and $\text{CuCrO}_2\text{-Air}$ in three-electrode PEC cell in pH 5 0.1 M acetate buffer with 5 mM DTDP under $E_{\text{appl}} = 0$ V vs. Ag/AgCl. Inset: Tauc plot of $(\text{IPCE} \cdot h\nu)^2$ vs E of $\text{CuCrO}_2\text{-N}_2$ (green) and $\text{CuCrO}_2\text{-Air}$ showing the band gap energies for indirect transition for both photocathodes through extrapolation to the x-axis. The electrolyte was purged with N_2 for 15 min. before the measurement.

5.5.4 Optical characterisation

To determine the optical properties of the material the diffuse reflectance measurements were carried out on the photocathodes in reflectance and transmittance mode (Figure 5.12). The measurement showed a large difference in the broad absorption between $\text{CuCrO}_2\text{-N}_2$ and $\text{CuCrO}_2\text{-Air}$ films. This could be due to Cu^{2+} impurities in the $\text{CuCrO}_2\text{-Air}$ sample, which increase the absorption in the visible spectrum as CuO (cupric oxide), formed as impurity, is in its pure form a narrow band gap semiconductor absorbing the high energy photons.²⁰ Both reflectance and transmittance measurements showed a transition at 600 nm which is previously reported as a d-d transition in Cr^{3+} octahedra¹³. It is reasoned that because

the transitions are localised within Cr^{3+} octahedra, the photon absorption does not result in charge separation and therefore, doesn't contribute to photocatalysis.

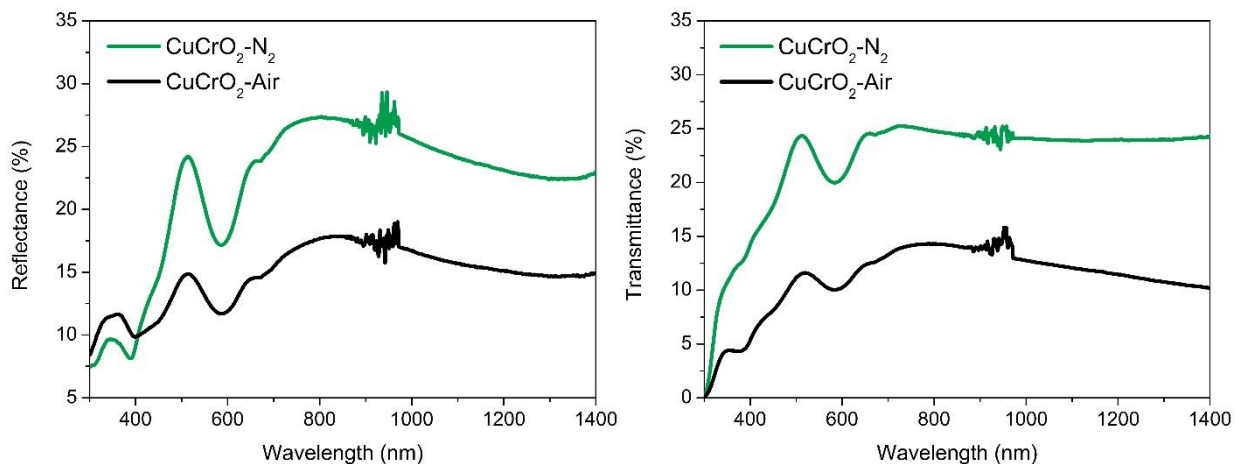


Figure 5.12 Diffuse reflectance (left) and transmittance (right) of $\text{CuCrO}_2\text{-N}_2$ (green) and $\text{CuCrO}_2\text{-Air}$ (black) films.

5.5.5 Surface characterisation

X-ray photoelectron Spectroscopy (XPS) surface analysis was performed to determine if there are differences in surface chemistry between the $\text{CuCrO}_2\text{-Air}$ and $\text{CuCrO}_2\text{-N}_2$ samples, which could be the reason behind the different PEC performance of the photocathodes. The Cr 2p region shows that this is indeed the case. The $\text{CuCrO}_2\text{-Air}$ sample shows a substantial peak at 579.8 eV, which can be assigned to Cr^{6+} (Figure 5.12.a).²⁰ On the $\text{CuCrO}_2\text{-N}_2$ Cr 2p region, however, this peak is not observed (Figure 5.12.b). It suggests that during the post-calcination annealing under N_2 atmosphere, all the Cr^{6+} is reduced to Cr^{3+} . This can be reasoned as due to the loss of oxygen. Cr 2p is shown to contain several doublet-split components in Cr(III) oxides, so all three components 1, 2 and 3 on Cr 2p scan (Figure 5.12.a and b) are assigned to Cr^{3+} , of which the main component 2 is at 576.1 eV.^{20,56,57} The weak satellite feature on the Cu 2p scan for both $\text{CuCrO}_2\text{-Air}$ (Figure 5.12.c) and $\text{CuCrO}_2\text{-N}_2$ (Figure 5.12.d) shows that the main Cu species present in the photocathodes is Cu^+ .²⁰ The main difference between $\text{CuCrO}_2\text{-Air}$ and $\text{CuCrO}_2\text{-N}_2$ Cu 2p region is that the $\text{CuCrO}_2\text{-Air}$ contains a substantial second component (2), which is much less pronounced on $\text{CuCrO}_2\text{-N}_2$ Cu 2p region. In addition, the $\text{CuCrO}_2\text{-Air}$ Cu 2p region has more pronounced satellite features than the $\text{CuCrO}_2\text{-N}_2$ Cu 2p region. Both observations suggest that the $\text{CuCrO}_2\text{-Air}$ Cu 2p region has a small amount of Cu^{2+} present in the sample.

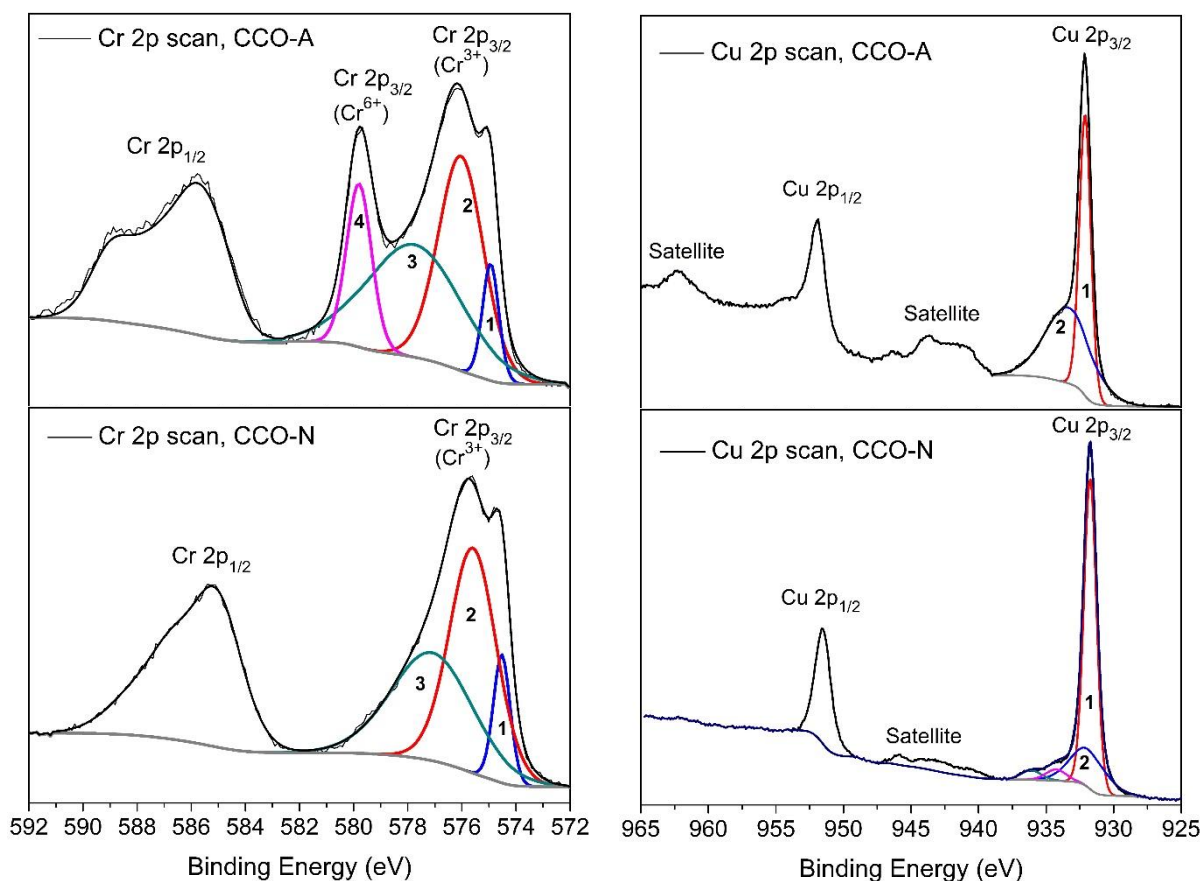


Figure 5.13. XPS results of Cr 2p scan for $\text{CuCrO}_2\text{-Air}$ (left, up, a) and $\text{CuCrO}_2\text{-N}_2$ (left, below, b), and Cu 2p scan for $\text{CuCrO}_2\text{-Air}$ (right, up, c) and $\text{CuCrO}_2\text{-N}_2$ (right, below, d).

5.5.6 Electrochemical impedance spectroscopy

Electrochemical Impedance Spectroscopy (EIS) measurements showed that the charge transfer resistance was higher for the $\text{CuCrO}_2\text{-Air}$ samples than for the $\text{CuCrO}_2\text{-N}_2$ samples, which had gone through a post-calcination annealing treatment under N_2 (Figure 5.13). In addition, EIS under light illumination (AM1.5 , 100 mW cm^{-2}) also showed that light illumination has a positive effect on the charge transfer resistance, by decreasing it as expected. During light illumination, the electrons are excited from VB to the CB and from there to the photocathode surface, where they drive the H_2 evolution. The $\text{CuCrO}_2\text{-Air}$ sample had a charge transfer resistance of 610Ω under light illumination, while the $\text{CuCrO}_2\text{-N}_2$ sample showed a charge transfer resistance of 520Ω .

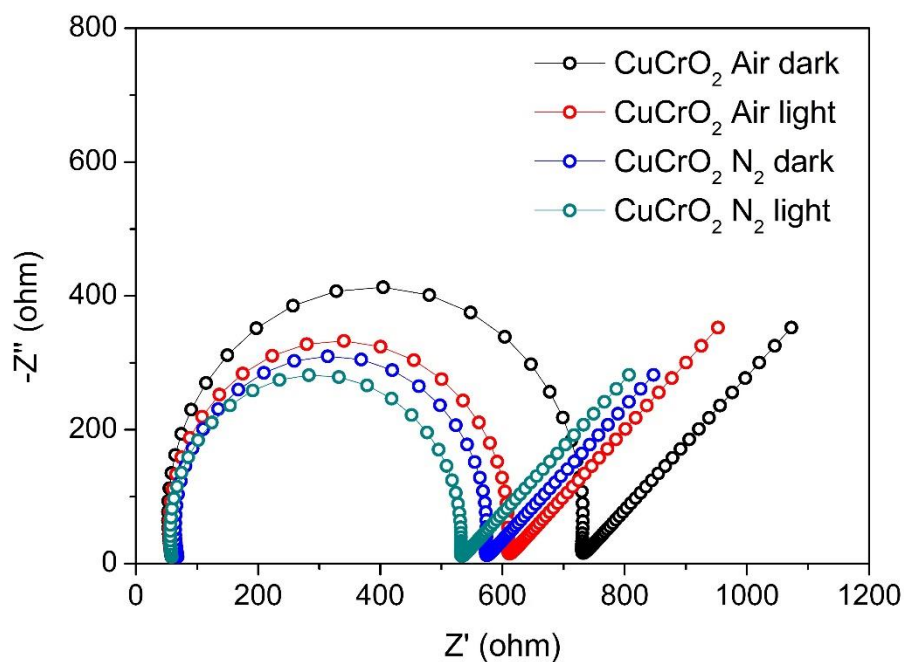


Figure 5.14. EIS Nyquist plot of CuCrO_2 -Air and CuCrO_2 - N_2 in the dark and under 1 sun (1.5 AM , $100 \text{ mW}\cdot\text{cm}^2$) light illumination, under -0.2 V vs Ag/AgCl (0 V vs NHE) The measurement was carried out in a three-electrode custom-made PEC cell with Ag/AgCl (3.0 M NaCl) reference electrode in $\text{pH}5$ 0.1 M acetate buffer. The experimental data was fitted using IviumSoft Equivalent Circuit Analysis. The electrolyte was purged with N_2 for 15 min. before the measurement.

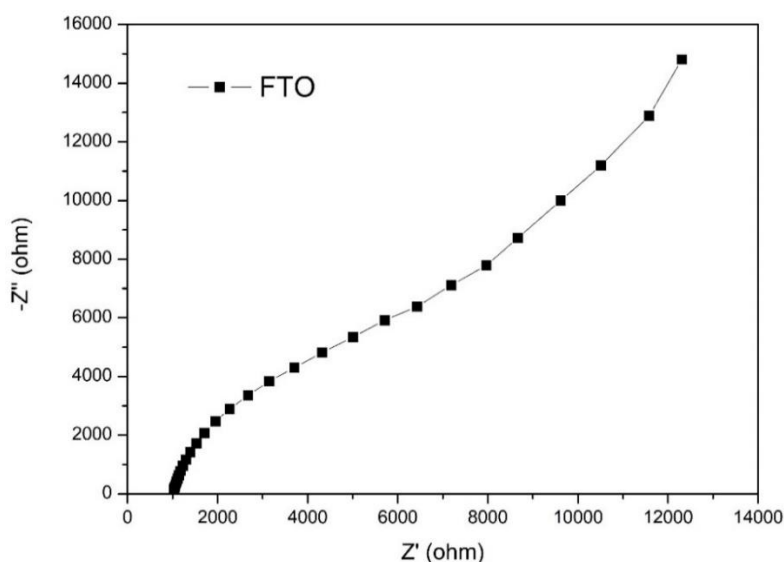


Figure 5.15. EIS of FTO in $\text{pH}5$ 0.1 M acetate buffer. Measured in a custom made one compartment three electrode cell with $\text{Pt}|\text{FTO}$ CE and Ag/AgCl reference (3.0 M NaCl). The measurement was performed by *J. Mallows* according to instructions of *N. Pöldme*.

As the results from the PEC measurements showed (Chapter 5.5.2) and are confirmed also by PEC measurement combined with GC analysis in Chapter 5.5.6, the processes under light illumination in CuCrO₂-Air are mostly governed by photocorrosion. This increases also the charge transfer resistance, since there is lower driving force for electrons to be transferred to the electrode surface. The lower charge transfer resistance supports the findings from the photoelectrochemical measurements where higher photocurrent was observed for the CuCrO₂-N₂ photocathodes. The EIS of bare FTO electrode measured under same experimental conditions is presented as a comparison (Figure 5.15), showing a conductor-like behaviour.

5.5.7 H₂ evolution and faradaic efficiency

H₂ evolution was detected and quantified by analysing the gas from the headspace of the PEC reactor after 1 h chronoamperometry measurement, under constant light illumination (Figure 5.17). During these measurements, an applied potential of -0.2 V vs. Ag/AgCl was applied (approximately 0 V vs NHE, see Chapter 2.3.6) H₂ evolution was measured on CuCrO₂-N₂ and CuCrO₂-Air in pH 5, 0.1 M acetate buffer, without the co-catalyst and on the CuCrO₂-N₂ in the same buffer solution with co-catalyst C1, (Bu₄N)Co(bdt)₂ (where bdt – 1,2-benzenedithiolate), added to the solution (Figure 5.16). The C1 organometallic catalyst was previously synthesised according to the modified literature method, described in Chapter 2.2.6.⁴⁴ The faradaic efficiency, η_{Far} , was calculated for every measurement with CuCrO₂-N₂ to compare the efficiency of the H₂ evolution on photocathodes with different C1 concentrations in solution.

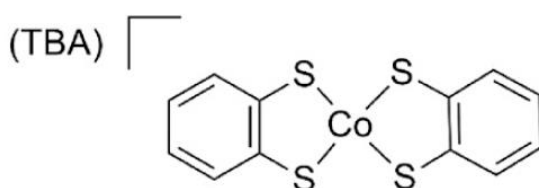


Figure 5.16. Structure of the co-catalyst C1, (Bu₄N)Co(bdt)₂ (where bdt – 1,2-benzenedithiolate).

The initial reason to use an inorganic co-catalyst in solution, which led to the C1 to be chosen for this study, was that the initial tests with electrodeposited catalysts on CuCrO₂ electrode surface failed and it was reasoned that using an inorganic catalyst in solution could

be a better strategy to increase the Faradaic efficiency of the H₂ evolution process. The co-catalyst C1 has been reported previously to be active photocatalyst for H₂ evolution with turnover number, TON, of 2700 over 12 h.⁴⁴ It was chosen due its suitably low redox potential, $E_{\text{redox}} = -0.4$ vs NHE (-0.6 vs Ag/AgCl) and because it dissolves in low concentrations in aqueous electrolyte.⁴⁴

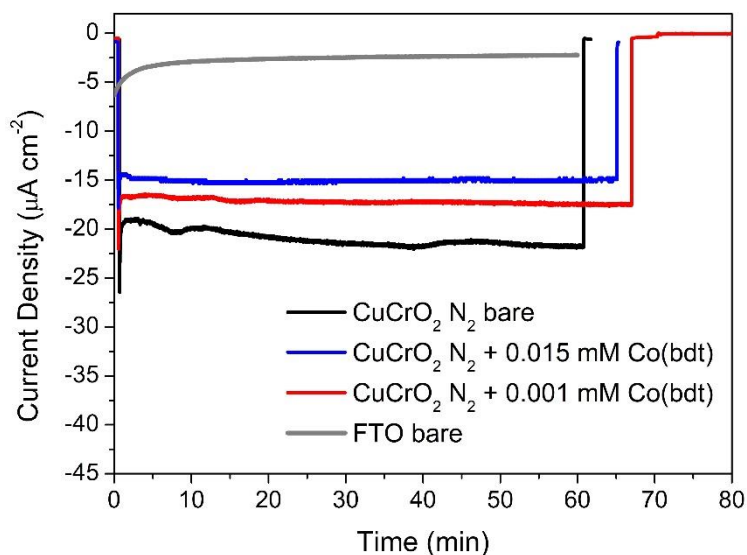


Figure 5.17. Chronoamperometry of CuCrO₂-N₂ with varying concentrations of C1 co-catalyst in solution. Measured under -0.2 V vs Ag/AgCl applied potential and constant 1 sun illumination in a three electrode PEC cell. Chronoamperometry of the bare FTO electrode under constant light and -0.6 V vs. Ag/AgCl is added as a control. Measurement was conducted in a three-electrode custom made PEC cell using Ag/AgCl reference electrode (3.0 M NaCl). The electrolyte was purged with N₂ for 15 min. before the measurement.

	η_{Far} (%)	J_{photo} ($\mu\text{A cm}^{-2}$)*	H ₂ produced (mol h ⁻¹)	Charge (C cm ⁻²)
CuCrO ₂ -Air	No H ₂ was detected	5 ± 1	-	
CuCrO ₂ -N ₂	24.9 ± 1	22 ± 2	76 ± 3	0.059
CuCrO ₂ -N ₂ + 0.001 mM C1	36.0 ± 1	17 ± 2	118 ± 5	0.056
CuCrO ₂ -N + 0.015 mM C1	40.9 ± 2	15 ± 1	98 ± 5	0.046

Table 5.2. Faradaic efficiencies, η_{Far} , moles of H₂ produced, photocurrents, J_{photo} , and charge produced during the CA of CuCrO₂-N₂ with and without catalyst, C1. The H₂ was collected

after the measurement from the headspace of the PEC cell. *Photocurrent values for CuCrO₂-Air sample was taken in the end of the measurement just before the light was turned off.

The chronoamperometry of CuCrO₂-Air showed a rapid decrease in photocurrent which was measured to be only few $\mu\text{A cm}^{-2}$ by the end of the 1 h measurement (Figure 5.18). In addition, no H₂ was detected with the GC when gas from the PEC cell headspace was analysed in the end of the measurement. The photocurrents during measurements with CuCrO₂-N₂, however, were stable during the whole 1 h measurement and stayed around between 15 – 25 $\mu\text{A cm}^{-2}$. Also, H₂ was detected with the GC for measurements without the C1 co-catalyst and also during measurements where the C1 was added to the buffer solution.

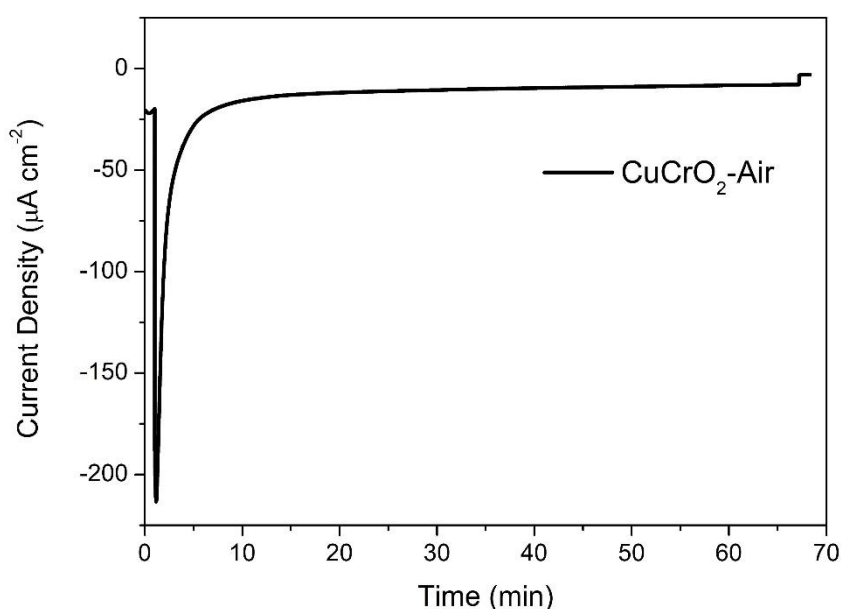


Figure 5.18. CA of CuCrO₂-Air photocathode under -0.2 V vs Ag/AgCl in pH 5 0.1 M acetate buffer. Measurement was conducted in a three-electrode custom made PEC cell using Ag/AgCl reference electrode (3.0 M NaCl). The electrolyte was purged with N₂ for 15 min. before the measurement.

The processes taking place when the light illumination is applied to the CuCrO₂-N₂ photocathode with and without the co-catalyst C1 are presented on Figure 5.19. When the electrode is illuminated, electrons are excited from the CuCrO₂ VB to the CB (1), from there, electrons transfer to the CuCrO₂ surface and either directly catalyse the H₂ evolution (H⁺ reduction half-reaction, equation 5.2) (2) and/or reduce the C1 co-catalyst which then in turn catalyses the H⁺ reduction (3).

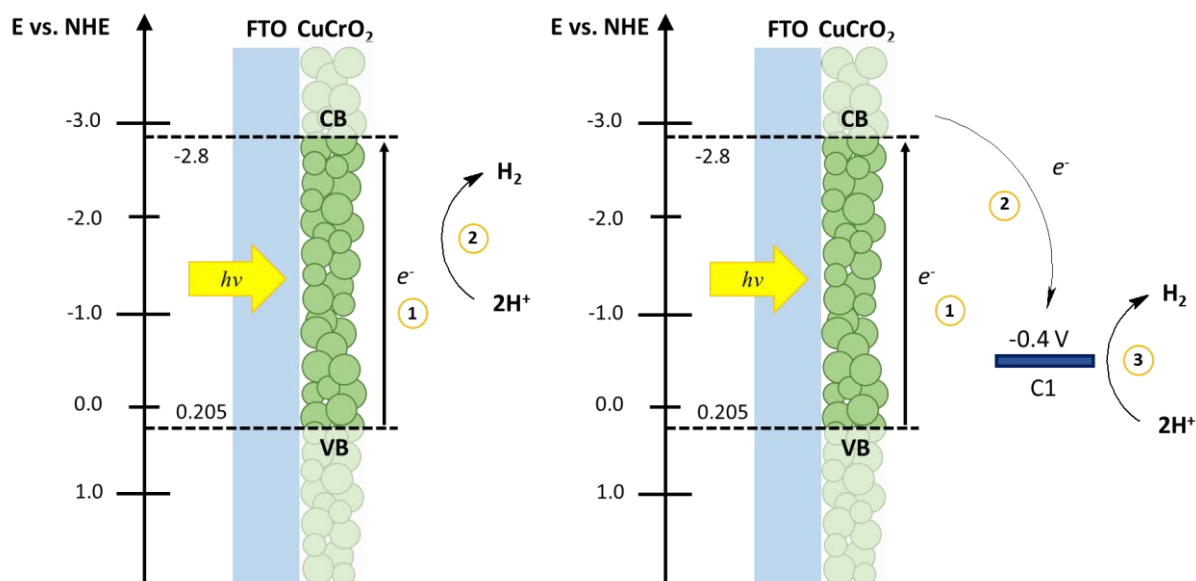


Figure 5.19. Schematics of the working principle of the PEC H_2 evolution on the $CuCrO_2-N_2$ photocathode. Left - $CuCrO_2-N_2$ without C1 co-catalyst: electrons are excited from the $CuCrO_2$ VB to the CB (1), H^+ reduction half-reaction takes place on the $CuCrO_2$ surface (2). Right - $CuCrO_2-N_2$ with C1 co-catalyst: electrons are excited from the $CuCrO_2$ VB to the CB (1), excited electrons reduce the C1 (2), reduced C1 catalyses H^+ reduction half-reaction (3).

For the measurement with $CuCrO_2-N_2$ without any C1 in solution the $\eta_{Far} = 25\%$, which is surprisingly low. When the C1 co-catalyst was added to the solution, the calculated faradaic efficiencies were, however, higher for specific concentrations of C1. The highest efficiencies were calculated for $c[C1] = 0.001$ mM with $\eta_F = 36\%$ and for $c[C1] = 0.015$ mM with $\eta_{Far} = 41\%$ (Table 5.2). Although the efficiency is still low, the results clearly show that with the additions of suitable co-catalyst the efficiency of the process can be increased as predicted from the experiment with electron acceptor (Figure 5.10 in Chapter 5.5.2). The losses in efficiency could be due to photocorrosion of the $CuCrO_2$ due to the inefficient electron transfer from the CB of $CuCrO_2$ to the catalyst as the electrons, which are transferred to the catalyst, would instead reduce the material itself. Other source of losses in efficiency could be due to recombination of H_2 and O_2 since there is no membrane in the PEC cell and also since loss of collected gas could happen when the gas sample is collected from the cell.

5.5.8 Functionalisation of CuCrO_2 with an organic dye

Since CuCrO_2 mainly absorbs photons in the UV region of the solar spectrum, then the strategy to functionalise the material with additional photoabsorbers which could absorb photons in the visible region of the light would be very beneficial. Recently Reisner and co-workers were able to functionalise the CuCrO_2 photocathodes with an organic dye and generate H_2 when co-sensitising the photocathode with an organometallic catalyst.⁴⁴ In this study, the aim was to adopt a similar strategy to see if the CuCrO_2 synthesised with our method can be similarly functionalised, but with a different, smaller organic dye molecule D3, which is commercially available benchmark p-type dye used in DSSCs and dye-sensitised PEC applications.⁴³ It was also used to study the photocurrent generation and H_2 evolution on dye-sensitised D3|NiO photocathode in Chapter 3.5.

The CuCrO_2 electrodes were sensitised with D3 dye in a dye bath (0.3 mM in EtOH) and were subsequently characterised using a chopped light LSV measurement with the addition of 5 mM DTDP (dithiodipyridine) in solution, which acts as an electron acceptor. The aim of the experiment was to test whether the dye adsorbed on the photocathode surface would increase the photocurrent generated under illumination with white light. Using the EA to drive a one electron reduction assured that the charge transfer dynamics are not limited by the catalysis step and maximum photocurrent for the given system can be determined.

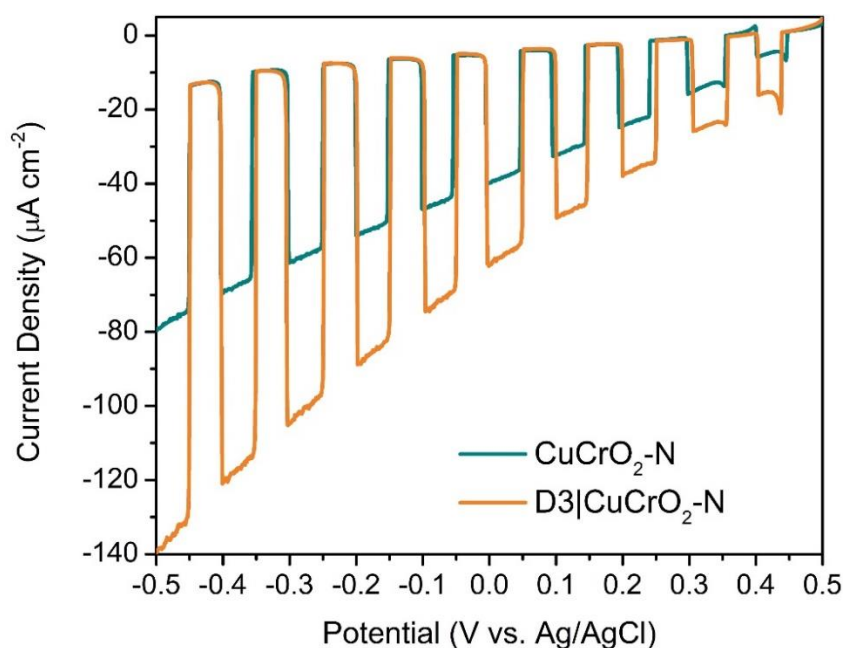


Figure 5.20. LSV of $\text{CuCrO}_2\text{-N}_2$ photocathodes under chopped light illumination (30 s dark / 30 s light in pH5 0.1 M acetate buffer with 5 mM DTDP electron acceptor. Green – bare

CuCrO₂-N, Orange – CuCrO₂-N₂ with P1 dye. Measurement was conducted in a three-electrode custom made PEC cell using Ag/AgCl reference electrode (3.0 M NaCl). The electrolyte was purged with N₂ for 15 min. before the measurement.

The LSV measurement showed an increase in the photocurrent when the CuCrO₂ photocathode was sensitised with the D3 dye (Figure 5.20). The photocurrent for bare CuCrO₂-N₂ photocathode was 55 $\mu\text{A cm}^{-2}$ at -0.2 V vs Ag/AgCl, while at the same applied potential the D3| CuCrO₂-N₂ generated 90 $\mu\text{A cm}^{-2}$. It can be concluded that the dye does work and contributes to the photocurrent when the EA is in the solution to accept the excited electron from the dye.

To further confirm that the CuCrO₂ functionalisation with the dye has been successful, the IPCE measurement was carried out (Figure 5.21). The IPCE measurement showed the contribution at the wavelengths of the D3 absorption (Chapter 3.5.3) and an IPCE of *ca.* 1.2% at 520 nm. This is considerably lower than reported in literature on D3|NiO photocathode, for which an IPCE of 64 % was achieved.⁵¹ The comparison however cannot be directly made because the literature value accounts for a DSSC cell with organic electrolyte and redox couple in the electrolyte.

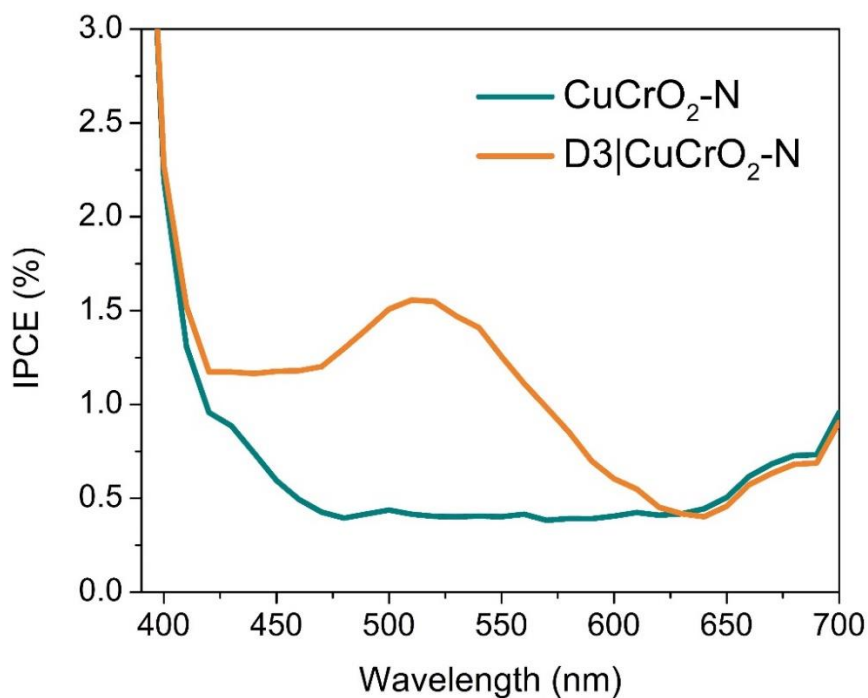


Figure 5.21. IPCE of a bare CuCrO₂-N₂ (green) and P1| CuCrO₂-N₂ photocathode (orange) measured in a three-electrode PEC cell under 0 V vs Ag/AgCl. Measurement was conducted

in a three-electrode custom made PEC cell using Ag/AgCl reference electrode (3.0 M NaCl). The electrolyte was purged with N₂ for 15 min. before the measurement.

In addition, it is important to take account that the CuCrO₂ particle size for samples used in this study was considerably larger (0.5 μm to 2 μm) than for optimised NiO samples reported in literature and also used in this thesis in Chapters 3 and 4, which is approximately 20-30 nm.

IPCE measurement under comparable conditions was made by Creissen et al. showing IPCE of 0.6 % for their CuCrO₂ photocathode co-sensitised with a phosphonated diketopyrrolopyrrole dye (DPP-P) with a Ni-bis(diphosphine) (NiP) catalyst.³⁹ However, they reported a particle size of approximately 70 nm in length and thickness of approximately 18 nm.

It can be concluded that the dye-sensitisation in this project was successful and increase in photocurrent density was observed when using EA in solution. In addition, comparable results to the literature values in terms of IPCE were obtained. However, since there is a lack of reports with similar dye-sensitised systems based on CuCrO₂, direct comparison can't be made with the existing literature and further studies are needed to make more thorough conclusions.

5.6 Effect of partial chromium substitution with iron: photoelectrochemical study of $\text{CuCr}_{0.5}\text{Fe}_{0.5}\text{O}_2$

5.6.1 Introduction

An additional study was made where Fe was added to the CuCrO_2 to form $\text{CuCr}_{0.5}\text{Fe}_{0.5}\text{O}_2$ mixed metal delafossite. It has been shown that the introduction of Fe^{3+} to the Cr^{3+} site results in the expansion of the crystal lattice. This in turn induces the oxygen insertion to the lattice and thereby increases the hole concentration.⁵² CuFeO_2 is another photoactive delafossite with a narrow band gap of approximately 1.47 eV.²⁴ Prevo et al. showed that thin film CuFeO_2 electrode can produce considerable photocurrents under illumination when coated with Al doped ZnO (AZO)| TiO_2 using ALD deposition with Pt catalyst on top, but without the coating the material is unstable producing nearly negligible photocurrents due to photocorrosion.²⁴ Stable photocurrents were shown when O_2 was used as the sacrificial agent in 0.1 M NaOH (pH 13) at +0.4 V vs RHE, which corresponds to approximately -0.57 V vs Ag/AgCl.²⁴ This however makes the material expensive when applied industrially, because ALD is an expensive technique and the cathodic overpotential needed for stable photocurrents is high resulting in high running costs of the process. Therefore, finding a material which could produce high photocurrents at lower overpotentials while being stable under the operating conditions is vital.

The aim of this study was to see how the Fe^{3+} addition to the delafossite crystal lattice influences the photoelectrochemical performance and stability of the material, since the band gap of the material should decrease as a result of the Fe addition and so the lower energy photons in the visible spectrum could also be harvested. The same time, it would be interesting to see if the stability of CuCrO_2 is retained by the material as the high stability of N_2 annealed CuCrO_2 was already demonstrated in previous section (Chapter 5.5).

5.6.2 Results and discussion

5.6.2.1 Structural characterisation

The $\text{CuCr}_{0.5}\text{Fe}_{0.5}\text{O}_2$ was synthesised using a sol-gel route described in detail in Chapter 2.2.3. The synthesis, paste fabrication and photocathode fabrication from the paste was carried out by K. Sardar. The sol-gel route was chosen instead of solid-state route as for the CuCrO_2 due the ease and precision of adding additional components to the material. The as-synthesised powder was annealed for 10 h under N_2 at 1000°C. The 10 h annealing time was

chosen according to the CuCrO_2 annealing time and the temperature was chosen arbitrarily to make sure the pure phase is formed leaving room for future optimization.

The pXRD measurement was carried out on the $\text{CuCr}_{0.5}\text{Fe}_{0.5}\text{O}_2$ powder to determine the phase and purity of the material. Measurements were carried out using Bruker 2D Phaser diffractometer on powders synthesised in air and N_2 (See experimental section in Chapter 2.3.3). The diffraction pattern of $\text{CuCr}_{0.5}\text{Fe}_{0.5}\text{O}_2$ powder is presented on Figure 5.22 along with the diffraction pattern of CuCrO_2 powder. It can be observed that the $\text{CuCr}_{0.5}\text{Fe}_{0.5}\text{O}_2$ diffraction pattern shows pure delafossite phase with slight shift of peak positions to the lower 2θ angle. This is a good indication of the successful Fe insertion into the crystal lattice, since the Fe atoms are larger in size than Cr atoms and the lattice will expand resulting in peak shifts to the smaller angles.

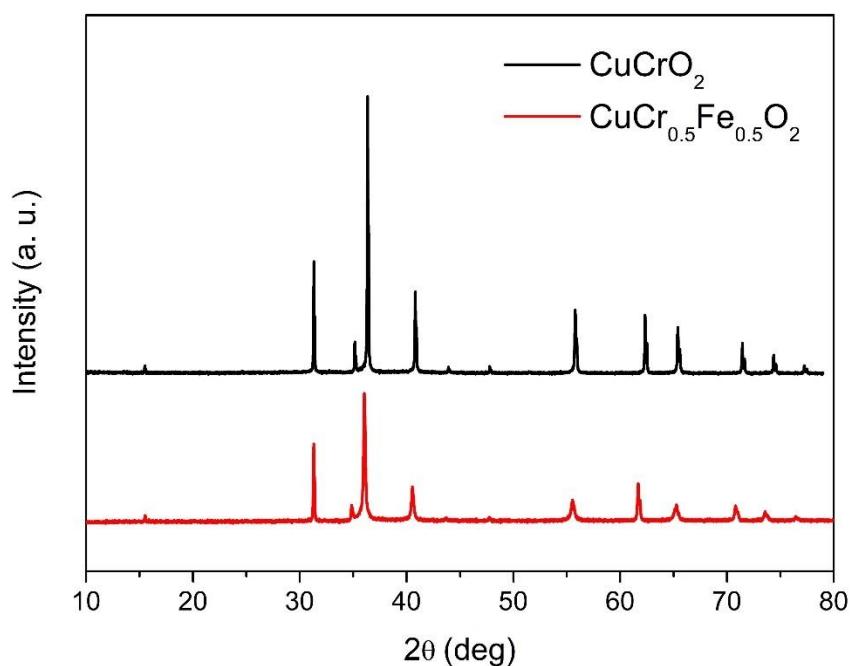


Figure 5.22. Powder X-ray diffraction pattern of $\text{CuCr}_{0.5}\text{Fe}_{0.5}\text{O}_2$ (red) and CuCrO_2 (black) powders. The $\text{CuCr}_{0.5}\text{Fe}_{0.5}\text{O}_2$ was synthesised via sol-gel route (see Chapter 2.1.1.3) and annealed under N_2 at 1000°C for 10 h and the CuCrO_2 powder was synthesised via solid-state route (see Chapter 2.1.1.2) under N_2 and annealed at 900°C for 10 h.

SEM was conducted on the $\text{CuCr}_{0.5}\text{Fe}_{0.5}\text{O}_2$ films to determine the differences in film morphology depending on the synthesis and treatment properties (see Chapter 2.3.2 for experimental procedure). The images of the films show inhomogeneous surface morphology with particles varying greatly in size (Figure 5.23). The particle size was estimated to be approximately $700\text{ nm} \pm 300\text{ nm}$.

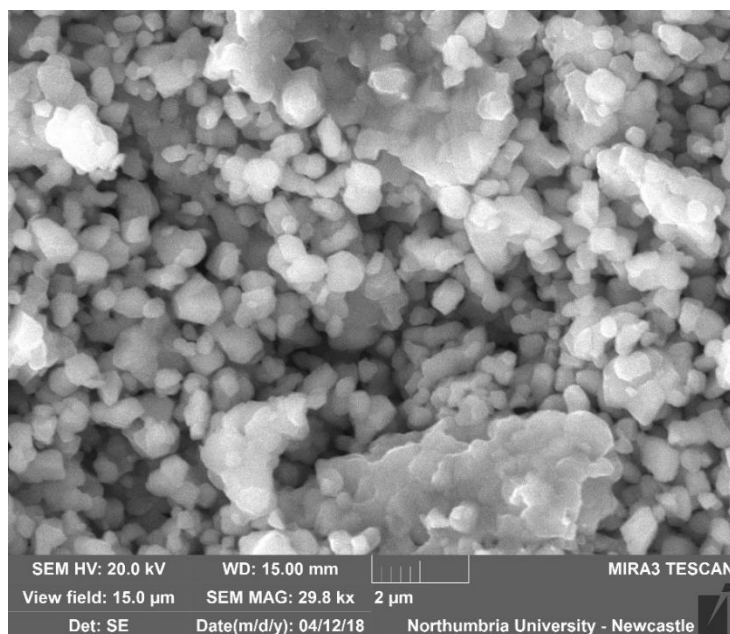
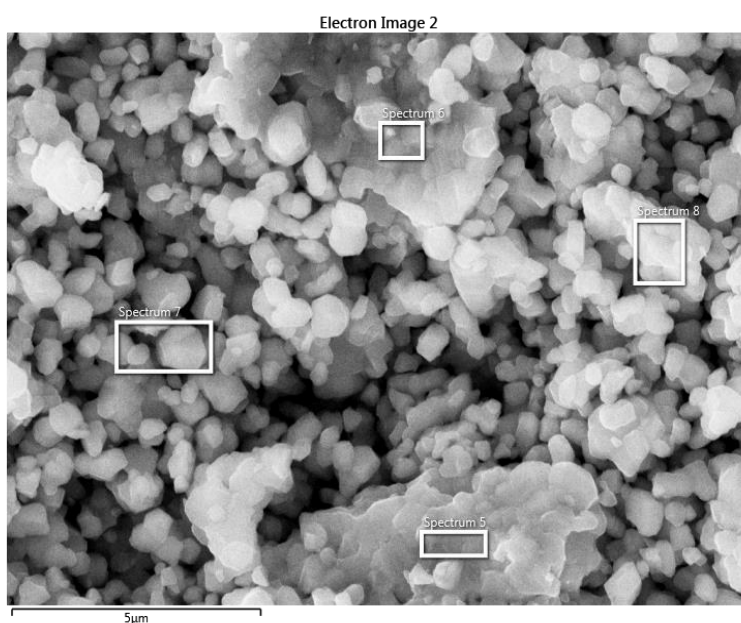


Figure 5.23. SEM image of the $\text{CuCr}_{0.5}\text{Fe}_{0.5}\text{O}_2$ film. The measurement was carried out by P. Maiello in Northumbria University.

In addition, Energy-dispersive X-ray spectroscopy (EDS) was carried out on the $\text{CuCr}_{0.5}\text{Fe}_{0.5}\text{O}_2$ film to check atomic percentages of elements in the sample (Figure 5.24). The EDS measurement showed that there was 25.5 ± 0.3 At% of Cr, 24.9 ± 0.4 At% of Fe and 49.6 ± 0.7 At% of Cu in the sample (Table 5.3). All values are within the error margin of the measurement, which is 2 At%, therefore it can be concluded that the $\text{CuCr}_{0.5}\text{Fe}_{0.5}\text{O}_2$ stoichiometry is correct and the synthesis was successful.



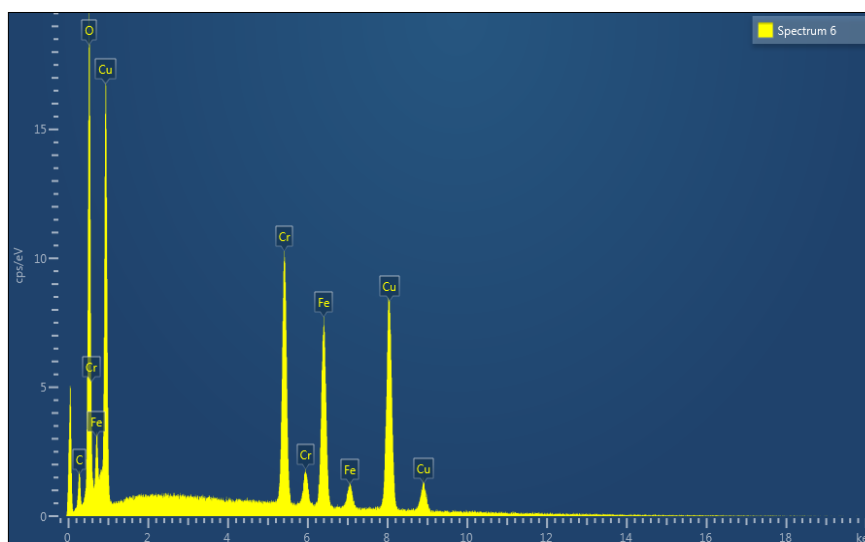


Figure 5.24. Up - SEM image of $\text{CuCr}_{0.5}\text{Fe}_{0.5}\text{O}_2$ sample showing the regions (white boxes) used for the EDS measurement. Down – EDS measurement results for $\text{CuCr}_{0.5}\text{Fe}_{0.5}\text{O}_2$ sample corresponding to region 6 on the SEM image on the left. 4 regions were used to take the average At% of elements in the sample. *Analysis was performed by P. Maiello in Northumbria University.*

Spectrum Label	Spectrum 5 (At%)	Spectrum 6 (At%)	Spectrum 7 (At%)	Spectrum 8 (At%)	Average (At%)
Cr	24.94	25.81	25.66	25.73	25.5 ± 0.3
Fe	24.31	25.11	24.95	25.05	24.9 ± 0.4
Cu	50.75	49.08	49.39	49.22	49.6 ± 0.7
Total	100.00	100.00	100.00	100.00	100

Table 5.3. Atomic percentages of elements in $\text{CuCr}_{0.5}\text{Fe}_{0.5}\text{O}_2$ sample obtained from EDS measurement (Figure 5.24). *Analysis was performed by P. Maiello in Northumbria University.*

5.6.2.2 Photoelectrochemical characterisation

The PEC performance of the $\text{CuCr}_{0.5}\text{Fe}_{0.5}\text{O}_2$ photocathode was further studied with CA and LSV measurement in the dark and under illumination. CA measurement was carried out under different applied potentials to observe the photocurrent generation and stability (Figure 5.25).

It showed a large difference in photocurrent density depending on the applied potential, large differences in dark current depending on the applied potential, which indicates an underlying reduction process taking place, and also unstable photocurrents over time. At $E_{appl} = -0.1$ V vs. Ag/AgCl a dark current of ca. $50 \mu\text{A cm}^{-2}$ was recorded and photocurrent showed charge-discharge characteristics when light illumination was applied and stopped, with current density of ca. $60 \mu\text{A cm}^{-2}$ (Figure 5.25). Under $E_{appl} = -0.2$ V vs Ag/AgCl the dark current increased to ca. $100 \mu\text{A cm}^{-2}$ and initial photocurrent of ca. $200 \mu\text{A cm}^{-2}$ was shown, which then decreased to ca. $150 \mu\text{A cm}^{-2}$ after 5 min of chopped light measurement (Figure 5.25). The considerable decrease in photocurrent over a short period of time is an indication of photocorrosion of the electrode.

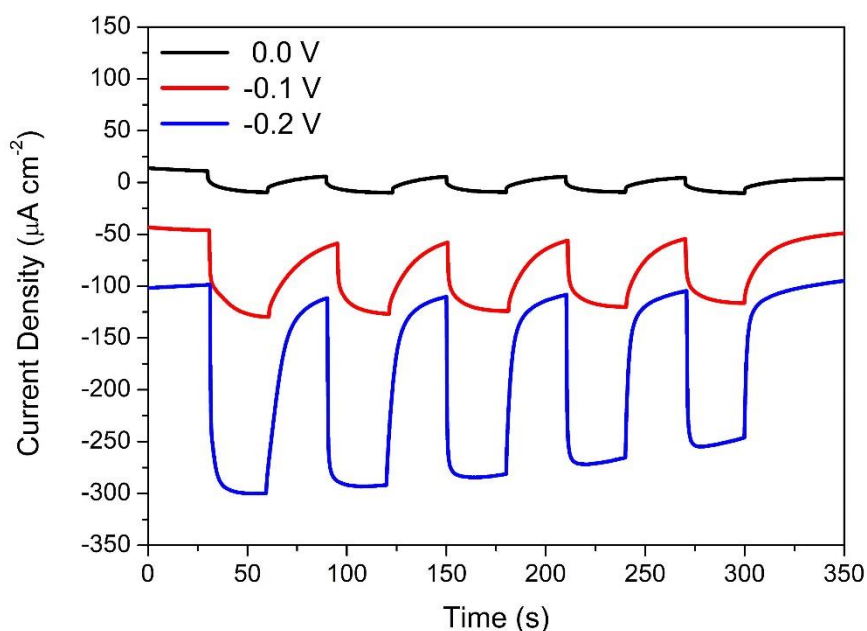


Figure 5.25. CA of $\text{CuCr}_{0.5}\text{Fe}_{0.5}\text{O}_2$ under different applied potentials in pH5 0.1 M acetate buffer and under chopped light illumination (100 mW cm^{-2}). Chopped light illumination was applied with 30 s intervals (30 s in the dark / 30 s under illumination). Measurement was conducted in a three-electrode custom made PEC cell using Ag/AgCl reference electrode (3.0 M NaCl). The electrolyte was purged with N_2 for 15 min. before the measurement.

LSV measurements were carried out on the $\text{CuCr}_{0.5}\text{Fe}_{0.5}\text{O}_2$ photocathode in the dark and under constant and chopped light illumination (Figure 5.26). The LSV in the dark showed a considerable increase in the cathodic current when potential was scanned from 0.5 V to -0.5 V vs. Ag/AgCl. It also showed that there was a reduction process taking place at $E_{red} = -0.28$ V (Figure 5.26, left (black)). This process was further enhanced when the light illumination was applied (Figure 5.26, left (red)). The LSV under chopped light illumination showed that the photocurrent is quite modest compared to the current increase due to the dark current

(Figure 5.26, right). It indicates that most of the current comes from the underlying reduction process which over time reduces the photocurrent due to the reduction of the photoactive species on the surface of the photocathode. This also explains the unstable photocurrents generated during the CA (Figure 5.25).

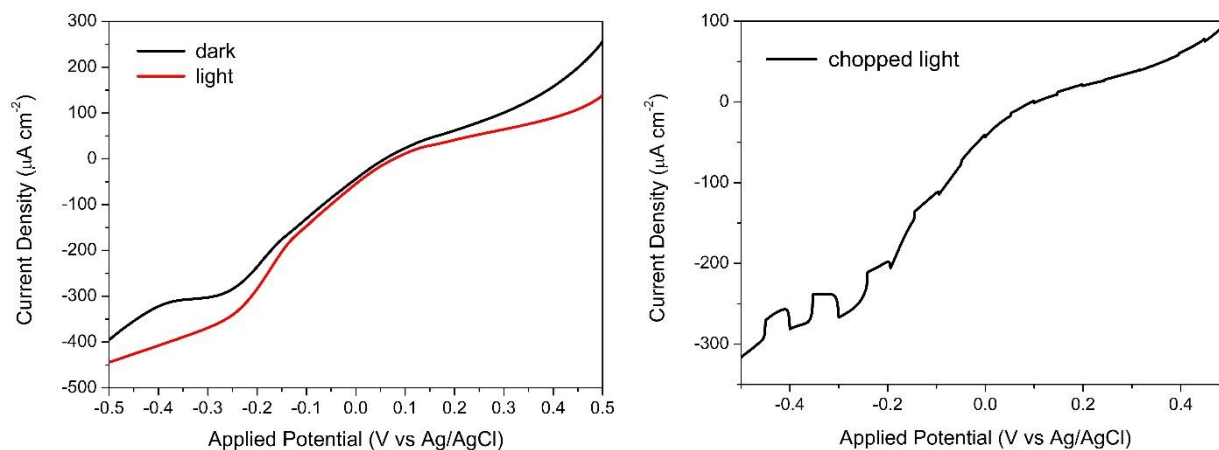


Figure 5.26. LSV of $\text{CuCr}_{0.5}\text{Fe}_{0.5}\text{O}_2$ in pH5 0.1 M acetate buffer, scan rate of 10 mV s^{-1} was applied. Left – LSV in the dark and under light illumination (100 mW cm^{-2}). Right – LSV under chopped light illumination. The light illumination was applied with 5 s intervals (5 s in the dark / 5 s under light). Measurement was conducted in a three-electrode custom made PEC cell using Ag/AgCl reference electrode (3.0 M NaCl). The electrolyte was purged with N_2 for 15 min. before the measurement.

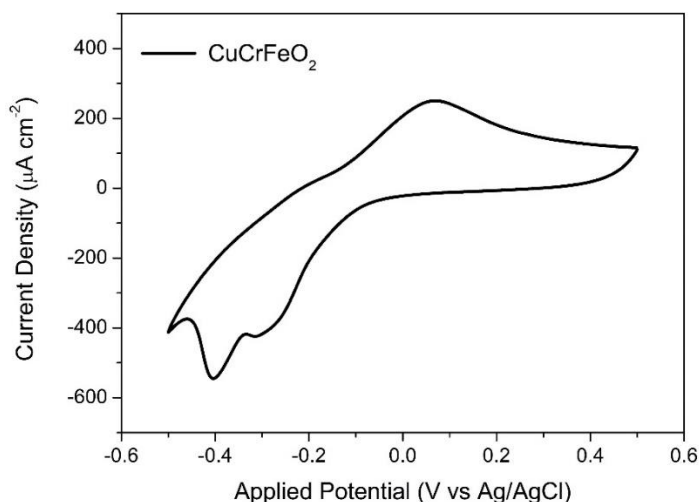


Figure 5.27. CV of $\text{CuCr}_{0.5}\text{Fe}_{0.5}\text{O}_2$ in pH 7 0.1 M phosphate buffer in the dark, scan rate of 50 mV s^{-1} was applied. Measurement was conducted in a three-electrode custom made PEC cell using Ag/AgCl reference electrode (3.0 M NaCl). The electrolyte was purged with N_2 for 15 min. before the measurement.

This reasoning was further confirmed by the CV measurement on the $\text{CuCr}_{0.5}\text{Fe}_{0.5}\text{O}_2$ photocathode in the dark (Figure 5.27), which showed two subsequent reduction processes on cathodic scan from 0.5 to -0.5 V vs. Ag/AgCl occurring at $E_{\text{appl}} = -0.3$ V and -0.4 V vs. Ag/AgCl. The pH of the electrolyte was 7, therefore the $E_{\text{red}} = -0.4$ V corresponds to the reduction process on the LSV, $E_{\text{red}} = -0.28$ V (Figure 5.26, left (black)) according to the Nernst eq. (see Chapter 2.2.6.). The first redox process, $E_{\text{red}} = -0.28$ V, could be associated with the reduction of Cu^{2+} impurities to Cu^+ , while the second process could be attributed to the reduction of Fe^{3+} to Fe^{2+} .

To see if the photocurrent produced during the CA measurement under $E_{\text{appl}} = -0.2$ V vs. Ag/AgCl could be stabilised if the electrons which are excited to the CB of the $\text{CuCr}_{0.5}\text{Fe}_{0.5}\text{O}_2$ would be transferred away from the electrode surface, an EA was added to the electrolyte solution. The $[\text{Co}(\text{NH}_3)_5\text{Cl}]\text{Cl}_2$ was chosen because it is known to produce reasonable photocurrent with NiO (see Chapter 3.5.1). CA and LSV measurement were carried out on the $\text{CuCr}_{0.5}\text{Fe}_{0.5}\text{O}_2$ photocathode (Figure 5.28). The CA under $E_{\text{appl}} = -0.2$ V vs. Ag/AgCl showed similar photocurrents as for the measurement without the EA, but both the photocurrent and dark current was unstable during the measurement.

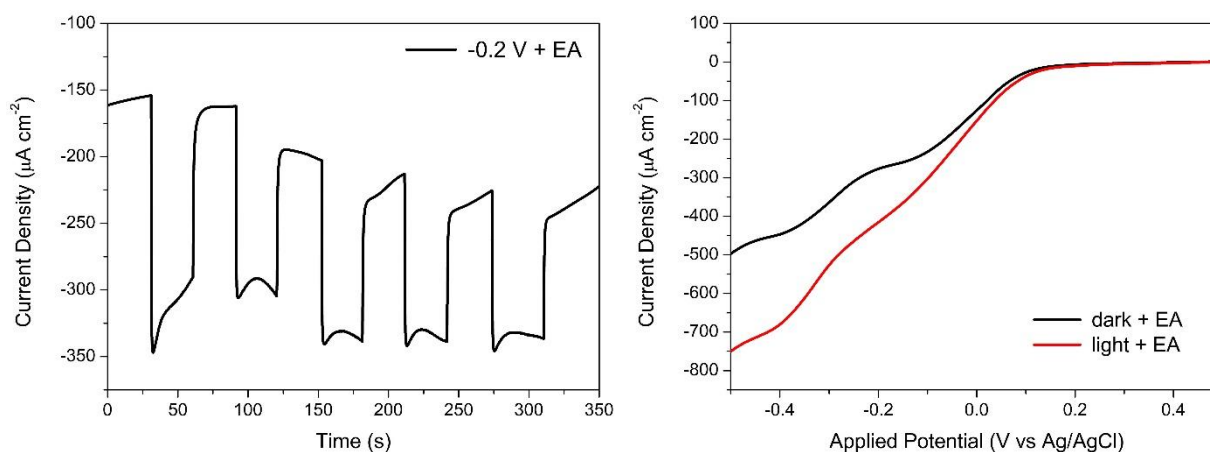


Figure 5.28. Left – CA of $\text{CuCr}_{0.5}\text{Fe}_{0.5}\text{O}_2$ under -0.2 V vs Ag/AgCl applied potential in 0.1 M acetate buffer with 10 mM $[\text{Co}(\text{NH}_3)_5\text{Cl}]\text{Cl}_2$ under chopped light illumination. Chopped light illumination was applied with 30 s intervals (30 s in the dark / 30 s under illumination). Right – LSV of $\text{CuCr}_{0.5}\text{Fe}_{0.5}\text{O}_2$ in the dark and under light illumination (100 mW cm^{-2}), scan rate of 10 mV s^{-1} was applied. Measurement was conducted in a three-electrode custom made PEC cell using Ag/AgCl reference electrode (3.0 M NaCl). The electrolyte was purged with N_2 for 15 min. before the measurement.

Due to the instability of the $\text{CuCr}_{0.5}\text{Fe}_{0.5}\text{O}_2$ photocathode further experiments could not be conducted. However, for future studies, different strategies for photocathode protection

can be employed. Prevo et al. used ALD method to protect the CuFeO_2 photocathode against corrosion. They used a similar strategy as was used for Cu_2O stabilisation and deposited Al doped ZnO and TiO_2 layers on the photocathode surface. This enabled the electron transfer to the photocathode surface, while protecting the surface from water. Pt nanoparticles were then deposited on the covering layers to catalyse the H_2 evolution.^{20,24} Other strategies to stabilise the photocathode are also possible and could be even more beneficial to try, since the ALD method described above is expensive and challenging for scale-up.⁵⁴ For example using a fusible alloy coating on the surface of the photocathode to transfer charges while protecting the surface.⁵⁴

5.7 Conclusions

In this study, the pure-phase CuCrO_2 photocathode was shown to catalyse the H_2 evolution half reaction from water in near-neutral condition and under 0 V vs NHE without the use of any sacrificial agents. The CuCrO_2 powder was synthesised via solid-state route and porous thin film photocathodes were fabricated from the powder using a modified paste formulation route. An in-depth study on the effects of post-calcination annealing under N_2 atmosphere was carried out showing that the annealing step is crucial to obtain stable and efficient system for H_2 production. In addition, the origins of this enhancement in stability and performance lie in the changes of surface chemistry of the photocathodes, shown by XPS surface analysis. Finally, the system was successfully optimised with the use of an inorganic cobalt co-catalyst in solution, and it was demonstrated that the addition of the right concentration of this catalyst increases the faradaic efficiency of the H_2 evolution reaction.

Additionally, successful functionalisation of the CuCrO_2 photocathode was shown with considerable increase in photocurrent under light illumination with EA in the solution and IPCE comparable to results reported in literature.

This study shows that the CuCrO_2 photocathodes can be efficiently used for H_2 evolution. More importantly, because the material absorbs light mainly in the UV region, it has high potential to be functionalised with additional light absorbers harvesting the light energy at higher wavelengths. The high positive photocurrent onset potential also suggests that these photocathodes could be good candidates for tandem PEC cells where they can be coupled with suitable photoanodes to drive the full water splitting reaction.

In addition, an initial PEC study of $\text{CuCr}_{0.5}\text{Fe}_{0.5}\text{O}_2$ photocathode was carried out to test the performance and stability of the material. However, it was shown that the material is

unstable in water even when EA was used. For future optimisation, strategies to protect the photocathode against corrosion could be employed.

References

- 1 F. E. Osterloh, *Chem. Soc. Rev.*, 2013, 42, 2294-2320.
- 2 A. Fujishima, K. Honda, *Nature*. 1972, 238, 37-38.
- 3 R. Memming, G. Schwandt, *Electrochim. Acta* 1968, 13, 1299.
- 4 E. Aharon-Shalom, A. Heller, *J. Electrochem. Soc.* 1982, 129, 2865-2866.
- 5 S. S. Kocha, J. A. Turner, A. J. Nozik, *J. Electroanal. Chem.* 1994, 367, 27.
- 6 R. N. Dominey, N. S. Lewis, J. A. Bruce, D. C. Bookbinder, M. S. Wrighton, *J. Am. Chem. Soc.* 1982, 104, 467-482.
- 7 M. Hara, T. Kondo, M. Komoda, S. Ikeda, K. Shinohara, A. Tanaka, J. N. Kondo, K. Domen, *Chem. Commun.* 1998, 357-358.
- 8 P. E. De Jongh, D. Vanmaekelbergh, J. J. Kelly, *J. Electrochem. Soc.*, 2000, 147, 486-489.
- 9 W. Siripala, A. Ivanovskaya, T. F. Jaramillo, S. H. Baeck, E. W. McFarland, *Sol. Energy Mater. Sol. Cells*, 2003, 77, 229-237.
- 10 C. C. Hu, J. N. Nian, H. Teng, *Sol. Energy Mater. Sol. Cells*, 2008, 92, 1071-1076.
- 11 J. N. Nian, C. C. Hu, H. Teng, *Int. J. Hydrog. Energy*, 2008, 33, 2897-2903.
- 12 L. Tong, A. Iwase, A. Nattestad, U. Bach, M. Weidener, Günther Götz, A. Mishra, P. Bäuerle, R. Amal, G. G. Wallace, A. J. Mozer, *Energy Environ. Sci.*, 2012, 5, 9472-9475.
- 13 R. J. Kamire, M. B. Majewski, W. L. Hoffeditz, B. T. Phelan, O. K. Farha, J. T. Hupp, M. R. Wasielewski, *Chem. Sci.*, 2017, 8, 541-549.
- 14 M. Le, M. Ren, Z. Zhang, P. T. Sprunger, R. L. Kurtz, J. C. Flake, *J. Electrochem. Soc.* 2011, 158 (5), 45-49.
- 15 S. Ohya, T. Suzuki, K. Ohta, S. Kaneco, H. Katsumata, *Catal. Today*, 2009, 148, 329-334.
- 16 A. Önsten, J. Weissenrieder, D. Stoltz, S. Yu, M. Göthelid, U. O. Karlsson, *J. Phys. Chem. C*, 2013, 117, 19357-19364.
- 17 P. E. de Jongh, D. Vanmaekelbergh, J. J. Kelly, *Chem. Mater.*, 1999, 11, 3512-3517.
- 18 I. Sullivan, B. Zoellner, P. A. Maggard, *Chem. Mater.* 2016, 28, 5999-6016.
- 19 M. G. Walter, E. L. Warren, J. R. McKone, S. W. Boettcher, Q. Mi, E. A. Santori, N. S. Lewis, *Chem. Rev.* 2010, 110, 6446-6473.
- 20 A. Paracchino, V. Laporte, K. Sivula, M. Grätzel, E. Thimsen, *Nat. Mat.* 2011, 10, 456-461.
- 21 C. G. Morales-Guio, S. D. Tilley, H. Vrubel, M. Grätzel, X. Hu, *Nat. Commun.* 2014, 5, 4059-4059.

- 22 J. Luo, L. Steier, M. K. Son, M. Schreier, M. T. Mayer, M. Grätzel, *Nano Lett.* 2016, 16, 1848–1857.
- 23 B. K. Meyer, A. Polity, D. Reppin, M. Becker, P. Hering, P. J. Klar, T. Sander, C. Reindl, J. Benz, M. Eickhoff et al. *Phys. Status Solidi B*, 2012, 249, 1487–1509.
- 24 M. S. Prévot, N. Guijarro, K. Sivula, *ChemSusChem*, 2015, 8, 1359–1367.
- 25 M. Yu, T. I. Draskovic, Y. Wu, *Phys. Chem. Chem. Phys.* 2014, 16, 5026–5033.
- 26 A. Nattestad, X. Zhang, U. Bach, Y-B. Cheng, *J. Photonics Energy* 2011, 1, 011103–011103.
- 27 M. Yu, G. Natu, Z. Ji, Y. Wu, *J. Phys. Chem. Lett.* 2012, 3, 1074– 1078.
- 28 Z. Xu, D. Xiong, H. Wang, W. Zhang, X. Zeng, L. Ming, W. Chen, X. Xu, J. Cui, M. Wang, et al. *J. Mater. Chem. A* 2014, 2, 2968–2976.
- 29 S. Powar, D. Xiong, T. Daeneke, M. T. Ma, A. Gupta, G. Lee, S. Makuta, Y. Tachibana, W. Chen, L. Spiccia, Y-B. Cheng, G. Götz, P. Bäuerle, U. Bach. *J. Phys. Chem. C* 2014, 118, 16375–16379.
- 30 D. Xiong, Z. Xu, X. Zeng, W. Zhang, W. Chen, X. Xu, M. Wang, Y-B. Cheng, J. Mater. Chem. 2012, 22, 24760– 24768.
- 31 D. O. Scanlon, K. G. Godinho, B. J. Morgan, G. W. Watson. *J. Chem. Phys.* 2010, 132, 024707, 1-10.
- 32 D. O. Scanlon, G. W. Watson, *J. Mater. Chem.*, 2011, 21, 3655-3663.
- 33 T. Okuda, Y. Beppu, T. Onoe, N. Terada and S. Miyasaka, *Phys. Rev. B*, 2005, 77, 134423, 1-5.
- 34 W. Ketir, S. Saadi, M. Trari, *J. Solid State Electrochem.*, 2012, 16, 213–218.
- 35 Y. Ma, X. Zhou, Q. Ma, A. Litke, P. Liu, Y. Zhang, C. Li, E. J. M. Hensen, *Catal. Lett.*, 2014, 144:1487–1493.
- 36 A. K. Diaz-Garcia, T. Lana-Villarreal, R. Gomez, *J. Mater. Chem. A*, 2015, 3, 19683-19687.
- 37 A. Varga, G. F. Samu, C. Janaky, *Electrochimica Acta*, 272, 2018, 22-32.
- 38 T. Jiang, X. Li, M. Bujoli-Doeuff, E. Gautron, L. Cario, S. Jobic, R. Gautier, *Inorg. Chem.* 2016, 55, 7729–7733.
- 39 C. E. Creissen, J. Warnan, E. Reisner, *Chem. Sci.*, 2018, 9, 1439-1447.

- 40 A. P. Amrute, Z. Łodziana, C. Mondelli, F. Krumeich, J. Pérez-Ramírez, *Chem. Mater.* 2013, 25, 4423–4435.
- 41 *Zeitschrift fuer Kristallographie (1979-2010)* (1996) 211, 482-482
- 42 NIST X-ray Photoelectron Spectroscopy Database, Version 4.1 (National Institute of Standards and Technology, Gaithersburg, 2012); <http://srdata.nist.gov/xps/e>
- 43 P. Qin, H. Zhu, T. Edvinsson, G. Boschloo, A. Hagfeldt, L. Sun, *J. Am. Chem. Soc.*, 2008, 130, 8570-8571.
- 44 W. N. McNamara, Z. Han, P. J. Alperin, W. W. Brennessel, P. L. Hollan, R. Eisenberg. *J. Am. Chem. Soc.* 2011, 133, 15368–15371.
- 45 D. Li, X. Fang, A. Zhao, Z. Deng, W. Dong and R. Tao, *Vacuum*, 2010, 84, 851–856.
- 46 R. Bywalez, S. Gotzendorfer and P. Lobmann, *J. Mater. Chem.*, 2010, 20, 6562–6570.
- 47 P. W. Sadik, M. Ivill, V. Craciun and D. P. Norton, *Thin Solid Films*, 2009, 517, 3211–3215.
- 48 W. T. Lim, L. Stafford, P. W. Sadik, D. P. Norton, S. J. Pearton, Y. L. Wang and F. Ren, *Appl. Phys. Lett.*, 2007, 90, 142101.
- 49 S. Zhou, X. Fang, Z. Deng, D. Li, W. Dong, R. Tao, T. Meng and X. Zhu, *J. Cryst. Growth*, 2008, 310, 5375–5379.
- 50 M. O’Sullivan, P. Stamenov, J. Alaria, M. Venkatesan and J. M. D. Coey, *J. Phys.: Conf. Ser.*, 2010, 200, 052021.
- 51 P. Qin, M. Linder, T. Brinck, G. Boschloo, A. Hagfeldt, L. Sun. *Adv. Mater.* 2009, 21, 2993–2996.
- 52 R. Bywalez, S. Götzendorfer, P. Löbmann, *Mater. Chem.*, 2010, 20, 6562–6570.
- 53 J. W. Ager, M. R. Shaner, K. A. Walczak, I. D. Sharp, S. Ardo, *Energy Environ. Sci.*, 2015, 8, 2811-2824.
- 54 M. Crespo-Quesada, E. Reisner, *Energy Environ. Sci.*, 2017, 10, 1116-1127.
- 55 A. J. Bard, L. R. Faulkner. *Electrochemical Methods: Fundamentals and Applications*, 2nd Edition. 2000.
- 56 MC Biesinger et al. *Applied Surface Science*, 257, 2011, 2717-2730.
- 57 M Aronniemi et al. *Surface Science*, 578, 2005, 108-123.

- 58 P. A. Kohl and A. J. Bard, *J. Am. Chem. Soc.*, 1977, 99, 7531-7539.
- 59 R. A. Fredlein and A. J. Bard, *J. Electrochem. Soc.*, 1979, 126, 11, 1892-1898.
- 60 N. Potts. PhD Thesis. Newcastle University. 2019.

Chapter 6. Photocathode exchange current density estimation and PEC cell modelling using finite element analysis.

Abstract

In this chapter the experimental results obtained from projects presented and discussed in Chapters 3 and 4 were used to estimate the exchange current densities, J_0 , from Tafel plot (Tafel graph) for photocathodes Pt|D3|NiO|FTO (Chapter 3.5.3), 1|NiO|FTO and 2|NiO|FTO (Chapter 4). The J_0 results were then used to build an initial proof-of-concept two-dimensional semi-empirical model of a PEC cell for electrolyte potential and electrolyte current density using COMSOL Multiphysics software.¹ This is achieved by using the obtained values of J_0 in Butler-Volmer equation which is applied to the photocathode-electrolyte interface as a boundary condition. The results of this modelling study are discussed considering the applicability of the approach for PEC cell modelling, limitations of the approach and comparing it to previously applied models for PEC cells discussed in the literature.

6.1 Introduction

The purpose of the computational modelling of the PEC cell is to predict the performance of the cell by changing cell geometry and different input parameters like exchange current density without the need to build the corresponding PEC cell in real life in the lab with specific materials and carry out experiments. Therefore, it saves a lot of time and is cost efficient approach for cell optimisation and scale-up. While keeping some parameters of the cell constant, like cell geometry and electrolyte conductivity for example, other parameters can be changed to see how the performance of the cell changes.³ The performance can be reflected in the electrolyte current density change, like in this study, or in change of H₂ yield, or in the distribution in potential and current density in the cell. The input variables can be acquired experimentally, or they can be changed arbitrarily to determine the values of an ideal material, for example to obtain best performance.

In this proof of concept study, the aim was to build an initial simplified model of the PEC cell which could serve as a starting point for future studies, where the model can be optimised. The variable which is changed is the exchange current density obtained experimentally. Other cell parameters like cell geometry, potentials on the electrodes and electrolyte conductivity were held constant.

First the theoretical background of the exchange current density and kinetic expressions applied in the model are introduced and explained. Then the exchange current density determination from experimental data is presented followed by the introduction of two-dimensional PEC cell model with computed results of the electrolyte current density distribution in the cell.

6.2 Current density and overpotential relationship

At equilibrium potential on the semiconductor-electrolyte interface there is no net reaction taking place on the electrode that can be observed and the net current is zero. The equilibrium potential is determined by the concentrations of reduced and oxidised species in the electrolyte and is expressed through Nernst equation (Eq. 1.3). However, there are still charge transfer processes happening on the atomic scale. The anodic and cathodic reactions are competing against each other resulting in charge transfer from the electrolyte to the electrode and vice versa. Since the net current is zero, the current densities of the anodic and cathodic reactions at equilibrium potential must be equal and the magnitude of both of those currents is called the exchange current density, J_0 .²

To drive the chemical reactions taking place on an electrode to either anodic or cathodic directions, an overpotential, η , needs be applied on the electrode. The fundamental relationship which describes the current density, J , dependence on the overpotential on an electrode is called the Butler-Volmer equation and it is expressed as follows^{2,3}

$$J(\eta) = J_0 \cdot \left\{ \exp\left(\frac{\alpha_a n F \eta}{RT}\right) - \exp\left(\frac{\alpha_c n F \eta}{RT}\right) \right\} \quad (6.1)$$

where α_a is the anodic charge transfer coefficient, α_c is the cathodic charge transfer coefficient, n is the number of electrons involved in the reactions on the electrode surface, F is the Faraday constant ($F = 96485 \text{ C mol}^{-1}$), R is the universal gas constant ($R = 8.314 \text{ J K}^{-1} \text{ mol}^{-1}$) and T is temperature.^{2,3}

The Butler-Volmer equation describes a situation on the electrode when there are no mass-transfer effects. This is when the electrolyte is stirred or when the overpotential is low enough so that there would not be considerable differences between concentrations of reduced or oxidised species on the electrode surface compared to the bulk of the electrolyte. In that case, the overpotential is required only to overcome the activation energy needed to drive the heterogeneous chemical reaction on the electrode surface. The magnitude of exchange current

density shows how good are the kinetics of this process. If the value of the J_0 is low, larger overpotential is needed to overcome the activation energy.²

When either anodic or cathodic overpotential is large enough, one of the exponential terms in the Butler-Volmer equation (Eq. 6.1) becomes negligible.

For example, if the cathodic overpotential is large enough, then

$$\exp\left(\frac{\alpha_c n F \eta}{RT}\right) \gg \exp\left(\frac{\alpha_a n F \eta}{RT}\right) \quad (6.2)$$

And therefore, the equation can be written as follows

$$J(\eta) = J_0 \exp\left(\frac{\alpha_c n F \eta}{RT}\right) \quad (6.3)$$

The overpotential, η , can then be expressed as follows

$$\eta = \frac{RT}{\alpha F} \ln J_0 - \frac{RT}{\alpha F} \ln J \quad (6.4)$$

The Eq. 6.4. has the form of a Tafel equation. This would be the case for example for high cathodic overpotential, where anodic current is negligible. The Tafel equation for high cathodic overpotential is written as follows

$$\eta = a + b \log J \quad (6.5)$$

where

$$a = \frac{2.3RT}{\alpha F} \log J_0 \quad \text{and} \quad b = \frac{-2.3RT}{\alpha F}$$

The Tafel equation can be applied when less than 1% of the current is generated by the back reaction:

$$\frac{\exp\left(\frac{-\alpha n F \eta}{RT}\right)}{\exp\left(\frac{(1-\alpha)n F \eta}{RT}\right)} = \exp\left(\frac{n F \eta}{RT}\right) \leq 0.01 \quad (6.6)$$

It can be derived from the Eq. 6.5. that $|\eta| > 118 \text{ mV}$ (at 25°C).²

The Tafel relationship between current density and overpotential can be used to extract the exchange current density from the Tafel plot. The Tafel plot is plot where the

overpotential is plotted against the logarithm of current density, i. e. η vs. $\log J$. The linear part of the plot is the region where Tafel relationship (Eq. 6.5) applies and the exchange current density, J_0 , can be extracted from the plot by extrapolating the linear region to $\log J$ (Figure 6.1).

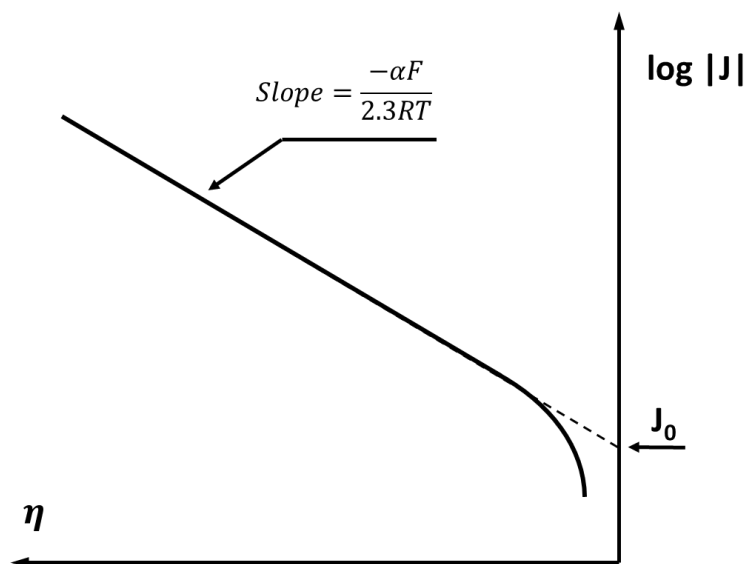


Figure 6.1. Annotated figure of Tafel plot for a cathodic process, where overpotential, η , is plotted against $\log |J|$. The linear region of the plot is extrapolated to the $\log |J|$ to estimate the value of J_0 . The Tafel slope = $-\alpha F/2.3RT$.²

When overpotential value approaches to zero, the Tafel relationship doesn't apply anymore, because the contribution to the current from back reactions increases, and the plot deviates substantially from linear behaviour.²

6.4. Results and discussion

6.4.1. Exchange current density estimation

The exchange current densities, J_0 , were determined for photocathodes Pt|D3|NiO|FTO (Chapter 3.5.3), 1|NiO|FTO and 2|NiO|FTO (Chapter 4) using the linear sweep voltammetry (LSV) experimental data obtained and presented in corresponding chapters and combined on Figure 6.2. The J_0 values for the photocathodes were extracted from Tafel plots using the method described in the previous chapter. The experimental LSV data (Figure 6.2) and corresponding Tafel plot is presented also for Pt|FTO electrode for comparison (Figure 6.3).

The Pt was deposited on FTO using the DPA electrodeposition method described in Chapter 2.1.8. This method was also used to deposit Pt catalyst on D3|NiO|FTO photocathode, therefore it is necessary to evaluate the performance of the Pt|FTO separately to compare the difference between electrodes where Pt is deposited on a dye sensitised NiO and where Pt is deposited directly on conducting FTO substrate.

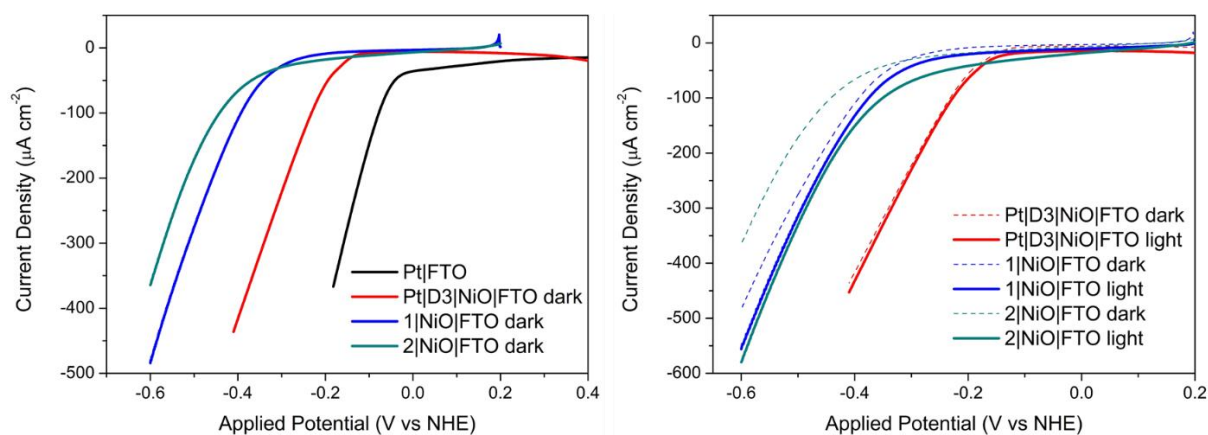


Figure 6.2. Left - LSV of Pt|D3|NiO|FTO, 1|NiO|FTO, 2|NiO|FTO and Pt|FTO in the dark. Right – LSV comparison of Pt|D3|NiO|FTO, 1|NiO|FTO, 2|NiO|FTO in the dark (dotted line) and under light illumination (100 mW cm^{-2}). The measurements were conducted in one compartment PEC cell in 0.1 M phthalate buffer (pH 3). The electrolyte was degassed for 15 min under N_2 before every measurement.

Experimental LSV data presented on Figure 6.2, left shows, that the overpotential for H_2 evolution in the dark is considerably lower for Pt|FTO electrode than for the dye sensitised photocathode, which is expected as the low conductivity of NiO limits the charge transfer from the back contact to the electrode surface thereby increasing the overpotential required for the reaction. On Figure 6.2, right, the LSV of the dye sensitised photocathodes Pt|D3|NiO|FTO, 1|NiO|FTO and 2|NiO|FTO in the dark (dotted lines) are compared to the LSV when the photocathodes are under light illumination (solid lines). It is shown that for Pt|D3|NiO|FTO the overpotential needed for H_2 evolution in the dark and under light illumination is lower than for 1|NiO|FTO and 2|NiO|FTO. It is also shown that when comparing the LSV in the dark and under light illumination for the dye sensitised photocathodes, then for Pt|D3|NiO|FTO and 1|NiO|FTO the photocurrents are quite modest and there is a small difference between the curves in the region where the current starts to increase rapidly. However, for the 2|NiO|FTO, the difference between the dark current and photocurrent is larger.

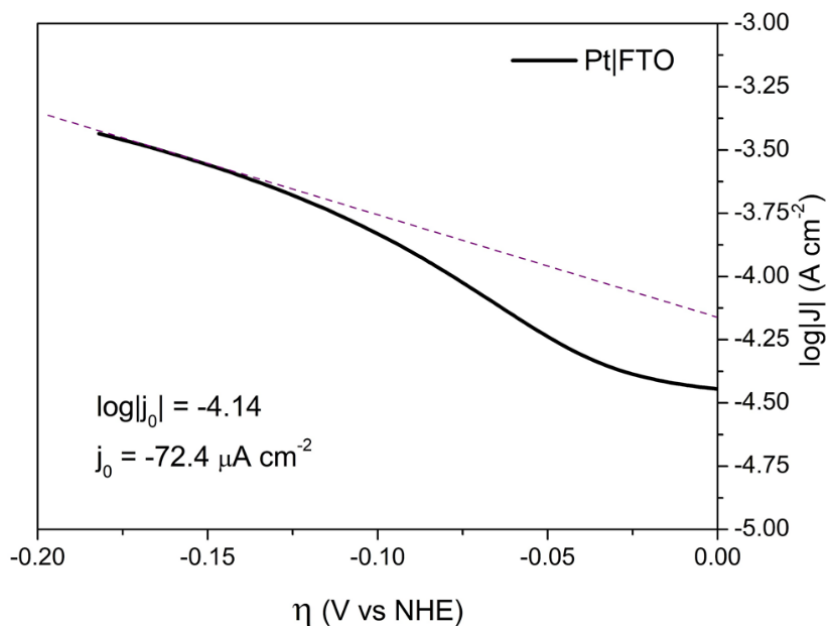


Figure 6.3. Tafel plot of Pt|FTO electrode constructed using the experimental LSV data presented on Figure 6.2, left (black line). The linear region of the curve is extrapolated to the y-axis ($\log|J|$) to determine the exchange current density, J_0 , for the H_2 evolution on this electrode.

The exchange current density values were determined from Tafel plots for Pt|FTO in the dark and for Pt|D3|NiO|FTO, 1|NiO|FTO and 2|NiO|FTO in the dark and under illumination. The results showed that the Pt|FTO had the highest exchange current density, as expected, with the value $J_0 = -72.4 \pm 0.2 \mu\text{A cm}^{-2}$ (Figure 6.3). The second highest values were determined for Pt|D3|NiO|FTO photocathode, with exchange current density in the dark being $J_{0,d} = -54.9 \pm 0.2 \mu\text{A cm}^{-2}$ and under illumination $J_{0,p} = -58.8 \mu\text{A cm}^{-2}$. The photocathodes with dye-catalyst assemblies on the NiO surface, 1|NiO|FTO and 2|NiO|FTO, gave lower values. The exchange current density for 1|NiO|FTO in the dark was $J_{0,d} = -18.6 \pm 0.2 \mu\text{A cm}^{-2}$ and under illumination $J_{0,p} = -21.9 \pm 0.2 \mu\text{A cm}^{-2}$. For the 2|NiO|FTO the exchange current densities were as follows: $J_{0,d} = -6.9 \pm 0.2 \mu\text{A cm}^{-2}$ and $J_{0,p} = -20.9 \pm 0.2 \mu\text{A cm}^{-2}$. It can be observed that for all the photocathodes in this study, the exchange current densities increase when light illumination is applied to the electrode. For Pt|D3|NiO|FTO and 1|NiO|FTO the change is quite negligible compared to the overall value. However, for 2|NiO|FTO, the increase is quite considerable.

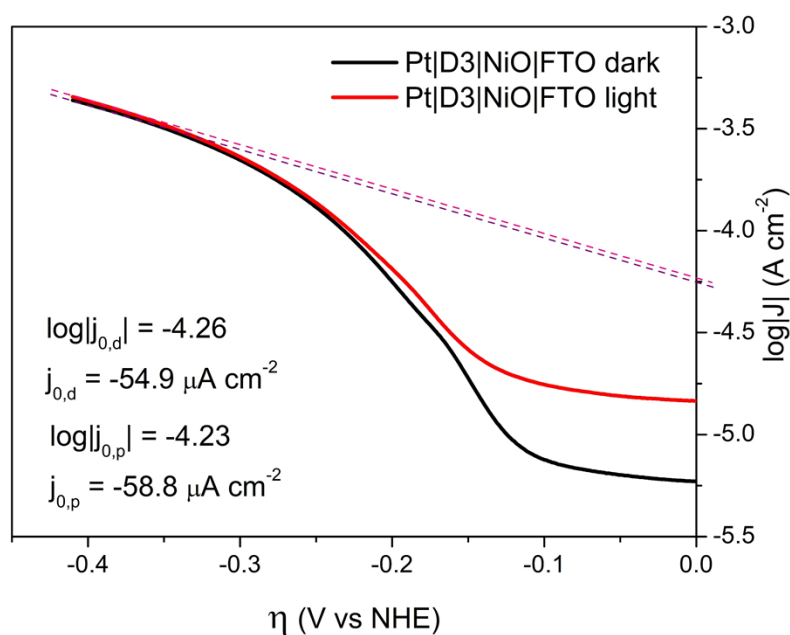


Figure 6.4. Tafel plot of Pt|D3|NiO|FTO electrode in the dark (black line) and under illumination (red line), constructed using the experimental LSV data presented on Figure 6.2, right (red dotted line – in the dark, red solid line – under illumination). The linear regions of the curves are extrapolated to the y-axis ($\log|J|$) to determine the exchange current density, J_0 , for the H_2 evolution on this electrode. $J_{0,d}$ – exchange current density in the dark, $J_{0,p}$ – exchange current density under illumination.

It is important to note, that there is a different mechanism at play when H_2 is evolved from the photocathodes under light illumination compared to the electrolytic process in the dark. This difference is explained in Chapter 1.6.2 discussing the charge-carrier generation in semiconductors in the dark and under illumination and in Chapter 1.6.4 explaining the charge-carrier generation in dye sensitised photocathodes. In this case, since the photocathodes discussed here are dye sensitised, the charge carrier generation under illumination happens when the dye absorbs photons thereby exciting electrons to a higher energy level. This process creates an electron-hole pair, from which the electron is injected to the catalyst and the hole is injected to the VB of the semiconductor onto which the dye is absorbed. In the dark, this process does not take place and the charge transfer from the back contact to the surface of the photocathode is driven solely by the applied external potential. Because the mechanisms are different then it can be assumed that the kinetics of the H_2 evolution reaction is also different under light illumination compared to the process in the dark and this is reflected also in the determined exchange current density values. The increase in exchange current density under light illumination shows that the kinetics of the reaction are improved.

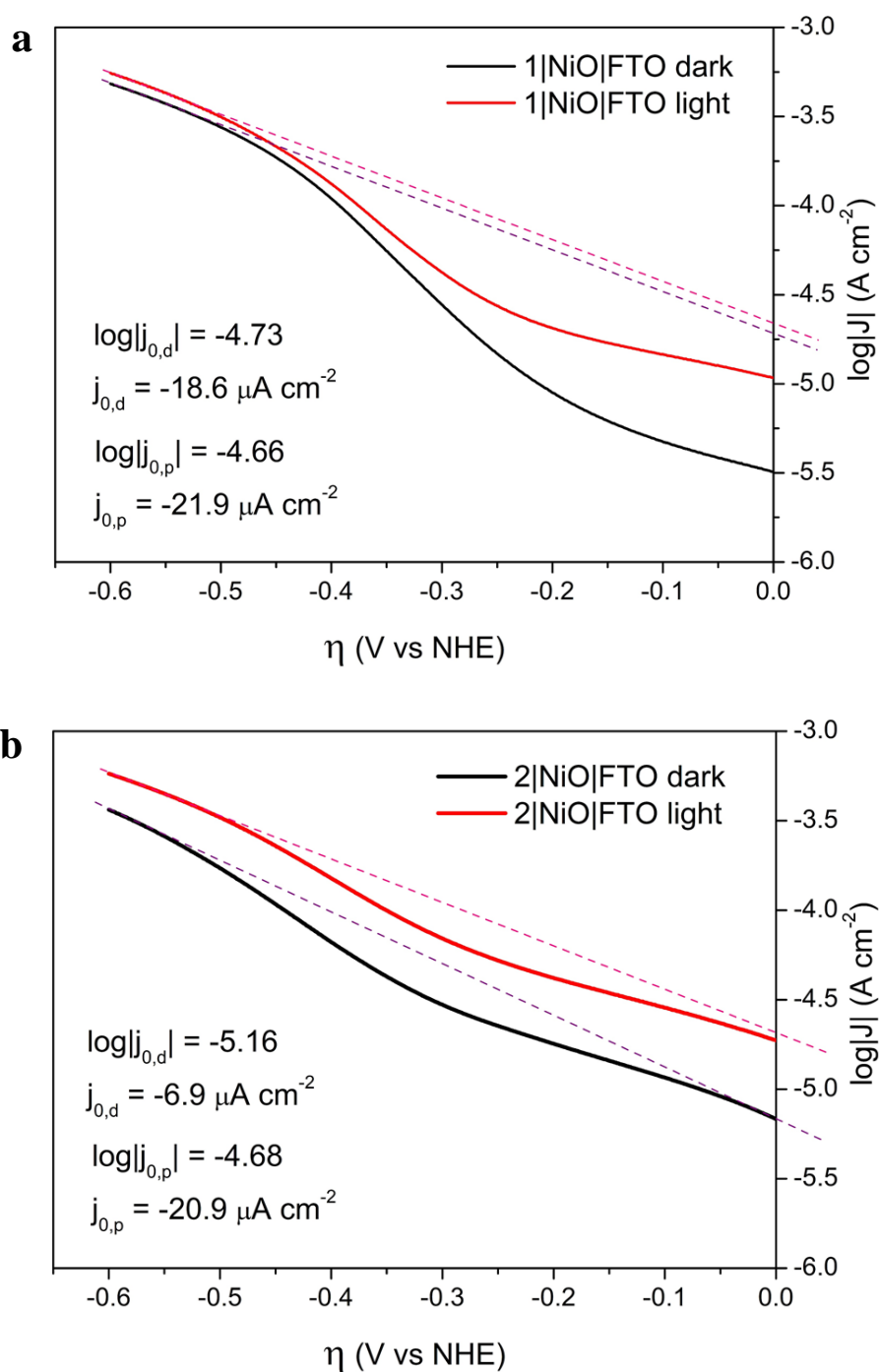


Figure 6.5. Tafel plot of 1|NiO|FTO (a) and 2|NiO|FTO (b) electrodes in the dark (black line) and under illumination (red line), constructed using the experimental LSV data presented on Figure 6.2, right (blue dotted line – 1|NiO|FTO in the dark, blue solid line – 1|NiO|FTO under illumination, green dotted line – 2|NiO|FTO in the dark, green solid line – 2|NiO|FTO under illumination). The linear regions of the curves are extrapolated to the y-axis ($\log|J|$) to determine the exchange current density, J_0 , for the H_2 evolution on this electrode. $J_{0,d}$ – exchange current density in the dark, $J_{0,p}$ – exchange current density under illumination.

6.4.2. PEC cell modelling

A simplified steady-state PEC cell model was created using the current density values obtained from the experimental data of Section 6.4.1. The purpose of this model was to build a basis for predicting electrolyte current densities to create a starting point for future optimisation of the model. The modelling study was conducted with COMSOL Multiphysics simulation software (version 5.4) based on finite element analysis approach.¹

A two-dimensional PEC cell geometry was created using the measurements from the two-compartment PEC cell (Figure 2.2 in Chapter 2). The use of real PEC cell geometry is beneficial because then in the future studies the predicted values in the model can be compared to the experimental values. The two-dimensional geometry of the PEC cell is presented on Figure 6.6 along with the extra fine mesh, which was applied for finite element analysis to perform the simulation.

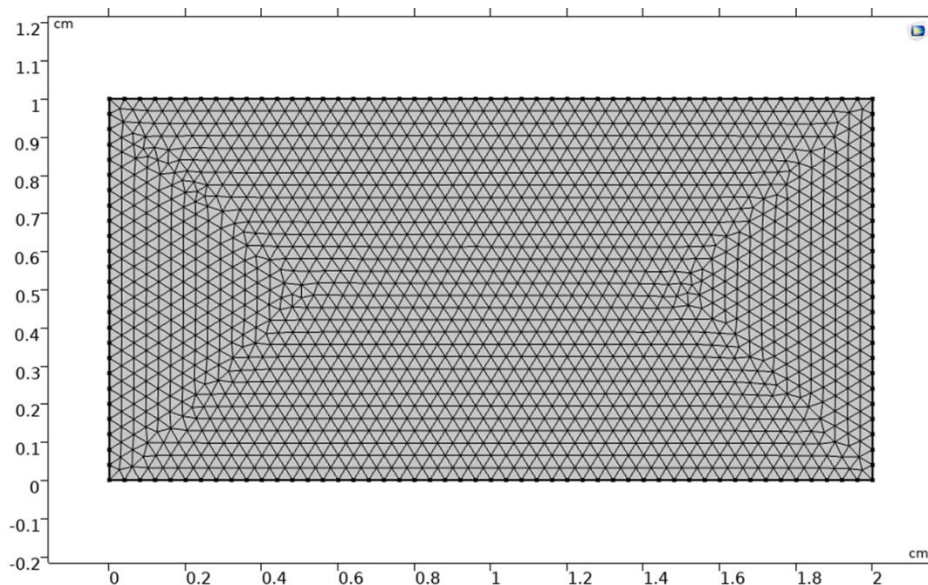


Figure 6.6. Model PEC cell geometry (2 x 1 cm, the scale is presented on the Figure) with extra fine mesh for finite element analysis. Left side – cathode, right side – anode.

The secondary current distribution node was applied to the PEC cell, determining the electrolyte conductivity, electrode reaction potential on the cathode-electrolyte boundary and the electrolyte potential on the anode-electrolyte boundary. No mass transport node like transport of diluted species in the electrolyte was included to this simplified model. The

simulation using only the secondary current distribution interface solves the model for the following equations:

$$\text{Electrode: } i_s = -\sigma_s \nabla \phi_s \quad \text{with } \nabla \cdot i_s = Q_s \quad (\text{Eq. 6.7})$$

$$\text{Electrolyte: } i_l = -\sigma_l \nabla \phi_l \quad \text{with } \nabla \cdot i_l = Q_l \quad (\text{Eq. 6.8})$$

where i_s is the current density in the electrode (A m^{-2}), i_l is the current density in the electrolyte (A m^{-2}), σ_s is the conductivity of the electrode (S m^{-1}), σ_l is the conductivity of the electrolyte (S m^{-1}), and Q_s and Q_l denote the general current source term (A m^{-3}).

In this model the simulation was calculated for the electrolyte and electrode was only considered as a boundary where physics is applied, therefore excluding the influence of electrode conductivity. Cathodic current densities were computed using the Butler-Volmer equation (Eq. 6.1) with the experimentally determined exchange current densities for corresponding electrodes (Chapter 6.4.1). The overpotential on the anode was assumed to be equal to the water oxidation equilibrium potential, $E^0(\text{O}_2/\text{H}_2\text{O}) = 1.23 \text{ V vs NHE}$. The overpotential on the cathode was assumed to be equal to the equilibrium potential for the H_2 evolution, $E^0(\text{H}^+/\text{H}_2) = 0 \text{ V vs NHE}$. The results of the PEC cell modelling for electrolyte current density and electrolyte potential are discussed below. The electrolyte conductivity was determined to be 1.29 S m^{-1} .

Boundary conditions for the steady-state simulation on cathode

Electrolyte potential on the cathode: $E_{\text{cathode}} = 0 \text{ V}$

Electrode reaction equilibrium potential, $E_{\text{eq}} = 0 \text{ V}$

External electric potential, $E_{\text{ext}} = 0 \text{ V}$

Physics applied to the to the cathode-electrolyte boundary:

Butler-Volmer equation (Eq. 6.1), where anodic and cathodic transfer coefficients are both taken 0.5.

Boundary conditions on anode:

Electrolyte potential on the anode, $E_{\text{anode}} = 1.23 \text{ V}$

An example of the two-dimensional PEC cell simulation result is the Pt|FTO cathode in the dark showing electrolyte potential and electrolyte current density distribution in the cell presented on Figure 6.7. The left side of the model represents the Pt cathode and the

electrolyte current density on the cathode-electrolyte boundary is calculated to be 6.47 mA cm^{-2} . The electrolyte current density on the anode boundary is 6.48 mA cm^{-2} . In a steady-state simulation, like this one here, the current is uniform across the simulation domain. The slight difference in current density can be considered within the error margins of the measurement. In addition, since the cell is symmetrical, there is no variation in the potential parallel to the electrodes.

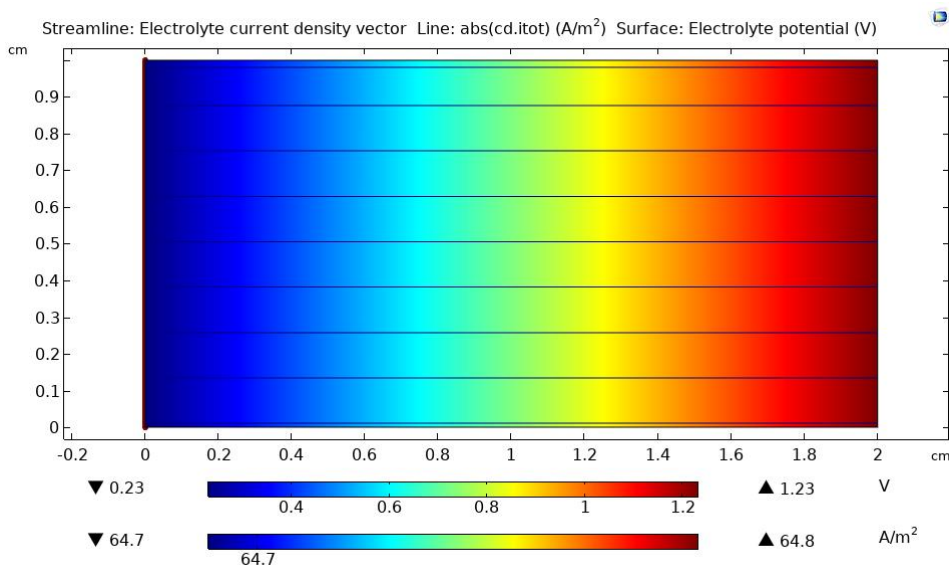


Figure 6.7. Two-dimensional PEC cell model for Pt|FTO cathode in the dark showing electrolyte potential and electrolyte current density distribution in the cell. The left side of the geometry represents the cathode to which a potential of $E^0(\text{H}^+/\text{H}_2) = 0 \text{ V}$ vs NHE was applied along with the Butler-Volmer relationship using the experimentally determined exchange current density value.

Simulation was repeated with different exchange current density values estimated from Tafel plots in Chapter 6.4.1 and similar results were obtained. The simulation with Pt|D3|NiO|FTO cathode gave current density of 6.1 mA cm^{-2} and with 1|NiO|FTO the result was also 6.1 mA cm^{-2} in the cell. Simulations with exchange current density values obtained for photocathodes under illumination did show only marginal difference in current density. This shows, that more complex model is needed to obtain more meaningful data, which would enable to model the photocathode performance. For example, a transient study with complex variables for the photocathode and the PEC cell in asymmetrical geometry.

6.5. Discussion

This model is a first attempt to computationally model the PEC cell and therefore also a simplification with several limiting assumptions. Mass transport phenomena like transport of diluted species was not included, but the results show that for more meaningful result it is needed. The potentials on electrodes and the cell potential was set to be constant and the only variable which was changed was the exchange current density. There are several different additional factors that affect the electrolyte current density and potential, which were not considered here. For example, the film resistance, recombination in the film, bubble formation, pH gradient in the electrolyte and mass transfer in the electrolyte. All these variables could be added to the model in the future studies when the model is optimised. In this study the aim was to build a model which could serve as a starting point for predicting current density distribution in the PEC cell when different photocathodes are used. The results of this initial study showed that the current density changes can be modelled in two dimensions when changing the exchange current density value in the boundary conditions applied to the electrolyte-photocathode interface and that the results showed increase in electrolyte current density when exchange current density was increased, as was expected. It was also shown that the electrolyte current density on the photocathode is uniformly distributed in this geometry, which is how it should be since additional variables were not applied. In future studies, the geometry of the cell could be changed to follow the change of electrolyte current density and to determine which geometries are not suitable for PEC cell. In addition, complexity to the model can be added by computing the cell in three dimensions in asymmetrical geometry.

The knowledge for future optimisation can be taken from the corresponding literature on PEC cell modelling. Even though the field is quite new, several studies have been made using different approaches and variable level of complexity for the models.³⁻¹⁸ Review by Gerischer discussed the general possibilities of modelling electrochemical devices coupled with semiconductors.³ Carver et al. and Haussener et al. carried out modelling studies on electrochemical devices focusing mostly on electrolyzers.^{4,5} Work by Berger et al. expanded the approach on the devices with membranes.^{6,7} A solar driven PEC cell modelling was introduced by Jin et al. taking into account pH gradients and membrane effect on the losses in the cell.⁸ They didn't include bubble formation on the electrodes but did show the current density distribution difference on the electrodes. This model was optimised further to take into account also the electrolyte flow in systems with membranes.⁹ Recently the work by Haussener et al. also included the temperature dependence when concentrated solar irradiation

is used.¹⁰⁻¹² The effect of perforations on PEC cell performance was studied by Hankin et al.¹³ A work on PEC cell modelling by Bedoya-Lora et al. is a good example of a full PEC cell model which can be taken as an example in future work to optimise the model.¹⁴ Their included a photocurrent density prediction using a Gärtner-Butler equation^{15,16}, surface recombination on electrode surfaces, mass transfer effects in the electrolyte and diffusion of dissolved species in the electrolyte. Most importantly, they also accounted for bubble formation and gas desorption on electrodes, which enabled the estimation of gas evolution efficiency. In their study they produced a one-dimensional model using COMSOL Multiphysics software, but their model can be optimised for two- or three-dimensional geometry.

6.6. Conclusions

In this chapter the exchange current densities for photocathodes Pt|D3|NiO|FTO, 1|NiO|FTO and 2|NiO|FTO were determined from experimental data and then applied in Butler-Volmer expression to create a PEC cell model. An initial proof-of-concept two-dimensional semi-empirical model of a PEC cell for electrolyte potential and electrolyte current density using COMSOL Multiphysics software was built. The exchange current density results showed highest exchange current density values for Pt|D3|NiO|FTO photocathode, both in the dark and under light illumination. For all photocathodes, the exchange current density increased under light illumination. The largest difference between the exchange current densities in the dark and under light illumination was observed for 2|NiO|FTO photocathode. The purpose of the PEC cell model was to serve as a starting point for future studies, where the model can be optimised. Therefore, the model was made with several simplifications and only the exchange current density as the changing variable. The modelling results showed the expected behaviour in the cell as the electrolyte current density increased on the photocathode when the exchange current density was increased. These results can be used to further optimise the model by applying additional variables and inputs described in literature.¹⁴

References

- 1 COMSOL Multiphysics. <https://www.comsol.com/products>
- 2 A. J. Bard, L. R. Faulkner, *Electrochemical Methods: Fundamentals and Applications*, 2nd Ed., 2001, 87-106.
- 3 Das et al., *Journal of Electroanalytical Chemistry*, 2007, 604, 72–90.
- 3 H. Gerischer, *Electrochim. Acta*, 1990, 35, 1677–1699.
- 4 C. Carver, Z. Ulissi, C. K. Ong, S. Dennison, G. H. Kelsall and K. Hellgardt, *Int. J. Hydrogen Energy*, 2012, 37, 2911–2923.
- 5 S. Haussener, C. Xiang, J. M. Spurgeon, S. Ardo, N. S. Lewis and A. Z. Weber, *Energy Environ. Sci.*, 2012, 5, 9922–9935.
- 6 A. Berger and J. Newman, *J. Electrochem. Soc.*, 2014, 161, E3328–E3340.
- 7 A. Berger, R. A. Segalman and J. Newman, *Energy Environ. Sci.*, 2014, 7, 1468–1476.
- 8 J. Jin, K. Walczak, M. R. Singh, C. Karp, N. S. Lewis and C. Xiang, *Energy Environ. Sci.*, 2014, 7, 3371–3380.
- 9 M. R. Singh, C. Xiang and N. S. Lewis, *Sustainable Energy & Fuels*, 2017, 1, 458–466.
- 10 S. Tembhurne and S. Haussener, *J. Electrochem. Soc.*, 2016, 163, H988–H998.
- 11 Y. K. Gaudy and S. Haussener, *J. Mater. Chem. A*, 2016, 4, 3100–3114.
- 12 T. Bosserez, L. Geerts, J. Rong'e, F. Ceysens, S. Haussener, R. Puers and J. A. Martens, *J. Phys. Chem. C*, 2016, 120, 21242–21247.
- 13 A. Hankin, F. E. Bedoya-Lora, C. K. Ong, J. C. Alexander, F. Petter and G. H. Kelsall, *Energy Environ. Sci.*, 2017, 10, 346–360.
- 14 F. E. Bedoya-Lora, A. Hankin, G. H. Kelsall. *J. Mater. Chem. A*, 2017, 5, 22683.
- 15 M. A. Butler, *J. Appl. Phys.*, 1977, 48, 1914–1920.
- 16 W. W. Gärtner, *Phys. Rev.*, 1959, 116, 84–87.

Chapter 7. Conclusions

During my PhD project the aim was to investigate new hybrid dye-sensitised photocathodes for photoelectrochemical water splitting and develop a system that would enable efficient photoelectrochemical H₂ production.

First, the NiO based dye-sensitised photocathode benchmarking was carried out under different experimental conditions to understand the effect of the experimental environment on the photoelectrochemical performance of the dye-sensitised NiO photocathode and to study how the performance is influenced by each different parameter. The optimal conditions were determined and applied in further studies to compare the performance of different dyes on NiO and the determined the H₂ evolution efficiency with different catalysts.

This study led to the investigation of a new approach to increase the faradaic efficiency of dye-sensitised photocathodes for H₂ evolution from water using integrated photocatalysts instead of separate dye and catalyst. Superiority to previously reported photocathodes was demonstrated, showing higher photocurrent and high faradaic efficiency. In addition, surface analysis of the photocathodes before and after photoelectrocatalysis revealed that the photocatalyst was photochemically stable, highlighting the benefits of the approach towards robust, hybrid solar-to-fuel devices.

Thirdly, an alternative photocathode material to NiO was studied. Stable H₂ production on the CuCrO₂ photocathode from water was shown and the efficiency of the process was further increased with the use of inorganic cobalt co-catalyst in solution. It was also observed that the post-calcination of the photocathodes under N₂ atmosphere changes the surface chemistry of the CuCrO₂ photocathodes which translates into superior stability and efficiency. In addition, successful sensitisation of the CuCrO₂ photocathode with an organic dye was demonstrated resulting in considerable increase in photocurrent when using electron acceptor in solution.

Finally, a proof-of-concept modelling study of a PEC cell was performed using experimental parameters obtained during studies discussed in Chapters 3 and 4. A simplified model of the PEC cell was created based on exchange current density data for different photocathodes. This model can serve as a starting point for future development and optimisation of multiphysics models, which can then be used to predict the PEC cell performance with different materials under different experimental conditions.

Future research could focus on the further development of the integrated photocatalysts that can be used with NiO. It would also be beneficial to develop photocatalysts based on earth-abundant elements. The post-catalysis surface analysis should be applied as a standard characterisation for photocathodes to further increase the understanding of the stability of the systems. Future research on CuCrO₂ photocathodes could focus on decreasing the particle size to increase the active surface area, which could also lead to enhanced dye adsorption. Ball milling could be one of the techniques which could be used for that purpose. In addition, further studies on long term stability of the CuCrO₂ with different catalysts could be beneficial to determine the limitations of the system and find the most suitable catalyst for H₂ production.

Appendix

Appendix to Chapter 3

Figures A1 – A2

Appendix to Chapter 4

Figures A3 – A12

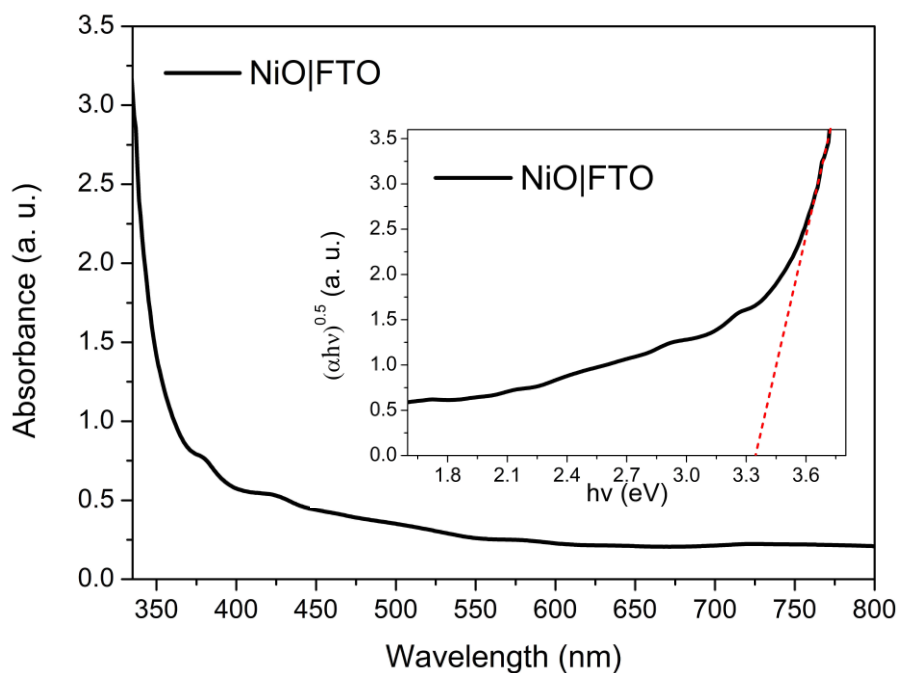


Figure A1. UV-vis of nanostructured 3-layer NiO film deposited on FTO. Inset – Tauc plot constructed from UV-vis data to determine the indirect band gap of NiO.

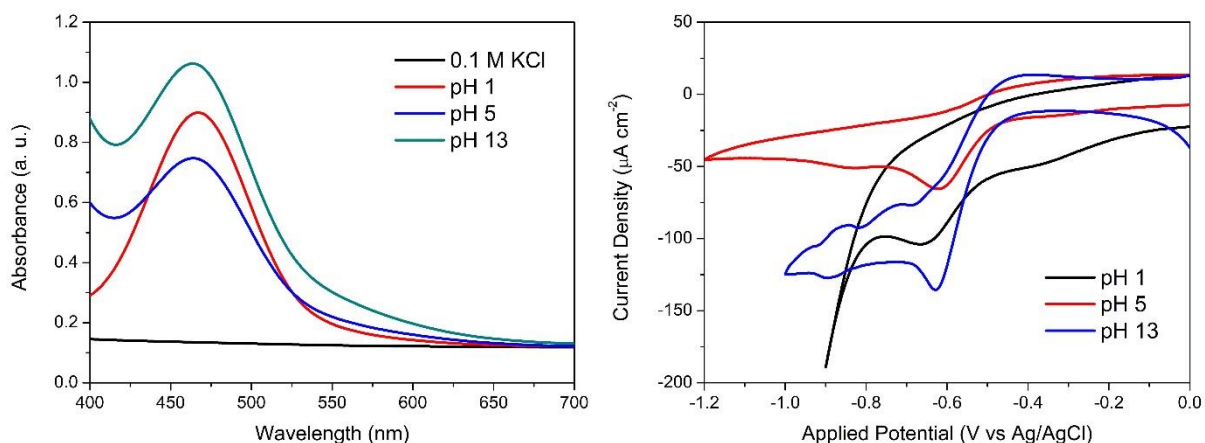


Figure A2. Left – UV-vis spectra of 10 mM $[\text{Co}(\text{en})_3]\text{Cl}_2$ in 0.1 M KCl with different pH: pH1 – red, pH 5 – blue, pH 13 – green, 0.1 M KCl without EA – black. Right – CV of the same $[\text{Co}(\text{en})_3]\text{Cl}_2$ solutions in 0.1 M KCl with different pH: pH1 – black, pH 5 – red, pH 13 – blue.

Appendix to Chapter 4

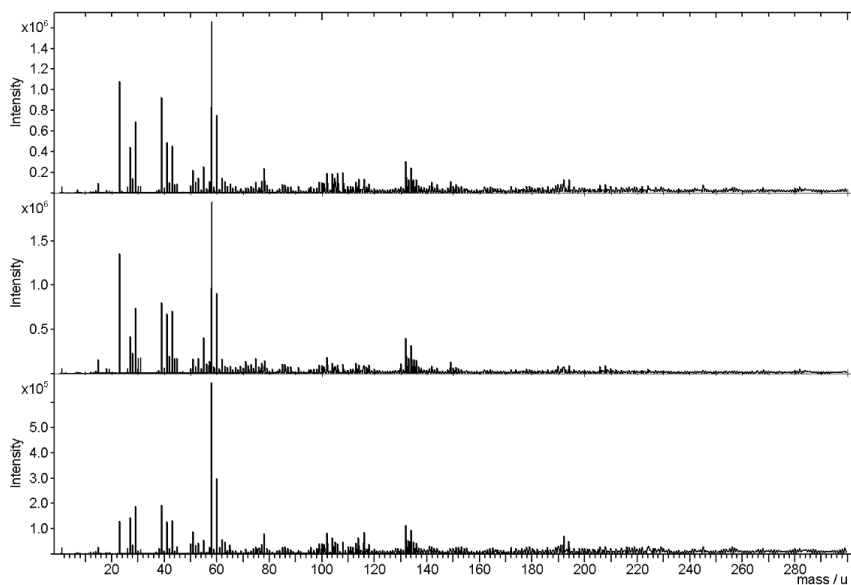


Figure A3. ToF-SIMS positive ion spectra of 1|NiO taken from three different samples: top: – pre-catalysis, middle: post-catalysis -0.4 V vs. Ag/AgCl, and bottom: post-catalysis at -0.6 V vs. Ag/AgCl. 0 – 300 mass / u range. Ni^+ calcd. $m/z = 58$.

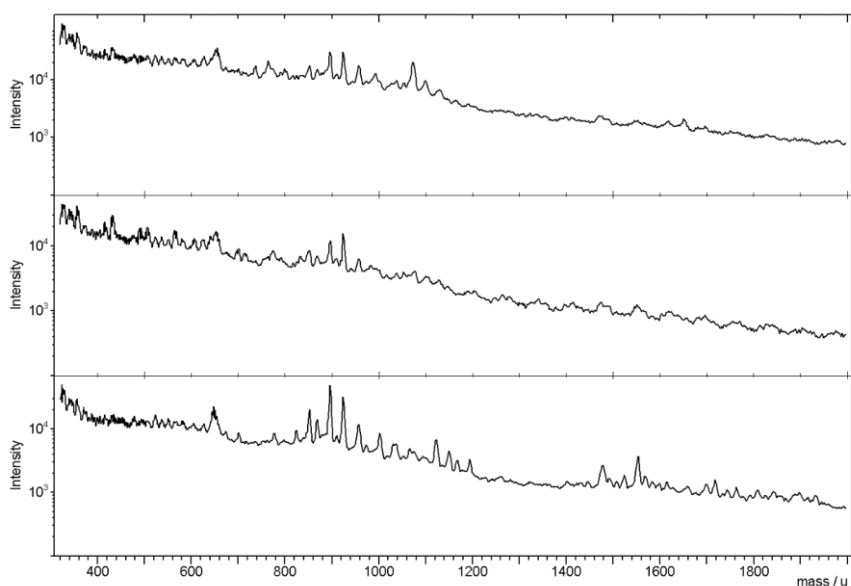


Figure A4. ToF-SIMS positive ion spectra of 1|NiO taken from three different samples: top: – pre-catalysis, middle: post-catalysis at -0.4 V vs. Ag/AgCl and bottom: post-catalysis -0.6 V vs. Ag/AgCl. 300 – 2000 mass / u range.

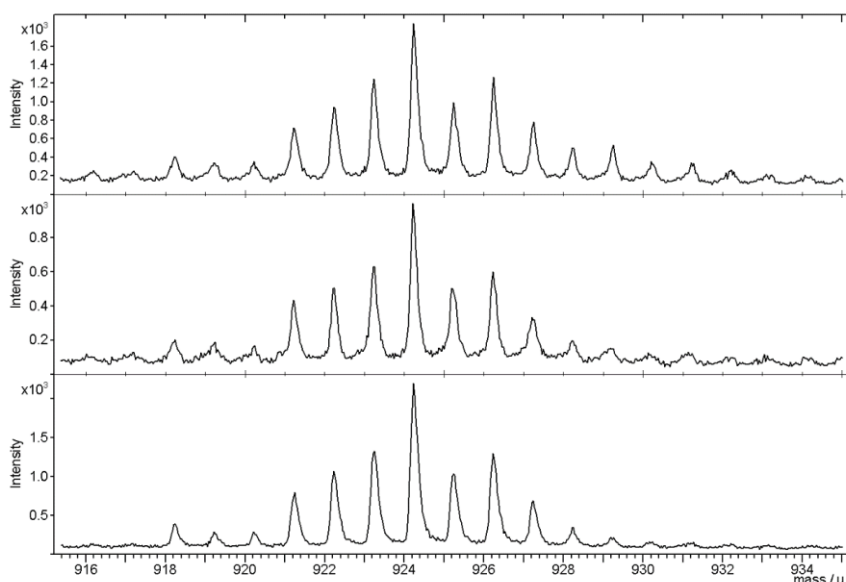


Figure A5. ToF-SIMS positive ion spectra of 1|NiO taken from three different samples: top: – pre-catalysis, middle: post-catalysis at -0.4 V vs. Ag/AgCl and bottom: post-catalysis -0.6 V vs. Ag/AgCl. 915 – 935 mass / u range. $[\text{Ru}(\text{dceb})_2(\text{bpt})]^+$ calcd. $m/z = 924$.

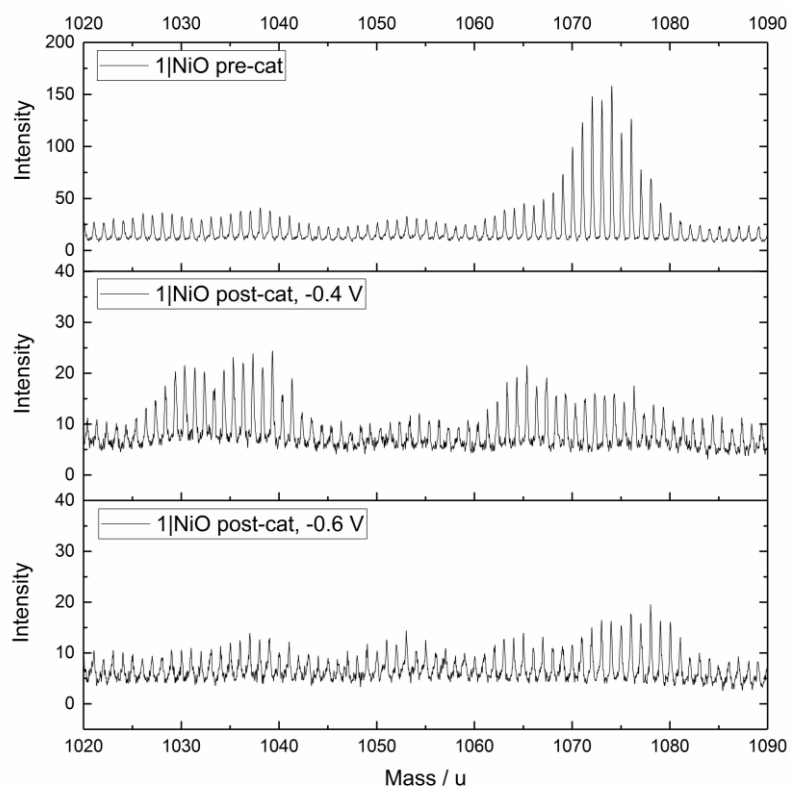


Figure A6. ToF-SIMS positive ion spectra of 1|NiO taken from three different samples: top:– pre-catalysis, middle: post-catalysis at -0.4 V vs. Ag/AgCl and bottom: post-catalysis -0.6 V vs. Ag/AgCl. 1020 – 1090 mass / u range. $[\text{Ru}(\text{dceb})_2(\text{bpt})\text{Pd}]^{2+}(\text{Cl}^-)$ calcd. $m/z = 1065$, $[\text{Ru}(\text{dceb})_2(\text{bpt})\text{Pd}]^{2+}$ calcd. $m/z = 1030$.

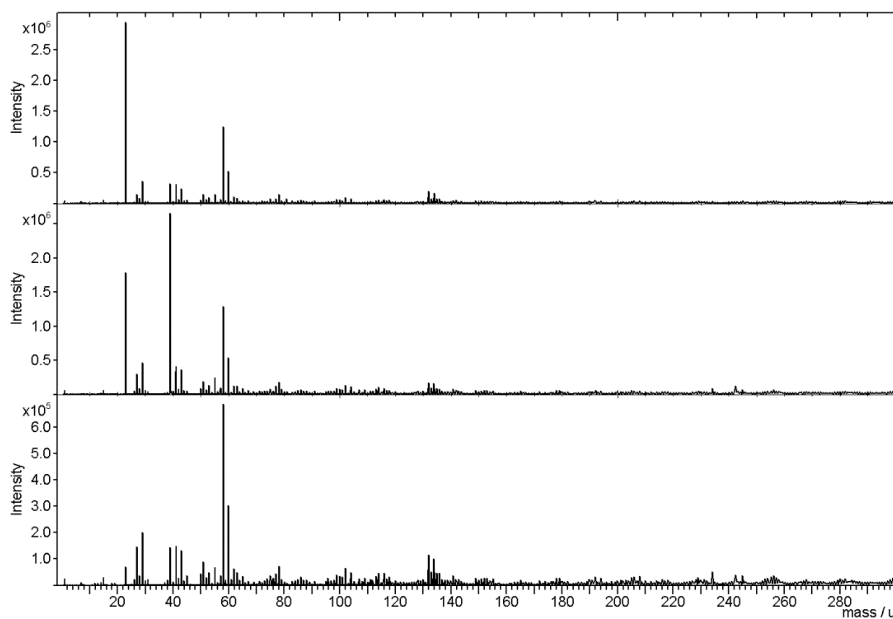


Figure A7. ToF-SIMS positive ion spectra of 2|NiO taken from three different samples: top: – pre-catalysis, middle: post-catalysis at -0.4 V vs. Ag/AgCl and bottom: post-catalysis -0.6 V vs. Ag/AgCl. 0 – 300 mass / u range. Ni^+ calcd. $m/z = 58$.

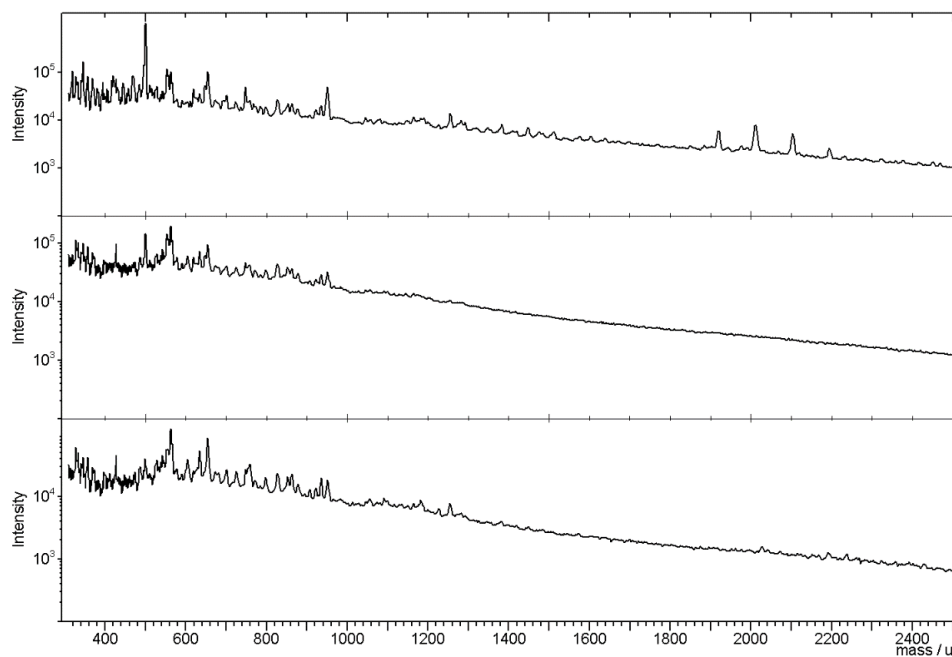


Figure A8. ToF-SIMS positive ion spectra of 2|NiO taken from three different samples: top: – pre-catalysis, middle: post-catalysis at -0.4 V vs. Ag/AgCl and bottom: post-catalysis -0.6 V vs. Ag/AgCl. 300 – 2500 mass / u range.

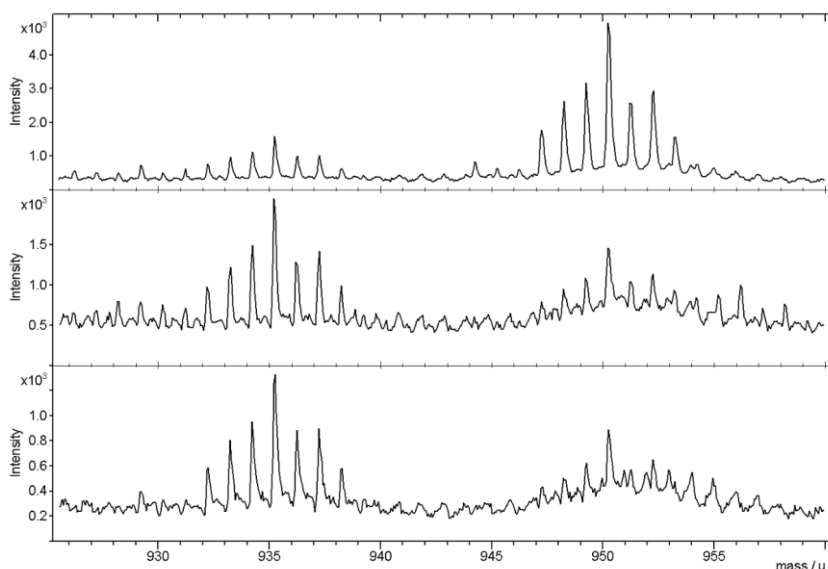


Figure A9. ToF-SIMS positive ion spectra of 2|NiO taken from three different samples: top: – pre-catalysis, middle: post-catalysis at -0.4 V vs. Ag/AgCl and bottom: post-catalysis -0.6 V vs. Ag/AgCl. 925 – 960 mass / u range. $[\text{Ru}(\text{bpy})_2(2,5\text{-bpp})]^+$ calcd. $m/z = 935$, $[\text{Ru}(\text{bpy})_2(2,5\text{-bpp})]^{2+}(\text{OH}^-) = 951$.

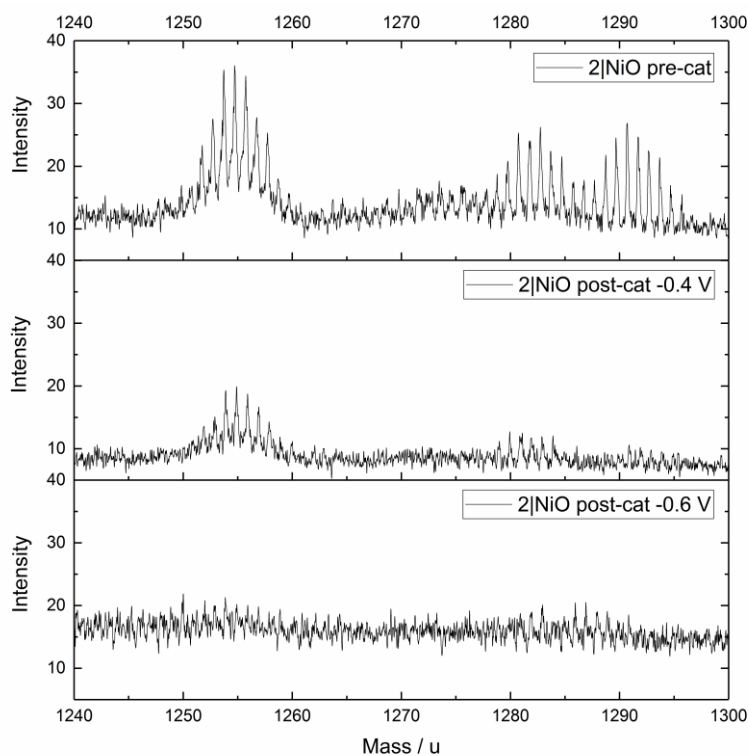


Figure A10. ToF-SIMS positive ion spectra of 2|NiO taken from three different samples: top: – pre-catalysis, middle: post-catalysis at -0.4 V vs. Ag/AgCl and bottom: post-catalysis -0.6 V vs. Ag/AgCl. 1240 – 1300 mass / u range. $[\text{Ru}(\text{bpy})_2(2,5\text{-bpp})\text{PtI}]^+$ calcd. $m/z = 1255$, $[\text{Ru}(\text{bpy})_2(2,5\text{-bpp})\text{PtI}]^+ \text{CH}_3\text{CN}$ calcd. $m/z = 1296$.

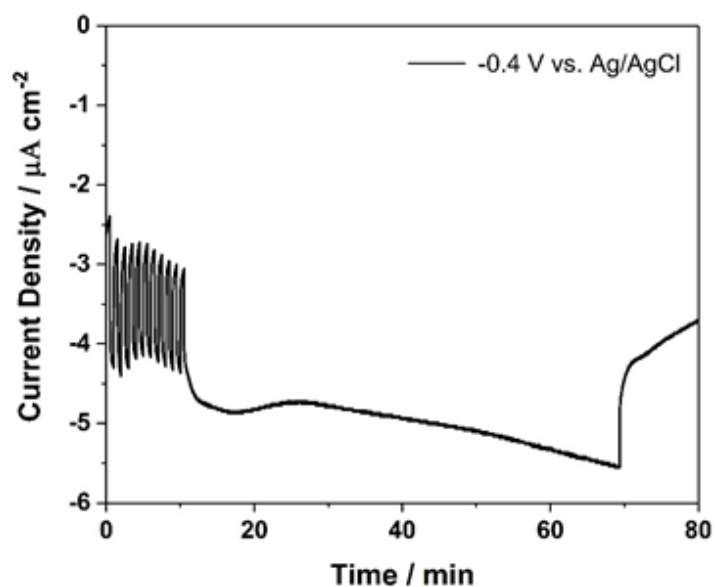


Figure A11. Chronoamperometry measurement of tris(2,2'-bipyridine-4,4'-dicarboxylic acid)-ruthenium(II) dichloride | NiO in pH 3 aqueous electrolytes with 0.1 M potassium hydrogen phthalate. $E_{\text{appl}} = -0.4 \text{ V vs. Ag/AgCl}$ reference electrode (3.0 M NaCl). Chopped light illumination was applied with 30 s intervals (10 cycles of dark current/photocurrent) followed by constant light illumination. Small photocurrent ($1.5 \mu\text{A}$) was recorded, but no hydrogen was detected when outlet gas from the PEC cell was analysed.

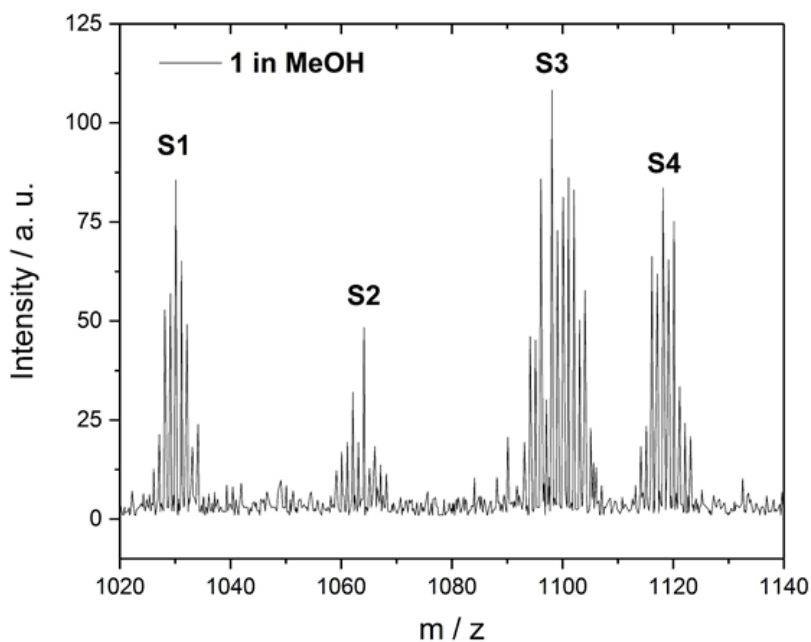


Figure A12. Mass Spectrometry of photocatalyst 1 in MeOH. Positive ion spectra. S1 - $[\text{Ru}(\text{dceb})_2(\text{bpt})\text{Pd}]^{2+}$ calcd. $m/z = 1030$, S2 - $[\text{Ru}(\text{dceb})_2(\text{bpt})\text{Pd}(\text{CH}_3\text{OH})]^{2+}$ calcd. $m/z = 1063$, S3 - $[\text{Ru}(\text{dceb})_2(\text{bpt})\text{Pd}(\text{CH}_3\text{OH})(\text{H}_2\text{O})_2]^{2+}$ calcd. $m/z = 1098$, S4 - $[\text{Ru}(\text{dceb})_2(\text{bpt})\text{Pd}(\text{CH}_3\text{OH})(\text{H}_2\text{O})_3]^{2+}$ calcd. $m/z = 1117$. Cl^- is substituted with MeOH in solution.